QUANTITATIVE MICROSCOPY WORKFLOWS FOR THE STUDY OF CELLULAR RECEPTOR TRAFFICKING

by

JEREMY ANDREW PIKE

A thesis submitted to
The University of Birmingham
for the degree of
DOCTOR OF PHILOSOPHY

PSIBS Doctoral Training Center
The University of Birmingham
June 2016

Abstract

The process of cellular signalling and signal transduction is a vital process enabling cells to respond to and interact with their environment. Extracellular signalling molecules bind to receptors on the plasma membrane, which in turn are internalised to endosomes and trafficked to various locations. The trafficking and signalling of receptors are complex, intertwined processes with many feedback mechanisms, often regulated by groups of small GTPases, Guanine exchange factors (GEFs) and GTPase activating proteins (GAPs).

Confocal microscopy is a powerful tool to study the trafficking of receptors. Within the field, quantitative methods to acquire and analyse data are often poorly specified, manual, biased and lacking in reproducibility. In this work, robust, quantitative workflows and tools to quantify and visualise receptor localisation, with and without endosomal colocalization, are presented with epidermal growth factor receptor (EGFR) used as a model system.

Specific attention is given to 4D (3D time-lapse) live cell confocal microscopy. A state of the art 4D level set approach is developed to enable the accurate cellular segmentation using only EGFR-GFP signal. Additionally it is used for label free nuclear segmentation. Temporal constraints are introduced to further improve segmentation accuracy. This novel approach is thoroughly validated, and statistically significant performance increase over equivalent 2D and 3D approaches is demonstrated. These techniques could be adapted and used for a large variety of segmentation problems.

A critical review of current approaches to the quantification of colocalization between receptors and endosomes is presented. Improvements to existing techniques and complete workflows are provided. These approaches are validated and used to quantify colocalization between EGFR and early endosomes after ligand stimulation in the presence of various drug treatments.

Finally a confocal microscopy siRNA screen of GEFs and GAPs is presented. Quantitative methods to identify genes which perturb the trafficking of receptor are presented. Together the screen and 4D live cell protocols provide a complete microscopy based platform to identify and investigate regulators of receptor signalling and trafficking.

ACKNOWLEDGEMENTS

I would like to express my gratitude to my supervisors; John Heath, Joshua Rappoport and Iain styles for their guidance throughout my PhD. I would also like to thank Debbie Cunningham for the SILAC data, EGFR-EGFP HeLa cell line and advice. Additionally, all previous members of the Rappoport lab, in particular; Abdullah Khan, William Pikeathly, Julie Mazzolini, Emily Guggenheim, Laura Lewis and Phil Smith. I am also greatful to the rest of the 8th floor, in particular Alessandro Di Maio and the Tomlinson lab.

Throughout the entire PhD my soon to be wife; Cathy, and my parents; Kevin and Sue, have kept me going. I couldn't have done it without you!

Finally, I would like acknowledge the EPRSC for funding through a studentship from the PSIBS Doctoral Training Center (EP/F50053X/1).

CONTENTS

LIST OF FIGURES

List of Tables

Conventions

p-values and significance stars

Unless otherwise stated the use of one or more asterisks within a figure corresponds to the following levels of significance;

$$* \rightarrow p < 0.05,\ ** \rightarrow p < 0.01,\ *** \rightarrow p < 0.001;$$

In the case of multiple hypothesis testing levels are based on corrected p-values.

CHAPTER 1

THESIS AIMS AND CONTRIBUTIONS

1.1 Background

Cellular receptor signalling and trafficking are highly interlinked and essential processes [1]. Fluorescence microscopy provides a powerful tool to investigate these processes and the cross-talk between them. Microscopy based screens can be used to identify regulators of signalling and trafficking [2, 3, 4, 5]. RNA interference is used to inhibit the expression of individual genes and screens can be performed across a range of genes, up to whole genome level. Cells are treated with ligand and the subsequent imaging of fluorescently labelled receptor, or ligand, can be used to identify genes which regulate trafficking. To do this, image analysis workflows are employed to extract relevant measurements from the image data. For example, endosome number, size and clustering, the percentage of internalised receptor and cell shape and size can all be quantified [3].

In addition to screening applications, confocal, or deconvolved wide-field, microscopy can be used to validate hits and study how a specific treatment regulates the trafficking of receptor. It is advantageous to perform such studies using live cell time-lapse data to better capture the temporal dynamics of the trafficking. Performing the acquisition in 3D is also superior, as the entire cellular volume can be sampled. In this work, two different strategies are considered. The first identifies sub-cellular regions of interest (ROIs). The relative intensity of fluorescently labelled receptor, or ligand, is quantified for each ROI. Typically, this approach is used to quantify receptor internalisation by placing a ROI around the edge of the cell, and another ROI in the interior [6, 7].

The second strategy uses an additional flurophore to label sub-cellular structures of interest, for example early endosomes, or lysosomes. Pixel based colocalization analysis can then be performed to quantify the co-occurrence and correlation between the receptor and the secondary marker [8, 9]. It is important to identify if either the level of colocalization is higher than what one would expect for randomly distributed signal, or if there is a change in the level of colocalization between conditions [10].

1.2 Aims

Cellular segmentation is conventionally a key step in the image analysis workflows used to quantify receptor trafficking. One important aim of this work is to develop robust and accurate protocols to segment the cellular boundary using only the signal from a fluorescently labelled receptor. This problem is relatively simple if the majority of the receptor is membrane bound but after ligand treatment, when the majority of the receptor can be internalised, it is complex.

We also aim to develop adaptable workflows for the screening of trafficking regulators using 2D fixed cell confocal microscopy. These workflows should be applicable for small to medium scale screens, and should be suitable as a secondary screening protocol, using the results of larger screens. We propose to take the results from a SILAC protemics screen and then apply our microscopy based protocol to identify GEFs and GAPS which are regulators of trafficking. To do this we aim to construct a single ROI based measurement which should characterise changes to the trafficking response. We choose to define, and use, a single measure only so that robust statistical tests can be used without losing significance as a result of multiple hypothesis correction.

Screen hits can be further validated using 3D time-lapse microscopy. Therefore our final key aim is to develop adaptable workflows for this purpose. Specifically, the workflows should verify and classify temporal changes to the ligand induced trafficking response. To do this we propose to extend the ROI based approach, where a single ROI is placed at the membrane, to a band-based analysis of the entire cellular volume. We should also develop workflows for the visualisation and quantification of colocalization between receptor and endosomes. These workflows should employ current best practice and be able to identify population level changes in colocalization, both between treatments and between time-points.

1.3 Contributions

In chapter 3 we present, to the best of our knowledge, the first application of 4D level set segmentation to microscopy datasets. This approach uses a single level function to segment the entire 4D volume [11, 12]. By incorporating temporal information, a statistically significant improvement in segmentation performance, over equivalent 3D and 2D implementations, is demonstrated. Two seminal level set frameworks are extended to 4D, specifically the geodesic edge based and Chan-Vese region based formulations [13, 14]. To the best of our knowledge we are the first to implement an edge based level set framework in 4D. In all cases a distance regularized level set evolution term is introduced to the energy functional. This prevents the need for re-initialization and facilitates a simple finite difference update scheme. Novel strategies for the scaling of the temporal derivatives are presented. Finally, temporal constraints are introduced to further improve segmentation performance. For example the segmentation can be encouraged to maintain a constant volume over time.

In chapter 4, a single measurement strategy for the analysis of fluorescent microscopy based RNA interference screens for receptor trafficking is presented. In the proposed measure, the cellular volume is split into banded regions based on distance from the cellular edge. The percentage of total cellular receptor in each band is then calculated. This characterises the sub-cellular receptor distribution based on distance from the membrane. A robust statistical analysis is then presented to identify hits using this banded measure. A siRNA screen, across sixteen GEFs and GAPs, using 2D fixed cell confocal microscopy is performed. Five hits are identified. Specifically IQSEC1, VAV2, TBC1D10B, TBC1D5 and USP6NL.

In chapter 5, adaptable workflows for the quantification of receptor trafficking using live cell 4D datasets are presented. In all workflows cellular and nuclear segmentation is facilitated using the 4D level set protocols introduced in chapter 3. The band-based measure introduced in chapter 4 is extended to 3D and used to characterise the change in receptor distribution over time. We also present automated protocols to quantify receptor colocalization with endosomal sub-populations over time. These approaches are validated by perturbing the trafficking response with three drug treatments; dynasore, AG1478 and dasatanib. Using the band-based workflows, statistically significant changes to ligand induced trafficking response are observed for the dynasore and AG1478 treated populations (relative to an untreated control). Using the colocalization workflows, a statistically significant change in the level of co-occurrence between EGFR and rab5 positive endosomes is demonstrated for the dynasore and AG1478 treated populations.

CHAPTER 2

INTRODUCTION

2.1 Receptor Tyrosine Kinase Signalling

2.1.1 Structure

In 1954 neuronal growth factor was first described [15] and in 1962 epidermal growth factor (EGF) was discovered and purified from mouse salivary gland extracts [16]. Over a decade later the cellular EGF receptor, EGFR, was identified and shortly after the intrinsic kinase activity was demonstrated [17, 18]. Since this seminal work, fifty-eight receptor tyrosine Kinases (RTKs) have been identified in the human genome, which in turn can be divided into twenty subcategories [19]. Cellular signalling by RTKs regulates a wide range of important processes including embryonic development, mitosis, cell cycle control, differentiation, apoptosis, cell migration, and wound healing [20, 21, 22, 23, 24, 25]. Since RTKs are key regulators in so many pivotal processes, aberrant signalling can dramatically affect the development and progression of numerous diseases, including cancer [26].

All RTKs are transmembrane spanning and have a conserved architecture. The intracellular region consists of a juxtamembrane region, a tyrosine kinase domain(s) and a carboxyl(C-) terminal. The extracellular region contains ligand binding domains which are linked to the intracellular region via a transmembrane helix [27]. Inactive, plasma membrane localised receptors usually exist as monomers which oligomerise when activated by ligand binding [28]. However in some cases RTKs exist as oligomers before ligand binding [29]. Upon ligand binding and oligomerization, a stable complex is formed and conformational changes activate the tyrosine kinase domain. This triggers the autophosphorylation of various intracellular sites which is performed in a controlled and precise order [30, 31]. Following activation, a highly regulated combination of signalling and scaffolding proteins are recruited to the activated sites, which in turn triggers downstream signalling cascades.

2.1.2 Epidermal Growth Factor Receptor and the ERBB Receptor Family

This thesis uses the epidermal growth factor receptor (EGFR) as a platform for the development of both computational and experimental workflows designed for more generalised use in the field of receptor trafficking and signalling. EGFR and its ligand, EGF, were one of the first receptor-ligand systems to be discovered and is still the subject of extensive study [17]. Therefore by using EGFR as a platform we aim to reach the largest possible audience. However, EGFR is not a prototypical RTK and has a distinct structure and function [32, 33].

EGFR (also known as ERBB1) is part of the ERBB family of RTKs which has three other members; ERBB2/3/4. ERBB receptors are expressed in tissue types of epithelial, mesenchymal and neuronal origin and mediate a wide range of biological responses. ERBB ligands can be split into three subgroups [34]. The first has specificity for EGFR and consists of EGF, amphiregulin, transforming growth factor receptor-α (TGF-α) and epigen. The second has specificity for EGFR and ERBB4 and includes heparin binding EGF, epiregulin and betacellulin. The final group has specificity for ERBB3 and ERBB4 and consists of neuregulins. Consequently, EGFR has a total of seven known ligands [33].

Interestingly, ERBB2 has no known ligands and ERBB3 has no significant kinase activity. However, both can form hetero-dimers (or oligomers) with other family members to initiate ligand stimulated signalling. Furthermore ERBB2 is the preferred partner of other family members (including EGFR), acting as an amplifier by initiating prolonged and extensive activation of signalling pathways [35, 36].

The mechanism of ligand dependent activation for ERBB receptors is unusual in that it is entirely receptor mediated and the ligands themselves are not involved directly in the dimerisation interface [37]. Upon ligand binding, the conformation of the receptor changes to expose extracellular binding sites which allows direct dimerisation between receptors [38]. The intracellular tyrosine kinase domains consist of an activation loop, a N-Lobe and a C-lobe. These three components interact to remove auto-inhibitory interactions and allow the kinase domains to adopt active conformations. Again the ERBB mechanism is unusual in that the dimer is asymmetric and no activation loop phosphorylation is required [39, 40]. Therefore the active confirmation is achieved solely by conformational changes within the dimer.

2.1.3 The EGFR Signalling Network

After ligand binding, dimerization and the activation of the intracellular kinase domains, specific tyrosine residues are trans-autophosphorylated in a controlled and precise order [30]. This second phase of activation enables the recruitment of cytoplasmic proteins with either Src homology 2 (SH2) or phospho-tyrosine binding (PTB) domains [28]. This is followed by the corresponding recruitment of docking proteins, either directly or indirectly via adaptor proteins. For example growth-factor-receptor bound-2 (GRB2), Src-homology-2-containing (Shc) and signal transducer and activator of transcription-5 (STAT5) are all recruited directly to activated EGFR [41]. This feeds into a complex network of signalling cascades and feedback mechanisms (figure 2.1). Key pathways ac-

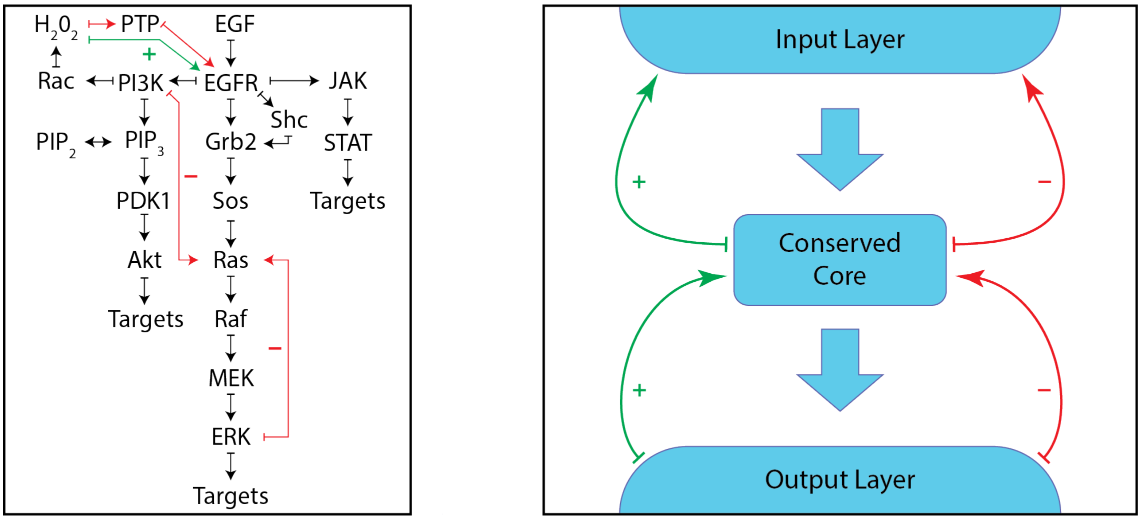

(a)

(b)

Figure 2.1: The EGFR signalling network. (a) Activation and auto-phosphorylation of EGFR triggers a complex network of signalling pathways with built in positive and negative feedback loops. (b) The EGFR signalling network has a *bowtie* architecture. The analogue early response phase consists of many variable inputs, including ligand type and concentration and binding partner identity. Input information is processed by the conserved core, including the MAPK/ERK and PI3K/AKT signalling structures. Finally the binary outputs are implemented often transcriptionally by the outer layer. All three layers communicate and regulate the overall response by early and late response feedback mechanisms. Figure adapted from [28].

tivated by EGF stimulation of EGFR include the MAPK/ERK, PI3K/AKT, PLC/PKC and JAK/STAT pathways [42]. Pathways have characteristic functional outputs, for example the MAPK/ERK pathway is linked to cell cycle entry and PI3K/AKT to cell survival and cell proliferation [43, 44, 45, 46]. Describing the details of this network is beyond the scope of this study, however a basic understanding of the overall structure of the network and the mechanisms employed to regulate it is important.

The EGFR signalling network can be effectively modelled with *bowtie* configuration consisting of three key components (figure 2.1)[47]. The first component, the *input layer*, consists of a broad range of analogue signals. Signals from the input layer are interpreted and processed by a highly conserved *core*, the second component, to produce a digital decision. This decision is then implemented by the 3rd layer, the *output layer*, to produce functional results.

This structure provides robustness which in turn ensures that the network can process inconsistent signals and minimise the effects of system damage [36]. Crucially the network is modular, consisting of autonomous sub-systems. At every level the network has extensive redundancy. Redundancy is the existence of non-identical components which achieve the same result. This allows the system to achieve a result even if some components are perturbed, damaged or inactive.

The three layers are heavily interlinked with feedback mechanisms providing highly sensitive regulation. These mechanisms control and tune signalling amplitude, duration and response, and can either be positive or negative, increasing or decreasing the response.

Feedback can be split into two categories; early and late response. A key component of early response regulation is the control of endocytosis, trafficking and degradation. This is discussed in more detail in section 2.2. Regulation is also often achieved by upstream or inter-pathway phosphorylation events [48]. For example ERK phosphorylates an inhibitory site of RAS, an upstream component of the MAPK/ERK pathway, hence attenuating signalling for this specific pathway [49]. Conversely, activity in the PI3K/AKT pathway will enable PI3K to phosphorylate RAS hence providing an additional route for negative regulation of the MAPK/ERK pathway [50].

Additionally, signalling can be regulated by direct de-phosphorylation of EGFR kinase by protein tyrosine phosphatases (PTPs) [51]. Furthermore, as an example of positive feedback, EGFR signalling can induce rapid production of hydrogen peroxide which inhibits PTPs and reduces de-phosphorylation of EGFR [52, 53].

The regulation mechanisms discussed so far are all early response and are the most relevant class with respect to this study. Late responses are typically transcriptional and drive the production of new RNA and proteins, which in turn regulates signalling [48]. These responses can begin to affect signalling approximately 45 minutes post EGF stimulation.

Finally microRNAs provide an alternative mechanism for signal regulation [54, 55, 56]. MicroRNA targets specific mRNA molecules to suppress protein expression and act on both early and late time-scales. Avraham *et al.* (2010) show a coordinated reduction in miRNA in response to EGF and demonstrate that miRNA can act as attenuators of EGFR signalling [57].

2.2 Regulation of Signalling through Endocytosis and Trafficking

Endocytosis, trafficking and signal transduction are heavily interconnected processes with complex regulatory structure. In this section we cover the fundamental mechanisms of endocytosis and trafficking before discussing the connection with signalling with an emphasis on the ERBB family. Finally, we discuss with examples, how the cross-linking of these systems can influence development and disease, with an emphasis on cancer.

2.2.1 Endocytosis

Once activated, receptor activity is controlled by internalisation and manipulation in various endocytic pathways. For RTKs, clathrin mediated endocytosis (CME) is the most well characterised mechanism for receptor internalisation, and in most cases is thought to be dominant (figure 2.2) [58, 59]. However, it has been shown that clathrin independent endocytosis (CIE) such as the caveolar or dynamin independent CDC42 regulated mechanisms play an important role [60]. Interestingly, Sigismund *et al.* (2005) provide evidence that low EGF concentrations induce predominantly CME of EGFR whereas high concentrations result in a roughly equal ratio of CME to CIE [61]. Moreover a follow up study revealed that most EGFR internalised by CME was recycled back to the plasma membrane, attenuating the signalling response. Conversely, CIE was shown to commit

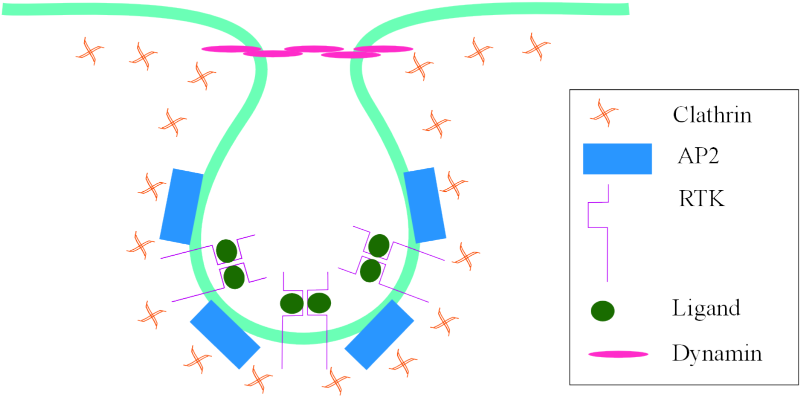

Figure 2.2: Clathrin mediated endocytosis of RTKs. A simple model for clathrin mediated endocytosis of RTKs [64]. Activated receptors cluster in clathrin rich regions of the membrane. The membrane invaginates in these clathrin rich regions, encapsulating a cargo of receptors and adaptor proteins including AP2. The mechanisms which control and trigger the formation of these clathrin coated pits (CCPs) are complicated and much remains to be understood. It is clear that AP2 plays a crucial role in the recruitment and stabilisation of the clathrin coat. The GTPase dynamin plays a crucial role in the formation of a constricting ring which severs the CCP from the plasma membrane.

EGFR to eventual degradation in lysosomes [62]. Therefore it is concluded that ligand concentration and the endocytic entry route can combine to regulate the amplitude of a signalling response. Moreover a recent study has shown that the ubiquitination of EGFR is a threshold controlled process and strongly correlated to EGF concentration and endocytic entry route [63]. Receptor ubiquitination plays a pivotal role in the designation of receptor for degradation and is mediated by the direct recruitment of Cbl (a family of ubiquitin protein ligases) and Grb2. Together, these studies show that EGF concentration can regulate receptor ubiquitination and the ratio of CIE. This is turn has consequences for receptor degradation rate, signal amplitude and duration.

Ligand type can also influence the ratio of CIE and thus regulate signal attenuation. Henriksen *et al.* (2013) suggest that EGF treatment initiates only CME, whereas other ligands including heparin-binding EGF induced both CME and CIE [65]. Note that this contradicts the Sigismund *et al.* studies discussed above [61, 62, 63]. Both studies use the

HeLa cell line so this contradiction is attributed to variation in EGFR expression level, thus suggesting another layer of regulation. Clearly much remains to be understood about the mechanisms controlling the endocytic entry routes for EGFR [66].

The use of ligand concentration to control endocytic entry route is not unique to EGFR; De Donatis *et al.* (2008) propose that for platelet derived growth factor receptors (PDGFRs), the route of endocytosis is used as a switch to determine if signalling triggers proliferation or migration [67]. The control for this switch is shown to be ligand concentration such that high ligand concentration triggers CIE and a proliferation response, whereas low ligand concentration triggers CME and a migratory response. This example also demonstrates that endocytosis and trafficking are not simply a means to control signal amplitude and duration, through either inactivation or degradation of receptor, but can have functional influence. This is a key concept which will be discussed further in the next section.

2.2.2 The Endocytic Network

Once internalised, receptors are processed within the endocytic network (figure 2.3) and (predominantly) designated for one of two destinations: recycling back to the plasma membrane or eventual degradation in lysosomes. The regulation of this network is complex and intrinsically interlinked to the receptor signalling response (figure 2.1).

The reversible ubiquitination of receptor plays a prominent role in the regulation of receptor trafficking and, as noted in the previous section, this can be regulated by the endocytic route of entry [71]. Importantly, ubiquitinated receptor is identified and sorted into intraluminal vesicles within multi-vesicle bodies (MVBs) by the ESCRT (endosomal sorting complexes required for transport) machinery, a *point of no return* for a degradative receptor fate.

Interestingly, the dimer partner of a receptor can influence its trafficking [72]. For

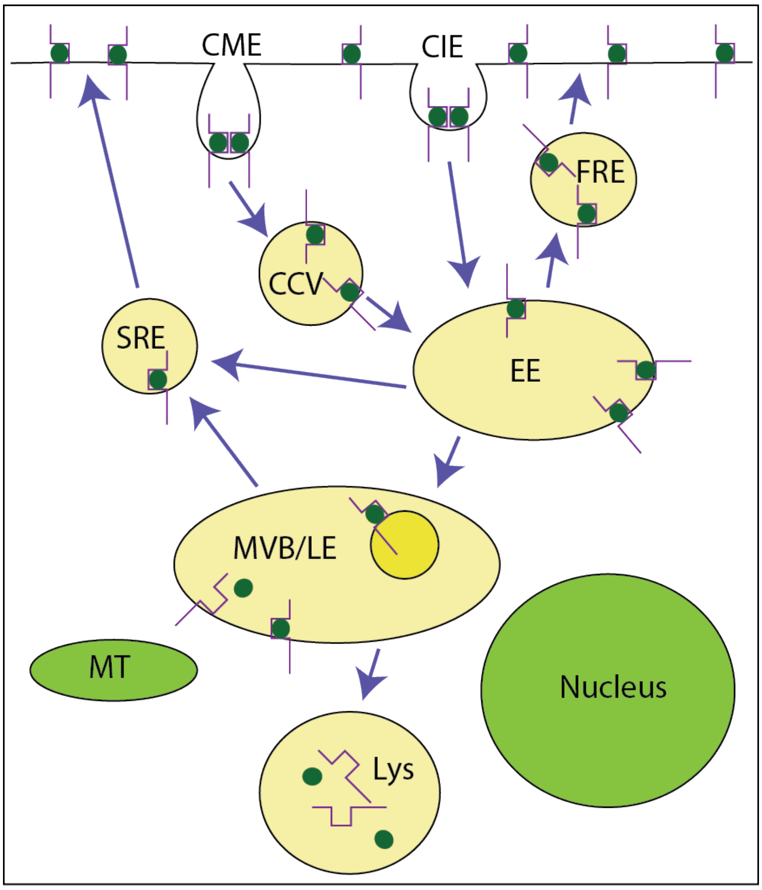

Figure 2.3: The endocytic network. Once internalised by either clathrin mediated (CME) or clathrin independent endocytosis (CIE), vesicles fuse with early endosomes (EE). Note clathrin coated vesicles (CCV) lose their coat before fusion with EEs. RTKs in early endosomes can then either be recycled back to the plasma membrane or remain in early endosomes which mature to form multi vesicular bodies / late endosomes (MVB/LE). In general there are two recycling mechanisms. Firstly, there is recycling by fast recycling endsomes (FRE) which is regulated by Rab4 and Rab35. Secondly, there are slower pathways requiring a Rab11 positive intermediate endocytic recycling compartment (SRE) [68]. Receptors are labelled for degradation via ubiquitination. Ubiquitinated receptors are internalised into intraluminal vesicles within the MVB. This is done with the help of endosomal sorting complexes required for transport (ESCRT). The MVBs then fuse with lysosomes (Lys) where the receptors are degraded. RTKs can also be transported to other destinations, such as the nucleus [69] and mitochondria (MT) [70]. Figure adapted from [59].

example, when EGFR forms a heterodimer with ERBB2, then Cbl recruitment and the consequential ubiquitination of the receptor is impaired [73]. Consequently, in cells expressing high levels of ERBB2, where the EGFR/ERBB2 hetero-dimer receptor pair is more abundant, there is an associated reduction in degradation and increase in recycling of receptor.

In addition, the pH stability of the ligand receptor interaction is important as ligand dissociation is associated with de-ubiquitination [74, 66]. Therefore, in addition to controlling the endocytic entry route (section 2.2.1), ligand type can also increase signal amplitude by dissociating at an early stage in the endocytic pathway. For example unlike EGF/EGFR, the TGF-α/EGFR pair will dissociate in endosomes and avoid degradation [75].

In the above discussion of trafficking and endocytosis there is a recurring theme; various input parameters converge on the ubiquitination of receptor (a core process) to determine receptor fate. Therefore, recycling of endosomes is often viewed as the default option, taken if receptors are not actively labelled for degradation [66]. This is supported by a study which uses a non-Ubiquitinated EGFR mutant to demonstrate an increase in recycling from MVBs and an inability to internalise EGFR in intraluminal vesicles [76]. However this is also evidence for more active regulation of recycling. Specifically CAML, eps15S and odin have all been identified as effectors of EGFR recycling [77, 78, 79, 66].

Interestingly, translocation of receptor to alternative organelles, including the nucleus and mitochondria is possible. Since the initial observation of nuclei localised EGFR in Hepatocytes by Marti *et al.* (1991) the field has been slow to realise its importance [80]. However, more recent work has highlighted the functional affects of nuclear RTKs, including the regulation transcription and DNA-repair [81, 69]. Similarly Mitrocondial EGFR localization has also been observed and linked to regulation of mitochondrial function and apoptosis [70, 82]. Clearly, much more work is needed to fully understand the mechanisms regulating trafficking to these organelles.

2.2.3 Signalling within the Endocytic Network

It was originally thought that regulation of receptor signalling by endocytosis and trafficking was limited to the control of the quantity of receptor on the plasma membrane, providing a means to modulate signal attenuation and amplitude. However the endocytic network is also essential for regulation of the signalling outcome. We have seen examples of this and the converse; trafficking regulation by signalling in sections 2.2.1 and 2.2.2 . Moreover the hypothesis that receptors can continue to signal after internalisation within endosomes has transformed our understanding of the relationship between signalling and trafficking. Early evidence for such *signalling endosomes* was provided by Di Guglielmo *et al.* (1994), where it was demonstrated that activated EGFR, SHC, GRB2 and SOS complexes (key components of the MAPK/ERK pathway) can exist in endosomes [83]. Additional early evidence was reported for neurons, where it was hypothesised that TrkA receptor signalling within endosomes was necessary to explain the range and speed of communication between the synapse and cell body [84, 85].

There is now a large quantity of evidence to support the signalling endosome hypothesis. However two key concepts remain disputed; firstly, can endosomal signalling contribute significantly to the overall signal amplitude, secondly can endosomal signalling trigger functionally distinct responses [86]? We will now briefly review several studies which provide evidence to support these concepts for EGFR signalling.

Viera *et al.* (1996) showed that inhibiting dynamin dependent endocytosis results in a significant reduction in ERK activation, thus providing the first evidence that endosomal signalling is significant in amplitude and can affect specific signalling pathways [58]. Furthermore Teis *et al.* (2006) demonstrated that MAPK/ERK complexes are anchored to late endosomes by the adaptor protein p14. The authors disrupted p14 to demonstrate that MAPK/ERK signalling from late endosomes is required to maintain tissue homeostasis and regulate cell proliferation [87]. This is particularly interesting as it suggests signalling response can be controlled within specific sub-endosomal populations. This is true of other types of endosomes, for example Miaczynska *et al.* (2004) suggest that a sub-population of early endosomes positive for rab5, APPL1 and APPL2 can regulate cell proliferation [88]. It is proposed that in response to EGF internalisation, APPL1 is released from the endosomal membrane to translocate to the nucleus. The concept of sub-endosome specific signalling can be explained by the variable biochemical environments available to receptors in different endosome types. These distinct endosomal platforms can enable or restrict access to various signalling molecules and control ligand dissociation though pH differences (section 2.2.2) [1].

Recent work has highlighted potential roles for endosomal signalling under physiological conditions. Fortian *et al.* (2014) use live cell confocal microscopy to demonstrate, through colocalization of EGFR and Grb2 in endosomes, that endosomal signalling is significant under (near) physiological conditions and suggest it may even be dominant for low expression levels of EGFR [6]. Interestingly, they also propose that receptor signalling may continue even after dissociation of ligand. Finally, Villasenor *et al.* (2015) provide evidence, through FRET microscopy, that the mean quantity of phosphorylated EGFR present in individual endosomes remains approximately constant with increased EGF stimulation but the amount of EGFR positive endosomes increases [89]. Notably they also show that a change in endosomal distribution of EGFR can trigger a functional response, specifically a change in EGF distribution triggered neuronal differentiation in PC12 cells.

Clearly the role of endosomal signalling is significant, the emphasis of future work will be understanding its regulation and the full extent of the complex interlinking of the signalling, trafficking and endocytic networks.

2.2.4 Consequences for Cancer

Here we review the importance of receptor endocytosis, trafficking and signalling in cancer research and treatment. We will do this with several non-exhaustive but illustrative examples and refer the interested readers to more complete reviews. Oncogenic signalling has access to the same core regulatory processes used by healthy tissue but the positive and negative feedback loops are manipulated to change functional responses (figure 2.1). Typically this is initiated either by gene amplification/suppression or genetic mutation [90]. Based on the previous discussions in this section it should be clear how simply the control processes could be hijacked to facilitate oncogenesis. For example, simply over-expressing ERBB2 will increase the proportion of EGFR/ERBB2 hetero-dimers which resist ubiquitination and subsequent degradation leading to increased signal amplitude and duration (section 2.2.2). It is unsurprising then that gene amplification leading to ERBB2 over-expression is seen in many cancers, including a prominent role in breast cancer [91, 90]. Similarly, over-expression of ERBB3 in non-small cell lung cancer (NSCLC) leads to an increased ratio of EGFR/ERBB3 hetero-dimers which in turn increases activation of the PI3/AKT pathway [92].

Ligand-independent dimerisation of EGFR triggered either by receptor mutations or over-expression plays an important role in oncogenesis [93, 66]. There is evidence that constituently active EGFR mutations present in NSCLC do not effectively recruit Cbl and therefore avoid ubiquitination and degradation [94]. Moreover Chung *et al.* (2009) demonstrate that mutant EGFR has increased colocalization with recycling endosomes [95]. The authors suggest that the recycling endosomes provide a signalling platform with increased access to Src, a key mediator of oncogenesis in NSCLC [96].

The sprouty family (SPRY) of proteins are negative regulators of RTK signalling and often down-regulated in cancer. Down-regulation of SPRY2 increases activation of the PI3/AKT pathway [97, 66]. Interestingly this triggers increased receptor internalisation and also signalling from early endosomes, dependent on the presence of phosphatase and tensin homolog (PTEN) [98]. This example is particularly noteworthy as the regulation of signalling pathways, endocytosis and trafficking are all manipulated simultaneously to produce an oncogenic response.

To date, there are only two treatment strategies which demonstrate anti-tumour efficiency and target EGFR; tyrosine kinase inhibitors (TKIs) and monoclonal antibodies. Tyrosine kinase inhibitors such as lapatinib and gefitinib, target the intracellular kinase domains of EGFR, whereas monoclonal antibodies such as cetuximab target the extracellular ligand binding domains [66]. Cetuximab has been shown to increase overall survival rates for specific cancers in combination with standard radio/chemo-therapy, which is attributed to a reduction in EGFR expression levels [99]. Regulation of DNA repair and anti-apoptotic responses leading to drug resistance have been associated with aberrant stress induced trafficking of receptor. In conclusion, the regulatory mechanisms for endocytosis and trafficking of receptor play important roles in cancer and there is significant scope for treatments targeting these systems.

2.3 Small G Protein regulation by GEFs and GAPs

2.3.1 GEF and GAP Function

Small G-proteins are a large family of proteins which act as key components of signalling pathways. Small G-proteins exist either in an active GTP bound state or an in-active GDP bound state. Active small G-proteins recruit effector proteins and contribute in many signalling scaffolds. In general, GTP is hydrolysed slowly and GTP/GDP are tightly bound so both the active and in-active states are inherently stable [100]. Therefore the critical and reversible *switch* between active and inactive states is predominantly induced and regulated by two further classes of proteins; guanine exchange factors (GEFs) and GTPase-activating proteins (GAPs).

GEFs recruitment catalyses the release of both bound GTP and GDP from small G-proteins. Conversely, GTP/GDP recruitment will induce dissociation of the GEF. Therefore, increased GEF activity will dramatically increase the rate of switching between bound and unbound states [101]. Although there is typically no significant preference for the GTP bound state, the cellular concentration of GTP is typically ten times higher than GDP. Therefore the net effect of GEF activity is a rapid increase in the proportion of the GTP bound state, hence GEFs act as the activating switch (figure 2.4a) [102].

As already noted the basal rate of hydrolysis for GTP bound small G-proteins is very low. GAPs function to catalyse and increase the hydrolysis rate, hence deactivating G-proteins (figure 2.4b) [103]. Therefore it should be clear that together small G-proteins, GEFs and GAPs form a three fold machinery which form and regulate biochemical switches.

2.3.2 Ras regulation in Signalling and Trafficking

The Ras super-family are an important class of small G-proteins, heavily implicated in signal regulation and with well established oncogenic consequences. There are 5 sub-families of Ras proteins; Ras, Rab, Arf, Rho and Ran [104]. The Rab and Arf families are of particular interest to this study due to numerous key roles in the regulation of intracellular and membrane trafficking [105, 106]. In the interest of space we omit a complete review of Ras signal regulation by GEFs and GAPs. Instead we briefly review several illustrative examples focussing on two members of the Ras super-family; rab5 and ARF6.

Rab proteins are essential regulators for all the core mechanisms of endocytic trafficking including sorting, motility, (un)coating, fusion and tethering [105]. Rabs are localised to the membranes of specific endosome sub-populations where they can act as specialised recruiters for a large variety of effectors. rab5 is localised to a subpopulation of early endo-

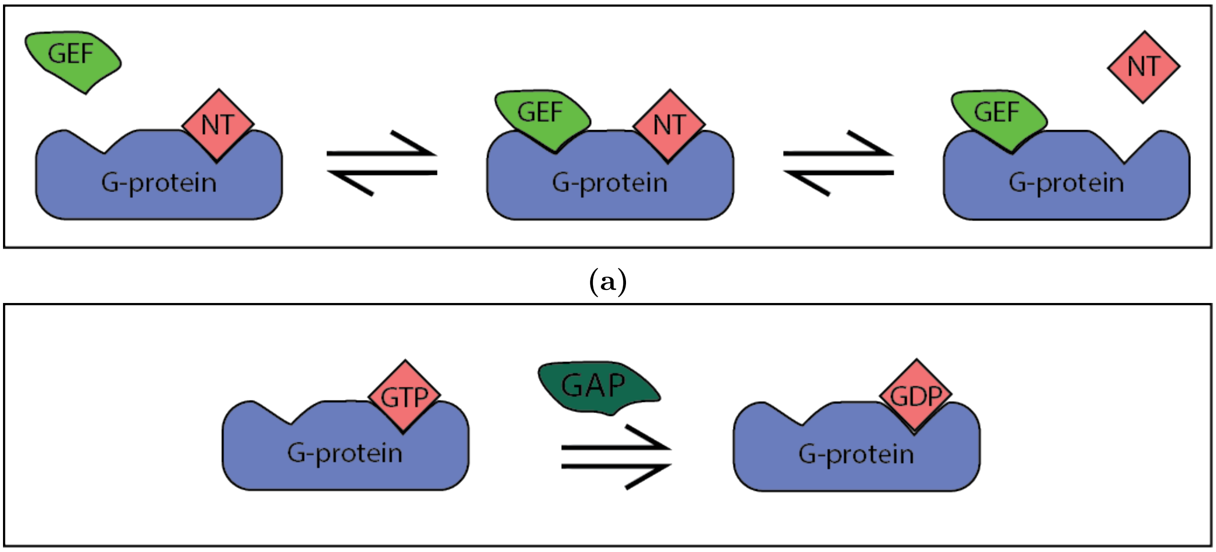

(a)

(b)

Figure 2.4: GEF and GAP function. (a) Guanine exchange factors (GEFs) bind to small G-proteins and trigger the release of the bound nucleotide (NT) (GDP or GTP). The process is reversible and the binding of GDP/GTP will trigger the release of the GEF. This increases the rate of exchange towards an equilibrium where the ratio of bound GTP to GDP is approximately equal to the unbound ratio. In physiological conditions this is heavily weighted towards GTP, hence GEF activity facilitates activation of the small G-protein. (b) GTPase-activating proteins (GAPs) facilitate the hydrolysis of bound GTP and the consequential deactivation of the small G-protein. The mechanism is specific to the type of GAP and G-protein. Figure adapted from [102].

somes and has numerous well studied roles in the regulation of signalling and trafficking. For example Semerdjieva *et al.* (2008) showed that in an active state, rab5 facilitates the shedding of AP2 from clathrin coated vesicles, a necessary step for fusion with early endosomes [107]. Furthermore, it is suggested that the rab5 GEF, hRME-6 but not rabex-5 (a second rab5 GEF) is responsible for regulating this process. Hence the activation of rab5 to facilitate the shedding mechanism is shown to be induced by specific GEFs. This highlights that GEFs and GAPs can regulate the functional effect of the switch as well as the on/off state. This specificity can be understood by the existence of distinct activation sites on the small G-proteins. Alternatively, the GEF/GAP may act as a scaffold capable of recruiting specific effectors [102]. Other roles for rab5 include facilitating endosomal fusion [108, 109] and regulating transport along microtubules [110].

As discussed in section 2.2, there is inherent cross talk between the regulation of signalling and trafficking. To see an explicit example of this for rab5 we note that EGF stimulation of EGFR will induce recruitment of Grb2 to the phosphorylated receptor (section 2.1.3), this will trigger activation of Ras by the GEF SOS1 [105]. Activated Ras will bind to and activate RIN1, a GEF for rab5. We have already seen an example of EGF induced GEF activation of rab5 in section 2.2.3 where the rab5 effectors APPL1 and APPL2 trigger transduction of EGFR signalling to the nucleus [88]. In addition to nuclear transduction, rab5 recruitment of APPL1 in signalling endosomes has been demonstrated to regulate cell survival in zebrafish development [111]. Furthermore RIN1 activation of rab5 has been shown to regulate EGFR endocytosis , endosome fusion [112] and promote receptor degradation over recycling [113]. A recent study by Balaji *et al.* (2012) demonstrates that the proportion of receptor recycling can be regulated by RIN1 through control of the balance between rab5 and ABL tyrosine kinase activation [114].

ARF6 is localised to either the plasma or endosomal membranes and is heavily implicated in the regulation of endosomal trafficking and actin organisation [115]. ARF6 has been shown to regulate endosomal recycling for various receptor systems [116]. Interestingly, active ARF6 can induce different trafficking and physiological outcomes dependent on the specific receptor being trafficked [117]. For example ARF6 activity can increase receptor recycling and signal duration for EGFR and integrins [118] but increase lysosomal targeting for E-cadherin [119]. Allaire *et al.* (2013) suggest a mechanism involving interplay with rab35 and the ARF6 GAP; ACAP2 to explain this [117].

2.3.3 Implications for Cancer

As seen in the previous section the regulation of signalling, trafficking and endocytosis by the Ras super-family is a very complex interwoven process with many integral feedback loops. GEFs and GAPs provide a focal point in many of these mechanisms and can act as both on/off and decision making switches. Unsurprisingly then, the GEFs and GAPs of the Ras super-family are extensively associated with cancer. Here we give two examples of where aberrant GEF and GAP activity is implicated in oncogenic EGFR signalling. For a more complete review we refer to Vigil *et al.* (2010) [104]. The potential of GEFs and GAPs for targeting drug delivery is also briefly discussed.

The Arf subfamily, notably ARF1 and ARF6, are implicated in cancer. For example ARF6 is implicated in the growth and invasion of breast cancer [120] and melanoma [121, 104]. The ARF6 effector, AMAP1, is linked to cancer invasion and the ARF6 GEF, IQSEC1 (also known as GEP100), links EGFR signalling to ARF6 activation and AMAP1 recruitment [122]. This is achieved by direct binding of IQSEC1 to EGFR after ligand stimulation. Furthermore AMAP1 and ARF6 are over-expressed in breast cancer and this pathway is implicated in ductal cancers [123].

VAV2 is a GEF for the Rho subfamily of Ras. VAV2 hyper-activation has been implicated in tumour growth of several cancers [124, 104] and specifically linked to a EGFR signalling response for head and neck squamous cell carcinoma (HNSCC) [125]. In a noteworthy study, Thalappilly *et al.* (2010) demonstrated that VAV2 knockdown increased the rate of EGF stimulated EGFR degradation and net internalisation [126]. Furthermore VAV2 over-expression was shown to increase phosphorylation of ERK and Akt, while knockdown reduced cell growth.

The specificity and importance of the mechanisms regulated by GEFs and GAPs make for desirable drug targets. However the chemical characteristics of GEFs/GAPs make them unsuitable for commonly employed methods of small molecule inhibition. However some proof of concept drugs such as the Arf GEF inhibitors, Brefeldin A [127] and LM11 [128, 104] have been developed. There is substantial optimism in the field that a wider range of targeted inhibitors for both GEFs and GAPs will be developed for cancer treatment [104].

2.4 Fluorescence Microscopy

2.4.1 The Stokes' Shift

The first observations of the fluorescence process is commonly attributed to John Herschel (1845) who observed that when illuminated by sunlight, the outer regions of a quinine solution (tonic) would admit blue light, an effect amplified by adding ethanol (gin) [129]. Gabriel Stokes' seminal work (1852) built on these observations by designing an experiment using two bandpass filters [130]. The first, the excitation filter (a blue stained glass window), selected wavelengths less than approximately $400nm$. This filtered light was used to illuminate the quinine solution and the second filter, the emission filter, (glass of white wine with yellow tint) was used to filter light passing though this solution. Stokes could not observe the non-visible UV excitation light but could see the visible component through the emission filter. As the second filter would only pass wavelengths greater than $400nm$ is was concluded that the quinine solution was absorbing the UV light and emitting a light of longer wavelength (lower energy).

The process described by Stokes is fluorescence and the difference between the wavelengths of the emission and excitation profile peaks is referred to as the Stokes' shift (figure 2.5b). In Stokes' experiments quinine is responsible for the observed fluorescence and is the first example of a fluorophore. The fluorescence mechanism can be easily understood by use of a Jablonski diagram as shown in figure 2.5a [131].

2.4.2 The Epi-fluorescence Microscope

Oskar Heimstädt [132] invented the fluorescence microscope by introducing emission and excitation filters into the optical path (1911). A typical configuration for a modern inverted fluorescence microscope in shown in figure 2.6.

Before considering the process of image formation for a light microscope first, note that the wave-like properties of light demand that light passing though a convergent lens must diffract. Therefore, if we consider the theoretical imaging of an infinitesimally small fluorescent point source, the light focused onto the image plane will have a 3D diffraction pattern. The corresponding image captured by the camera will be a discretized representation of this pattern. The fringes of the diffraction pattern depend on two key parameters. Firstly, the wavelength of light will determine the location of the peaks formed by constructive and destructive interference. The smaller the wavelength the finer the pattern. The second key parameter is the numerical aperture, NA, of the objective lens which is defined as,

$$\mathrm{NA} = n \sin\theta \tag{2.4.1}$$

where n is the refractive index of the working media and θ is the half angle of the maximal cone of light collected by the lens. The numerical aperture characterises the efficiency of the objective lens to collect the emission light and the information it carries. Therefore a high NA will result in both a brighter signal and finer diffraction fringes.

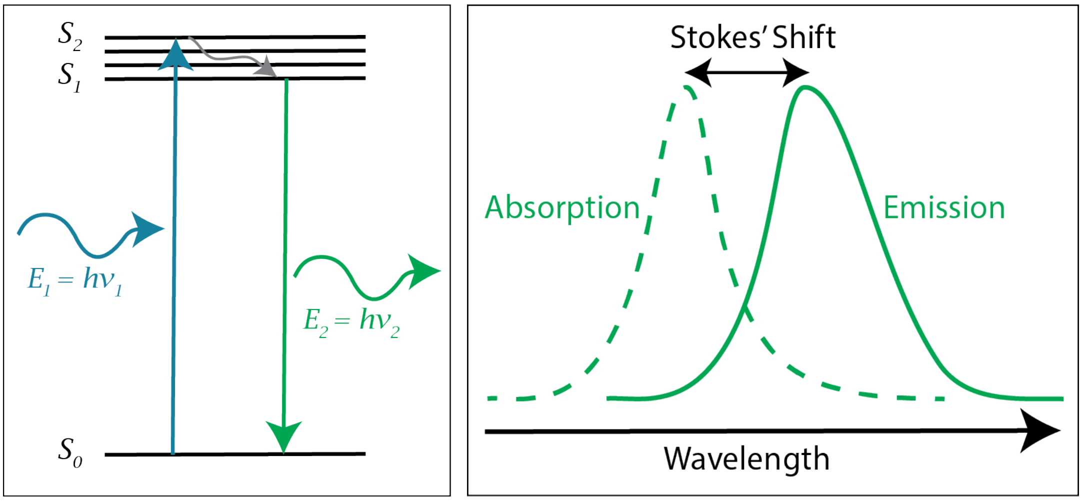

(a) (b)

Figure 2.5: Fluorophore properties. (a) A simplified Jablonski Diagram showing a subset of the quantised electron energy states for a fluorophore. Electrons in the ground state, S_0, can absorb photons from incident light with energy, E_1, in the neighbourhood of the energy transition and corresponding frequency, v_1, and move to the excited state, S_2. Electrons in S_2 can decay to a lower energy excited state, S_1, without emitting photons. This internal energy conversion is typically achieved by radiative heat loss. Electrons in the S_1 state which radiatively decay to S_0 will emit photons of (average) lower frequency, v_2, than the excitation light due to the smaller energy difference. Photons can also move back to S_0 by non-radiative decay from various mechanisms including heat loss or transfer of energy to adjacent molecules. An important (wavelength dependent) property of a fluorophore is the ratio of emitted to absorbed photons which is referred to as the quantum yield. (b) A fluorophore will absorb a range of incident wavelengths with varying efficiency. This is referred to as the emission spectra. Similarly, a fluorophore will emit at a range of wavelengths with varying probability as seen in the emission spectra. The difference between the excitation and absorption maximum is referred to as the Stokes' shift. In fluorescence microscopy, a large Stokes' shift is desirable as it minimises spectral overlap, which is turn enables effective separation of the emitted and excitation light. The brightness of a fluorophore at a particular wavelength is defined as the product of the absorption and quantum yield. The brighter the fluorophore the lower the required illumination intensity necessary to achieve sufficient image contrast. Low illumination intensity is beneficial as it reduces bleaching and photo-toxic effects.

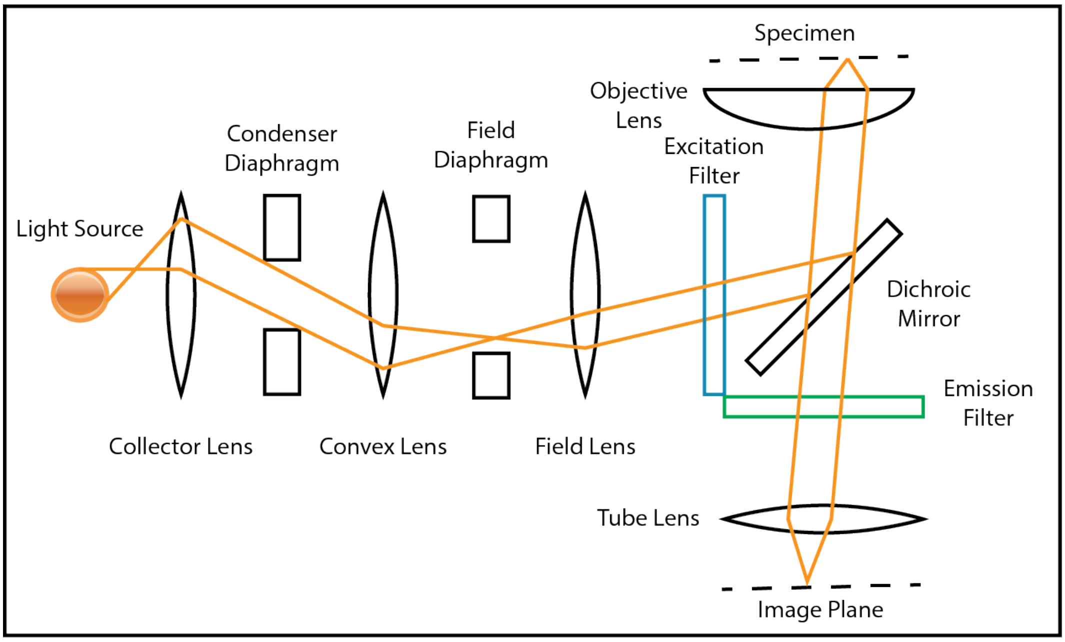

Figure 2.6: The epi-fluorescence microscope. To understand the modern epi-fluorescence microscope, it is beneficial to first review the basics of epi-illumination microscopy. First, consider sample illumination where the entire field of view should be exposed to the excitation light source. Typical light sources include mercury or xenon lamps but newer systems may use LED sources which offer more flexible and specific wavelength coverage. It is desirable for the sample illumination to be even. Even illumination is produced by a combination of lenses which combine to ensure that light is perfectly de-focussed at the sample plane. This is called Köhler illumination and is, in practice, achieved by correct calibration of the collector, field, convex and objective lenses [133]. Once illuminated, light from the sample should be collected and magnified to an image plane where a detection device can be placed. This is achieved by the objective and tube lenses. Modern objective lenses typically consist of many individual lenses designed to correct for spherical, chromatic and off axis aberrations. A dichroic mirror is used to separate the two converging light paths. The detection device is typically a highly sensitive CCD chip which converts the continuous signal into discrete image data. Finally, consider the two filters necessary for epi-fluorescence microscopy. The excitation filter should select wavelengths necessary to excite the fluorophore(s) of interest. The emission filter should select the longer wavelength emission light and be distinct to those selected by the excitation filter. Modern filters often employ interference rather than absorption and allow for multiple narrow bands of transmission.

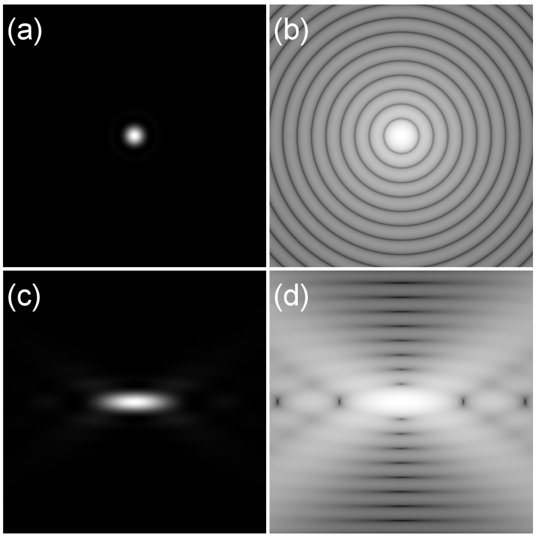

Figure 2.7: The theoretical point spread function. Point spread function, PSF, for an epi-fluorescence microscope. (a) The lateral plane (xy) of the diffraction pattern is an Airy function. (b) With contrast enhancement the fringes are easily visible. The distance between fringes limit the resolution of the microscope. (c) The axial (xz) form of the point spread function is more blurred than the lateral cross section. (d) Axial view with contrast enhancement. The fringes are spread further apart, hence axial resolution is worse than lateral. PSF generated in Matlab (2015a) using the PSF generator developed by the Biomedical Imaging Group (EPFL, Switzerland) [134].

The 3D diffraction pattern created by a point emitter is referred to as the point spread function, PSF, of the microscope. Note, here and in all further discussion when referring to the PSF, we are referring to the intensity projection. The theoretical PSF for an epi-fluorescence microscope is shown in figure 2.7. When viewed in the xy plane, the PSF has the form of an airy disk.

It is worth noting that the theoretical PSF is a best case scenario and inevitably, small imperfections and aberrations in the system mean it can never be achieved in practice. When considering a real system we do not have ideal isolated point-emitters but highly complex biological samples emitting a combined signal, which we denote, $f(x, y, z)$. In this case the image formation process can be described by the convolution,

$$I(x, y, z) = (f \otimes PSF)(x, y, z) = F^{-1}(F(f) \times F(PSF)) \qquad (2.4.2)$$

where $F : \mathbb{R} \to \mathbb{C}$ is the Fourier transform and $I(x, y, z)$ is the optical image formed at the image plane which is subsequently digitised by a CCD camera.

Having described the image formation process, it should be clear that the resolution is limited by the PSF. If we define resolution as the minimal separation distance for which two point emitters can be distinguished then there are several different ways of describing the resolution limit. The Rayleigh criterion is commonly used in microscopy which defines the resolution limit, R, as the distance between the centre and the first minimum of the PSF [135]. For the lateral and axial cases this is given by,

$$R_{xy} = \frac{0.61\lambda}{\text{NA}} \qquad\qquad R_z = \frac{2n\lambda}{\text{NA}^2} \tag{2.4.3}$$

where λ is the wavelength of the emitted fluorescence and n is the refractive index of the mounting/immersion medium. Note that the axial resolution limit is significantly worse than the lateral. As an example, consider imaging at $\lambda = 400$nm with a 100× 1.4NA oil ($n = 1.5$) objective, then the lateral and axial resolution limits as defined by the Rayleigh criterion will be $R_{xy} \simeq 174$nm and $R_{xy} \simeq 612$nm respectively.

Finally consider the sampling of the CCD camera. To capture all the available information at the highest possible resolution, and avoid aliasing artefacts, the sampling rate should be at least twice the limit of resolution. This is known as the Nyquist rate. As an example consider a lateral resolution limit, $R_{xy} \simeq 200$, then each pixel in the image should represent less than 100nm in real space. It is worth noting that sampling at a rate substantially above the Nyquist rate is wasteful and will result in unnecessary large data sets. Sampling below the Nyquist rate can be used to limit data size, increase acquisition speed (for line scanning methods) or increase signal (through binning) at the cost of resolution and the risk of artefacts.

2.4.3 The Confocal Microscope

In many applications the key drawback of epi-fluorescence microscopy is the lack of an intrinsic ability to distinguish between in-focus and out of focus light sources. This can be addressed computationally by a class of techniques referred to as deconvolution. This can produce excellent results but is typically computationally expensive. Alternately, or in parallel, the optical configuration can be modified to minimise out of focus contributions to the image. In confocal microscopy this is done by placing a pinhole in the plane conjugate to the sample. This will (predominantly) block light originating from out of focus sources. Combined with a focused laser beam for excitation, this is refereed to as optical sectioning (figure 2.8). To construct an image, the laser beam is raster scanned across the sample. A 3D volume can be easily acquired by moving the sample in small steps through the focal plane where an image (slice) is acquired for each step.

A principal drawback of confocal microscopy is that acquisition time is limited by the scan speed of the laser, typically about 1 second per image. To combat this, sophisticated scanning devices such as resonance scanners, which use oscillating mirrors, can be incorporated to greatly increase acquisition speed. Alternately, multiple excitation volumes can be generated using a micro-lens array. With this approach many spatially distinct measurements can be recorded simultaneously using an array of pinholes and a camera. This is called spinning disk confocal microscopy.

To consider the theoretical resolution limit for a confocal microscope, it is important to note that the excitation volume is restricted to a near-diffraction limited spot. Therefore the point spread function of a confocal microscope, PSF_{con}, will be the product of the point spread functions for the observation, PSF_{obs} and the illumination, PSF_{ill}, optics [137]. In the case where the same optics are used for illumination and acquisition this product can be approximated as follows,

$$PSF_{con} = PSF_{obs}(\lambda_{ex}) \cdot PSF_{ill}(\lambda_{em}) \simeq PSF_{obs}^2 \tag{2.4.4}$$

where λ_{ex} and λ_{em} are the wavelengths of the excited and emitted fluorescent light respectively. Therefore, the point source diffraction pattern for a laser scanning micro-

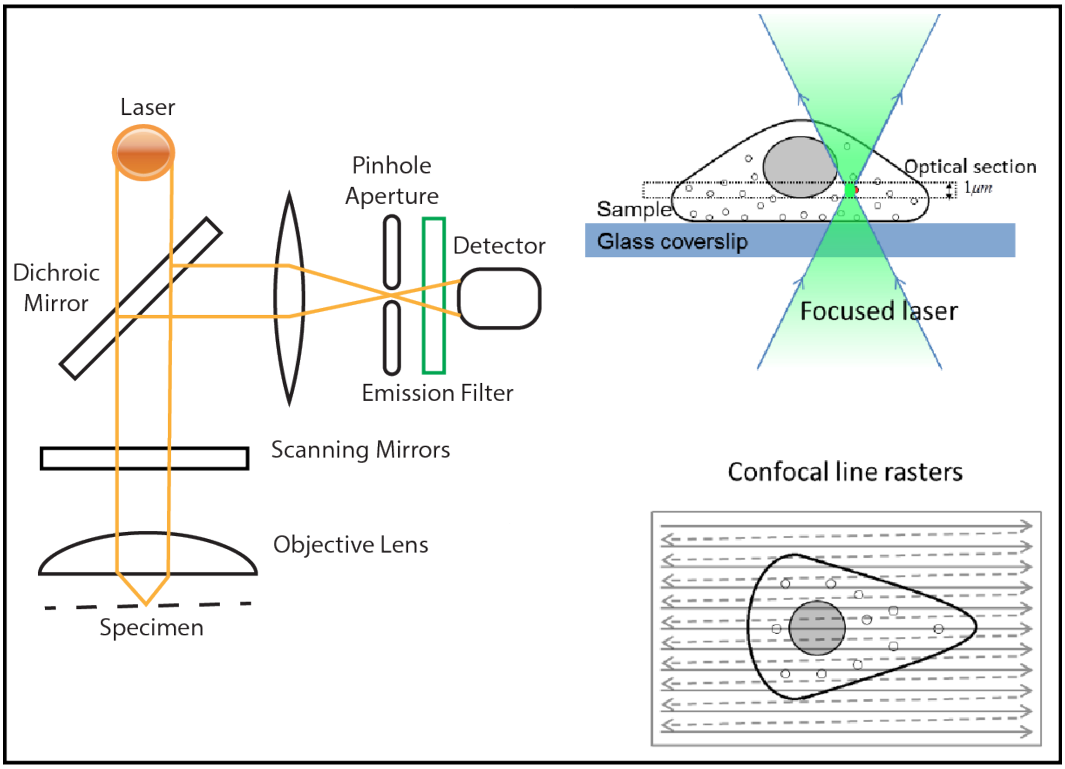

Figure 2.8: The confocal microscope. In confocal microscopy a collimated laser beam is focused by the objective lens onto a small focal volume on the sample plane. The in-focus light is filtered by placing a pinhole aperture at the conjugate sample plane. The intensity read out for this single excitation volume can then be recorded by a detector. Typically a photo multiplier tube (PMT) is used due to high read speed. To image off axis, the laser beam is raster scanned across the sample using two galvanometers (oscillating mirrors). The light is then de-scanned (the off axis perturbation is reversed) by the same mirrors to ensure that the in-focus light passes through the pinhole. Figure partly reproduced with permission from [136].

scope will have finer fringes than the pattern produced by an epi-illumination microscope and the corresponding resolution limit will be improved. For a confocal microscope the Rayleigh criterion is given by,

$$R_{xy} = \frac{0.44\lambda}{\mathrm{NA}} \qquad\qquad R_z = \frac{1.5n\lambda}{\mathrm{NA}^2} \tag{2.4.5}$$

which represents a small improvement over the epi-fluorescence microscope (equation 2.4.3).

The effect of the pinhole aperture should also be considered as it will further modify the axial resolution; the smaller the pinhole the better the axial resolution. However reducing the pinhole size will reduce the signal to noise ratio (SNR) and hence there must be a practical compromise. Typically, the pinhole is set to the diameter of the central Airy peak but for dim or live samples it may need to be larger.

2.4.4 Noise in Fluorescence Microscopy

When working with any imaging system it is useful to understand the various sources of noise corrupting the image formation process. Typically, the noise generated in the digital acquisition of fluorescence microscopy images can be modelled as originating from three sources [138, 139];

1. **Dark** (or thermal) noise is inherent to the detection device (typically a CCD or PMT) and is independent of the incident illumination signal. Dark noise is well modelled by a Poisson distribution. Typically, dark noise is triggered by the thermal excitation of electrons and is therefore dependent on the temperature of the detector. Detector cooling systems are often employed to reduce dark noise.

2. **Read** (or amplifier) noise is associated with the amplification of a signal to ob-

tain a voltage reading that is subsequently digitalised. This form of noise is more predominant in CCDs than PMTs and can be modelled with an additive Gaussian distribution. Read noise is also signal independent.

3. **Shot** (or photon) noise is caused by inherent statistical variation in the arrival time of photons at the detector . This quantum mechanically derived stochastic process is unavoidable and provides a theoretical limit for the SNR. Shot noise can be modelled as a Poisson distribution. Note however that for large numbers of incident photons, the Poisson statistics will tend towards a symmetric normal distribution.

Collectively system noise can be modelled as a mixed Poisson-Gaussian distribution [140];

$$I = \text{Gaussian} + \text{Poisson}(\omega, I_0) \tag{2.4.6}$$

where I_0 and I are the incident and noisy signals respectively and ω is the detector gain. In the regime where the signal is strong, dark and read noise are dominant and the photon noise is normally distrusted. Therefore under these conditions the total noise can be approximated with Gaussian statistics. However in fluorescence microscopy the signal is often weak and photon (Poisson) noise is dominant. This is likely to be the case in live-cell imaging where low illumination intensity (and high detector gain) is used to avoid photo-damage.

2.4.5 Choosing Fluorescent Probes

Fluorescent microscopy has become one of the most extensively used and insightful tools in biological research. This is due to two key advantages it has over other high resolution imaging techniques. Firstly, the contrast between signal and background is inherently high, and secondly the specificity for molecules of interest is unparalleled. This specificity is provided by a wide range of fluorescent probes and corresponding labelling techniques.

When choosing a probe it is essential to consider properties such as brightness and the spectral absorption and emission as discussed in figure 2.5. It is also necessary to consider the photo-stability and photo-toxicity of the probe, especially for live cell imaging [141]. When undergoing repeated fluorescence excitation, all fluorophores will eventually *photobleach*; an irreversible process involving interactions with surrounding molecules such that the fluorophore can no longer fluoresce. Probes with poor photo-stability will bleach at a higher rate and thus may be unsuitable for time-lapse or 3D imaging.

When performing multi-colour fluorescence microscopy, it is also necessary to consider spectral overlap between probes, the light source(s) and the emission and excitation filters to avoid crosstalk (bleed-through) [142]. Crosstalk is the detection of signal from one probe in a second probe's channel, and it is particularly important to avoid when performing colocalization analysis. The various sources of crosstalk are described in figure 2.9. Note, the terms crosstalk and bleed-through are often used interchangeably to describe all the situations presented in figure 2.9 (this is the approach taken in this thesis). However, in some studies cross-emission is referred to as bleed-through (figure 2.9a), and cross-excitation as crosstalk (figure 2.9b).

Prevalent labelling techniques include immuno-labelling, genetic tagging and direct conjugation of fluorophore. However there are numerous other approaches including the use of quantum dots (semi-conducting nano-crystals) which are very bright, photo-stable and have highly adaptable spectral properties [144]. Immuno-labelling uses antibodies to attach small fluorophores to proteins of interest. Typically, primary antibodies are used to recognise the protein of interest and secondary antibodies to attach the fluorophore. This approach is not normally applicable to live cell imaging as the sample should be fixed and permeabilized. Live cell imaging has been combined with immuno-labelling to visualise internalised proteins but may trigger oligomerization [145].

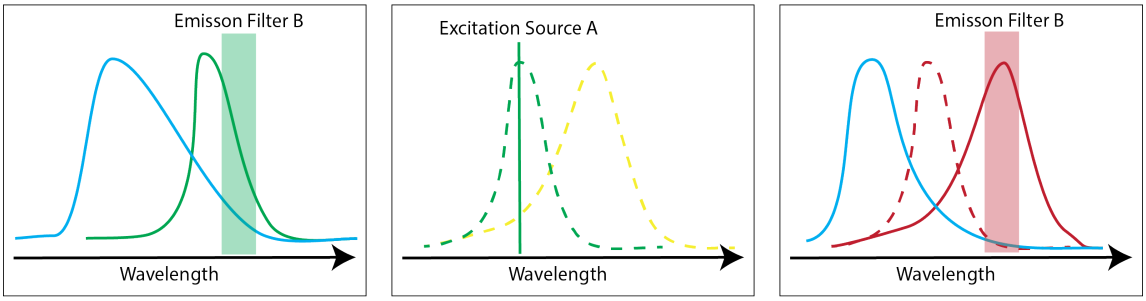

(a) **(b)** **(c)**

Figure 2.9: Sources of crosstalk. Crosstalk (or bleed-through) is a common problem in multi-channel fluorescence microscopy. Dashed and solid lines represent absorption and emission spectra respectively. Probe A represents the probe with lower peak absorption. There are three sources of crosstalk; (a) Emission from probe A (DAPI) overlaps with emission filter for probe B (Alexa Fluor 488). (b) Excitation of probe A (RFP) also excites probe B (YFP) (c) Emission from probe A (CFP) overlaps with excitation filters and/or absorption spectra for probe B (RFP). To avoid crosstalk, probes with well separated spectra must be chosen and sequential (as opposed to simultaneous) excitation and acquisition of colour channels can greatly reduce some effects. It is often necessary to perform singly labelled controls which can be used for computational correction. Figure adapted from [143].

In genetic tagging approaches, the fluorophore is bonded covalently to the protein of interest. The binding is typically achieved by introducing cDNA with transfection or transgenic protocols. This approach was revolutionised by the discovery and purification of the green fluorescent protein (GFP) from the jellyfish; Aequorea victoria [146, 147], and later the red fluorescent protein dsRed from anthozoan corals [148]. These and other natural fluorescent proteins have been modified to provide many variants with desirable properties such as greater photo-stability, narrow and varied absorption and emission spectra, pH sensitivity and increased brightness. Genetic tagging is ideal for live cell imaging, but over-expression, and the size/bonding of the fluorescent protein may affect the protein function.

2.5 Selected Noise Removal Strategies for Fluorescence Microscopy

Noise removal (or de-noising) is the process of computationally removing corruption within data, which was generated during acquisition. Typically this is done by devising strategies which are based on a statistical model for the noise, $n(I)$, and assumptions about the underlying gradient of the true signal, I_0. As discussed in section 2.4.4, noise in fluorescence microscopy is well modelled by a mixed Poisson-Gaussian distribution (equation 2.4.6) which is often dominated by its Poisson component. Here we review a combination of basic and sophisticated strategies for noise removal. This review is not exhaustive and emphasis is placed on the methods used in this work. For a more complete review we refer the interested reader to Buades *et al.* (2005) and the literature referenced throughout this section [149].

2.5.1 Matched filtering and Gaussian blurring

In a matched filtering approach the underlying signal is modelled as a construct of a specific impulse response, and the maximum signal to noise ratio (SNR) is restored by convolution with the conjugated time-reversed impulse [150]. In fluorescence microscopy, the PSF can be considered the impulse response for the system. Note that Gaussian approximations for the PSF are accurate in 2D for epi-fluorescence, and in both 2D/3D for confocal microscopy. Therefore, the use of Gaussian blurring can be considered a matched filtering approach with the PSF [151]. Gaussian blurring is a very popular and simple approach to de-noising fluorescence microscopy data, and can be described as;

$$I_G = I(x,y) \otimes G(x,y,\sigma) \tag{2.5.1}$$

where I_G is the blurred data, $I(x,y)$ is the raw data and $G(x,y,\sigma)$ is the Gaussian kernel with standard deviation σ;

$$G(x, y, \sigma) = \frac{1}{2\pi\sigma^2} \exp\Big(- \frac{x^2 + y^2}{2\sigma^2} \Big) \tag{2.5.2}$$

In this approach there is an assumption of additive noise which is true for Gaussian but not Poisson noise [152]. However, in practice this procedure will often produce adequate results if the signal is bright. As already noted under this regime, the Poisson distribution will tend towards a normal distribution where an additive noise assumption is valid. Typically the standard deviation of the kernel, σ, is set to the width of the PSF (although it can be higher for larger features of interest); note this will suppress sub-diffraction limit spatial frequencies which are characteristic of noise.

2.5.2 Other Simple Filtering Schemes

There are many other examples of simple filtering schemes for de-noising. Notable methods include mean, median and Laplacian of Gaussian (LoG) filtering. Mean and median filters replace each pixel with the mean or median of its local neighbourhood respectively. Mean filtering is linear and computationally cheap but unwanted smoothing effects are significant. Median filtering is a non-linear process which is effective for removal of *salt and pepper* impulse noise and edge preservation.

LoG filtering is the process of Gaussian smoothing followed by Laplacian filtering and can be calculated by convolution with the following function,

$$LoG(x, y, \sigma) = -\frac{1}{\sigma\pi^4}\Big(1 - \frac{x^2 + y^2}{2\sigma^2}\Big) \exp\Big(- \frac{x^2 + y^2}{2\sigma^2} \Big) \tag{2.5.3}$$

LoG filtering is an effective and computationally cheap method for detection of *spot like* objects in fluorescence microscopy [153, 154].

2.5.3 Wavelet Transforms

Wavelet transforms are an important class of transforms which can represent image data with an orthonormal series derived from a wavelet. This is analogous to the well known Fourier transform which represents an image as a series of sinusoidal waves [155]. Thresholding within wavelet domains provides a powerful platform for image de-noising by allowing subtle and targeted access to spatial-frequency information [156].

Undecimated wavelet transforms (UWTs) are often used for image de-noising in fluorescence microscopy. The transforms are undecimated, meaning that there is no down-sampling step as used in more conventional discrete transforms, such as the bi-orthogonal wavelet transform used in JPEG2000 file compression [157]. The main advantage of using an undecimated approach is translational invariance (important for images), but redundancy in the wavelet coefficients means computational costs are higher [158]. This approach was first implemented by Holschneider *et al.* (1989) with the well known and elegant *algorithme á trous* [159].

The isotropic undecimated wavelet transform (IUWT) is a specific example of an UWT, with origins in astronomy where isotropic objects such as stars are commonplace. It is also well matched to the isotropic objects often found in fluorescence microscopy [160].

UWTs are multi-resolution approaches where the image is decomposed into a series of N images, each sampling at a different resolution. In the popular B3-spline implementation of the *á trous* algorithm as proposed by Stark *et al.* (1995) we can describe the wavelet planes, W_n, where $n = 1, ..., N$ as [161],

$$W_n(x, y) = I_0(x, y) \otimes h_{n-1} - I_0(x, y) \otimes h_n = I_{n-1}(x, y) - I_n(x, y) \tag{2.5.4}$$

where $h_1, ...h_N$ represent the kernels for a set of filters which sample at increasing resolution [152]. In this multi-resolution representation, individual thresholds can be applied to each wavelet coefficient to remove noise. This can be done with either hard or more complicated soft thresholding schemes to produce modified wavelet planes, $\widetilde{W}_1, ..., \widetilde{W}_N$. Finally the inverse transformation is computed;

$$I_W(x, y) = I_N(x, y) + \sum_{n=1}^{N} \widetilde{W}_n(x, y) \tag{2.5.5}$$

where I_W is the de-noised image. Wavelet de-noising schemes are very effective but may introduce artifacts at edges or point like objects [157]. Standard wavelet approaches are well suited to Gaussian noise. To account for Poisson noise, non-linear variance stabilising transforms, such as the Anscombe transform [162], can be used as a pre-processing step to produce approximately Gaussian data [163]. This step must be reversed by inverse transforms after the wavelet de-noising. There are additional strategies for processing Poisson noise including wavelet domain Wiener filters [164] and hypothesis testing [165].

2.5.4 Noise Removal using the PURE-LET Scheme

Here we briefly describe the PURE scheme for noise removal of Poisson or mixed Poisson-Gaussian noise as introduced in two papers by Luisier *et al.* (2010, 2011)[166, 140]. We provide detail on this approach as it is used extensively in this work.

In the PURE-LET scheme for Poisson noise removal the Haar discrete wavelet transform (HDRT) is used as it preserves Poisson statistics at some resolution planes [166]. The authors design a wavelet domain mean squared error estimate for Poisson corruption termed the Poisson unbiased risk estimate (PURE). The orthogonality of the wavelet basis allows for independent minimisation of the PURE in each wavelet plane using a set of linear parameterisations for de-noising processes, termed the linear expansion of thresholds (LET) [167].

This approach has lower computational requirements than comparable techniques for Poisson noise removal at no cost in performance. Crucially, it can operate parameter free where all necessary information is derived automatically from the image. The extension to mixed Poisson-Gaussian noise requires a different mean squared error estimate and must be optimised in the image domain due to loss of a guaranteed orthonormal basis [140].

2.6 Colocalization Analysis

In fluorescence microscopy, colocalization studies compare the spatial distributions of multiple fluorescent labels. Typically this is done to establish if two labelled proteins *colocalize* to the same organelle or sub-cellular location. This is one of the most common and important applications of fluorescence microscopy, however it is often misunderstood or poorly implemented. In this section we critically review the different colocalization strategies commonly used in the study of receptor trafficking, and cover recent developments in methodology. For the interested reader there are several excellent reviews on the subject [168, 169, 9, 170].

It is worth noting that due to the physical limits on spatial resolution, conventional fluorescence microscopy techniques are inappropriate for determining the existence of direct protein-protein interaction (equations 2.4.3, 2.4.5) [9]. Even super-resolution techniques such as SIM [171], STED [172], or localization microscopy [173, 174] are not well suited for the confirmation of direct interaction. However, techniques such as Förster Resonance Energy Transfer (FRET) microscopy [175] or Fluorescence Cross-Correlation Spectroscopy (FCCS) [176] can be used for this purpose. Conversely, dipole-dipole coupling is required for FRET, hence it is unsuitable for determining association over larger distances, for example within endosomes [168].

Formally, colocalization studies should confirm the existence of a (statistically signif-

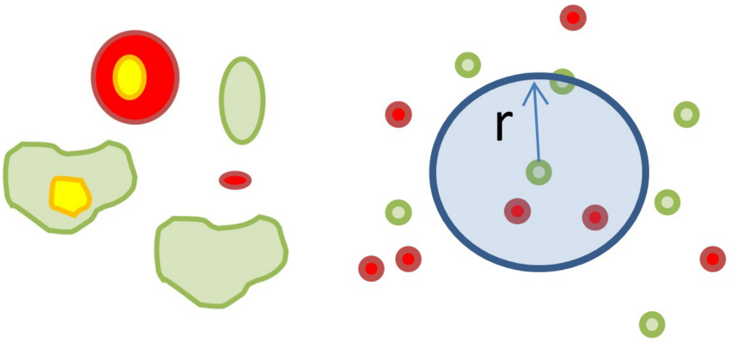

(a) (b)

Figure 2.10: Pixel and object based colocalization analysis. (a) Pixel based colocalization analysis measures the correlation and/or overlap of each pixel separately. (b) Object based colocalization analysis use spot detection protocols to calculate clustering statistics such as Ripley's K-function over varying distance scales, r.

icant) relationship between two or more spatial distributions of fluorophores on a (often unknown) distance scale, r. If r is less than the resolution limit of the microscope, then we can look at correlation and/or overlap between channels on a pixel by pixel basis, but cannot determine r (section 2.6.1, figure 2.10a). An alternative approach is to detect the COM of individual objects and calculate clustering related statistics to determine colocalization (section 2.6.2, figure 2.10b). Such *object based* approaches are applicable for all r, and if r is greater than the resolution limit, its range can be specified.

The testing of statistical significance when quantifying colocalization is a vital but often ignored element of colocalization analysis. Clearly it is necessary to perform statistical tests to determine if the measured colocalization is greater than the basal level where each fluorophore is randomly distributed within the region of interest (ROI), for example the cytoplasm. If this step is skipped, then it is not known if the *colocalization* is simply a result of the random overlap (or proximity) between fluorophores.

Finally, before discussing specific quantitative measures for colocalization, we note that in many studies colocalization is determined qualitatively by visual inspection of the data. There are two primary methods for doing this. Firstly, images can be placed side by side or overlayed to produce a composite RGB colour image where colocalization is interpreted by the presence of yellow pixels (in the case of red and green look up tables)(figure 2.11c). This is not informative and clearly very dependent on (usually unconscious) user bias. Moreover, relatively small changes in the way the data is visualized (contrast, brightness, look up tables etc) can dramatically change the interpretation. A second, more informative way to visualise colocalization for two channels, is to plot the data as a joint histogram (figure 2.11e) where the presence of a linear trend is conventionally seen as good evidence for colocalization. However, joint histogram visualisation should complement and not replace quantitative analysis. Moreover (as discussed in detail in chapter 5) a linear correlation does not well model the spatial temporal dynamics for colocalization between receptor and endosomes.

2.6.1 Pixel-based Colocalization Measures

In pixel-based measures there are two fundamental strategies for measuring colocalization [177]. Firstly, there is the measurement of co-occurrence or (weighted) overlap. Secondly, there is the more abstract measurement of statistical correlation where the relationships between the relative intensities for each pixel are considered.

The Pearson Coefficient (PC)

The Pearson coefficient (PC), R, is a popular correlation measure which was first used for colocalization analysis in fluorescence microscopy by Manders *et al.* (1992) [178]. It is defined as,

$$R(C_1, C_2) = \frac{\sum_i (C_{1,i} - \overline{C}_1)(C_{2,i} - \overline{C}_2)}{\sqrt{\sum_i (C_{1,i} - \overline{C}_1)^2} \sqrt{\sum_i (C_{2,i} - \overline{C}_2)^2}} = \frac{\mathrm{cov}(C_1, C_2)}{\sigma_1 \sigma_2} \tag{2.6.1}$$

where C_1, C_2 are vectors containing the data from the two spectral channels such that $C_{j,1}, ..., C_{j,n}$ are the individual pixels values for channel j. $\overline{C}_j$ and σ_j are the mean

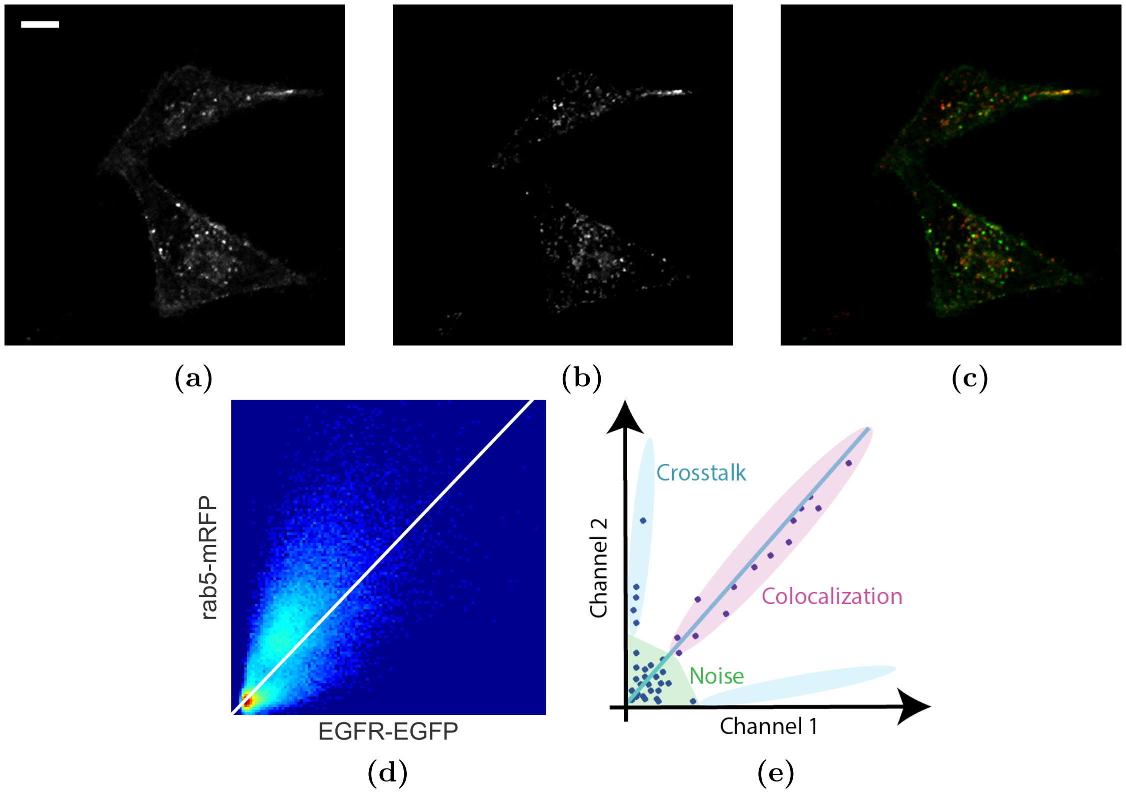

Figure 2.11: Visualising colocalization. (a) Distribution of EGFR-EGFP (b) Distribution of rab5-mRFP. (c) Visualising the colocalization between EGFR-GFP and rab5-RFP using an overlay isn't informative and is very dependent on image display parameters. (d) A joint histogram (log scale) is a superior way to visualise colocalization. If the majority of the data points are well represented by a linear fit, this is considered good evidence for colocalization (visual inspection). Ideally the joint histogram should be calculated using only voxels within a biologically relevant ROI. (e) Interpretation of a joint histogram. Well correlated pixels are centered around a linear fit (pink). Note the gradient of the fit will only by equal to one if the intensity distribution of both fluorophores is the same. Background noise (green) will be centered around the origin. If crosstalk is present it will appear as a linear distribution of points near the axis (blue). Figure adapted from [170].

and standard deviation for each channel, and cov() is the covariance operation. The PC can take values in the range [-1,1] where 1 represents perfect correlation, -1 perfect anti-correlation and 0 no correlation. A common criticism of the PC is that researchers can find intermediate values difficult to interpret.

Note the PC is a measure of how well the data in a joint-histogram plot can be modelled with a linear relationship and hence provides an elegant un-biased measure to complement visual interpretation of joint-histogram plots (figure 2.11e) [170]. When using the Pearson coefficient it is assumed that the datasets are linearly related, normally distributed and without outliers.

For unbiased results the PC should be calculated over a subset of pixels which correspond to either a biologically relevant ROI (for example the cytoplasm), or restricted only to pixels containing signal from both channels. The former will typically involve either a manual or automated segmentation procedure. The later involves isolating the *true* biological signal in each channel from the background signal and noise. Adler *et al.* (2010) justify this approach as the removal of all background pixels (pixels without signal) from the calculation to prevent inaccurate inflation of the PC [8]. Dunn *et al.* (2011) argue that the former approach is better when there is substantial signal overlap but a poor linear relationship [9]. However we note that for data with a poor linear relationship but high signal overlap, a co-occurrence measure would be more appropriate.

The Manders' Overlap Coefficient (MOC)

The Manders' Overlap Coefficient (MOC), R_M, is a modification to the PC where the subtraction of mean values is removed from the calculation,

$$R_M(C_1, C_2) = \frac{\sum_i C_{1,i} C_{2,i}}{\sqrt{\sum_i C_{1,i}^2 \sum_i C_{2,i}^2}} \tag{2.6.2}$$

The MOC was first introduced by Manders *et al.* (1993), motivated by the desirable property $R_M(aC_1, bC_2) = R_M(C_1, C_2)$, where a and b are positive constants [179]. Note this property does not hold for the PC which suggests it may be sensitive to the relative signal magnitude differences between channels which are often present in fluorescence microscopy data. However a recent thorough study has shown that signal magnitude differences (including changes in the level of detector gain) have little effect on the PC [8]. Moreover as the mean values are no longer subtracted, the MOC is very sensitive to background intensities and detector offset. Finally, the MOC measures a combination of co-occurrence and correlation making it difficult to interpret. For these reasons we do not recommend the MOC for colocalization analysis.

The Manders' Coefficients (M_1, M_2)

In addition to the MOC, Manders *et al.* (1993) also introduced a pair of co-occurrence colocalization measures, commonly referred to as the Manders' Coefficients (MCs); $M1$ and $M2$ [179]. $M1$ is defined as the percentage of the total (intensity sum) signal in channel 1 overlapping with signal in channel 2 and similarly for $M2$;

$$M1(C_1, C_2) = \frac{\sum_i C_{1,i} h(C_{2,i})}{\sum_i C_{1,i}} \qquad M2(C_1, C_2) = \frac{\sum_i C_{2,i} h(C_{1,i})}{\sum_i C_{2,i}} \tag{2.6.3}$$

where $h(x)$ is a step function such that,

$$h(x) = \begin{cases} 0 & \text{if } x \leqslant 0, \\ 1 & \text{if } x > 0, \end{cases} \tag{2.6.4}$$

The MCs have minimum and maximum values of 0 and 1 corresponding to 0% and 100% signal overlap (for either channel 1 or 2). Therefore the MCs provide easy to interpret results which are applicable even if the colocalization is not well modelled by a linear relationship. Moreover $M(aC_1, bC_2) = M(C_1, C_2)$ so the MCs are inherently insensitive to signal magnitude differences. To calculate the MCs it is necessary to accurately isolate biologically relevant signal in both channels. Note if done correctly this will remove dependency on offset and background.

In conclusion we consider the calculation of both the PCC (with signal isolation) and the MCs to be best practice for most applications. The PCC is an excellent indicator of (linear) correlation, while the MCs provide co-occurrence information. Together they can provide information about, not only the presence of colocalization, but also the nature of the statistical relationship.

Novel Colocalization Measures

Here we briefly discuss two recent and novel approaches. Singan *et al.* (2011) propose a paired metric (W_1 and W_2) which measures a combination of correlation and co-occurrence [180]. The authors falsely claim that theirs is the first colocalization measure to combine both correlation and co-occurrence (see the MOC for an explicit example). The authors also state this as the primary advantage for the method. We do not agree and consider separate calculations of both the PC and MCs to be more informative as it is important to distinguish between correlation and co-occurrence. However the measure is shown to be both robust and accurate for a variety of synthetic and real image data. W_1 and W_2 can be expressed as modified MCs where the spectral difference in the intensity ranking of pixels, w_i, is used as a weighting factor;

$$W1(C_1, C_2) = \frac{\sum_i w_i C_{1,i} h(C_{2,i})}{\sum_i C_{1,i}} \qquad W2(C_1, C_2) = \frac{\sum_i w_i C_{2,i} h(C_{1,i})}{\sum_i C_{2,i}} \tag{2.6.5}$$

Humpert *et al.* (2015) adapt a correlation-matrix method for spectral-temporal correlation analysis to the standard spectral-spatial setting [181]. The measure for this method

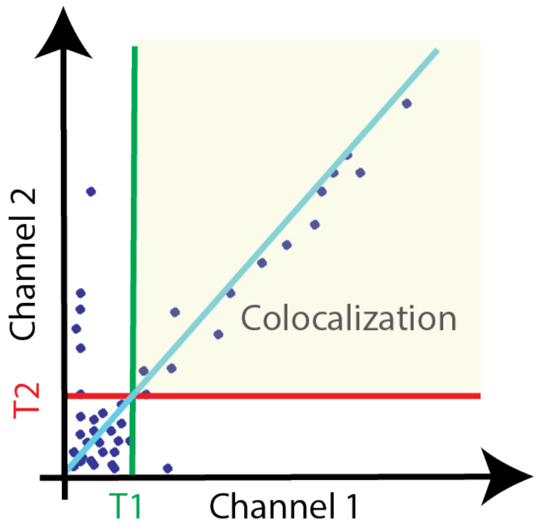

Figure 2.12: Costes' thresholding. In a Costes' thresholding approach the linear line of best fit for the joint histogram of the entire data set is used to define the relationship between the threshold values, $T1$ and $T2$. The threshold values are iteratively decreased until the Pearson Coefficient, $R \leqslant 0$, when calculated over the subset of voxels less than both threshold values. At this point pixels below both threshold values have no or negative correlation and are interpreted as noise and background. All voxels above the threshold values are defined as signal [182].

is proposed to be robust to low SNR and non-symmetric distributions of label intensity. It also extends to an arbitrary number of spectral channels and can be used to visualise maps of significant colocalization. However, we expect this formulation is too abstract and difficult to interpret for widespread application.

Strategies for Signal Isolation

As discussed above, signal isolation is essential for calculation of MCs, and under most circumstances best practice when calculating the PC. Typically, this is achieved by applying either a global, or local, thresholding operation to the image. Manually selected global thresholding is not a good strategy as user bias can influence results. Costes *et al.* (2004) introduced an elegant automated global thresholding strategy specifically designed for colocalization analysis (figure 2.12) [182]. Briefly, a linear line of best fit is calculated for the joint histogram of the data. The point on this linear fit below which there is no, or negative, correlation in the data is used to define the global threshold values.

The Costes' thresholding approach has been extensively and successfully used in many studies, for example [183, 184, 185], and is implemented in popular image processing software applications such as Fiji and Imaris [186]. It is worth noting that in the case of uneven background signal, or low SNR, global thresholding of the raw data will not accurately segment the signal. Therefore, to apply a global threshold, uneven background and noise should be removed by pre-processing the data with de-noising (section 2.5) and/or background subtraction algorithms. For example, Dunn *et al.* (2006) subtract a median filtered image from the original to remove background, and subsequently quantify rab10 colocalization within endosomes [187]. Finally, it has been suggested that when there is a large disparity between probe label density, or if label density is too high, the requirement for $R \leqslant 0$ may be too strict leading to Costes' threshold values which are too low to isolate the biologically relevant signal [9, 188].

Villalta *et al.* (2011) propose an algorithm for the isolation of colocalizing signal which instead of intensity thresholding, selects pixels based on the product of the PC and the MOC ($R \times R_m$) [189]. This novel approach is shown to work for non-symmetric and high label densities where Costes' thresholding fails. However, the algorithm has free parameters which have to be set empirically and makes extensive use of the MOC, the disadvantages of which are discussed above.

Statistical Significance

Here we discuss common strategies for testing of colocalization measurements against the null hypothesis that the probes are randomly distributed within the ROI. This is a difficult task for several reasons; firstly, fluorescence microscopy images have inherent auto-correlation. When the spread of the PSF extends over multiple pixels, neighbouring pixels will have similar values and auto-correlation is inevitable [9]. Secondly, defining the ROI can be difficult. For example, if studying receptor trafficking then it is necessary to isolate the intracellular region (the cellular boundary) but exclude the nuclear region. Moreover there will be other organelles, such as mitochondria or the ER, which can skew statistical tests if included in the ROI. However, it is normally impractical to isolate all relevant structures [9].

A common strategy is to randomise the position of pixels for one channel within the ROI and re-calculate the colocalization measure with respect to the unscrambled channel. This process is repeated many times and the test value, p is set as the fraction of values greater or equal than the original. This approach does not account for autocorrelation leading to false detection of significant colocalization. Costes *et al.* (2004) introduced the concept of block scrambling where instead of randomizing the positions of individual pixels, the position of squares (or cubes in 3D) the same size as the PSF are randomized [182]. Note, it has been suggested that a superior block size is the width of a typical object of interest [9]. Block randomization greatly reduces the effects of autocorrelation but it has been demonstrated that the effects are not removed completely [190, 168].

In the case where the objects of interest are smaller than the resolution limit of the microscope, synthetic images can be generated where the signal is randomly distributed within the ROI. This approach preserves autocorrelation effects from the PSF but will not preserve autocorrelation effects from objects larger than the PSF [9]. Moreover, generation of accurate synthetic data is a complex task which requires knowledge of various system parameters such as the form of the PSF and noise models.

A different approach involves translating the signal from one channel with respect to the other and repeating the calculations many times to obtain the p value [190]. This approach better preserves autocorrelation than block randomization but difficulties can arise for small ROIs as the number of possible translations is limited by ROI size. Moreover, edges must either be excluded or distorted (in *wrap around* approaches [191]) which can also lead to false detection.

All of the approaches discussed to this point consider each ROI, within each image, independently. A recent study by Mcdonald and Dunn (2013) proposes to use the distribution of measurements taken over multiple ROIs to perform a one sample Student's t-tests [10]. For the PC the mean across all ROIs is tested against a zero expected value; $E(P) = 0$. For the MCCs we note that the expected value for a random distribution, $E(M_j)$ are ROI dependent and equal to the fractional area of a ROI occupied by signal j. The authors validated this approach on synthetic data and suggest it provides an accurate and simple way to test for statistical significance.

2.6.2 Object-based Colocalization Measures

In object based methods, features of interest are segmented and represented by their (intensity weighted) center of mass (COM) position. Statistical clustering measures can then be used to highlight colocalization over varying length scales, r (figure 2.10b). These approaches are clearly only applicable when objects are well represented by their COM, i.e. *spot like*. Moreover, intensity information, which is related (not necessarily linear) to fluorophore density, is discarded. However, unlike pixel based methods they can identify colocalization for r greater than the resolution limit and are therefore ideal for the analysis of data from super-resolution microscopy. In a recent review, Lagache *et al.* (2015) found that object based measures outperformed pixel based measures for simulated and TIRF (total internal reflection fluorescence) microscopy data [168].

Spot (feature) detection is an essential preprocessing step for all object based measures. There are many approaches, typically with de-noising (section 2.5) and/or detection steps. For example Olivo-Marin (2002) uses a B3-spline implementation of the undecimated wavelet transform (section 2.5.3) and adaptive thresholding in the wavelet domain to identify spots [192]. This approach is implemented in the open source image processing application Icy [193]. For an extensive review comparing different spot detection methods see Smal *et al.* (2010) [152].

Measures

We will briefly describe two clustering statistics which can be used for colocalization analysis. Firstly, the nearest neighbour measure, S_N, is given by [194],

$$S_N(r) = \frac{1}{n_1} \sum_{i=1}^{n_1} \min_j (d_{ij} h(r - d_{ij})) \tag{2.6.6}$$

where n_j is the number of detected objects in channel j and h is the step function as described in equation 2.6.4. d_{ij} is the euclidean distance between object i in channel 1 and object j in channel 2. Secondly, the Ripley-K function S_K is given by [195],

$$S_K(r) = \frac{|\Omega|}{n_1 n_2} \sum_{i=1}^{n_1} \sum_{j=1}^{n_2} d_{ij} h(r - d_{ij}) b(i, j, r) \tag{2.6.7}$$

where $|\Omega|$ is the area (or volume) contained within the ROI. $b(i, j, r)$ is a boundary correction term typically given by Ripley's Correction [196, 195].

The nearest neighbour approach is simplest but doesn't account for edge effects. Moreover the cumulative effect of including all objects within a radius, r instead of just the closest implies that Ripley's K function is more robust and informative than a nearest neighbour approach [197].

Statistical Significance

In statistical significance testing for object based measures, we test against the hypothesis that the point processes for both channels are randomly distributed with respect to the measure, S. This is problematic, largely due to edge effects for arbitrarily shaped ROIs. A common approach computes the critical quantiles for S, $q_{1-\alpha}(r)$, under the assumption of random distributions (for a chosen significance level α). Quantiles are typically computed by Monte-Carlo simulations [198] but a less computationally expensive method has been proposed by Lagache *et al.* (2013) for Ripley's K function [199].

Naively, the statistical condition for colocalization can then be defined as; $S(r) > q_{1-\alpha}(r)$. However a joint statistic, encompassing all distance scales, is superior to account for correlation between $S(r)$ at varying r. A joint measure has been proposed for the nearest neighbour but Ripley's K function remains problematic [200, 168]. Finally we note, modelling approaches can be used to extract quantitative information such as the interaction distance or the number of interacting objects from either the nearest neighbour or Ripley's K-function [200, 168].

2.7 Organisation of the thesis

Having concluded our discussion of the material necessary to understand and contextualize this work, we briefly outline the plan for the remainder of the thesis. The aim of this thesis is to develop a set of computational workflows to quantify receptor trafficking, using confocal microscopy. Importantly, all of the presented methods should be unbiased and reproducible.

Chapter 2: 4D Level Set Segmentation for Fluorescence Microscopy

Level set segmentation, as discussed in section 3.3, is a powerful tool for image segmentation. Image segmentation is the identification of target objects within image data, and a vital step in all of the workflows presented in this thesis. Accurate cellular segmentation in 4D (3D time-lapse data), using only the signal from a fluorescently labelled receptor is a difficult task. Motivated by this problem, novel extensions of popular edge and region based level set protocols to a 4D framework were developed. These approaches find a globally optimal segmentation solution across the entire data set simultaneously, to improve performance. In this chapter we formally present the details of the 4D level set protocols and validate these methods using both synthetic and real test data. Our methods demonstrate a statistically significant increase in performance over equivalent 2D and 3D implementations of the same algorithms. Finally, temporal constraints in the form of (near) constant volume and shape assumptions are introduced and validated.

Chapter 3: Screening for Regulators of Receptor Trafficking

In this chapter, data from a SILAC proteomics study is used to select a subset of GEFs and GAPs (section 2.3) which may regulate trafficking of EGFR. Using a siRNA library for the selected genes, a confocal microscopy screening platform is presented, which uses only widely available experimental equipment, to identify *hits* for further analysis. Acquisition is in 2D and hits are identified using only EGFR-GFP signal before and after treatment with ligand (EGF). Details of a novel, robust and automated image analysis workflow to select hits is presented.

Chapter 4: Workflows to Quantify Receptor Trafficking in 4D

Protocols in fluorescence microscopy used to quantify receptor trafficking and colocalization with sub-endosome populations are often poorly designed and implemented. In this chapter we highlight common pitfalls in analysis and design several fully automated and novel workflows to quantify trafficking and colocalization in 4D. To validate these methods, the trafficking response and colocalization of EGFR with early endosomes is quantified over time in response to various drug treatments (AG1478, dynasore and dasatinib). All workflows presented require accurate segmentation of the plasma membrane and nucleus. Both are segmented using only the EGFR and early endosome signal with the methods presented in chapter 3. Problems in current *best practice* guidelines for colocalization analysis are highlighted and solutions are suggested. Finally methods for visualisation of colocalization in 4D are presented. The workflows presented in this chapter provide computational tools for secondary screens to further study hits from siRNA screens, as presented in chapter 4.

Chapter 5: Final Discussion and Future Directions

A concise summary of the work and discussion of future directions is presented.

Chapter 6: Materials and Experimental Methods

A complete list of all experimental protocols and reagents used in this work, described in sufficient detail as to be reproducible.

Chapter 3

4D Level Set Segmentation for Fluorescence Microscopy

3.1 Introduction

In this chapter, a novel class of level set based techniques for the segmentation of 4D (3D+time) data is introduced. The discussion is kept abstract and analysis of explicit applications is limited. This is done to preserve generality and emphasise the wide range of potential applications. In chapter 5, explicit examples of practical applications are discussed. Specifically, workflows are presented which incorporate the techniques introduced in this chapter, to quantify receptor trafficking and endocytosis.

The structure for this chapter is as follows. In section 3.2 a brief overview of segmentation methods for fluorescence microscopy is provided. In section 3.3 level set segmentation is introduced with an emphasis on the methods adapted for this thesis. In section 3.4 we motivate the development of 4D level set segmentation and discuss related approaches. Section 3.5 concisely formulates the aims of the chapter. In section 3.6 the extension to 4D is presented and these approaches are validated on real and synthetic test data. In section 3.7 adaptations to the segmentation protocols which take advantage of temporal assumptions in the data are introduced. Finally, in sections 3.8 and 3.9 a discussion and conclusion is provided.

3.2 A Brief Review of Segmentation Strategies

In the context of biological studies, segmentation is the process of partitioning image data into regions with biological meaning. For example segmentation of whole cells, nuclei or endosomes from the background. There are a vast number of segmentation protocols available in the literature and many methods are designed for a specific dataset, or application, with limited generalisation. Sbalzarini (2016) classifies image analysis workflows into three distinct categories; filter based, model based and machine learning based [201]. Here we also use this general classification to briefly discuss segmentation strategies.

Filter based segmentation

In a filter based approach a series of filters, morphological operations and thresholds are applied sequentially to facilitate segmentation of target objects. Common filters include Gaussian, mean, median and Laplacian of Gaussian (section 2.5). More sophisticated filters can be wavelet based (section 2.5.3) [192]. Filters are used to either suppress undesirable components, for example noise, or enhance features of interest, for example endosomes. The use of a watershed transform to segment nuclei, or cells, is a classic example of a filter based approach [202]. Filter based approaches are typically designed, and optimised, for a specific application and therefore do not generalise well. Workflows designed using this approach can easily become convoluted with many steps and have a corresponding large number of free parameters. Moreover the rational for setting these parameters is often not clear. However filter based approaches are typically fast which is particular advantageous for large datasets where computational time can be the limiting factor.

Model based segmentation

In a model based approach, prior information about the acquisition process and/or the target objects is used to form a model which drives the segmentation [201]. The aim is to find the segmentation solution which best explains the data under the constraints of the model. An excellent framework for model based segmentation was introduced by Paul *et al.* (2013) [203]. The approach allows for the incorporation of an image formation model, a noise model and an object model. By incorporating the point spread function (PSF) and a noise model, for example a Poisson distribution, simultaneous image restoration and segmentation is performed. In the original algorithm, all target objects were modelled as having homogeneous intensity, but this was later extended to piecewise homogeneity, where intensity can vary between objects [204]. Other model based approaches include Chan-Vese level set segmentation [14], region competition [205] or modifications to the watershed transformation which merge regions based on models for the target objects [206, 207].

Model based approaches are based on prior knowledge and physical models, and hence have the key advantage of being well reasoned. However, the approach is only as good as the model used. Crucially some model based approaches generalise well for a variety of applications. For example in the Paul *et al.* (2013) approach, the noise model and PSF can easily be changed, but the underlying algorithm stays the same [203]. Therefore this approach can be used for many different datasets. However model based approaches are typically slower than filter based approaches. Moreover as the algorithms are mathematically technical the interpretation and setting of parameters can be difficult for a non-expert.

Machine learning based segmentation

Machine learning can be used to perform image segmentation using pixel classification approaches [208]. In these approaches, various features are calculated for each pixel based on its local neighbourhood. Typically features are intensity, colour or texture based. In a supervised approach manual annotation must be performed using training data. These manual annotations are then used to train a classifier across the specified range of features. Common classifiers include support vector machines [209, 210], adaptive boosting [211] and random forests [212]. Open source projects such as ilastik have made supervised pixel classification approaches easily accessible for non-experts [213]. Some classifiers will produce excellent results across a wide range of complex problems. However the training stage requires the time of a biological expert and computational times are typically larger than for filter based approaches.

In this chapter we consider the extension of two model based segmentation approaches to 4D. Specifically we extend the edge based approach introduced by Caselles *et al.* (1997) [13] and the region based approach introduced by Chan and Vese (2001) [14]. These approaches were chosen due to their wide-spread application. We aim to show that segmentation in 4D can improve the performance of these seminal approaches. A level set based framework for energy minimisation was chosen as the extension to 4D is mathematically trivial. Hence level set segmentation provides a simple framework for this point-of-principle testing [214]. This is discussed in more detail in the next section.

3.3 Level Set Segmentation

Deformable model approaches to bio-medical image segmentation are well established and have been extensively applied to a variety of imaging modalities and applications [215, 216]. In this section we review the the basic concepts and theory of level set segmentation, a sub-class of deformable model approaches, which are both applied and developed, throughout this work.

In a deformable model approach, a surface, or curve, matching the dimensionality of the data is evolved such that it converges towards the boundary of the target object(s). The evolution of the surface is controlled by external and internal forces. External forces are derived from the data set and move the surface towards object boundaries, whereas internal forces derive from the surface itself and control the smoothness and regularity of the segmentation.

The surface can be represented either explicitly or implicitly. Explicit techniques such as classical active contours, popularly known as snakes, model the curve using parametric representations for 2D segmentation of closed objects [217]. Some excellent, more recent, approaches use discrete explicit representations, such as triangular meshes, to segment objects in 3D [218, 219]. In both cases, the representation of the surface, or curve, must be regularly re-constructed although only locally in the case of triangular meshes. Explicit representations require subroutines to deal with topological changes such as the merging and splitting of cells and extensions to higher dimensions are non-trivial, often requiring additional subroutines.

Level set methods, originally proposed in the seminal work by Osher and Sethian, [214] use an implicit representation. The segmentation contour is embedded as the zero level set of a Lischitz surface of one dimension higher than the dataset. The zero level set is the set of points on which the level set function (the Lischitz surface) has value zero. Level set techniques have several desirable properties; firstly, as the representation is implicit there is no requirement for re-parametrization or reconstruction. Extensions to higher dimensions, as well as changes in the topology of the surface, are handled naturally as the level set function remains differentiable over its entire domain. However, computational costs are significantly higher than for most deformable model approaches due to manipulation of the high dimensional level set function.

The seminal work by Osher and Sethian was based on Hamilton-Jacobi formulations for evolving surfaces with a curvature dependent speed [214] . We take this as the starting point for our discussion and consider the evolution of a Lipschitz surface, ϕ, known as the level set function (LSF), where the segmentation contour is embedded as the zero level set of ϕ. The LSF is defined on a domain, Ω, such that $\phi(\mathbf{x}) : \Omega \rightarrow \Re$. Moreover ϕ is set to be equal to the signed distance from the zero level set with $\phi < 0$ inside the zero level set and $\phi > 0$ outside. In this framework, simple geometric properties of the LSF such as the normal vector, $\vec{N}$, and Euclidean curvature , κ, can be easily calculated [220];

$$\vec{N} = \frac{\nabla\phi}{|\nabla\phi|} \qquad\qquad \kappa = \operatorname{div}\left(\frac{\nabla\phi}{|\nabla\phi|}\right) \tag{3.3.1}$$

Osher and Sethian considered the evolution of the LSF such that the zero level set propagates at speed, V, in a direction normal to the surface, $\vec{N}$. The speed V was chosen such that it is proportional to the curvature of ϕ;

$$\begin{aligned}\tfrac{\partial\phi}{\partial\tau} &= V\vec{N}\cdot\nabla\phi \\ &= V|\nabla\phi| \\ &= b\kappa|\nabla\phi| \end{aligned} \tag{3.3.2}$$

where b is a constant. τ is the time parameter for the evolution of ϕ. Equation 3.3.2 is known as a level set equation (LSE) because it controls the dynamics of ϕ and determines the segmentation result. Here the LSE simply decreases the total curvature and hence has a smoothing effect on ϕ. Note that there is no inherent attraction to features within the image (I). To faciliate data dependence a function, $g(I)$, can be introduced, which is minimised on features of interest, such that [221];

$$\frac{\partial \phi}{\partial \tau} = g(I)(\kappa + c)|\nabla \phi| \tag{3.3.3}$$

where c is a constant which determines the magnitude of a constant velocity normal to ϕ (weighted by $g(I)$). This constant velocity can be thought of as force pushing the zero level set inwards or outwards and is necessary to segment non-convex objects. In an edge based approach $g(I)$ is chosen such that it is minimised on a perfect edge. A common choice for $g(I)$ is;

$$g(I) = \frac{1}{1 + |\nabla I_{smooth}|^p} \tag{3.3.4}$$

where $p = 1$ or 2 . I_{smooth} is a smoothed version of I typically formed by convolution with a Gaussian kernel (section 2.5.1) [221, 222]. Note, pixels located on a sharp edge will have large gradient values, $|\nabla I_{smooth}|$, and hence have small values for g. Therefore, on edges, the velocity proportional to the curvature will be small (equation 3.3.3).

3.3.1 The Energy Minimising Formulation

The evolution of the LSF should be controlled such that it approaches a steady state solution when the zero level set is located on target boundaries. In a variational approach this is achieved by the minimization of an energy functional, $E(\phi, D)$, which is constructed to have minimal values on targets boundaries [223, 221]. The energy functional consists of internal and external terms, denoted $E_{int}(\phi)$ and $E_{ext}(\phi, D)$;

$$E(\phi, I) = E_{int}(\phi) + E_{ext}(\phi, I) \tag{3.3.5}$$

External terms are dependent on the dataset and are minimised at the desired locations in the image, typically object boundaries. Internal terms are derived from the LSF only and are used to control the form of the LSF by manipulating its properties such as the smoothness of the zero level set, or the gradient of ϕ.

Caselles *et al.* (1997), in their seminal work on geodesic active contours, used an energy minimization formulation [13]. The authors first formed an active contour model based on geometric measures within the image. The model was then reinterpreted in a level set framework, therefore bridging the gap between active contour and level set methods. Consider a closed contour, $C(a)$, on $a = [0, 1]$. Instead of minimising the standard Euclidean length of the contour, $L_E(C)$, the following energy is minimised;

$$\begin{aligned} E &= \int_0^1 g|C'(a)| \,\mathrm{d}a \\ &= \int_0^{L_E(C)} g(I(C)) \,\mathrm{d}s \end{aligned} \tag{3.3.6}$$

where s is the Euclidean arc length. E differs from L_E in that it takes into account information from the image contained in the edge detector g. Minimising E and setting in a level set framework results in the following LSE;

$$\frac{\partial \phi}{\partial \tau} = g(I)(\kappa + c)|\nabla \phi| + \nabla g(I) \cdot \nabla \phi \tag{3.3.7}$$

where a constant force term dependent on free parameter c has been added. We will refer to equation 3.3.7 as the geodesic LSE. Comparing equation 3.3.3 and the geodesic LSE, it is clear that we have picked up an extra term, namely $\nabla g(I) \cdot \nabla \phi$. This term reinforces the evolution of the zero level set to boundaries within the image and crucially makes the result less sensitive to tunable parameters.

3.3.2 Implementation with Distance Regularized Level Set Evolution

To ensure convergence of the LSF to an accurate segmentation, it is necessary to require that the LSF, ϕ, be a signed distance function. In practice we require $|\nabla\phi| = 1$ around the zero level set only. Traditionally this is solved using reiteration schemes but in distance regularized level set evolution (DRLSE), an internal energy term is introduced which triggers a diffusion type effect on the LSF towards a signed distance function [224, 225]. Explicitly Li *et al.* (2010) [225] suggest the following potential energy,

$$P(|\nabla\phi|) = \begin{cases} (1 - \cos(2\pi|\nabla\phi|))/(2\pi)^2 & \text{if } |\nabla\phi| < 1 \\ (|\nabla\phi| - 1)^2/2 & \text{if } |\nabla\phi| \geqslant 1 \end{cases} \tag{3.3.8}$$

such that

$$E_{int}(\phi) = \mu \int_\Omega P(|\nabla\phi|)\,\mathrm{d}\mathbf{x} \tag{3.3.9}$$

where μ is a constant. The potential energy has two minimal points at $|\nabla\phi| = 1$ and 0. When E_{int} is minimised, this has the effect of inherently maintaining the signed distance property of the LSF around the zero level set and smoothing elsewhere. This distance regularizing term removes the need for reiteration subroutines (figure 3.1). Moreover it allows for narrowband implementations and large time-steps between iterations, thus reducing computational costs. Initialisation of the level set function is trivial and the diffusion effect can reform a binary step function. In this work we refer to the inclusion of the internal energy term shown in equation 3.3.9 as a distance regularized level set evolution (DRLSE) approach.

Recall the evolution of ϕ is captured by the level set equation (LSE) and note the LSE can be related to the energy function, E, by the Euler Lagrange equation which minimises

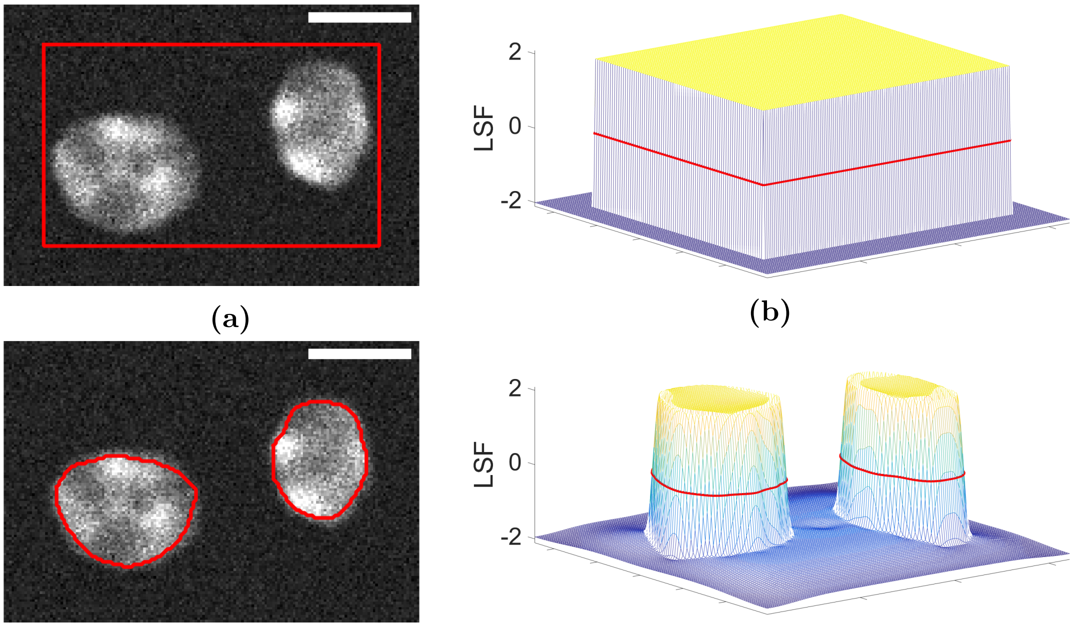

(a) (b)

(c) (d)

Figure 3.1: 2D Level Set Segmentation. (a) Synthetic fluorescence microscopy image of stained nuclei [226]. The initial position of the zero level set of level set function (LSF) is shown in red. (b) The LSF can be initialised with a binary step function when using a distance regularized diffusion term (section 3.3.2) (c) After energy minimization and the corresponding evolution of the LSF, the nuclei are segmented by the zero level set (red). In this example, a geodesic edge based approach was used (equation 3.3.6) (d) The LSF after evolution. Note the topological change in the zero level set is handled naturally by the LSF. Scales bars represent $5\mu m$.

E. In a DRLSE approach this can be expressed using the Gateaux derivative of E within a simple gradient descent scheme;

$$\frac{\partial \phi}{\partial \tau} = -\frac{\partial E}{\partial \phi} \tag{3.3.10}$$

where τ represents the time-parameter for evolution of the LSF. Iterations are repeated until the LSF reaches a (near) steady state. Moreover with a DRLSE approach, the derivatives for all of the energy terms used in this work can be calculated using simple finite difference approximations.

3.3.3 Level Set Segmentation without Edges

To this point, all of the discussed external energy terms have been based on edge detection (equation 3.3.4). For many applications an edge based approach can lead to bleed-through of the LSF into or out of the object due to boundary discontinuities. Here we describe the region based level set segmentation framework proposed by Chan and Vese (2001) which clusters the data based on relative pixel intensity [14]. The energy functional is given by

$$E_{ext}(\phi, I) = \beta \int_{\Omega} H(-\phi)|I - C(-\phi, I)|^2 + H(\phi)|I - C(\phi, I)|^2 \, \mathrm{d}\mathbf{x} \tag{3.3.11}$$

where $C(-\phi, I)$ and $C(\phi, I)$ are the average intensities of the data, I, within and outside the zero level set respectively. β is a constant and $H(x)$ is the Heaviside step function;

$$H(x) = \begin{cases} 0 & \text{if } x < 0, \\ 1 & \text{if } x \geqslant 0, \end{cases} \tag{3.3.12}$$

Note that the minimization of the Chan-Vese energy term is analogous to K-means clustering but in a level set framework [227]. Chan and Vese also used a smoothing internal term comparable to that in equation 3.3.6 but without weighting with an edge indicator;

$$E_{int}(\phi) = \lambda \int_{\Omega} \delta(\phi)|\nabla\phi| d\mathbf{x} + c \int_{\Omega} H(-\phi) \, \mathrm{d}\mathbf{x} \tag{3.3.13}$$

where $\delta(x)$ is the Dirac delta function defined such that;

$$\delta(x) = \frac{\mathrm{d}H(x)}{\mathrm{d}x} = \begin{cases} +\infty & \text{if } x = 0, \\ 0 & \text{if } x \neq 0, \end{cases} \tag{3.3.14}$$

Note the first term in equation 3.3.13 is a smoothing term and the second provides a constant force. Throughout this work we refer to the inclusion of Chan-Vese external term (equation 3.3.11) in the energy functional as a region based approach.

3.4 Motivation and Related Approaches

Following the discussion in section 3.3, recall that extension of a level set segmentation protocol to an arbitrary number of dimensions is both possible and mathematically natural. However, it is important to note that computational costs are significantly greater in higher dimensions. This is due to the demands of working simultaneously with the large number of voxels within a 4D dataset, and the corresponding level set function. This is an obvious limiting factor when working with 4D level set protocols.

To justify and contextualise our approach, we will briefly review other relevant strategies for the segmentation of 4D datasets. Note a 4D dataset consists of a time-lapse series recorded in all three spatial dimensions. To segment target objects within this 4D dataset, several different approaches are possible;

1. Each 3D time-point (or even each 2D image) can be segmented independently. This approach is wasteful as potentially useful temporal information and corresponding performance gain is lost.

2. The object is segmented for the first time-point, and this segmentation is used as a source of information to influence segmentation in subsequent time-points. After the targets in each time-point are segmented the temporal feedback loop can be updated. In this approach, errors are propagated from previous time-points and no temporal information is used for the first time-point. For example the segmentation from the previous time-point can be used to initialise the segmentation for the current time-point [228].

3. All time-points are processed simultaneously in what we will refer to as *true 4D segmentation*. Temporal information is incorporated both equally and globally for all time-points. As all time-points have equal weighting and are processed simultaneously the solution is not biased towards specific, or earlier, time-points. Intuitively this approach is superior and it is hypothesised that if properly implemented it should lead to more accurate segmentation.

There are many examples in the literature of the second approach [229, 228, 230]. However, there are surprisingly few examples of true 4D segmentation. Level set methods are a natural choice for the implementation of true 4D segmentation due to a lack of complicating subroutines and natural extension to arbitrary dimensions. In independent studies, Kohlberger *et al.* (2006) and Abufadel *et al.* (2008) proposed to *"treat time as an ordinary fourth dimension"* and segment the entire dataset simultaneously with a 4D LSF [11, 12]. These approaches were designed for and tested on cardiac SPECT and MRI data sets respectively. In both cases, the Chan-Vese region based scheme (section 3.3.3) is used and a shape model is incorporated into an additional energy function to assist segmentation [231, 232]. The shape model is calculated from a training data set using principal component analysis (PCA) prior to the implementation of the 4D level set algorithm.

Similarly Lynch *et al.* (2008) use a temporal model to segment cardiac MRI data but the model is updated with each iteration of the energy minimisation [233]. However, in this approach each time-point was segmented in parallel with a 3D level set approach.

Lombaert *et al.* (2011) use a graph cut method to perform true 4D segmentation of MRI and CT data. Briefly, graph cut approaches are closely related to level set methods, but use a graph based algorithm for energy minimisation over more traditional gradient descent approaches [234]. This can decrease convergence times and computational cost but imposes constraints on the form of the energy functional [235]. We restrict our efforts to level set methods to give greater flexibility and control over the energy functional. The allows for the easy introduction of customised temporal constraints as discussed in section 3.7.

Pastor *et al.* (2009) to the best of our knowledge, developed the first true 4D segmentation method to be successfully applied to time-lapse microscopy [236]. They use 4D structural elements to find globally optimal solutions for cell tracking which they apply to in-vivo studies [237]. However this framework is primarily designed for object tracking and not well suited to accurate segmentation of object boundaries. To counter this, a follow up study successfully introduced an extension of the watershed algorithm to 4D [238].

Finally, Padfield *et al.* (2006) have successfully used 3D level sets to segment cells from 2D time-lapse data and incorporate several models and constraints for cell cycle analysis in subsequent studies [239, 240, 241]. However, to the best of our knowledge no true 4D level set based segmentation methods have been used to analyse 4D microscopy data.

3.5 Chapter Aims

The aims for this chapter can be summarised as follows:

1. Adapt and improve existing 4D level set frameworks as a new approach to the segmentation of (confocal) microscopy data [11, 12].

2. Validate this novel approach on synthetic and real fluorescence microscopy datasets. We hypothesise an improvement in segmentation performance for a 4D approach over equivalent 2D and 3D implementations.

3. Suggest modifications to the level set equation which take advantage of temporal information and assumptions for the data to improve segmentation performance.

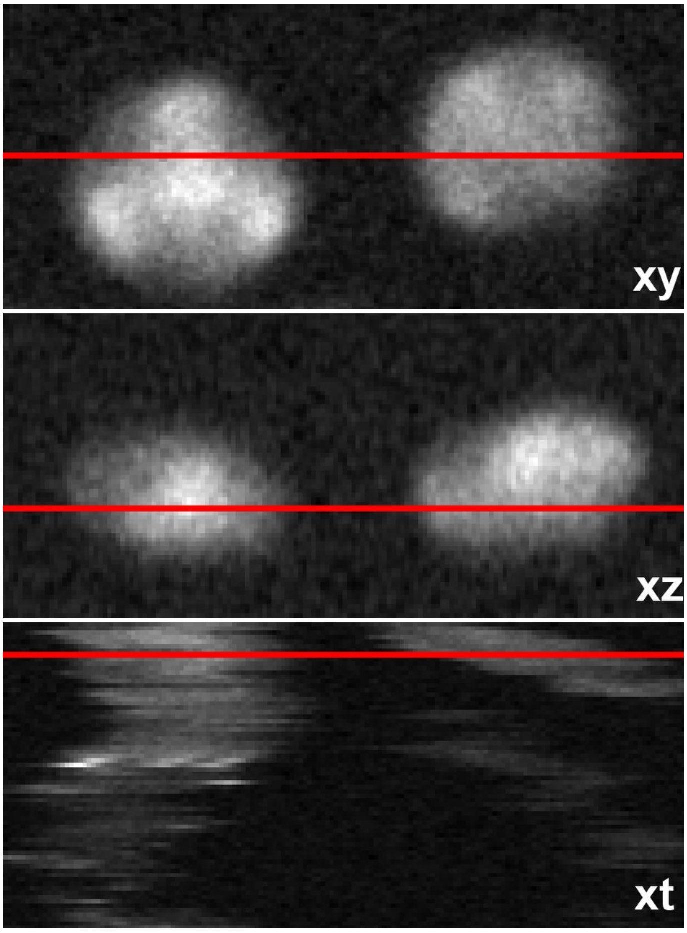

Figure 3.2: 4D data as a hyper-volume. 4D data can be constructed and handled as a single 4D array. Here we show representative 2D xy, xz and xt ortho-slices from the 4D hyper-volume [226]. The red lines represent the position of the frames within the 4D volume. Note, in the xt slice the movement and position of the nuclei can be observed. The aim of our method is to use this temporal information to improve segmentation performance. As a pre-processing step the data has been blurred with a Gaussian filter in the three spatial dimensions. The standard deviation of the kernel was set to the theoretical width of the point spread function.

Validate these approaches on the test data sets.

3.6 Framework for 4D Segmentation

In accordance with previous protocols for 4D level set segmentation, we choose to process the dataset by merging the data from each time-point to form a single 4D array; $I(\mathbf{x})$ where $\mathbf{x} = (x, y, z, t)$ (figure 3.2) [11, 12]. The volumetric data from each time-point is combined such that each voxel has a total of 8 neighbours (6 spatial and 2 temporal). In this framework the LSF maps each 4D voxel to a real number; $\phi(\mathbf{x}) : \Omega \to \Re$, where Ω is the domain of $I(\mathbf{x})$. Therefore the zero level of $\phi(\mathbf{x})$ is a 4D hyper-surface and after energy minimisation will represent a globally optimal segmentation for the entire dataset.

In this section a justification of this approach is provided, alongside the details necessary for reproducible implementation. In section 3.6.1 the adaptation of the DRLSE scheme (section 3.3.2) to 4D is presented. In section 3.6.2 the calculation and scaling of temporal derivatives is discussed. In section 3.6.3 the explicit form of the LSE for either edge, or region, based level set segmentation is provided. Initialisation of the LSF is discussed in section 3.6.4. Finally, the performance of the proposed framework is analysed on synthetic and real test data (sections 3.6.5 and 3.6.6).

3.6.1 Energy Minimisation with DRLSE

To implement level set segmentation in 4D a variational approach was taken. Recall, that in a variational approach the evolution of the LSF, ϕ, is determined by the minimisation of an energy functional and the associated level set equation (section 3.3.1). For all formulations presented in this thesis we always choose to include a DRLSE diffusion term in the energy functional (equation 3.3.9) [225]. This is an original approach for 4D level set segmentation and there are several important reasons for this choice, to summarise;

1. The DRLSE term maintains the signed distance property ($|\nabla\phi| = 1$) of the LSF around the zero level set (with $|\nabla\phi| = 0$ elsewhere). This removes the need for reinitialisation of the LSF.

2. Simple central difference schemes can be used to calculate partial derivatives within the energy functional (section 3.6.2).

3. The LSF can be initialised as a binary step function. This is discussed in more detail in section 3.6.4.

4. It allows for a simple finite difference update scheme for the implementation of the level set equation (LSE). The details of this update scheme for 4D level set evolution are described in the remainder of this section.

When using a DRLSE approach, the LSE can be discretised such that;

$$\phi^{m+1}_{x,y,z,t} = \phi^{m}_{x,y,z,t} + \Delta\tau \frac{\partial \phi}{\partial \tau}\bigg|_{x,y,z,t} \tag{3.6.1}$$

where $\Delta\tau$ is a constant, referred to as the update step. Recall that $\frac{\partial \phi}{\partial \tau}$ can be calculated from the energy functional using a gradient descent approach (equation 3.3.10). m represents the iteration count which is typically increased until convergence within a tolerance level. We choose to set this tolerance level as a percentage of the segmentation volume, V^m. Note that V^m can be easily calculated using the LSF;

$$V^m = \int_\Omega H(-\phi^m)\,\mathrm{d}\mathbf{x} \tag{3.6.2}$$

The algorithm implementing the described update scheme and stopping condition can be summarised as follows;

Algorithm 1 Evolution of LSF

```
while $|V^{m+1} - V^m| > s \times V^m$ do
    $\phi^{m+1} = \phi^m + \Delta\tau \frac{\partial \phi}{\partial \tau}$
end while
```

The stopping constant, s, is typically set to 0.0001. In practice a maximum number of iterations is also set. Note that the structure of this algorithm is very simple and lacks any complicating sub-routines. Explicit calculations of $\frac{\partial \phi}{\partial \tau}$ for both edge and region based approaches are presented in section 3.6.3.

To ensure the correct evolution of the LSF with a DRLSE term, the size of the constant, μ, from equation 3.3.9, should be constrained by the update step, $\Delta\tau$, and the derivative scaling factors (section 3.6.2). In 2D, with $\Delta x = \Delta y = 1$, this constraint is given by the Courant-Friedrichs-Lewy (CFL) condition [225, 242];

$$\mu \leqslant \frac{1}{4\Delta\tau} \tag{3.6.3}$$

With a 4D framework the equivalent CFL condition can be expressed as;

$$\mu \leqslant \frac{1}{2\Delta\tau}\left(\frac{1}{\Delta x^2}+\frac{1}{\Delta y^2}+\frac{1}{\Delta z^2}+\frac{1}{\Delta t^2}\right)^{-1}=\mu_l \tag{3.6.4}$$

This provides an upper bound on the value of μ for 4D DRLSE. Typically, we set the update step such that $\Delta\tau = 1$ and μ_l is calculated using this bound. To set μ we always subtract a small value from the theoretical bound. This is done to avoid the development of irregularities in the level set function as is demonstrated in figure 3.5.

3.6.2 Temporal Scaling

To compute the terms of the level set equation, it is necessary to calculate temporal derivatives for both the data, $\frac{\partial I}{\partial t}$, and the LSF, $\frac{\partial \phi}{\partial t}$. For example to compute the edge indicator, $g(I)$ (equation 3.3.4), in 4D it is necessary to calculate the gradient of the data,

$$\nabla I(\mathbf{x}) = \left(\frac{\partial I}{\partial x}, \frac{\partial I}{\partial y}, \frac{\partial I}{\partial z}, \frac{\partial I}{\partial t}\right) \tag{3.6.5}$$

As discussed in section 3.6.1, a DRLSE term is introduced into the energy functional. Using such a scheme, approximations for the partial derivatives can be calculated using a central difference scheme. For example;

$$\left.\frac{\partial I}{\partial x}\right|_{x,y,z,t} = \frac{I_{x+1,y,z,t} - I_{x-1,y,z,t}}{2\Delta x} \tag{3.6.6}$$

where x, y, z, t represent the coordinates of an individual voxel and Δx is the scaling factor for the first spatial dimension. Typically, the weighting for the lateral spatial dimensions are set to $\Delta x = \Delta y = 1$. The axial scaling factor is given by,

$$\Delta z = \frac{V_z}{V_{xy}} \tag{3.6.7}$$

where V_{xy}, V_z are the physical dimensions of the voxels in the lateral and axial dimensions respectively. In a 4D approach it is important to set the temporal scaling factor, Δt, relative to the spatial dimensions. For clarity, we note that in this case Δt is not an explicit measure of time, but a scaling factor between the temporal and spatial derivatives. Clearly the larger the chosen Δt the smaller the influence of the temporal gradient on the evolution of the LSF. We propose to set Δt such that;

$$\Delta t = \frac{\langle D \rangle}{V_{xy}} \tag{3.6.8}$$

where $\langle D \rangle$ approximates mean boundary displacement between time-points. This is done because the faster the boundary of the target(s) is moving, the less useful the time derivative is for segmentation. This is discussed in more detail in figure 3.3.

The parameter $\langle D \rangle$ can either be inferred from prior knowledge of the targets, or estimated directly from the data. For example, in the case of prior knowledge, if the targets are nuclei and it is known from previous studies the average velocity is expected to be $0.1 \mu m$ per minute, and the acquisition rate is 0.2 time-points per minute, then $\langle D \rangle = 0.1/0.2 = 0.5 \mu m$. Note, in this calculation there is an assumption that the target shape does not change significantly between time-points.

Alternatively, if there is no prior knowledge available, then schemes to estimate $\langle D \rangle$ directly from the data should be employed. A simple method to approximate $\langle D \rangle$ is described below, and its use is demonstrated on simulated data in figure 3.4;

1. Compute an approximate segmentation of the data using an algorithm with low computational cost. Approaches based on K-means clustering are used throughout this work. Note this *initial guess* can also be used to initialise the LSF (section 3.6.1).

2. Calculate the centre of mass (COM) of each object in every frame. For this simple test dataset, and for the purpose of estimating the scaling factor, touching objects

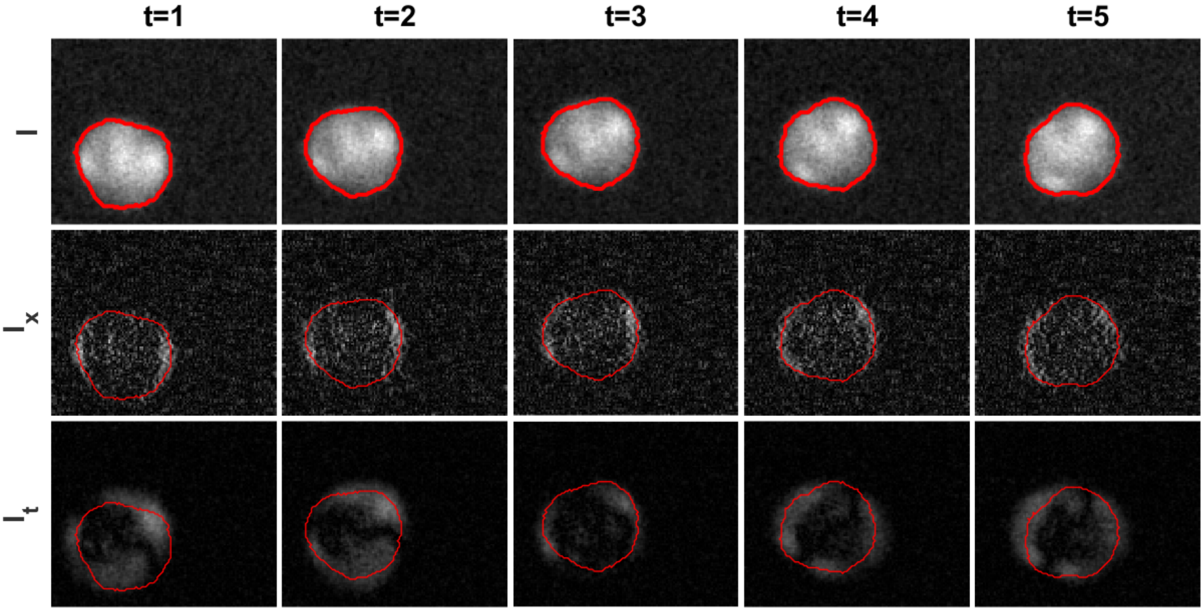

Figure 3.3: Temporal derivatives. The first row shows a single xy plane from 4D simulated fluorescence microscopy data, I, across 5 consecutive time-points. The second and third rows show the unscaled absolute value of the spatial derivative, $I_x = |\frac{\partial I}{\partial x}|\Delta x$, and the temporal derivative $I_t = |\frac{\partial I}{\partial t}|\Delta t$. These partial derivatives were calculated using the central difference of adjacent pixels. The object boundary (from ground truth) is shown in red. The data has been pre-processed with 3D Gaussian blurring across the spatial dimensions. Interestingly the spatial derivative, I_x, exhibits greater background variation and clearly the temporal derivative contains useful information about the object boundary. Note that the value of temporal derivative, I_t, is high in locations where the object boundary is moving in time. Also note that large boundary movement causes blurring of I_t around the object boundary. Therefore the smaller the movement of the object boundary between time-points, the more useful the temporal derivative is for object segmentation. This is why we propose to set Δt as the (approximate) mean boundary displacement between consecutive time-points.

can be adequately separated by image erosion and/or a watershed transform. In general, separating touching objects is a complex problem with no generalised solution.

3. Calculate the trajectories of objects using a simple tracking protocol. For simplicity and speed, a publicly available algorithm implemented in Matlab is used[1]. Briefly, the total Euclidean distance of all trajectories between adjacent frames is minimised.
4. The mean displacement between frames across all objects and time-points is used to estimate $\langle D \rangle$.

Note, the above algorithm can be performed on a subset of the data to reduce computational time. Recall the protocol assumes that the COM derived movement of the objects is the dominant source of boundary displacement. This is a reasonable assumption for nuclei but if there is large boundary localised movement, as is typical with whole cell segmentation, then a different approach will be needed. An example of such an approach is discussed in section 3.6.6.

3.6.3 Edge and Regions based Level Set Equations

In the previous two sub-sections, strategies for implementation of DRLSE in 4D and the calculation of temporal derivatives were presented. With these strategies standard formulations for edge and region based level set segmentation (as discussed in sections 3.3.1 and 3.3.3) can be implemented in 4D. In an edge based approach the LSE, as derived by gradient descent of the geodesic energy functional (equation 3.3.6), with a DRLSE term (equation 3.3.9) is given by [13, 225];

$$\frac{\partial \phi}{\partial \tau} = \lambda \delta_\alpha(\phi) \Big(g(I)(\kappa + c)|\nabla \phi| + \nabla g(I) \cdot \nabla \phi \Big) + \mu \operatorname{div} \Big(P'(|\nabla \phi|) \vec{N} \Big) \tag{3.6.9}$$

---

[1] http://uk.mathworks.com/matlabcentral/fileexchange/34040-simple-tracker. Accessed 01/16.

where λ and μ are constants and $P'(|\nabla\phi|)$ is the derivative of the potential given in equation 3.3.8. Similarly, a DRLSE term can be introduced into the Chan-Vese formulation (equation 3.3.11) to derive the following LSE [14];

$$\frac{\partial\phi}{\partial\tau} = \beta\delta_\alpha(\phi)\Big(|I - C(\phi, I)|^2 - |I - C(-\phi, I)|^2\Big)$$
$$\lambda\delta_\alpha(\phi)\Big((\kappa + c)|\nabla\phi|\Big) + \mu\,\mathrm{div}\,\Big(P'(|\nabla\phi|)\vec{N}\Big) \tag{3.6.10}$$

where β is a constant. In what follows the use of equations 3.6.9 or 3.6.10 is referred to as edge or region based DRLSE respectively.

Note the implementation of both edge and region based DRLSE requires computation of both the Dirac delta function and the Heaviside step function on a discretised array. As is common in level set methods, the Heaviside step function and the Dirac delta function can be approximated as follows [223];

Figure 3.4 *(following page)*: Setting the temporal scaling factor. Suggested protocol for estimating the mean boundary displacement of targets between frames; $\langle D\rangle$. This is used to calculate the temporal scaling factor; Δt. (a) Representative maximum intensity projection of simulated data from a single 3D time-point of a 4D dataset. Scale bar set to $5\mu m$. (b) After Gaussian blurring, K-means clustering (2 clusters) is performed on the 3D data from each time-point to acquire a quick and approximate segmentation result. This is then eroded using a spherical structural element ($1\mu m$ radius) to separate touching objects (maximum projection shown). The lateral positions for the centre of mass (COM) of each object are shown; calculated (red ×) and ground truth (green +). (c) The COM locations are calculated for 5 consecutive time-points. A simple and fast tracking algorithm is used to construct particle trajectories. $\langle D\rangle$ can then be calculated as the mean particle displacement between consecutive frames. (d) The above analysis was repeated for six simulated data sets. The measured and ground truth values of $\langle D\rangle$ are shown. Central mark is the mean and error is the standard deviation. The mean values for the measured and ground truth calculations for $\langle D\rangle$ are $0.6 \pm 0.1\mu m$ and $0.5 \pm 0.1\mu m$ respectively. Moreover, the measurement error between individual datasets is very small; $0.02 \pm 0.03\mu m$. Therefore, it is concluded that this protocol provides an accurate and reliable estimation of $< D >$ for the simulated test data.

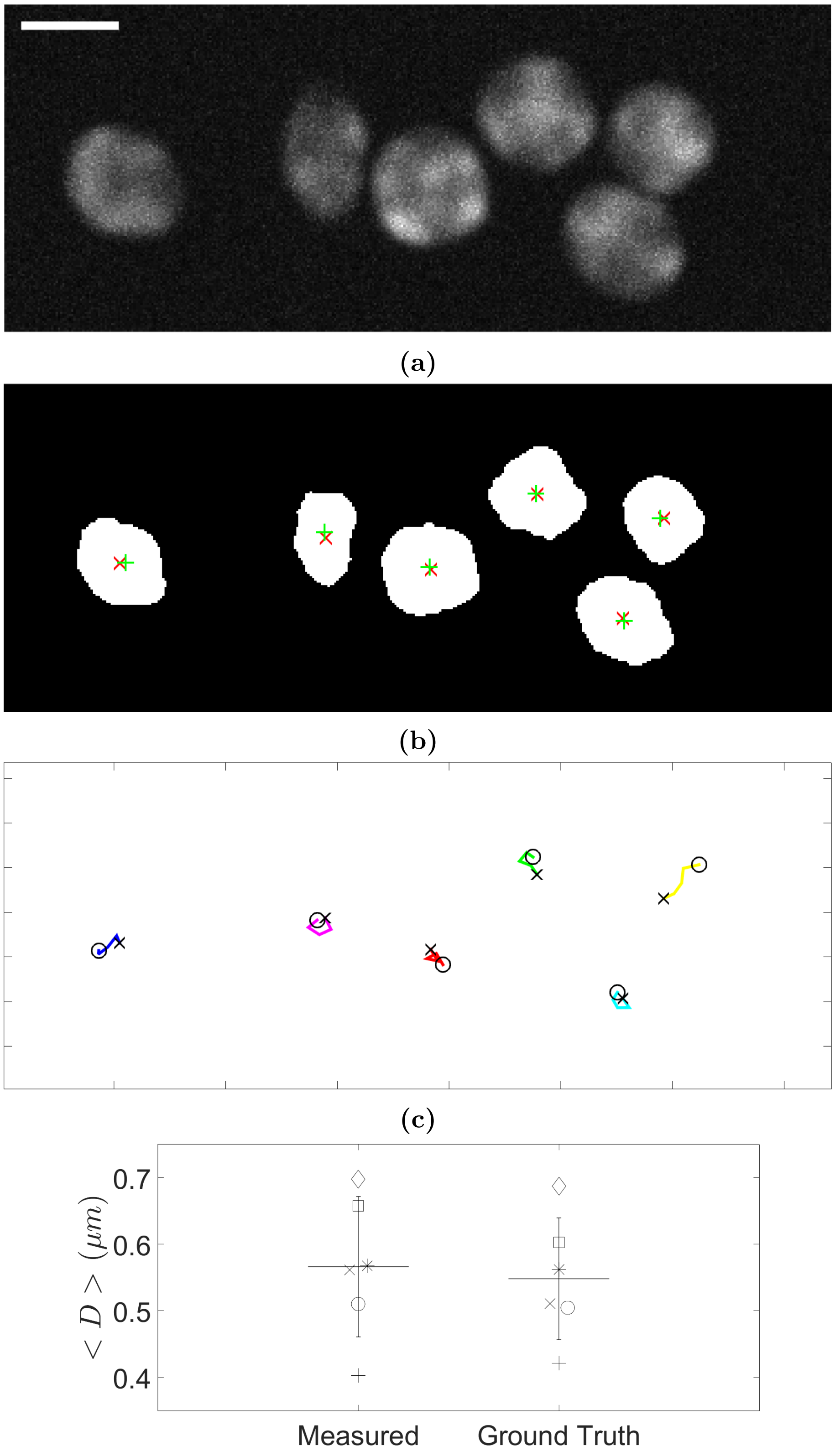

(a)

(b)

(c)

(d)

$$H_\alpha(x) = \begin{cases} \frac{1}{2}\left(1 + \frac{x}{\alpha} + \frac{1}{\pi}\sin\frac{\pi x}{\alpha}\right) & \text{if } |x| \leqslant \alpha, \\ 1 & \text{if } x > \alpha, \\ 0 & \text{if } x < -\alpha, \end{cases} \tag{3.6.11}$$

$$\delta_\alpha(x) = \frac{\mathrm{d}H_\alpha(x)}{\mathrm{d}x} = \begin{cases} \frac{1}{2\alpha}\left(1 + \cos\frac{\pi x}{\alpha}\right) & \text{if } |x| \leqslant \alpha, \\ 0 & \text{if } |x| > \alpha, \end{cases} \tag{3.6.12}$$

where α is the width of δ_α, which we typically set to 1.5.

3.6.4 Initialisation

The final component of the framework is the initialisation of the LSF. Within a DRLSE formulation, it is possible to simply initialise the LSF as a binary step function. This is advantageous as the initialisation does not need to be a signed distance function, and it is computationally simple to initialise the zero level set as an arbitrary hyper-surface. The LSF is conventionally given negative values within the zero level set and positive values outside. Moreover, the computational time for the segmentation protocol can be greatly decreased by initialising the LSF close to the solution. This is done using the result of a faster, but less accurate and robust algorithm. For example, the data can be blurred with a Gaussian (standard deviation set to width of PSF) and clustered with a K-means approach (two clusters) to provide the initial segmentation estimate. In this algorithm, each 3D time-point is processed individually. To initialise the LSF, voxels in the background cluster are set to a positive constant, h, and voxels in the signal cluster are set to $-h$. h controls the width of the signed distance band constructed by the DRLSE term. Li *et al.* (2010) suggest setting $h \geqslant 1$ and typically use $h = 2$ [225].

As an additional (optional) step, the initial segmentation estimate can be eroded or dilated with a structural element of fixed size to ensure the zero level set is initialised either

Parameter	
Voxel Size (μm)	$0.125 \times 0.125 \times 0.2$
Time-step (min)	28.85
Frame size (pixels)(xyzt)	$92 - 247 \times 112 - 371 \times 70 \times 10$
Objective Lens	40× Plan-apochromat 1.3 NA oil

Table 3.1: Dummy acquisition parameters for the synthetic test data.

inside, or outside the target. The choice should be matched to the sign of constant, c (equations 3.6.9 and 3.6.10), as positive c will push the zero level set inwards and negative c will push outwards.

In this approach the fast initialisation algorithm computes an approximate segmentation of the target object(s) and the level set evolution simply refines this approximation and corrects for errors. This concept is very important for 4D level set segmentation as computational costs are normally the limiting factor. Figure 3.5 shows an example of using K-means clustering to initialise 4D DRLSE.

3.6.5 Validation on Synthetic Data

In section 3.6 a practical framework for the implementation of 4D level set segmentation was introduced. In this section these approaches are validated on synthetic microscopy data from the public repository introduced by Maska *et al.* (2014) [226]. The validation dataset consists of 10 4D time-lapse movies showing fluorescently labelled nuclei. The data are cropped versions of the N3DH-SIM series from the public repository. The first 10 time-points, all 70 axial slices and a frame size in the range $92 - 247 \times 112 - 371$ pixels is selected. For reference, the acquisition parameters for this dataset are listed in table 3.1. A representative xy slice from the synthetic data is show in figure 3.4a.

In what follows, two key hypotheses are tested; that there is a performance difference between 2D/4D and 3D/4D implementations of equivalent level set segmentation algorithms. Note, the 3D implementation refers to segmentation over the 3 spatial dimensions.

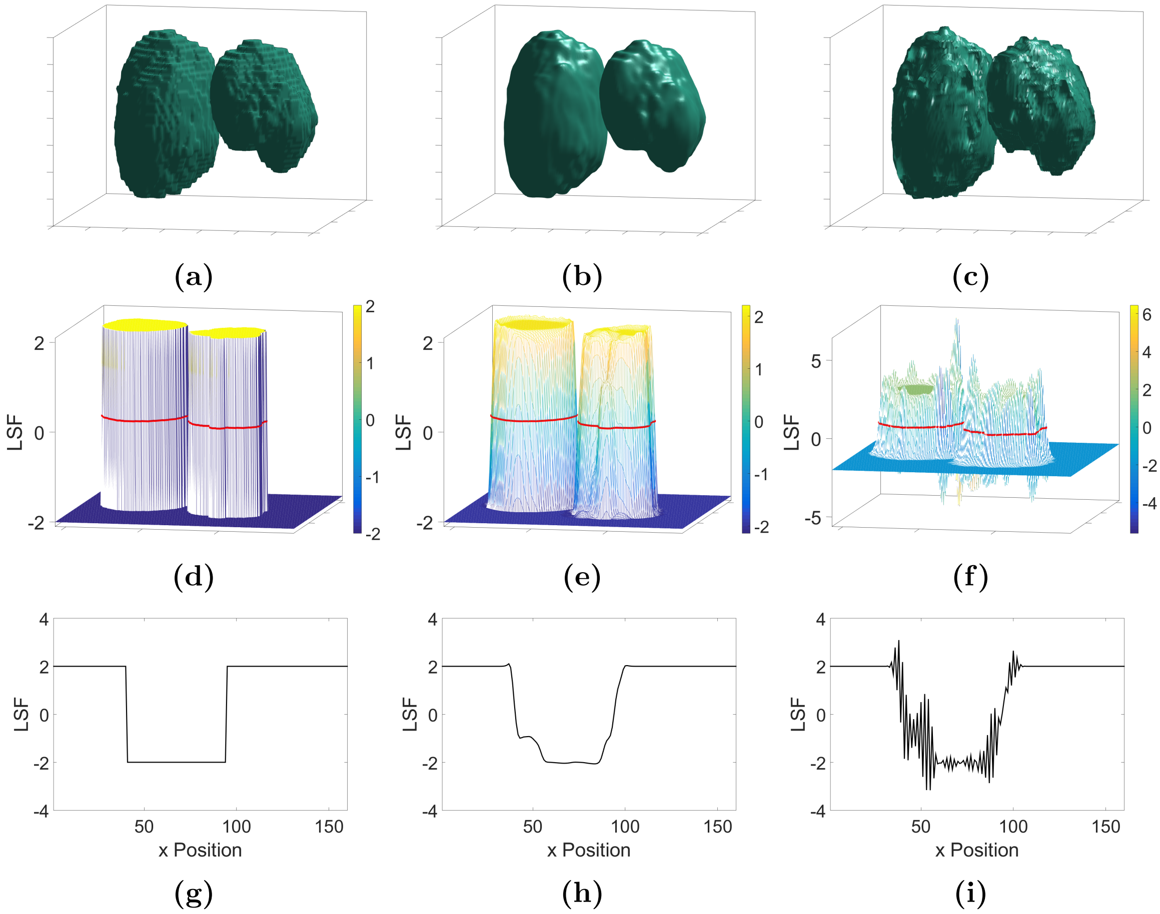

(a) (b) (c)

(d) (e) (f)

(g) (h) (i)

Figure 3.5: Distance Regularized Level Set Evolution in 4D. (a) 3D surface rendering showing the initial location of the zero level set (ZLS) of the level set function (LSF) for a single time-point. Note the ZLS is 4D hyper-surface and what is shown is only a single temporal plane. The LSF has been initialised as a binary step function using the result of a K-means clustering algorithm. (b) Surface rendering of the ZLS for the same time-point after 10 iterations of distance regularized level set evolution (DRLSE). The regularization term, μ, was set to be just less than the Courant-Friedrichs-Lewy constraint, μ_l, such that; $\mu = \mu_l - 0.05$. This was done to ensure the LSF evolves correctly; maintaining the signed distance property around the ZLS. (c) Here the same parameters were used except $\mu = \mu_l + 0.05$. Note the LSF has developed irregularities which can lead to poor segmentation results. (d)-(f) A cross section of the LSF corresponding to a single axial image (xy plane) under the same conditions as for (a)-(c). The ZLS is shown as a red band. Again note the irregularities when $\mu > \mu_l$. (g)-(i) Plots showing a single axial cross section of the LSF.

The target objects (nuclei) have clearly defined edges and relatively homogeneous intensity. Therefore, both edge and region based DRLSE level set approaches are suitable and tested (section 3.6.3). For 2D, 3D and 4D approaches, initialisation of the level set function was carried out using the K-means based protocol from section 3.6.4. For 4D implementations the temporal scaling factor was estimated using the approach suggested in section 3.6.2.

To quantify segmentation performance, the Jaccard similarity index was used. The Jaccard index was chosen due to extensive use within the community, for example it is used as the segmentation metric in the IEEE International Symposium on Biomedical Imaging cell tracking challenges [226]. The Jaccard index is defined as the volume of the intersection divided by the volume of the union between the segmentation, S, and the ground truth reference, G;

$$J(S,G) = \frac{|S \cap G|}{|S \cup G|} \tag{3.6.13}$$

Clearly it is not appropriate to assume that segmentation performance across movies within the dataset will be normally distributed. Therefore, non-parametric statistical testing should be used to compare between different segmentation algorithms.

Note that for each movie, the segmentation performance across the different algorithms is paired. Therefore, as an initial step the Friedman test, a non-parametric alternative to a multiple measures ANOVA, was used. If the Friedman test is significant at a level of $p < 0.05$ then a non-parametric test was performed for each alternative hypothesis (post-hoc testing). The sign test is chosen for these pair-wise comparisons, over the more powerful Wilcoxon sign test, as the symmetric distribution assumption of the latter does not hold. To see this, note the spread of the box-plots in figures 3.6 and 3.7. Note the sign test is a paired test for two distributions; X and Y with the hypothesis that the median of $X - Y$ is non-zero. Finally, the p-values returned for each hypothesis are corrected for multiple comparisons using the Bonferroni correction such that;

$$p_{cor} = \frac{p}{n} \tag{3.6.14}$$

where p_{cor} is the corrected p-value, to be compared to a given significance level, and n is the number of alternative hypothesis.

To demonstrate the performance difference between 4D level set segmentation and equivalent 3D and 2D implementations, it is appropriate to minimise the number of free parameters in the LSE. Therefore we set $c = 0$ for both the edge and region based DRLSE approaches. The constant μ was set to be just less than the theoretical 4D bound; $\mu = \mu_l - 0.05$ (equation 3.6.4). For simplicity we set $\Delta x = \Delta y = \Delta \tau = 1$. Δz was set using equation 3.6.7 and Δt was set using the procedure described in section 3.6.2. To implement a region based DRLSE we set the smoothing parameter , $\lambda = 0.1$ (equation 3.6.10). The complete list of fixed segmentation parameters is listed in table 3.2. Note, λ is the only remaining free parameter for edge based DRLSE (equation 3.6.9), and β the only free parameter for region based DRLSE (equation 3.6.10).

Using the described algorithms, figure 3.6 demonstrates that 4D edge based DRLSE provides superior segmentation performance when compared to the equivalent 3D and 2D edge based DRLSE algorithms on the synthetic test data. This key result is the first demonstration of improved performance when incorporating temporal information into a DRLSE approach. It is important to note that the aim is not to provide an optimal edge based protocol, where for example $c \neq 0$. Instead, a simplified and unbiased protocol is used to demonstrate that temporal information can be incorporated into popular level set formulations, to improve segmentation performance.

Specifically, figure 3.6b demonstrates that the mean performance of the 4D edge based algorithm is superior for all tested values of λ. Importantly, in figure 3.6c, it is shown that the increase in maximal performance (single λ selected for each algorithm) is statistically

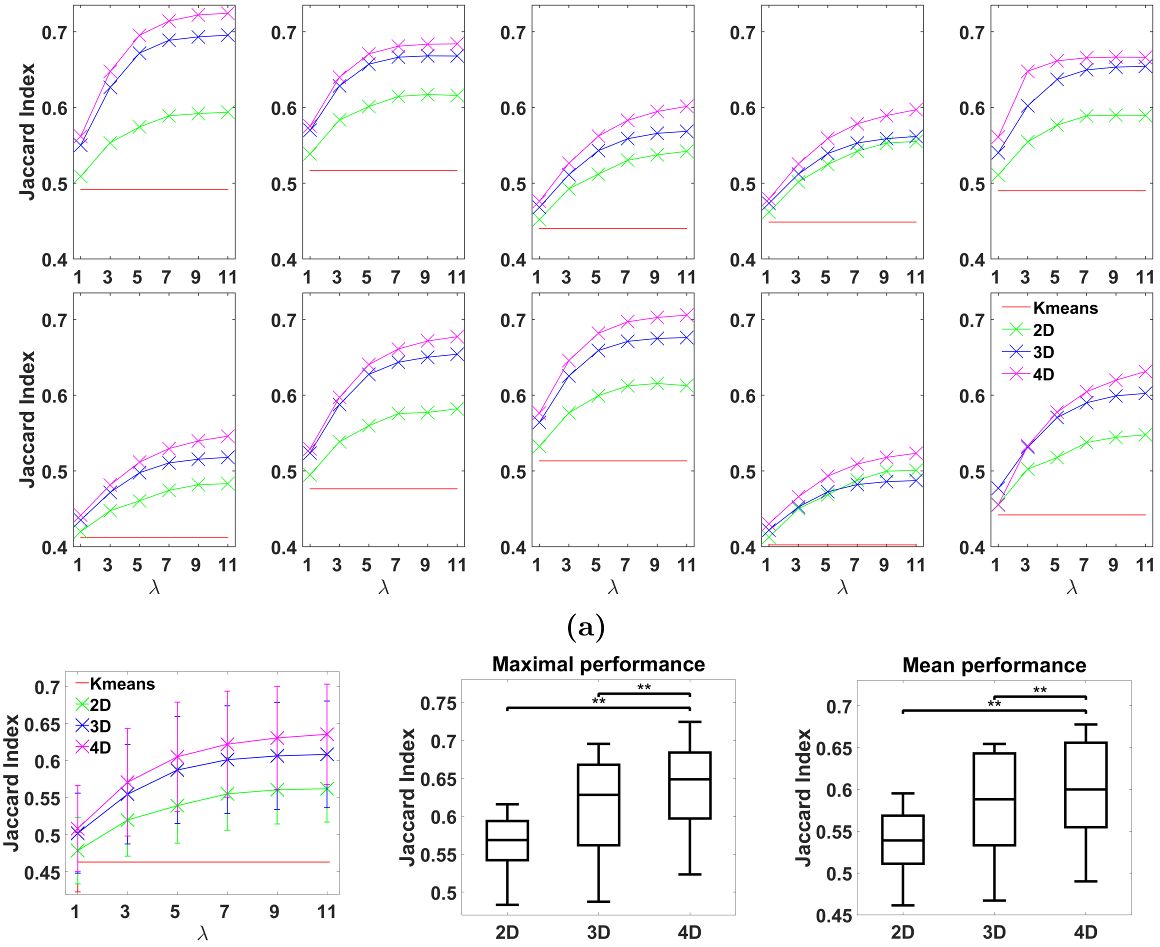

(a)

(b) (c) (d)

Figure 3.6: 4D edge based level set segmentation performance evaluation for synthetic data. (a) Segmentation performance with edge based, distance regularized level set evolution across all 10 synthetic movies, for 2D, 3D and 4D implementations. For each movie the level set function (LSF) was initialised by Gaussian blurring (σ = width of PSF), K-means clustering (2 clusters) and subsequent dilation (with spherical structural element, radius = $1.5\mu m$) (performance shown by red line). The erosion step was included to ensure the zero level set was initialised outside the target nuclei. Note the 4D approach produces superior segmentation results than both the 3D and 2D implementations for the full range of edge parameter, λ, and across all movies. (b) Mean performance across all movies. Error bars represent the standard deviation. (c) Statistical analysis of maximal performance across all movies and λ (single λ selected for each algorithm). Central mark on boxplot represents the median, and the edges of the box are the 25th and 75th percentiles. Friedman's test indicated statistically significant differences between the 3 segmentation algorithms ($p < 0.001$). Post-hoc testing by the sign test with Bonferroni correction (n=2) was used to calculate p-values for individual comparisons. (d) The same statistical analysis was repeated for mean performance across all movies and λ. Friedman's test returned $p < 0.001$.

Parameter	Edge	Region	Reference
Constant force term; c	0	0	equation 3.6.9 & 3.6.10
Lateral scaling factors; Δx, Δy	1	1	section 3.6.2
Axial scaling factor; Δz	1.6	1.6	equation 3.6.7
Temporal scaling factor; Δt	4.8	4.8	figure 3.4
Update step; $\Delta \tau$	1	1	equation 3.6.1
DRLSE factor; μ	0.155	0.155	equation 3.6.4
Binary step size; h	2	2	equation 3.6.4
Dirac-delta function width; α	1.5	1.5	equation 3.6.12
Gradient power; p	2	—	equation 3.3.4
Stopping constant; s	0.01%	0.01%	algorithm 1
Maximum number of iterations	50	50	section 3.6.1
Edge/smoothing term; λ	$0.5 - 11$	0.1	equations 3.6.9 & 3.6.10
Region term; β	—	$0.01 - 0.08$	equation 3.6.10

Table 3.2: Parameters for validation of 4D level set segmentation on synthetic data. For comparison of both 4D edge and region distance regularized level set evolution (DRLSE) protocols with equivalent 3D and 2D approaches.

significant when compared to both 3D and 2D implementations. This is also true for the mean performance across all tested λ (figure 3.6d). Therefore, it is concluded that 4D edge based DRLSE has superior peak performance and this effect is robust, insensitive to a substantial range of λ values.

Similarly, figure 3.7b demonstrates that region based 4D DRLSE is superior (over a range of β) when compared to the equivalent 3D and 2D approaches. As with the edge based formulation, maximal (figure 3.7c) and mean (figure 3.7d) performance across the parameter space (β) is superior and statistically different. Note also that the spread of the maximal performance measurements (figure 3.7c) is smaller for the 4D approach. Combined with the increase in performance, this indicates an improvement in both accuracy and precision.

Finally, note that maximal and mean segmentation performance is higher for the region based approaches (as compared to the edge based approaches) (figures 3.6 and 3.7). This indicates that for this dataset (fluorescently labelled nuclei), a region based approach is better suited than the edge based formulation.

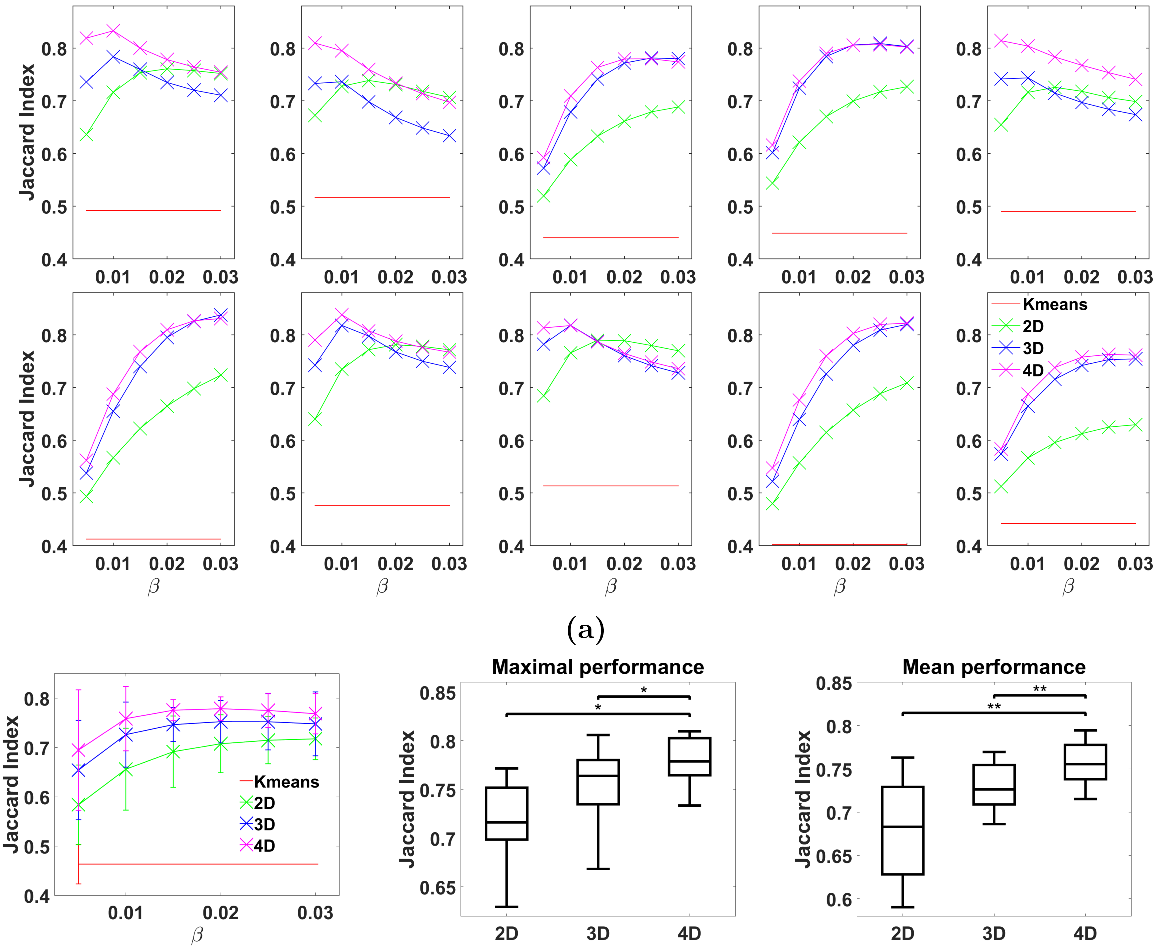

(a)

(b) **(c)** **(d)**

Figure 3.7: 4D region based level set segmentation performance evaluation for synthetic data. (a) Segmentation performance with region based, distance regularized level set evolution across all 10 synthetic movies for, 2D, 3D and 4D implementations. For each movie the level set function (LSF) was initialised by Gaussian blurring (σ = width of PSF), K-means clustering (2 clusters) and subsequent dilation (with spherical structural element, radius = $1.5\mu m$) (performance shown by red line). (b) Mean performance across all movies. Error bars represent the standard deviation. (c) Statistical analysis of maximal performance across all movies and β (single β selected for each algorithm). Central mark on boxplot represents the median, and the edges of the box are the 25th and 75th percentiles. Friedman's test indicated statistically significant differences between the 3 segmentation algorithms ($p < 0.001$). Post-hoc testing by the sign test with Bonferroni correction (n=2) was used to calculate p-values for individual comparisons. (d) The same statistical analysis was repeated for mean performance across all movies and β. Friedman's test returned $p < 0.001$.

Parameter	
Voxel Size (μm)	$0.1745 - 0.2486 \times 0.1745 - 0.2486 \times 0.3$
Time-step (min)	7.5
Frame size (pixels)(xyzt)	$174 - 439 \times 245 - 509 \times 51 \times 5$
Objective Lens	100× Plan-apochromat 1.49 NA oil

Table 3.3: Acquisition parameters for the real test data.

3.6.6 Validation on Real Data

In this sub-section, the use and performance of edge based 4D DRLSE segmentation on real test data is demonstrated. Specifically, the cellular segmentation of HeLa cells expressing EGFR-EGFP is considered. The validation dataset consists of 10 confocal time-lapse (3D+time) movies of individual cells. At time zero, the cells were treated with $100ng/ml$ EGF, and subsequent internalisation of the EGFR is triggered. Using a 4D DRLSE approach we aim to reliably and accurately segment the cells using only the EGFR-EGFP signal. This is a relatively simple task pre EGF treatment, where most of the signal is membrane localised. However it is much more complex post EGF treatment, where the signal intensity and signal to noise ratio (SNR) at the membrane boundary is much lower.

Note, a region based DRLSE algorithm would not be well matched to this dataset as the targets (cells expressing EGFR-EGFP) do not have an approximately homogeneous internal intensity distribution. Therefore, we do not evaluate the performance of the region based 4D DRLSE algorithm on the real test data.

The acquisition parameters for this dataset are summarised in table 3.3. Raw microscopy data was cropped, to produce individual regions of interest (ROIs) containing a single healthy cell expressing EGFR-EGF, using custom semi-automated selection software (Matlab). This was done blindly to select alive and non-mitotic cells.

Ground truth data was generated by the blind manual segmentation of 14 evenly spaced axial slices (excluding the very top and bottom of ROI) for each time-point in each movie. The top and bottom of the cells were not used as it was difficult to produce accurate and reliable manual segmentations of these regions due to out of focus contributions. It is important to note that manual segmentation isn't perfect, and will be influenced by both user error and bias. It is feasible that some of the automated methods presented in this chapter may outperform manual segmentation. Despite these limitations manual segmentation still provides a useful reference for the benchmarking of automated protocols.

In section 3.6.5 Gaussian blurring was used as a pre-processing step to remove noise from the synthetic test data. Here the more sophisticated PURE-LET denoising scheme was employed (ImageJ) (section 2.5.4) (figure 3.8b) [140, 166]. The PURE-LET plugin was set to estimate noise parameters automatically (global), the number of spin cycles was set to 4, and the multi-frame parameter was set to 3. This was followed by K-means clustering (4 clusters). The three clusters with the highest means were combined, dilated, filled and eroded with a spherical structural element (radius $= 1.5\mu m$) to produce the initial segmentation estimate used for initialisation of the LSF (figure 3.8c). More than two clusters were required due to the large variation in EGFR signal intensity, dependent on both sub-cellular localisation and time post EGF treatment. However, note that the K-means based initialisation is only used as a segmentation estimate and the result is not critical.

When using 4D level set segmentation, it is clearly important to correct for any stage drift, as it will distort temporal derivatives. To correct for drift within the real test dataset a simple registration algorithm was employed. First, consider the measured intensity for a given spatial position, (x, y, z), for time-point t; $I_{x,y,z,t}$, and for time-point $t + 1$; $I_{x,y,z,t+1}$. The data for time-point $t + 1$ is translated laterally in all three spatial dimensions (one pixel at a time) for all possible combinations in the range; $T_1, T_2, T_3 = [-1 : 1]\mu m$, such that the translated data, $T(I_{x,y,z,t+1}) = I_{x+T_1,y+T_2,z+T_3,t+1}$. For each translation, the product of the translated data and the data for time-point t is computed. The maximal product represents the translation with maximal signal overlap and is used to register the data;

$$\max_{T1,T2,T3} \sum_{x,y,z} T(I_{x,y,z,t+1}) \times I_{x,y,z,t} \tag{3.6.15}$$

It is important to note that the above registration protocol will not only correct for stage drift, but also small bulk cell movement. In this application, the aim is accurate segmentation, and not tracking, so this is an advantageous side effect. Note, after registration the main contributor to target movement, $\langle D \rangle$, will be shape change due to localised movement of the plasma membrane (section 3.6.2). Therefore to estimate the temporal scaling factor, Δt, the mean localised boundary displacement should be estimated. The protocol described in section 3.6.2 is only applicable to bulk object displacement so a different approach, detailed in figure 3.8, is employed. Using this procedure, the mean values for the measured and ground truth calculations for $\langle D \rangle$ were $1.3 \pm 0.4 \mu m$ and $1.8 \pm 0.6 \mu m$ respectively, where errors are given by the standard deviation.

The parameters for the edge based DRLSE segmentation were set using the same procedures as for the synthetic dataset (section 3.6.5), and are recorded in table 3.4. Note the scaling factors and the DRLSE factor, μ, vary due to variation in physical voxel size between movies.

In figure 3.9 an increase in performance for the 4D edge based DRLSE algorithm, over the equivalent 3D and 2D implementations, is demonstrated. Importantly, a statistically significant increase in maximal performance is seen when compared to both 2D and 3D implementations (figure 3.9c). A statistically significant increase in mean performance across the parameter space is seen when compared to 2D, but not 3D (figure 3.9d). Therefore we can conclude that the 4D approach has superior performance, for optimal setting of the edge parameter λ, over both 3D and 2D approaches. Moreover the 4D

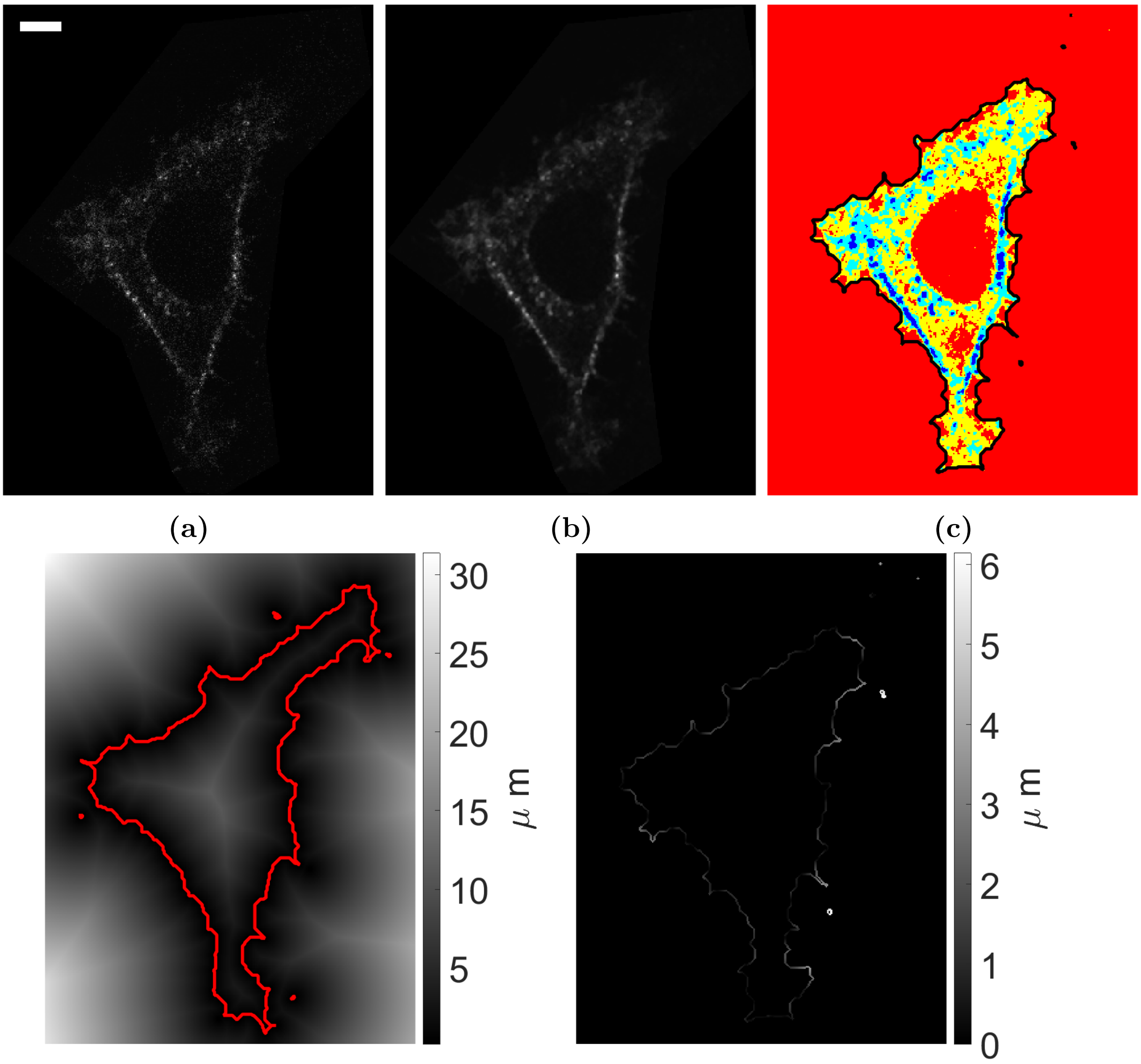

(a) (b) (c)

(d) (e)

Figure 3.8: Pre-processing of real test data and estimating mean boundary displacement. (a) Representative example of a raw confocal microscopy image showing a HeLa cell expressing EGFR-EGFP. The test dataset consists of 4D time-lapse movies of the EGFR-EGFP signal in response to EGF treatment The time-point shown is 7.5 minutes post EGF treatment. Scale bar represents $5\mu m$. (b) Data is de-noised using a PURE-LET scheme for Poisson corrupted images. (c) De-noised data is processed with a K-means clustering algorithm (4 clusters). Each cluster is represented by a different color. The 3 clusters with the highest means are combined, dilated, filled and eroded with a spherical structural element (radius $= 1.5\mu m$). This produces the initial segmentation estimate (black contour). (d) To estimate the mean boundary movement at time-point, t, the distance transform calculating the minimal euclidean distance from the segmentation estimate (red contour) for time $t + 1$ is computed. (e) The sum of all pixels from the distance transform for time $t+1$ which coincide with initial segmentation contour at time t is computed. The mean of the sum across all axial slices and time-points is used as an estimate for mean boundary displacement.

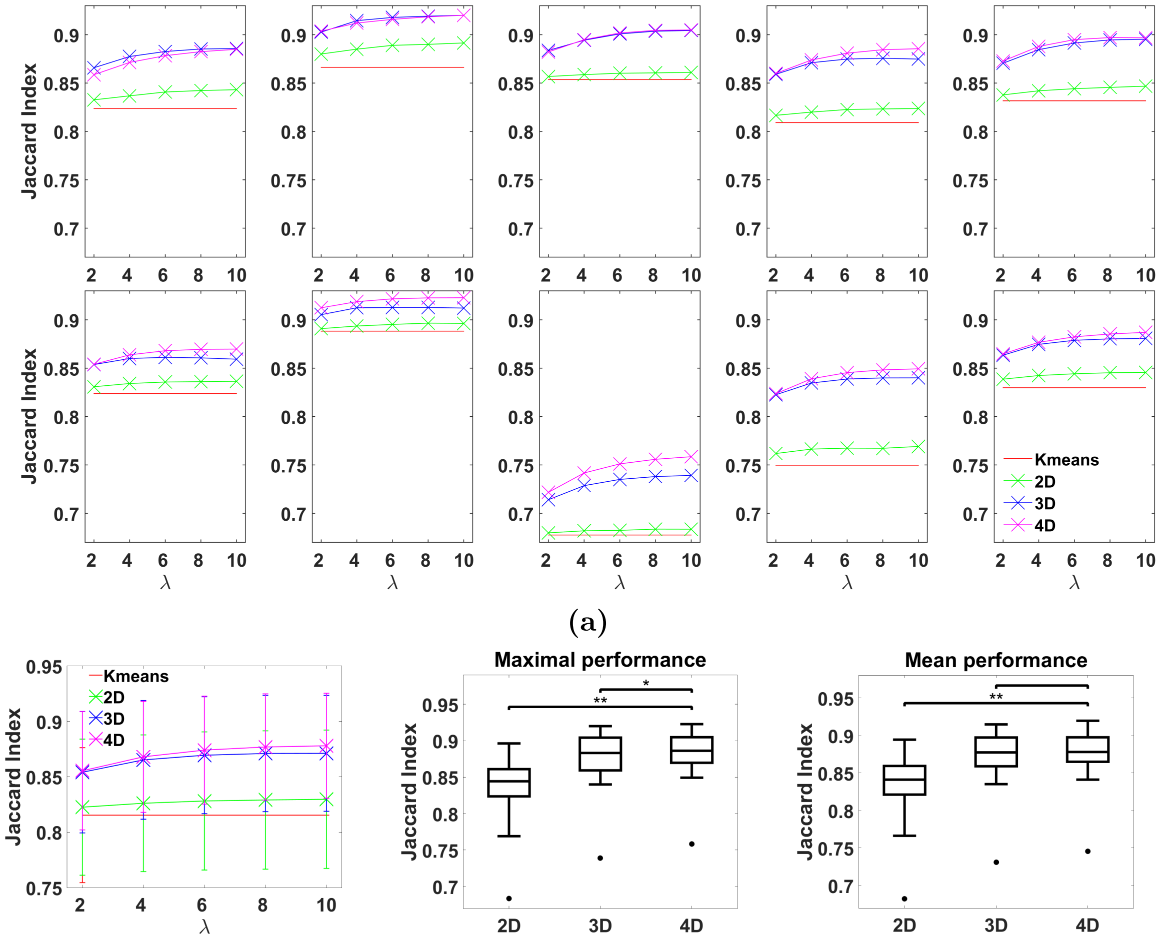

(a)

(b)

(c)

(d)

Figure 3.9: 4D edge based level set segmentation performance evaluation for real data. (a) Segmentation performance with edge based distance regularized level set evolution across all 10 real time-lapse movies for 2D, 3D and 4D implementations. For each movie the level set function (LSF) was initialised using a K-means based algorithm (red). (b) Mean performance across all movies. Error bars represent the standard deviation. (c) Statistical analysis of maximal performance across all movies and values of the edge constant λ (single λ selected for each algorithm). Central mark of the boxplot represents the median, and the edges of the box are the 25th and 75th percentiles. Friedman's test indicated statistically significant differences between the 3 segmentation algorithms ($p < 0.001$). Post-hoc testing by the sign test with Bonferroni correction (n=2) was used to calculate the p-values for individual comparisons. (d) The same statistical analysis was repeated for mean performance across all movies and λ. Friedman's test returned $p < 0.001$.

Parameter	Value	Reference
Constant force term; c	0	equation 3.6.9 & 3.6.10
Lateral scaling factors; Δx, Δy	1	section 3.6.2
Axial scaling factor; Δz	$1.21 - 1.72$	equation 3.6.7
Temporal scaling factor; Δt	$7.24 - 10.3$	figure 3.4
Update step; $\Delta \tau$	1	equation 3.6.1
DRLSE factor; μ	$0.135 - 0.163$	equation 3.6.4
Binary step size; h	2	equation 3.6.4
Dirac-delta function width; α	1.5	equation 3.6.12
Gradient power; p	2	equation 3.3.4
Stopping constant; s	0.01%	algorithm 1
Maximum number of iterations	50	section 3.6.1
Edge/smoothing term; λ	$0.5 - 11$	equations 3.6.9 & 3.6.10

Table 3.4: Parameters for validation of 4D level set segmentation on real data. For comparison of 4D edge based distance regularized level set evolution (DRLSE) protocols with equivalent 3D and 2D approaches.

approach demonstrates superior performance to the 2D approach across a large range of λ (mean performance), but we cannot conclude this for the comparison between the 4D and 3D algorithms. However, assuming the segmentation parameters are well set, we note that maximal, not mean performance is the more important measurement.

To conclude, in this section we have successfully implemented novel 4D DRLSE segmentation protocols for both edge and region approaches. These approaches were used to segment targets for applications in fluorescent microscopy and were validated on both synthetic (edge and region based) and real (edge based) test datasets. A statistically significant increase in maximal performance across the parameter space is seen in all cases, when compared to the equivalent 3D and 2D algorithms.

3.7 Customised Temporal Constraints

It is appropriate to think of true 4D segmentation as simultaneous segmentation and tracking. In conventional tracking approaches, assumptions about the changes to the targets' properties over time are routinely used. We propose to incorporate such assumptions within a true 4D segmentation protocol to improve segmentation performance. Specifically, within a 4D level set framework, terms within the level set equation were modified to take advantage of temporal assumptions and models for the target(s). We refer to these terms as temporal constraints. The concept is analogous to the approach taken by traditional cost based tracking algorithms. In this section two simple classes of temporal constraints are introduced and tested. However, note that temporal constraints are inherently application specific and thus there is large scope for customised development and extension of application targeted terms.

3.7.1 Volume Conserving Constraints

The first class of temporal constraints incorporates assumptions concerning target volume change over time [228]. Note that no prior knowledge about expected volume is required. Instead constraints on the range of (expected) volume change are used. For example, consider a cellular segmentation problem. If there is an assumption that the volume of the cells will not change by more than, for example, 10% between time-points, then this can be used to influence segmentation results without any knowledge of the absolute cell volume.

In the simplest case, the assumption is that the volume of the targets remains constant over time. To introduce this constraint into a level set formulation, we can modify the constant, c, from equations 3.6.9 and 3.6.10 such that,

$$c_1(\phi, t) = c_0 \frac{V(\phi, t) - \langle V(\phi, t) \rangle}{\langle V(\phi, t) \rangle} \tag{3.7.1}$$

where c_0 is a positive constant and $V(\phi, t)$ is the volume contained within the ZLS of ϕ for time-point, l. $\langle V(\phi, t) \rangle$ is the mean of $V(\phi, t)$ across all time-points. Note from equations 3.6.2 and 3.6.11, $V(\phi, t)$ can be easily computed as;

$$V(\phi, t) = \sum_{x,y,z} H_\alpha(-\phi_{x,y,z,t}) \tag{3.7.2}$$

The key concept is the modification of the constant force term, such that it is no longer constant, but proportional to the deviation from the mean volume over time. The sign of $c_1(\phi, t)$ determines if the force pushes *inwards* or *outwards*, and will be positive when the volume is higher than the mean, and negative when below.

In a different case, the assumption could be a maximum percentage change in volume between time-points. In such a case the constant, c, can again be adapted such that;

$$c_2(\phi, t) = \begin{cases} c_0 \times V_{dif}(\phi, t) & \text{if } |V_{dif}(\phi, t)| > p \\ 0 & \text{if } |V_{dif}(\phi, t)| \leqslant p \end{cases} \tag{3.7.3}$$

where p is the tolerance level (as a ratio) and $V_{dif}(\phi, t)$ is the mean percentage difference between adjacent time-points such that,

$$\begin{aligned} V_{dif}(\phi, t) &= \frac{1}{2}\Big(\frac{V(\phi, t) - V(\phi, t-1)}{V(\phi, t)} + \frac{V(\phi, t+1) - V(\phi, t)}{V(\phi, t)}\Big) \\ &= \frac{V(\phi, t+1) - V(\phi, t-1)}{2V(\phi, t)} \end{aligned} \tag{3.7.4}$$

To analyse performance change with the introduction of a volume based temporal constraint, a 4D edge based DRLSE framework was used. The real test dataset (section 3.6.6) was used and the assumption of constant cellular volume over time was exploited, using the constraint from equation 3.7.1. This is a reasonable assumption for non-mitotic HeLa cells over a 30 minute time period.

Segmentation parameters were set as shown in table 3.4. Note the edge constant was fixed at $\lambda = 8$. This value was selected, as performance gain above this point is minimal for the given dataset (figure 3.9b).

Figure 3.10a clearly demonstrates that the introduction of a volume conserving temporal constraint increases segmentation performance. Note an increase in performance is seen for all movies across all values of c_0. This mean performance across movies is shown in figure 3.10b. Importantly, the increase in maximal (figure 3.10c) and mean (figure 3.10d) performance when compared to the unmodified 4D edge based DRLSE algorithm (without the volume conserving term) is statistically significant. Note $n = 6$ for the Bonferroni correction of p-values (equation 3.6.14) as it is necessary to consider the comparison of the 4D algorithm with the other modifications presented in this section (figure 3.13).

3.7.2 Shape Conserving Constraints

In this sub-section the introduction of a shape based temporal constraint is considered. The concept is to use assumptions relating to target shape change over time to aid segmentation. Importantly, no shape prior is required. To illustrate this, consider the case where bulk target movement is minimal and shape changes over time are small. In this case we can introduce the following modification to the constant, c (equations 3.6.9 and 3.6.10), such that,

$$c_3(\phi_{x,y,z,t}) = c_0(\langle \phi_{x,y,z} \rangle - \phi_{x,y,z,t}) \tag{3.7.5}$$

where $\langle \phi \rangle$ is 3D matrix representing the mean of ϕ over all time-points. Here the ZLS of $\langle \phi \rangle$ is analogous to a shape prior often used in level set methods. The key point is that the expected shape is not derived from prior knowledge but from the LSF itself. For each iteration of ϕ, the expected shape is refined and is therefore adaptable to errors in the initial segmentation estimate.

Note when using a DRLSE approach, the magnitude of c_3 will be bounded. To see

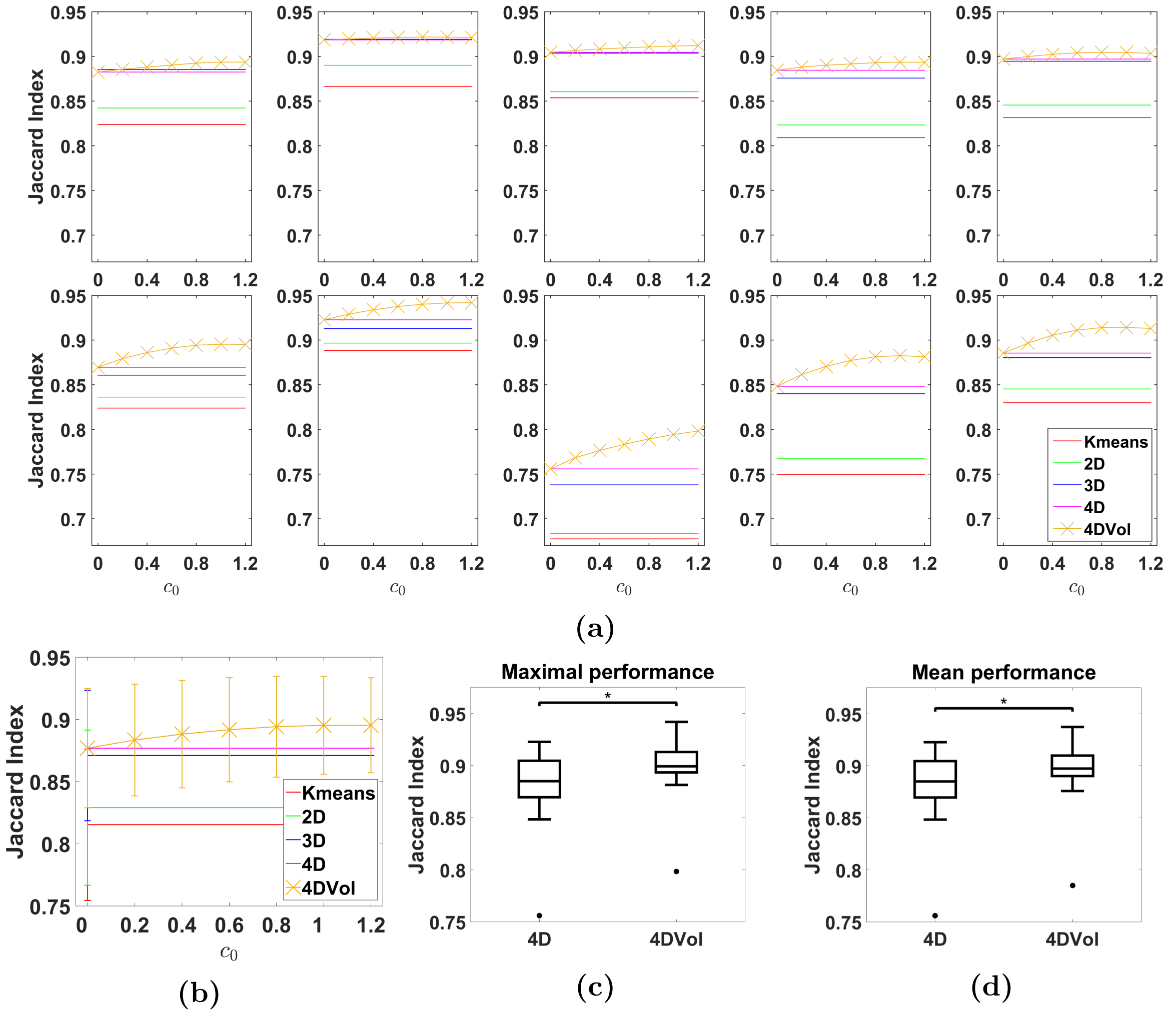

(a)

(b)

(c)

(d)

Figure 3.10: Constant volume constraint performance analysis for real test data. (a) Segmentation performance with 4D edge based distance regularized level set evolution and a constant volume temporal constraint across the real test dataset. The performance of comparable 2D, 3D and 4D implementations, without the temporal constraint, are shown for reference. For each movie the level set function (LSF) was initialised using a K-means based algorithm (red). (b) Mean performance across the dataset. Error bars represent the standard deviation. (c) Statistical analysis of maximal performance for all values of the constant, c_0. Central mark of boxplot represents the median, and the edges of the box are the 25th and 75th percentiles. After Friedman's test, post-hoc testing by the sign tests with Bonferroni correction (n=6) was used to calculate the corrected p-values for comparison with the unmodified 4D algorithm ($p = 0.012$). (d) The same statistical analysis was repeated for mean performance across all movies and c_0 ($p = 0.012$).

this, note that the diffusion effect of the DRLSE term is such that $|\nabla\phi| = 1$ around the ZLS, and $|\nabla\phi| = 0$ elsewhere (section 3.3.2). Therefore, if the diffusion term is having the correct effect, $|c_3| \leqslant 2c_0h$, where h is the size of the binary step function used to initialise ϕ. Typically, we do not consider this bound to be a problem, but if necessary it can be removed by reinitialising ϕ as a signed distance function across the whole domain before calculating c_3.

This simple shape based temporal constraint was tested on the real test dataset (section 3.6.6), where an assumption of minimal shape change and object movement is harsh but reasonable. As with the constant volume constraint (section 3.7.1), a 4D edge based DRLSE approach was used, and parameters were set as shown in table 3.4 ($\lambda = 8$). The results of this analysis are shown in figure 3.11. Importantly, a statistically significant increase in maximal performance is seen, when compared to the unmodified 4D DRLSE protocol (figure 3.11c). However after correcting for multiple hypothesis testing ($n = 6$), the mean performance increase across the parameter space is not statistically significant (figure 3.11d). It is striking that we see an improvement (in maximal performance) with such a harsh assumption as constant shape.

3.7.3 Comparison with Constant Force Term

In sub-sections 3.7.1 and 3.7.2, volume and shape based temporal constraints were introduced, and performance gain was demonstrated for the real test dataset over the equivalent 4D algorithm with no constant force term (equation 3.6.9) ($c = 0$). It could be argued that this is not a fair comparison, as it is conceivable that the introduction of a constant force term ($c \neq 0$) could also confer a similar increase in segmentation performance. To address this, the performance of 4D edge based DRLSE algorithm was analysed on the real test data with the same parameters as for previous experiments (table 3.4, $\lambda = 8$), but with non-zero (and constant) values for c (figure 3.12).

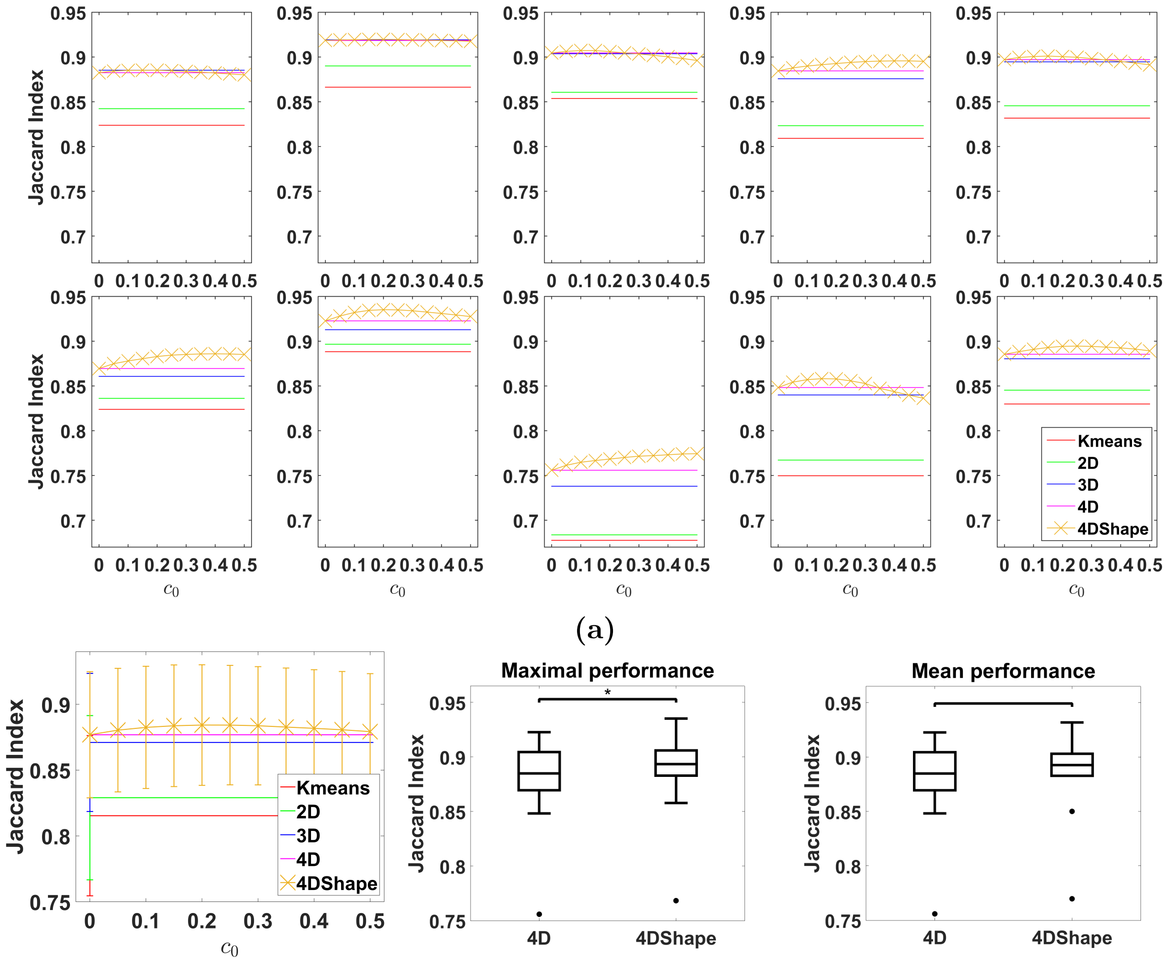

(a)

(b)

(c)

(d)

Figure 3.11: Constant shape constraint performance analysis for real test data. (a) Segmentation performance with 4D edge based distance regularized level set evolution and a constant shape temporal constraint across the real test dataset. The performance of comparable 2D, 3D and 4D implementations, without the temporal constraint, are shown for reference. For each movie the level set function (LSF) was initialised using a K-means based algorithm (red). (b) Mean performance across the dataset. Error bars represent the standard deviation. (c) Statistical analysis of maximal performance for all values of the constant, c_0. Central mark of boxplot represents the median, and the edges of the box are the 25th and 75th percentiles. After Friedman's test, post-hoc testing by the sign test with Bonferroni correction (n=6) was used to calculate the corrected p-values for comparison with the unmodified 4D algorithm ($p = 0.012$). (d) The same statistical analysis was repeated for mean performance across all movies and c_0 ($p = 0.13$).

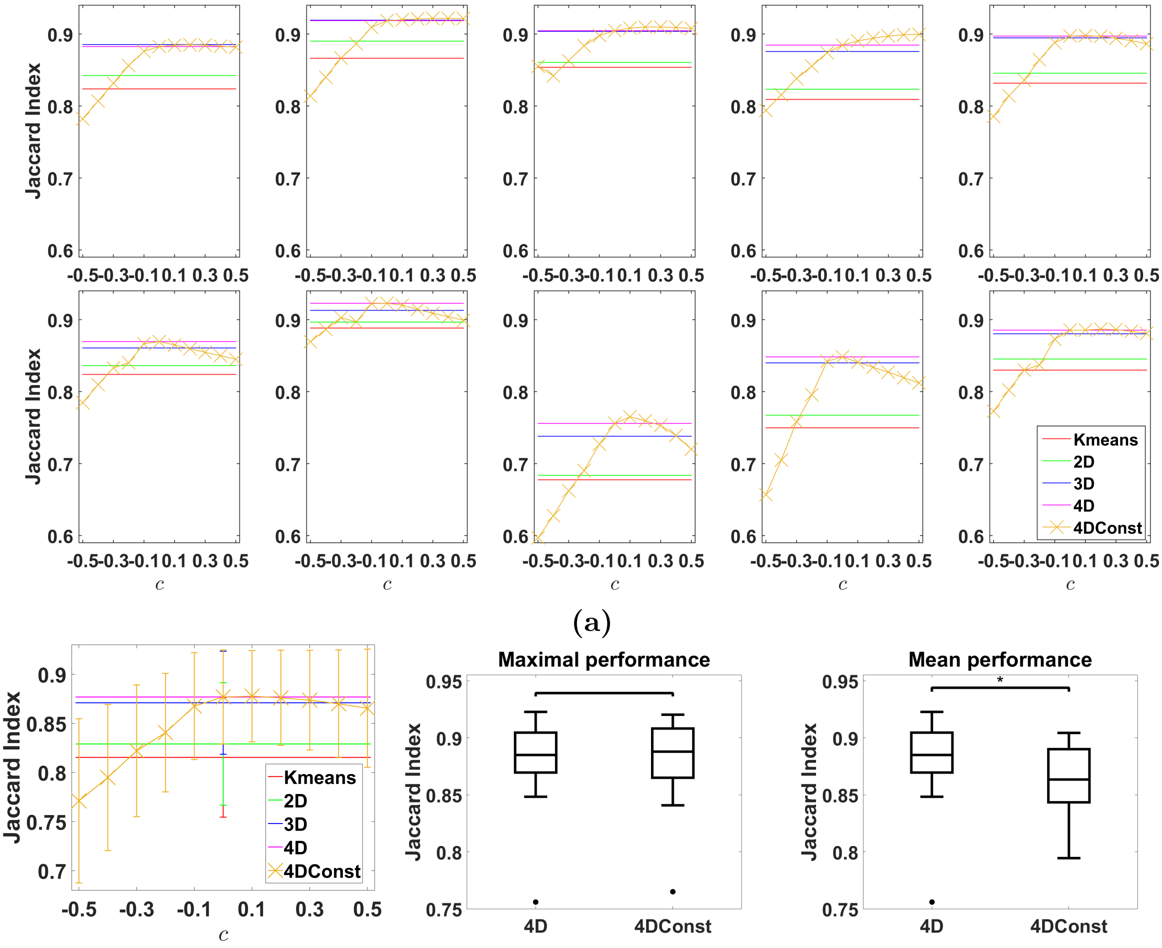

(a)

(b) (c) (d)

Figure 3.12: Constant force term performance analysis for real test data. (a) Segmentation performance with 4D edge based distance regularized level set evolution and a constant force term across the real test dataset. The performance of comparable 2D, 3D and 4D implementations, without the constant force term, are shown for reference. For each movie the level set function (LSF) was initialised using a K-means based algorithm (red). (b) Mean performance across the dataset. Error bars represent the standard deviation. (c) Statistical analysis of maximal performance for all values of the constant c. Central mark of boxplot represents the median, and the edges of the box are the 25th and 75th percentiles. Post-hoc testing by the sign test with Bonferroni correction (n=6) was used to calculate the corrected p-values for comparison with the standard 4D algorithm ($c = 0$) ($p = 2.1$). (d) The same statistical analysis was repeated for mean performance across the dataset and c_0. This revealed a statistically significant decrease in mean performance ($p = 0.012$).

It is clear from figures 3.12a and 3.12b that there is little to no performance gain for this dataset when a constant force term is introduced. For some movies, a performance increase is seen for a specific value of c. However, on other movies the same value of c will cause a significant decrease in performance. Figure 3.12c demonstrates that there is no statistically significant increase in the maximal performance. Moreover, a statistically significant decrease in mean performance across all tested values of c is seen (figure 3.12d). Therefore there is no significant performance gain from using a constant force term and if care is not taken to set the constant, c, the performance may decrease. This highlights a key advantage of the temporal constraint approach; the influence of the temporal constraint is automatically tuned to the movie being analysed, based on the underlying assumptions (for example, constant volume). If the assumptions are valid, then you would expect to see a performance increase across a range of c_0. Therefore, for the temporal constraint terms introduced, fine tuning of the value of c_0 is not critical. Conversely, the use of constant force term is likely to decrease segmentation performance if care and time is not taken to compute the optimal value for c.

To conclude, figure 3.13 summarises the mean and maximal performance of all the algorithms tested in this section. Importantly, the maximal performance of both the volume and shape based temporal constraints are superior (statistically significant) to the unmodified edge based 4D algorithm ($c = 0$). Moreover use of the constant volume constraint produces a statistically significant increase in maximal performance when compared to all tested algorithms; unmodified, constant shape constraint and constant force ($c \neq 0$).

Note the performance difference between the constant volume and shape constraints is a natural result for this dataset, as a constant volume assumption is more appropriate for the target objects (single cells over time).

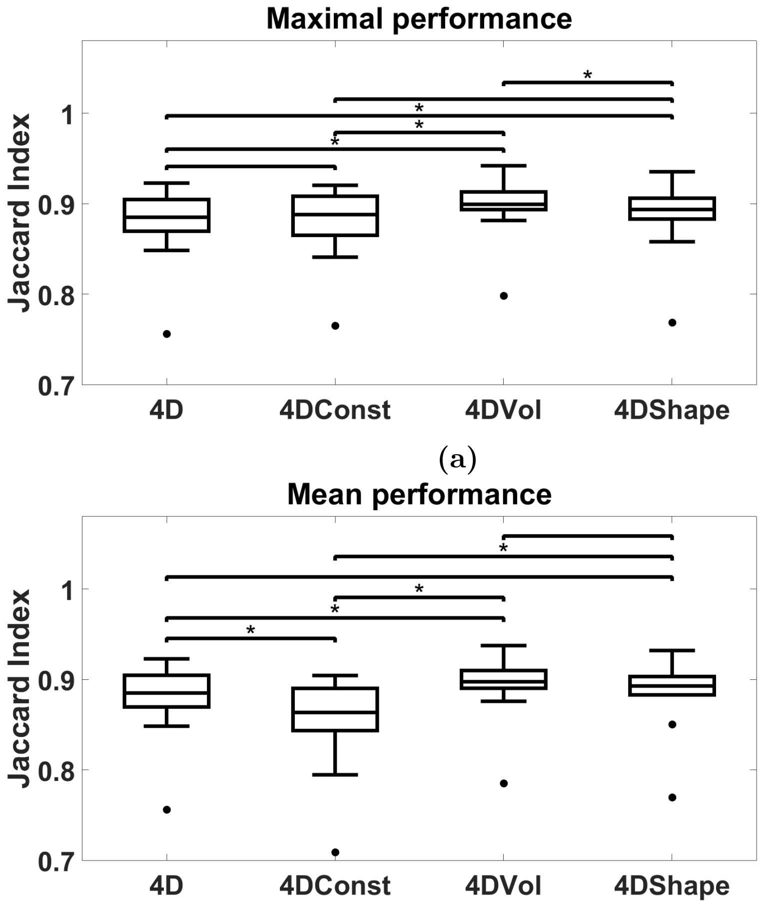

(a)

(b)

Figure 3.13: Summary of performance for 4D edge based level set segmentation protocols with and without temporal constraints. (a) Maximal performance for unmodified 4D edge based DRLSE approach ($c = 0$) (4D) and the same algorithm with the addition of constant force ($c \neq 0$) (4DConst), constant volume (4DVol) and constant shape (4DShape) terms. Friedman's test confirmed there was statistically significant differences in maximal performance between the algorithms ($p = 1.7 \times 10^{-5}$). Post hoc testing by the sign test with Bonferroni correction (n=6) was used to compute corrected p-values for pairwise comparison of algorithms. (b) The same analysis was repeated for the mean performance across the parameter space. Friedman's test returned $p = 4.2 \times 10^{-6}$ confirming statistically significant differences in mean performance.

3.8 Discussion

Recall from section 3.4 that there are very few examples in the literature of *true* 4D segmentation. Moreover, to the best of our knowledge, there are only two examples of 4D level set segmentation. Specifically, the studies by Kohlberger *et al.* (2006) and Abufadel *et al.* (2008) [11, 12]. The approaches to 4D level set segmentation presented in this chapter have many advantages over those presented in these two studies, and will now briefly be reviewed.

Firstly, the approaches presented, are the first example of the use of a DRLSE term in a 4D framework. There are many advantages to this regularization scheme which are discussed, in detail, in sections 3.3.2 and 3.6.1.

Kohlberger *et al.* and Abufadel *et al.* both implement only region based approaches (section 3.3.3) [14]. Therefore, the edge based techniques presented are the first validated adaptations of the geodesic active contour approach to 4D [13]. This adds adaptability to the 4D level set framework as either edge, or region based segmentation can be performed. This choice should be dependent on which is better suited to the data. Note, a combined region and edge based 4D approach can be easily implemented by weighting the smoothing internal energy term, from equation 3.6.10, with an edge finding function, g (equation 3.3.4).

Neither of the existing approaches consider the setting of the temporal scaling factor, Δt, with respect to the spatial dimensions (section 3.6.2). We consider this to be an important contribution, as it is vital to consider the weighting of the temporal derivatives for most level set formulations. It is particularly important when the target movement between frames is significantly greater that the physical dimensions of the voxels.

Kohlberger *et al.* validate their approach on manually segmented real test data, with respect to an equivalent 3D approach, across a range for a key parameter in the level set equation. However, the authors simply state the performance of the algorithms with respect to a performance measure and make no attempt at statistical analysis. Abufadel *et al.* also validate their approach on manually segmented, or rated, real test data, and compare to an equivalent 3D approach. It is not clear if the maximal performance across the key parameter space is considered for each algorithm. Despite this, the analysis is convincing, with discussion of accuracy, consistency and recovery from failure. The results compliment this work, and provide further evidence that the inclusion of temporal information can enhance segmentation performance.

The validation work performed in this chapter is important and unique for several reasons. Firstly, the validation of two seminal approaches; the Chan-Vese region approach and the geodesic edge based method, were performed without any additional internal, or prior information based, energy terms (sections 3.6.5 and 3.6.6). Non-parametric hypothesis testing was used to demonstrate a statistically significant improvement in performance for these fundamental level set techniques in 4D. These vital proof of concept experiments were performed not only on real test data, but also synthetic test data where there is no uncertainty with respect to the ground truth.

The approaches in Kohlberger *et al.* and Abufadel *et al.* were used to segment cardiac morphological features from SPECT, and MRI data respectively. Therefore the approaches presented in this work are the first 4D level set segmentation protocols suitable for use on fluorescence microscopy data. Moreover, as temporal scaling has been considered with a DRLSE term, and for several level set formulations, the approaches presented are vary adaptable, and could be implemented for a wide variety of imaging modalities.

Finally, the concept of incorporating temporal constraints into the energy functional for 4D level set segmentation is novel (section 3.7). Both previous studies incorporated spatial-temporal shape priors, which required a training dataset. The temporal constraints presented do not require any training data, and were validated by non-parametric hypothesis testing. A statistically significant improvement in performance over equivalent 4D implementations (without temporal constraints) was demonstrated.

Two avenues of future development for the presented approaches will now be discussed. Firstly, there is extensive potential for the development of sophisticated, and application targeted, temporal constraints. Specifically, methods for the training of shape priors could be incorporated into a 4D framework, where the prior is learnt from the LSF after each iteration [231, 232, 243]. In such a scenario, the set of shapes formed by the ZLS for each time-point act as the training set. This could provide a less rigid method for incorporating shape based assumptions than equation 3.7.5.

Alternatively, the unity between segmentation and tracking in 4D level set segmentation could be investigated by the introduction of *tracking* based temporal constraints. For example a constraint could be introduced which, using the results of a tracking algorithm, could influence the evolution of the LSF such that targets maintain constant velocity. The tracking of objects would be repeated after each iteration of the LSF. In such a scheme, the tracking and segmentation processes are performed in parallel and are able to influence each other.

Recall that the limiting factor for the widespread use of 4D level set segmentation is computational time. For the methods and datasets presented in this chapter, a computational time for a single movie, on a desktop PC, is typically 10-20 minutes. Therefore the second avenue for future development is the improvement of segmentation time. Note that many of the operations performed in the computation of the level set equation are parallelizable. Therefore optimisation of the algorithms in an efficient language, with implementation on the GPU would be advantageous.

A further route for investigation is the move from a 4D level set framework, to an explicit discrete 4D representation. This could dramatically reduce computational time but would require regular reparametrization of the segmentation contour and sub-routines to deal with topological changes. Defour *et al.* (2011) rewrite the energy minimisation framework in an explicit setting and perform segmentation in 3D using a triangular mesh framework [219]. An extension of this active mesh approach to 4D is conceivable but would require substantial work.

3.9 Conclusion

The protocols presented in the chapter provide a framework for the segmentation of fluorescence microscopy data, using 4D level set segmentation. In all approaches a DRLSE term was used, and the 4D bound for setting the weighting factor, μ, with respect to the update step was calculated (equation 3.6.4). Strategies for setting the temporal scaling factor, Δt, with respect to the spatial dimensions were considered. Moreover the initialisation of the LSF with an approximate segmentation estimate to reduce computational time was demonstrated.

All of the approaches introduced were thoroughly validated. Importantly, through non-parametric hypothesis testing, a statistically significant improvement in maximal performance of 4D approaches over equivalent 3D and 2D approaches was demonstrated. On the simulated test data, a significant improvement in mean performance was also seen. This demonstrates an increase in the stability, and robustness, of the solution with regards to the setting of key parameters. The introduction of novel temporal constraints was used to further target the segmentation protocol to the application. Specifically, assumptions about change in target volume and shape over time were incorporated into terms within the energy functional. For the real test data, a further increase in maximal and mean performance was demonstrated using volume based temporal constraints. This demonstrates that segmentation performance can be increased using temporal constraints with considerable stability. The techniques presented are highly adaptable and could be used for many applications.

Chapter 4

Screening for Regulators of Receptor Trafficking

4.1 Introduction

In this chapter a confocal microscopy based screening platform is introduced. 16 GEFs and GAPs (table 7.1) were screened for the pertubation of EGFR trafficking. This is done both with, and without, EGF stimulation. Before discussing our approach, we will briefly review several large scale screens, all of which use a microscopy based platform to identify regulators of receptor signalling and trafficking.

Pelkmans *at al.* (2005) performed a genome wide siRNA screen of human kinases to identify regulators of simian virus 40 and transferrin endocytosis [5]. Confocal images were manually processed by grouping into one of five pre-determined phenotypes.

Galvez *at al.* (2007) screened the human signalling proteome to show that transferrin uptake is positively regulated by the PI3K-mTOR signalling pathway [4]. Unlike the approach by Pelkmans *at al.* the analysis was fully automated. This is clearly superior when processing the large volume of data generated by a screen. However the image analysis workflows are not described in sufficient detail as to be reproducible. Moreover no validation of performance for the workflow is provided. This should be done either on synthetic or a manually processed subset of the data.

Collinet *et al.* (2010) used a (genome wide) siRNA screen to identify regulators of endocytosis for EGFR (and transferrin) [3]. Using fluorescent markers for the cytoplasm, nucleus and ligand, the authors were able to identify 58 measurement parameters including; number of endosomes, endosome area, endosome clustering and nuclear size. This powerful approach interestingly suggests that the distance of (ligand positive) endosomes from the nucleus is a key measurement parameter for the regulation of endocytosis.

Liberali *at al.* (2014) used 13 parallel siRNA screens to elucidate the roles of genes in the cross-talk and regulation of membrane trafficking [2]. 1132 genes were chosen for involvement in either endocytosis, signalling or regulation of the cytoskeleton. The fully automated image analysis workflows in this study are described in detail (reproducible) and well validated.

In this work we present a screening approach where experimental simplicity, alongside the reproducibility and accuracy of the image analysis workflows are the key advantages. We aim to define a single measurement which characterises the trafficking of receptor and highlights abnormalities. There are many possible measurement parameters, for example recall that Collinet *et al.* (2010) define fifty eight [3]. We choose to use only one measurement scheme so that conventional statistical tests and multi-hypothesis corrections can be used to process results without excessive suppression of p-values. The scale of our screen is small (16 genes) when compared to the discussed studies. These target genes were selected from an in-house stable isotope labeling by amino acids in cell culture (SILAC) proteomics screen (details provided in section 4.3).

With this approach the SILAC study provides the large scale screening capacity, as an alternative to the large scale microscopy screens discussed. A subset of *hits* from the SILAC screen is then analysed with a secondary microscopy screen to provide further evidence of receptor trafficking regulation. Secondary *hits* from the microscopy screen should then be further validated, using for example the protocols described in chapter 5. Therefore our screen provides a tool to bridge proteomics and microscopy based studies of receptor dynamics and signalling.

4.2 Chapter Aims

The aims for this chapter can be summarised as follows:

1. Identify a subset of target genes for microscopy based screening from SILAC proteomics data.
2. Perform a confocal microscopy screen using siRNA for the target genes. This should be done with a small budget and using only widely available experimental equipment.
3. Develop and implement a robust and reproducible image analysis workflow to identify *hits* from the confocal screen. This workflow should define a single measurement scheme which characterises sub-cellular receptor distribution. A statistical framework for hit detection should also be introduced.

4.3 Selection of GEFs and GAPs for Screening

Proteomics can be used to identify and quantify phosphorylated protein levels within cells, but a highly sensitive approach is required. A SILAC methodology is well suited as small changes in phosphorylation levels can be detected [244, 245]. Briefly, cells are cultured with either light (natural) or heavy (isotope labelled) amino acids. After the heavy amino acids have been fully incorporated, the samples can be combined, but remain distinguishable through a mass spectrum. Importantly, as the samples are processed together, much of the *noise* introduced will be present equally in both samples, hence relatively subtle changes in protein levels can be detected.

An in-house SILAC study was performed by Debbie Cunningham (School of Biosciences, University of Birmingham) [245]. Either fibroblast growth factor receptor 2 (FGFR2), or Src family kinases (key regulators of signal transduction [246]), were inhibited to identify downstream phosphorylation events post ligand treatment. Note that in our screen we analyse the variation in EGFR signal distribution in response to EGF stimulation (as opposed to FGFR2 variation with FGF stimulation). With this choice we aim to identify key regulators of receptor tyrosine kinase (RTK) trafficking which are implicated in multiple receptor systems. It would have been advantageous to first characterise FGFR2 events, but there were technical difficulties establishing a stably expressing FGFR2-GFP cell line within the time-frame of the project.

The results of the SILAC screen contained a subset of GEFs and GAPs. As discussed in section 2.3, GEFs and GAPs are key regulators of receptor GTPase-mediated trafficking, and potential therapeutic targets, often facilitating a switch type mechanism in parallel with small G-proteins. Due to budget and time restraints, a further subset of interesting GEFs and GAPs were selected for the screen based on a review of the literature (table 7.1). Since a key result of this work is the methodology, it was important to include some known regulators of EGFR trafficking for validation purposes. In the interest of space we omit a full discussion of all genes selected for the microscopy screen. However, a discussion of the relevant literature for all hits from the microscopy screen is presented in section 4.7.

4.4 Experimental Considerations

The screen presented in this chapter uses confocal microscopy to image an EGFR-EGFP, stably expressing, HeLa cell line (section 7.3.1). The HeLa cell line was chosen for practical ease and because it allows for direct comparison with the many relevant studies in the literature which use this cell line [3]. The main output of the chapter is image analysis workflows and protocols, so use of the HeLa cell line provides a good system for validation. However, the use of a non-transformed cell line would have provided greater physiological relevance.

The imaging in this chapter was performed in 2D, and on fixed cells (see chapter 5 for examples of live cell imaging in 3D). This limitation is imposed by the scale of the screen and the equipment available. Therefore, although the screen provides compelling evidence for novel regulators of EGFR trafficking, it is not conclusive, and should be backed up by additional studies performed in 3D on live cells. Note, the details of the fixing and imaging protocols are presented in section 7.4.1.

Field of view selection was performed manually. Note the first (alive and non-mitotic) located cells, expressing moderate levels of EGFR-EGFP, were always used. This removes user bias from the selection process. For larger scale screens, field of view selection could easily be automated using computer aided microscopy tools such as μManager [247]. Seven to ten fields of view were selected per well. The z-plane was fixed at $3\mu m$ above the coverslip. As noted in section 5.1, this is not ideal but less biased than manual plane selection.

Expression level of EGFR-EGFP was not constant across the population of cells. Hence for each field of view, 4 different acquisitions each with increasing laser power were taken (5%, 8%, 40% and 90% maximal power respectively) (figure 4.1). This ensured that at least one acquisition would have high SNR without pixel saturation. This approach was found to be more time-efficient than manual modification of acquisition settings for each field of view.

As the knockdown efficiency for any given siRNA was not known, three different siRNAs were used for each gene (as listed in table 7.1). This is common practice in the field and is done to increase the probability of effective knockdown for at least one siRNA. Multiple siRNAs were processed simultaneously using 24 glass bottomed dishes. For each siRNA replicate, one well was treated with $100ng/ml$ EGF for 30 minutes and one was left untreated. Three technical repeats were performed for each siRNA, and for every experimental repeat 7-10 fields of view were acquired. The order of treatments within a plate was changed between replicates to avoid any location bias. For practical reasons the screen was split into 5 groups. Each group had 3-4 genes (9-12 siRNA) and for each group, a non-silencing control (NSC) and positive control where performed in parallel. Known-down of the α-adaptin subunit of AP2 was chosen as the positive control and should block clathrin mediated endocytosis of EGFR [248].

A high concentration of EGF ($100ng/ml$) was used to saturate the signalling response and reduce variability across individual cells after 30 minutes EGF stimulation [63, 249]. Although $100ng/ml$ EGF treatment is regularly used in the literature to study EGFR trafficking, it should be noted that it is higher than measured physiological levels [250].

4.5 Analysis Workflow

4.5.1 Pre-processing

The aims of the pre-processing steps introduced in this section are as follows. Firstly, single cells are manually isolated. Secondly, the acquisitions with the highest signal to noise ratio and low pixel saturation levels are selected. Finally, an image restoration strategy which aims to reduce the effects of Poisson noise is applied.

The first step in the analysis workflow is the semi-automated selection of ROIs which contain single healthy cells using a custom graphical interface (Matlab). This is done completely blind and the data is presented to the user in a randomised order to prevent bias. The user is asked to draw polygons containing a single cell. After this initial step the remainder of the analysis is fully automated with no input from the user.

The second step is the selection of the acquisition with the most appropriate laser power for either cellular segmentation, or intensity based quantification of the EGFR signal (figure 4.1). In both cases, the acquisition with the highest laser power (SNR) and percentage of saturated pixels below a given tolerance level is used. For intensity based quantification, this tolerance level is set at a stringent 0.01%. This is done to prevent any distortion of the quantification due to detector saturation. For segmentation the tolerance level is relaxed to 0.1%. This relaxation is necessary post EGF treatment, where the cellular boundary can be indistinct at lower laser powers.

The final preprocessing step is image de-noising using a PURE-LET scheme (section 2.5.4) (Fiji) (parameters estimated automatically from images) [166, 140, 186]. Note that Fiji and the PURE-LET plugin were run within Matlab using the MIJ module [251]. This allowed the entire analysis workflow for the screen to be run within Matlab.

4.5.2 Cellular Segmentation

After pre-processing (including de-noising), the cellular membrane boundary was segmented. In this sub-section, the automated segmentation protocol employed to do this is described. Unlike many siRNA screens, no secondary markers were used so the segmentation must be performed using only the EGFR-EGFP signal. The advantages of using only a receptor marker are discussed in more detail in section 4.7.

Figure 4.1 *(following page)*: Image acquisition for the siRNA screen. (a),(c),(e),(g) Representative 2D confocal microscopy acquisitions of HeLa cell expressing EGFR-EGFP, fixed 30 minutes post $100ng/ml$ EGF treatment. Each field of view was imaged at 4 different laser power levels (5%, 8%, 40% and 90% maximal power respectively). Display range set between the minimum and half the maximum value for each image. Red lines represent the cellular boundary. Scale bar represents $5\mu m$. The percentage of saturated pixels are 0, 0, 0.013, 0.084% respectively. Therefore image (e) was used for cellular segmentation (0.1% tolerance) and image (c) for quantification of EGFR localisation (0.01% tolerance). (a),(c),(e),(g) The corresponding intensity histograms. Note the 12-bit dynamic range and the saturated voxels in (f) and (h).

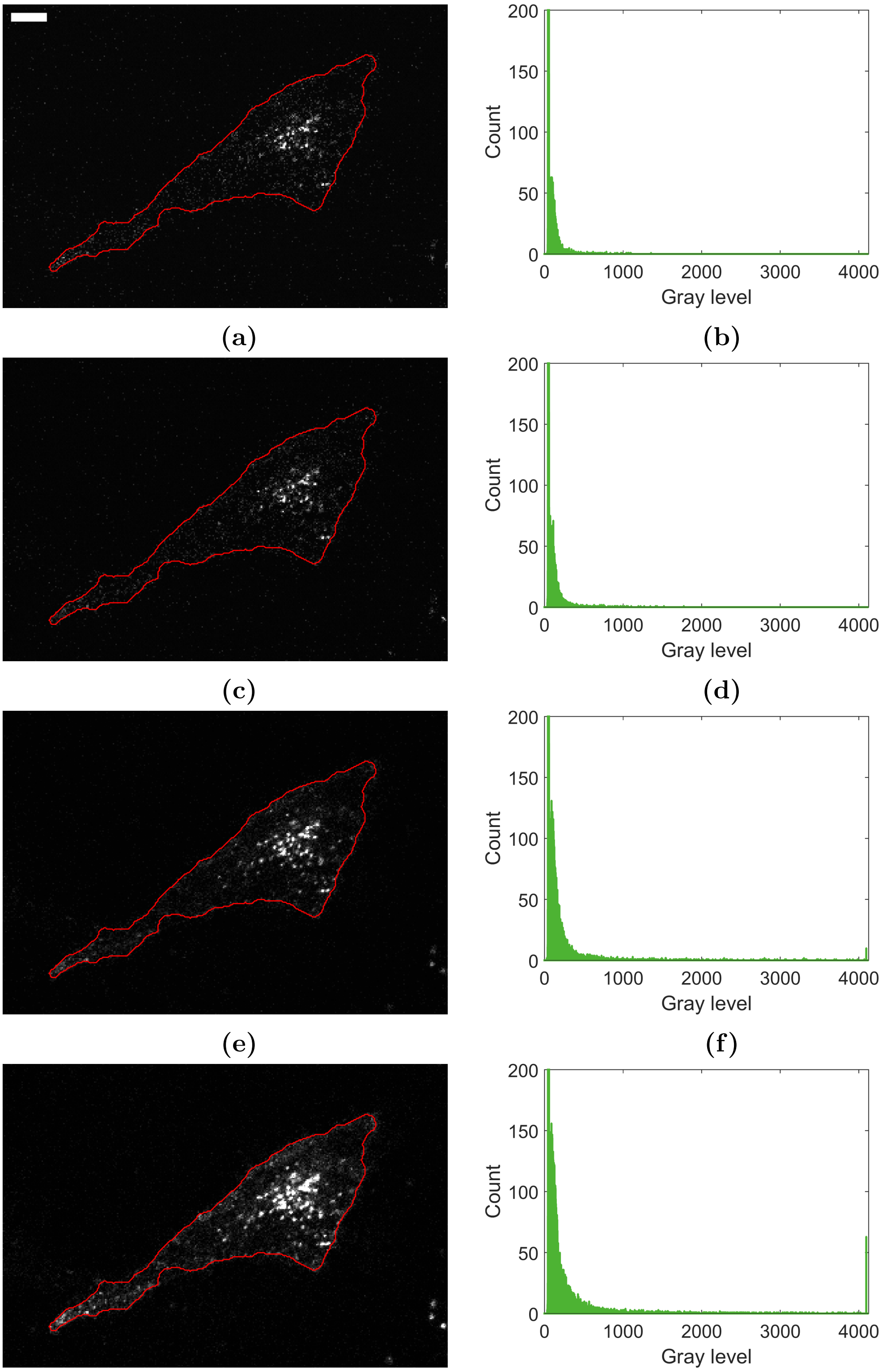

(a) (b)

(c) (d)

(e) (f)

(g) (h)

Parameter	Value	Reference
Constant force term; c	1, 0	equation 3.6.9 & 3.6.10
Lateral scaling factors; Δx, Δy	1	section 3.6.2
Update step; $\Delta\tau$	1	equation 3.6.1
DRLSE factor; μ	0.2	equation 3.6.4
Binary step size; h	2	equation 3.6.4
Dirac-delta function width; α	1.5	equation 3.6.12
Gradient power; p	0.5	equation 3.3.4
Stopping constant; s	1%	algorithm 1
Maximum number of iterations	50	section 3.6.1
Edge/smoothing term; λ	9	equations 3.6.9 & 3.6.10

Table 4.1: Parameters for cellular segmentation using 2D edge based distance regularised level set evolution.

Cells expressing fluorescent receptor have a clear edge at the plasma membrane, but inhomogeneous internal intensity and structure. Therefore an approach based on edge detection was chosen. Specifically 2D edge based distance regularised level set evolution (DRLSE) as described in section 3.3.2 [225]. This approach was chosen for its ability to detect weak boundaries using an edge based level set formulation, and without the need for complicating reinitialisation strategies. A implicit level set framework was used, over potentially faster explicit representations, for the simplicity of the implementation. The full list of parameters that were used to control the evolution of the level set function are listed in table 4.1. Note constant, c, controlling the constant force term (equation 3.6.9) is positive for the first 10 iterations and zero after. This is done to provide an initial *push* to escape any local minima in the energy functional.

Using an initial segmentation estimate to initialise the level set function can improve both the speed and accuracy of a level set approach. For the screen, a K-means clustering approach similar to that used for the validation of 4D level set segmentation on real data (section 3.6.6) was chosen. All but the cluster with the lowest mean value were combined to produce a binary mask. The mask was then processed by morphological closing; dilation and erosion using a circular structural element ($1.5\mu m$ radius). Any holes in the mask were subsequently filled to acquire a segmentation element.

Unlike the approach from section 3.6.6, the number of clusters is not fixed but initially set to two and increased iteratively. This iterative increase is stopped if the percentage area difference between sequential segmentation estimates is less than 20% twice in a row. More formally if we let $A(n)$ denote the area of the segmentation estimate for n clusters, then if $(A(n) - A(n-1))/A(n-1)$ and $(A(n+1) - A(n))/A(n)$ are both less than or equal to 0.2, the iterative increase in cluster number is stopped and K-means clustering with n clusters is used to generate the final segmentation estimate (figure 4.2a - 4.2d). A fixed number of clusters is not used, as the large variation in cellular EGFR distribution across the screen required an adaptive approach to produce consistent results.

To analyse the performance of the protocol, 27 cells from across the screen were manually segmented. The Jaccard index was then used to quantify the performance of the protocol for this subset of data (equation 3.6.13). The results of this analysis are shown in figure 4.2f. Importantly, the edge based DRLSE segmentation protocol is shown to be both accurate and consistent with a mean Jaccard index of 0.92 ± 0.03. Moreover the improvement in segmentation performance over the initial K-means based estimate is shown to be statistically significant ($p < 0.001$), as determined by the sign test. The sign test was chosen because it assumes neither normality or a symmetric distribution, both of which are unreasonable assumptions for the distribution of segmentation performance across cells.

4.5.3 Hit Detection

In the previous sub-section a cellular segmentation workflow was described. Here a protocol which uses this segmentation result to analyse the spatial intensity distribution of individual cells is presented. The results of this analysis, across all cells treated with siRNA targeting a specific gene, are compared to the distribution of cells from the NSC.

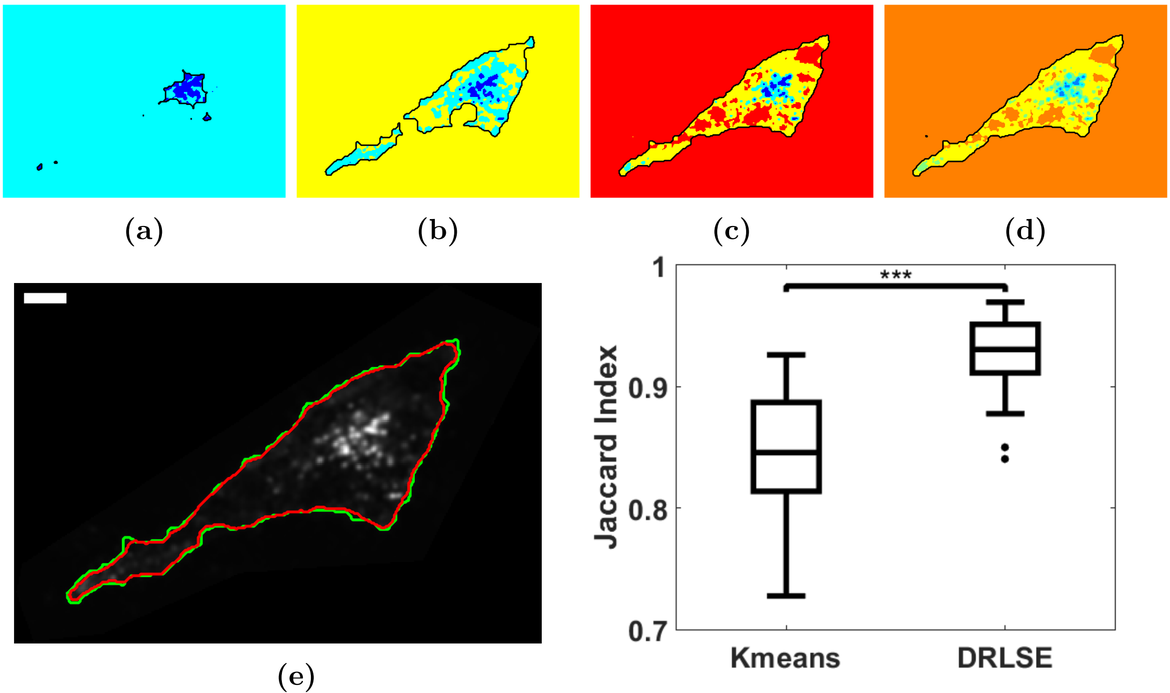

(a) (b) (c) (d)

(e)

(f)

Figure 4.2: Cellular segmentation protocol for the siRNA screen. (a)-(d) K-means clustering with varying number of clusters. All but the cluster with the lowest mean intensity are combined and then eroded and dilated to produce the segmentation estimate (black contours). If the percentage area difference between consecutive segmentation estimates is less than 20% twice, then the cluster after the first with less than 20% area difference, is used to initiate to initiate the level set function (LSF). (a) 2 clusters. (b) 3 clusters (area difference = 573%). (c) 4 clusters (area difference = 19.6%). (d) 5 Clusters (area difference = 2.1%). Therefore, the preceding estimate (4 clusters) is used. (e) Representative de-noised (PURE-LET) image of HeLa cell expressing EGFR-EGFP, fixed 30 minutes post EGF treatment. Scale bar represents $5\mu m$. Initial segmentation estimated from K-means based protocol shown in green. The final segmentation result produced by 2D edge based distance regularised level set evolution (DRLSE) is shown in red. (f) Quantification of segmentation performance using a manually annotated dataset (27 cells). The central mark is the median, the edges of the box are the 25th and 75th percentiles, the whiskers extend to the most extreme data points not considered outliers. Outliers are shown individually and included in all calculations. The mean Jaccard index for the initial K-means based estimate and the DRLSE based final segmentation are given by 0.85±0.05 and 0.92±0.03 (errors given by standard deviation). The difference between the means is statistically significant ($p < 0.001$) as determined by the non-parametric sign test.

This comparison is used to infer if the gene is a *hit*. The decision making process used for this hit classification is also presented.

Recall for intensity based quantification, the acquisition with the highest laser power and saturation level of less than 0.01% is used (section 4.5.1). After de-noising (figure 4.3a), a rolling ball background subtraction is applied to remove non-specific and/or auto-fluorescent signal which is not associated with the structures of interest (membrane and endosomal signal) (figure 4.3b). Briefly, in a rolling ball approach the image obtained by morphological opening (erosion then dilation), with a spherical structure element (the *rolling ball*), is subtracted [252]. The radius of the structural element is set to $1\mu m$, as features larger than this are considered background.

To classify hits it is necessary to define a measure (or measures) which emphasise and quantify any abnormalities in EGFR trafficking on a cellular level. To do this the cellular region, as defined by the segmentation, is split into banded sub-regions based on distance from the plasma membrane. The width of each band is constant and set such that the cellular region is split into 10 bands (figure 4.3c). Having identified which pixels correspond to each band, the percentage of the cell's total EGFR-EGFP signal contained in each band is calculated (figure 4.3d). This characterises a cell's receptor distribution based on relative distance from the membrane. We hypothesise that abnormalities in endocytosis and endosomal trafficking of receptor will be well characterised by this measure. Note by convention, band 1 is always the outermost band (adjacent to the plasma membrane), and band 10 the innermost.

Having defined a measure of cellular EGFR distribution, the next step is to design a statistical analysis for hit detection. First, recall the structure of the screen where for each gene there are 3 siRNAs, each with 3 technical replicates. For every gene there are 3 associated NSC replicates. The hit detection protocol should compare the results of each siRNA treatment to the corresponding NSC replicates. To do this, the mean for

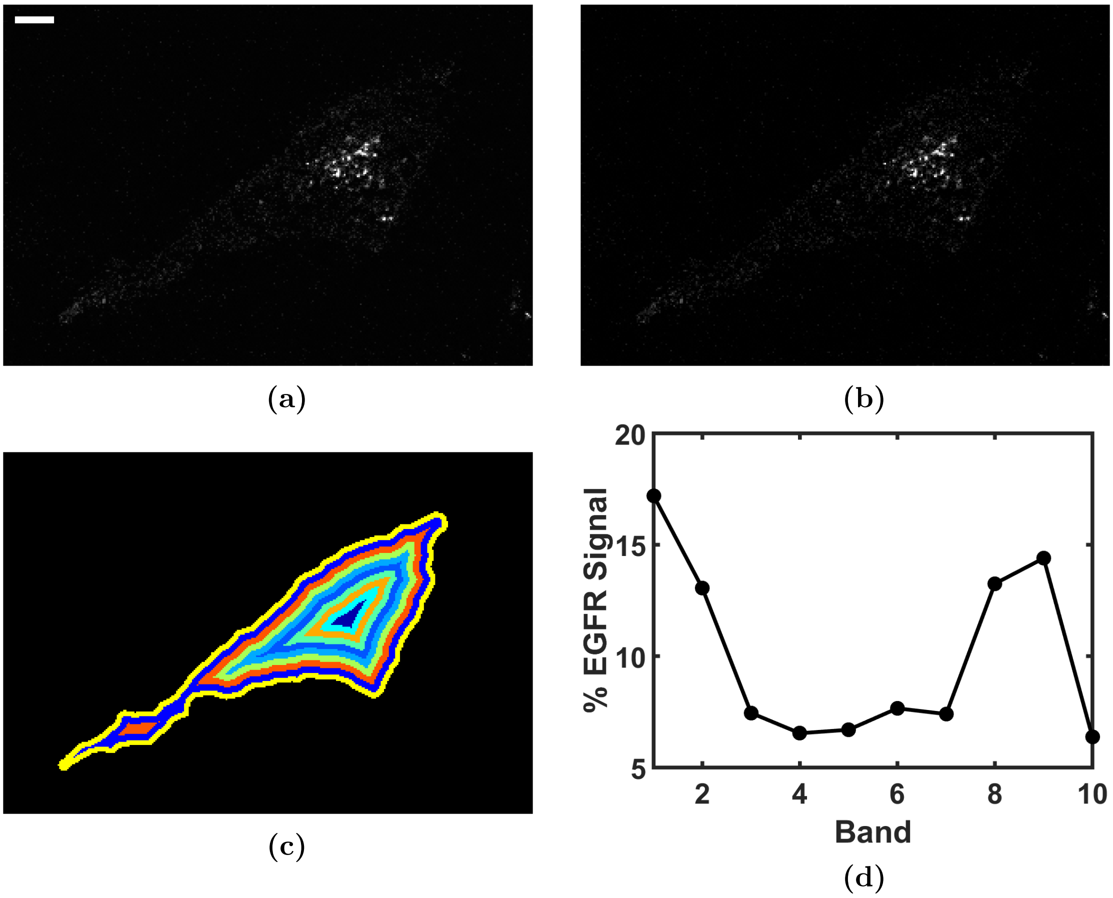

(a) (b) (c) (d)

Figure 4.3: Quantifying the sub-cellular distribution of receptor. (a) Representative acquisition (de-noised) of HeLa cell expressing EGFR-EGFP. A strict 0.01% pixel saturation level was used to select this image. Display range set between the minimum and half the maximum value. (b) Image after background subtraction using a rolling ball approach (radius set to $1\mu m$) (c) Using the automated cellular segmentation protocol, the intracellular region is split into 10 bands, all with equal width. (d) The percentage of the cells total EGFR signal in each band is quantified. This approach enables the quantification of the EGFR distribution on a single cell level.

each band across all individual cells in each replicate is calculated. A protocol is then employed to identify the band for which the EGFR distribution is most abnormal when compared to the NSC across all three siRNAs for a single gene. The aim here is to identify the band for which there is the greatest net effect for a particular gene knockdown. To do this, for every band, the sum of the t-statistic between each siRNA and the NSC and over all three siRNA treatments is calculated. The maximal sum is then used to identify the band used for further statistical analysis and hit detection;

$$\max_{bands} \sum_{i=1}^{3} t_i = \max_{bands} \sum_{i=1}^{3} \frac{\overline{X}_c - \overline{X}_i}{\sqrt{\frac{s_c}{n_c} + \frac{s_i}{n_i}}} \tag{4.5.1}$$

where t_i is the t statistic for the ith siRNA. $\overline{X}_c$ and $\overline{X}_i$ are the mean values across all replicates for the NSC and ith siRNA respectively. s_c and s_i are the standard deviations across replicates and n_c, n_i are the number of replicates, which for this screen is always equal to three.

Using the selected band, a two sample t-test can be used to obtain a p-value, p_i, for each of the three siRNAs. Note with a two sample t-test there is an assumption of normality in the replicate means. This assumption is hard to test due to having only 3 experimental repeats. Therefore results from this screen should be treated with caution and any hits should be followed up with further studies. This is discussed in more detail in section 4.7.

The p-values for the three siRNAs targeting a single gene are combined using Fisher's method to determine an overall p-value for each gene [253];

$$X_6^2 = -2 \sum_{i=1}^{3} \ln(p_i) \tag{4.5.2}$$

where the test statistic, X_6^2, has a chi-squared distribution with 6 degrees of freedom. Therefore a chi-squared cumulative distribution function can subsequently be used to determine a single p-value for each gene. Note it is not known if all, or indeed any, of the siRNA treatments will significantly knockdown the target gene. This can lead to false negatives in the hit detection process and for this reason negative results should not be considered informative.

Having calculated the p-value for each gene in the screen, multiple hypothesis testing should be corrected for. Here we chose to use the Benjamini-Hochberg procedure over the Bonferroni correction used in chapter 3 (equation 3.6.14). This is chosen as it is less stringent than the Bonferroni correction. For a siRNA screen this is appropriate, as the aim is to test many hypotheses and identify hits for further study. In a Benjamini-Hochberg approach, the p-values for all genes are arranged in ascending order; $p_1, p_2, ..., p_m$, where m is the total number of genes in the screen. For a given critical value, α, the largest p_j is found such that;

$$p_j \leqslant \frac{j}{m}\alpha \tag{4.5.3}$$

then all genes corresponding to $p_1, p_2, ..., p_j$ are considered hits [254]. Prior to analysing the data, we chose to set the false discovery rate, α, to 0.1 and consider this to be appropriately stringent for a screen.

4.6 Results

4.6.1 Quality Check across Control Groups

Recall that the structure of the screen is such that it is split into 5 groups each with 3 NSC replicates (section 4.4). As a quality control measure it is appropriate to analyse the variation of the NSC negative controls across groups. To do this the same approach to that used for hit detection is employed (section 4.5.3). Each group is compared to the replicates from all other groups. The band of maximal variation across all groups is found

	No EGF		Plus EGF	
Group	p-value	BH Significance	p-value	BH Significance
1	0.248	FALSE	0.248	FALSE
2	0.368	FALSE	0.228	FALSE
3	0.135	FALSE	0.912	FALSE
4	0.697	FALSE	0.098	FALSE
5	0.322	FALSE	0.065	FALSE

Table 4.2: Statistical testing for variation within control groups. p-values for variation within the non silencing control (NSC) groups. The replicates for each control group was compared to the replicates for all other control groups combined. This analysis was performed as a quality control measure. The results demonstrate there is no statistically significant variation within the NSC groups across the screen. The same workflow for gene hit-detection was used to determine the p-values and significance after Benjamini-Hochberg (BH) correction ($\alpha = 0.1$, $m = 5$).

using the t-statistic (equation 4.5.1). This approach is performed on both the data-sets (with and without EGF treatment) (figure 4.4).

Subsequently, p-values are calculated for each group (two sample t-test). These p-values were tested for significance (at level $\alpha = 0.1$) after Benjamini-Hochberg correction for multiple comparisons (equation 4.5.3, $m = 5$). The results of this quality control analysis are shown in table 4.2. Note that there is no statistically significant variation within the control groups both with and without EGF treatment. Therefore we can include all the data from the screen for further analysis and hit detection. Moreover as the same protocol was used for hit detection, it increases our confidence in this protocol to detect true positives.

Recall the positive control for the screen is knockdown of the α-adaptin subunit of AP2 using siRNA treatment. Western blotting was used to verify the effectiveness of the siRNA treatment for α-adaptin knockdown. A substantial reduction in expression level was observed (figure 4.5). The effects of the AP2 knockdown were analysed across the entire screen. The hit detection protocol as described in section 4.5.3 was used to obtain p-values of 0.080 and 0.017, with and without EGF treatment respectively. Therefore as

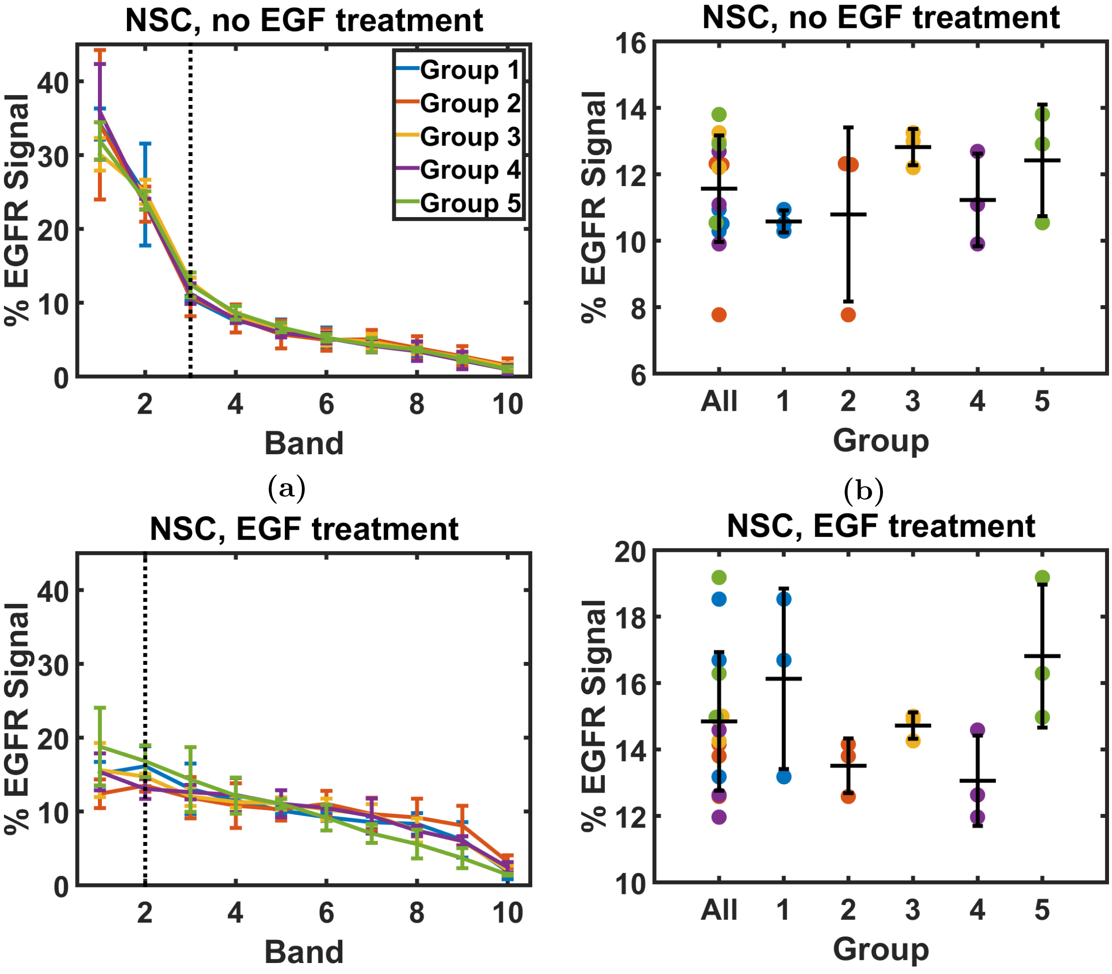

(a) (b) (c) (d)

Figure 4.4: Quality control analysis of variation between non silencing control (NSC) replicates. (a) Mean percentage EGFR signal across all banded regions for all NSC groups (no EGF treatment). Error bars are the standard deviation across the replicates. The dotted line highlights the band chosen for statistical testing (band 3). (b) Plot of individual replicate means across all NSC groups for band 3 (no EGF treatment). Central band represents the mean and the error bars are the standard deviation. (c) Mean percentage EGFR signal across all banded regions for all NSC groups (EGF treated). (d) Plot of individual replicate means across all NSC groups for band 2 (EGF treated).

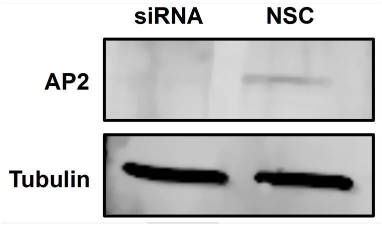

Figure 4.5: Western Blot for AP2 Knockdown. Note substantial reduction of AP2 expression when treated with siRNA. This was performed to verify the use of AP2 siRNA as a positive control.

expected, AP2 knockdown is detected as a positive hit.

4.6.2 Screen Hits

The full set of screen data (with and without EGF treatment) was analysed using the automated workflow detailed in section 4.5. The output of this workflow is a p-value for each siRNA treatment and a combined p-value for each gene. A Benjamini-Hochberg multiple hypothesis correction is then applied to determine if a gene is a hit. This output is recorded for all genes in the screen in tables 4.3 and 4.4 for no and $100ng/ml$ EGF treatment respectively.

Note there are no hits for data-set without EGF treatment and 5 hits for EGF treated data-set; IQSEC1, VAV2, TBC1D10B, TBC1D5 and USP6NL. Detailed graphical representations of the band based data analysis for each of the hits is presented in figures 4.7 - 4.11. This includes a plot of the mean percentage EGFR signal across all banded regions for each siRNA treatment, and a plot of the individual replicates for the band selected for statistical testing. In section 4.7.1, a detailed discussion of each hit is presented in the context of relevant literature.

4.7 Discussion

The screening approach presented in this chapter has several key advantages. Firstly, unlike any of the approaches discussed in section 4.1, the screen does not require any secondary labels for the cytoplasm or nucleus. The cellular segmentation and the mea-

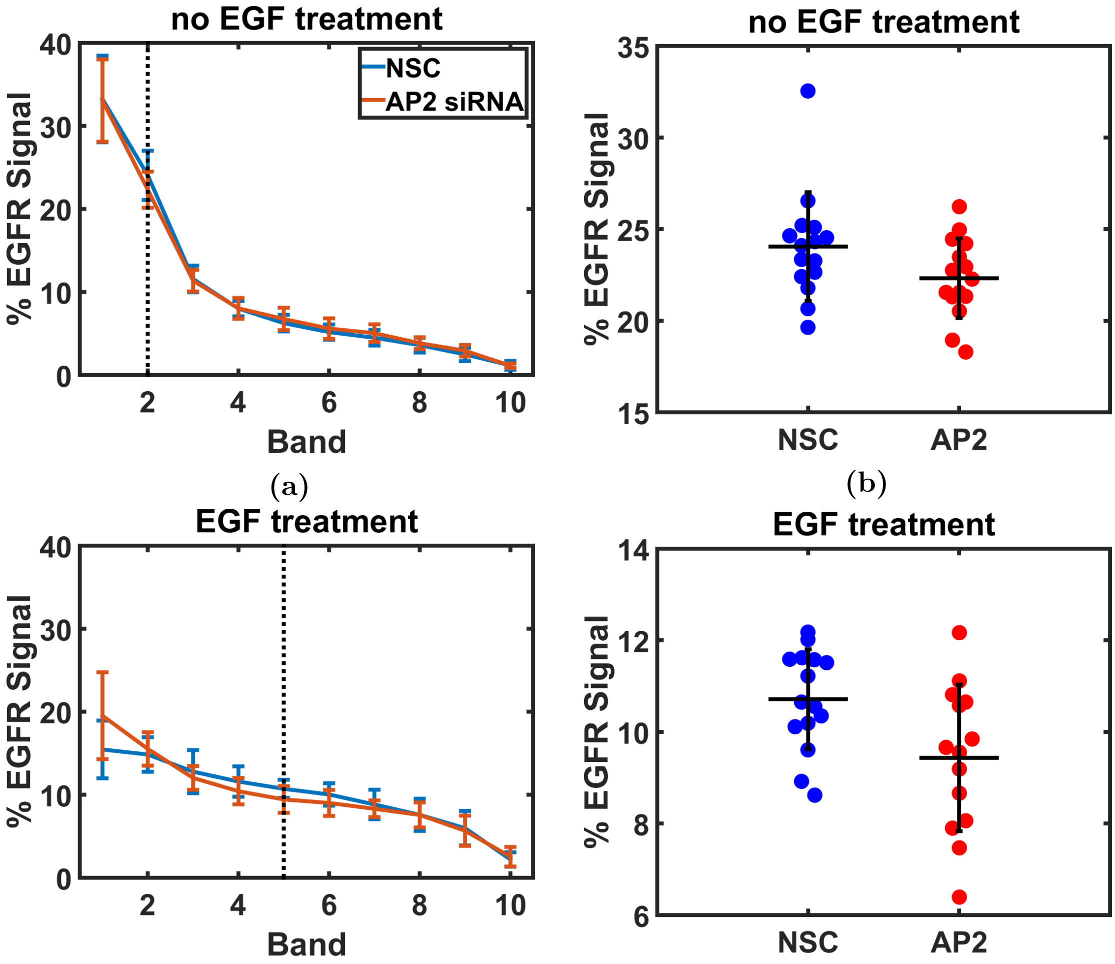

(a) (b) (c) (d)

Figure 4.6: AP2 knockdown as a positive control for the screen. siRNA targeting the α-adaptin subunit of AP2 was used to inhibit clathrin mediated endocytosis. (a) Mean percentage EGFR signal across all banded regions across the entire screen (no EGF treatment). Dotted line represents band chosen for further statistical analysis (band 2). Error bars are the standard deviation across the replicates. (b) Plot of individual replicate means across entire screen. Central band represents the mean and the error bars are the standard deviation. A two sample t-test returned a p-value of $p = 0.080$. (c) Mean percentage EGFR signal across all banded regions across the entire screen (EGF treated). (d) Plot of individual replicate means across entire screen for band 5. A two sample t-test returned a statistically significant p-value of $p = 0.017$.

Gene	p-value siRNA 1	siRNA 2	siRNA 3	Combined	BH Significance
ARFGEF2	0.181	0.624	0.051	0.112	FALSE
FGD1	0.158	0.888	0.003	0.016	FALSE
IQSEC1	0.486	0.102	0.589	0.314	FALSE
HERC1	0.508	0.615	0.280	0.560	FALSE
PSD3	0.298	0.256	0.377	0.312	FALSE
SOS1	0.562	0.256	0.147	0.260	FALSE
ASAP2	0.106	0.117	0.085	0.033	FALSE
TBC1D2	0.310	0.229	0.151	0.170	FALSE
VAV2	0.910	0.691	0.324	0.785	FALSE
TBC1D10B	0.543	0.712	0.420	0.725	FALSE
TBC1D4	0.994	0.265	0.647	0.738	FALSE
TBC1D5	0.496	0.635	0.231	0.513	FALSE
TBC1D14	0.649	0.037	0.409	0.159	FALSE
TBC1D15	0.303	0.217	0.130	0.146	FALSE
TSC2	0.850	0.293	0.263	0.487	FALSE
USP6NL	0.206	0.856	0.820	0.695	FALSE

Table 4.3: Summary of screen results (no EGF treatment). The p-value for each siRNA is shown, as is the corresponding combined p-value for each gene as determined by Fisher's combination method. The Benjamini-Hochberg (BH) method is used to make the *hit* decision with a critical value of $\alpha = 0.1$. There are no hits for the un-treated data-set.

Gene	p-value siRNA 1	siRNA 2	siRNA 3	Combined	BH Significance
ARFGEF2	0.834	0.876	0.027	0.252	FALSE
FGD1	0.550	0.604	0.749	0.836	FALSE
IQSEC1	**0.088**	**0.074**	**0.017**	**0.006**	**TRUE**
HERC1	0.220	0.957	0.223	0.411	FALSE
PSD3	0.835	0.193	0.375	0.468	FALSE
SOS1	0.320	0.436	0.303	0.388	FALSE
ASAP2	0.343	0.399	0.092	0.188	FALSE
TBC1D2	0.295	0.458	0.382	0.431	FALSE
VAV2	**0.050**	**0.940**	**0.020**	**0.030**	**TRUE**
TBC1D10B	**0.016**	**0.021**	**0.011**	**0.0003**	**TRUE**
TBC1D4	0.523	0.020	0.321	0.076	FALSE
TBC1D5	**0.130**	**0.028**	**0.002**	**0.001**	**TRUE**
TBC1D14	0.032	0.324	0.584	0.116	FALSE
TBC1D15	0.970	0.281	0.141	0.367	FALSE
TSC2	0.995	0.737	0.021	0.211	FALSE
USP6NL	**0.048**	**0.889**	**0.013**	**0.020**	**TRUE**

Table 4.4: Summary of screen results (EGF treated). The p-value for each siRNA is shown, as is the corresponding combined p-value for each gene as determined by Fisher's combination method. The Benjamini-Hochberg (BH) method is used to make the *hit* decision with a critical value of $\alpha = 0.1$. There are a total of 5 hits for the EGF treated data-set; IQSEC1, VAV2, TBC1D10B, TBC1D5 and USP6NL.

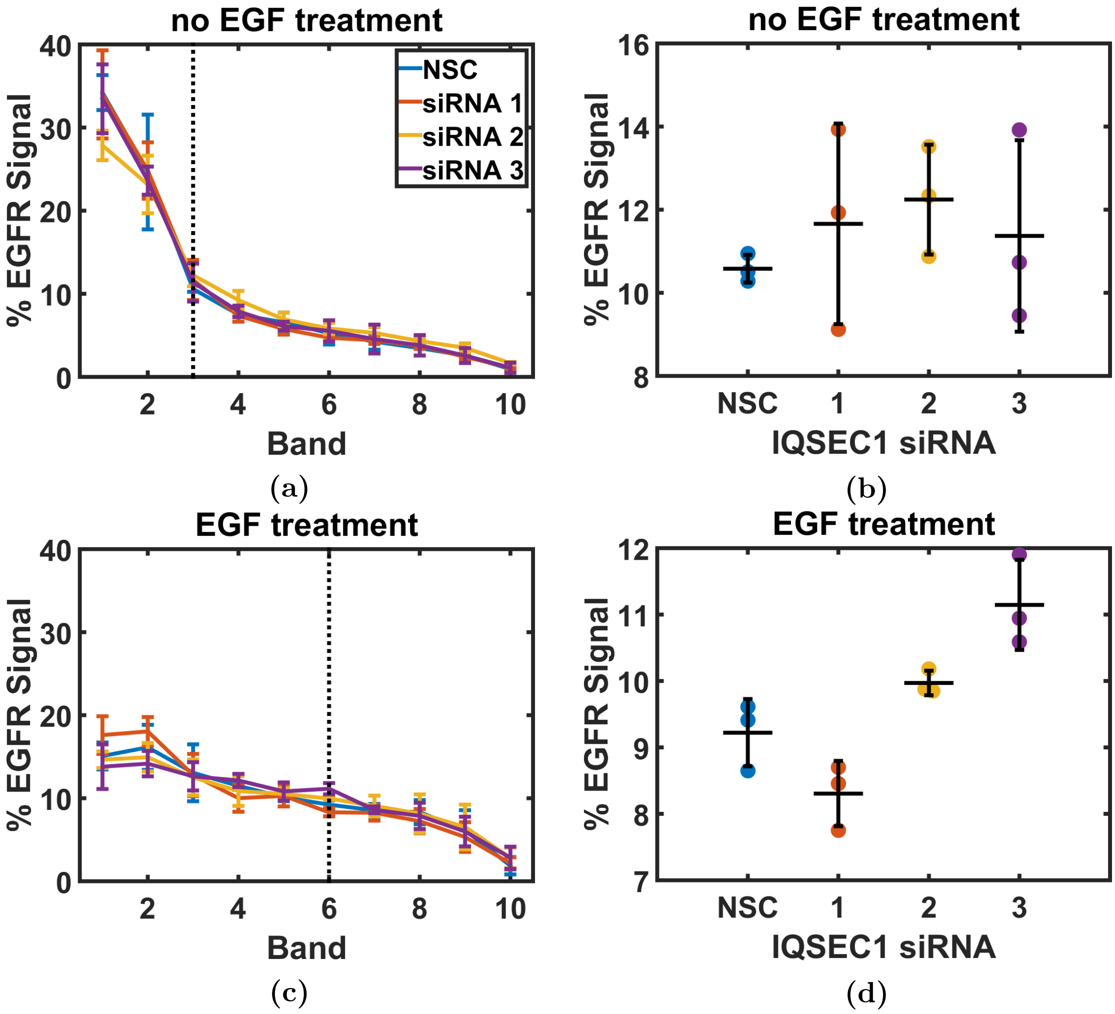

(a) (b)

(c) (d)

Figure 4.7: IQSEC1 is a screen hit. (a) Mean percentage EGFR signal across all banded regions for siRNA targeting IQSEC1 (no EGF treatment). Band 1 is the outermost and band 10 is the innermost. Dotted line indicates the band chosen for further statistical analysis (band 3). Error bars are the standard deviation across the replicates. (b) Plot of individual replicate means for band 3. Central band represents the mean and the error bars are the standard deviation. Two sample t-tests returned p-values of 0.486, 0.102 and 0.589 for the three siRNA treatments respectively. The combined p-value for the gene was 0.314 (no EGF treatment) which was not significant after Benjamini-Hochberg correction. (c) Mean percentage EGFR signal across all banded regions for siRNA targeting IQSEC1 (EGF treated). (d) Plot of individual replicate means for band 6. Two sample t-tests returned p-values of 0.088, 0.074 and 0.017 for the three siRNA treatments respectively. The combined p-value for the gene was 0.006 (EGF treated) which was significant after Benjamini-Hochberg correction.

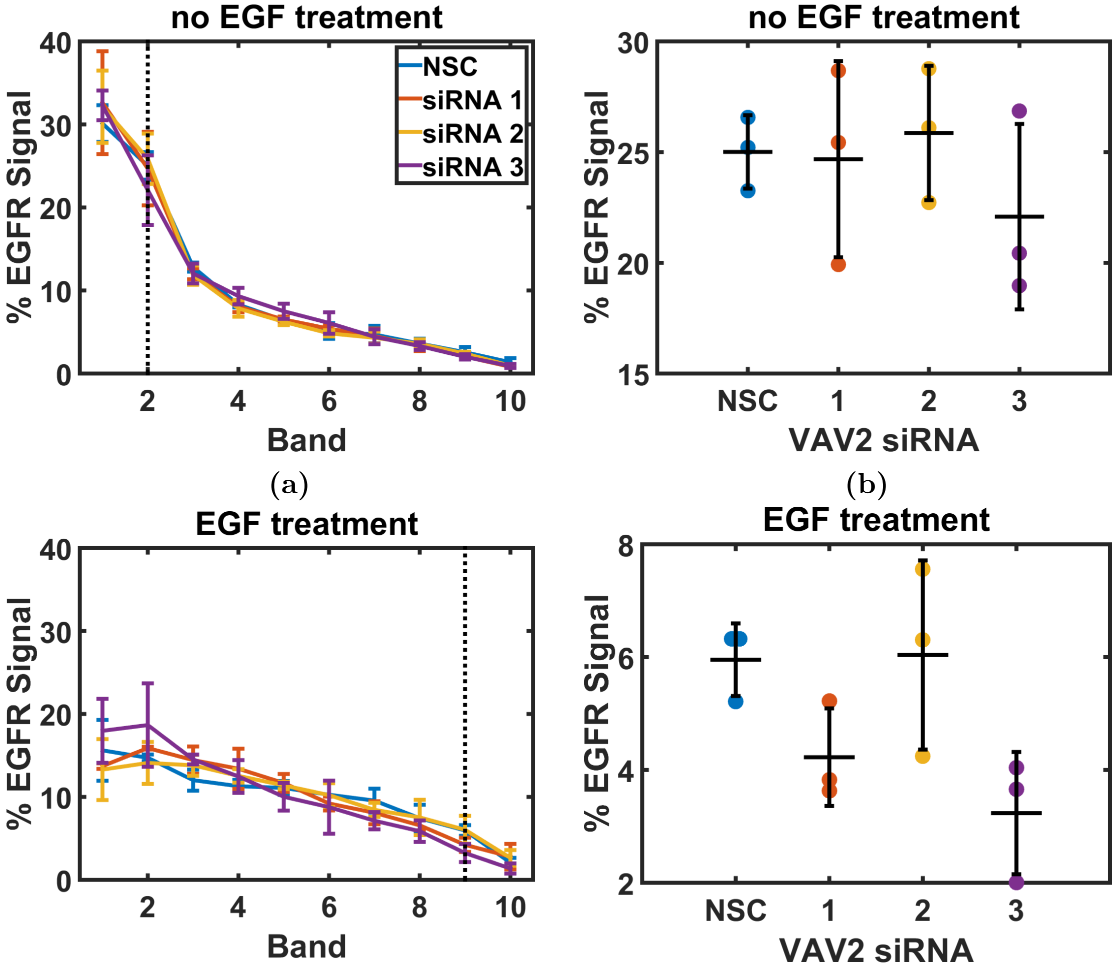

(a) (b) (c) (d)

Figure 4.8: VAV2 is a screen hit. (a) Mean percentage EGFR signal across all banded regions for siRNA targeting VAV2 (no EGF treatment). Band 1 is the outermost and band 10 is the innermost. Dotted line indicates the band chosen for further statistical analysis (band 2). Error bars are the standard deviation across the replicates. (b) Plot of individual replicate means for band 2. Central band represents the mean and the error bars are the standard deviation. Two sample t-tests returned p-values of 0.910, 0.691 and 0.324 for the three siRNA treatments respectively. The combined p-value for the gene was 0.785 (no EGF treatment) which was not significant after Benjamini-Hochberg correction. (c) Mean percentage EGFR signal across all banded regions for siRNA targeting VAV2 (EGF treated). (d) Plot of individual replicate means for band 9. Two sample t-tests returned p-values of 0.050, 0.940 and 0.020 for the three siRNA treatments respectively. The combined p-value for the gene was 0.030 (EGF treated) which was significant after Benjamini-Hochberg correction.

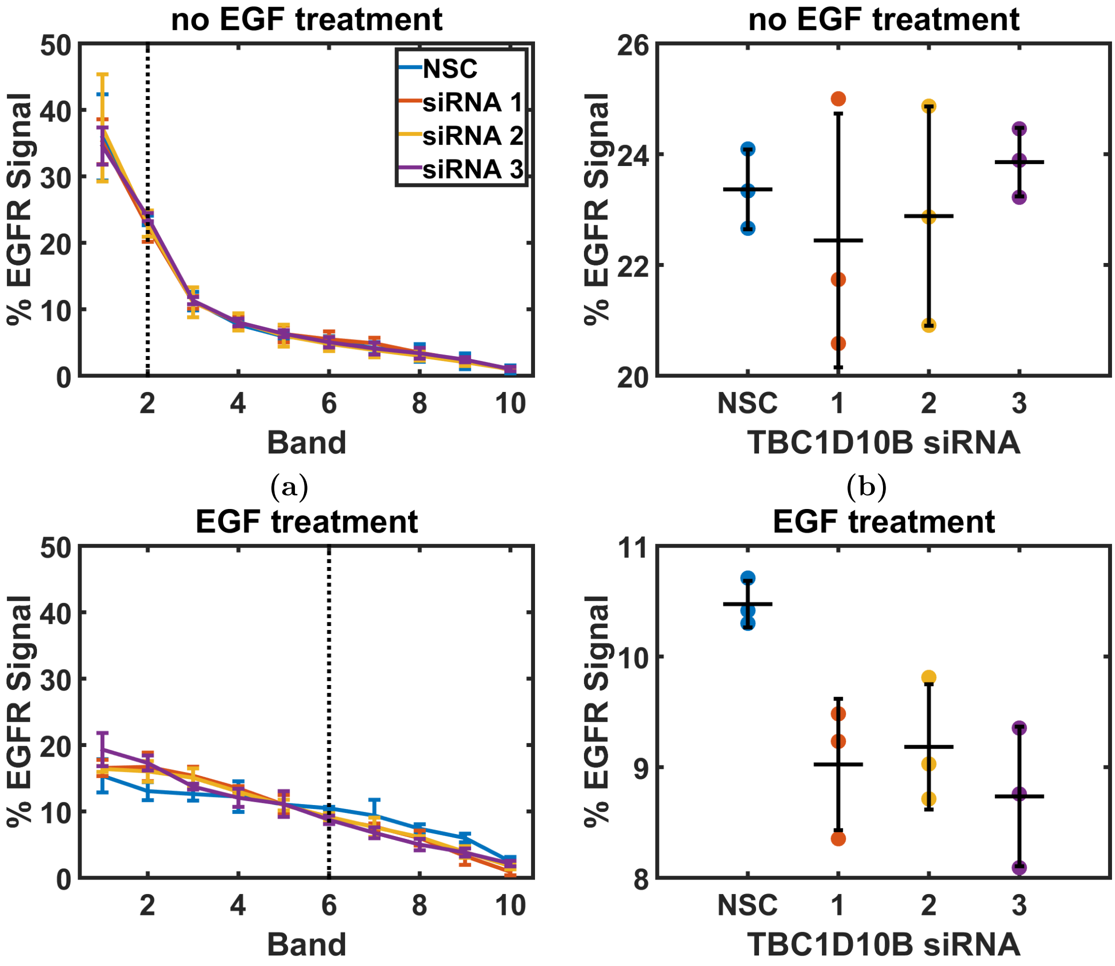

(a) (b)

(c) (d)

Figure 4.9: TBC1D10B is a screen hit. (a) Mean percentage EGFR signal across all banded regions for siRNA targeting TBC1D10B (no EGF treatment). Band 1 is the outermost and band 10 is the innermost. Dotted line indicates the band chosen for further statistical analysis (band 2). Error bars are the standard deviation across the replicates. (b) Plot of individual replicate means for band 2. Central band represents the mean and the error bars are the standard deviation. Two sample t-tests returned p-values of 0.543, 0.712 and 0.420 for the three siRNA treatments respectively. The combined p-value for the gene was 0.725 (no EGF treatment) which was not significant after Benjamini-Hochberg correction. (c) Mean percentage EGFR signal across all banded regions for siRNA targeting TBC1D10B (EGF treated). (d) Plot of individual replicate means for band 6. Two sample t-tests returned p-values of 0.016, 0.021 and 0.011 for the three siRNA treatments respectively. The combined p-value for the gene was 0.0003 (EGF treated) which was significant after Benjamini-Hochberg correction.

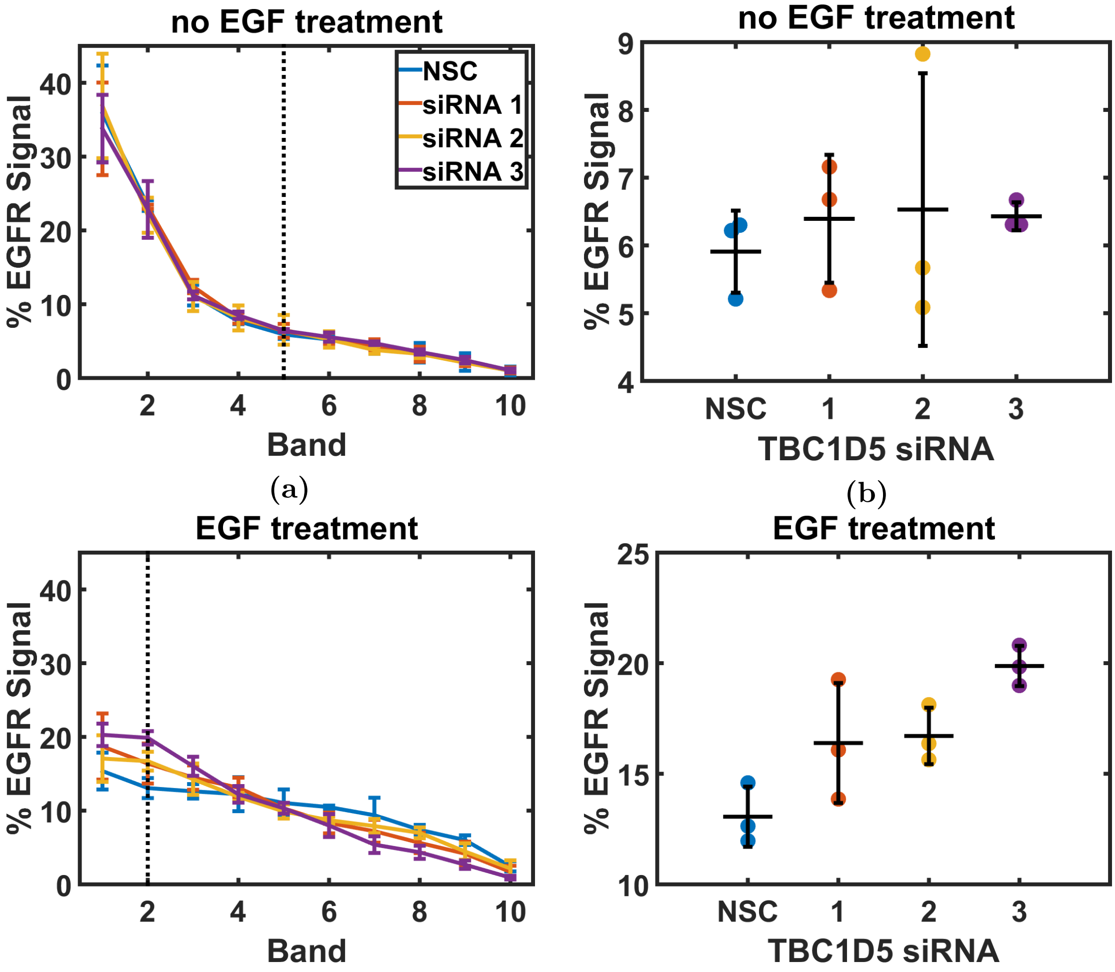

(a) (b) (c) (d)

Figure 4.10: TBC1D5 is a screen hit. (a) Mean percentage EGFR signal across all banded regions for siRNA targeting TBC1D5 (no EGF treatment). Band 1 is the outermost and band 10 is the innermost. Dotted line indicates the band chosen for further statistical analysis (band 5). Error bars are the standard deviation across the replicates. (b) Plot of individual replicate means for band 5. Central band represents the mean and the error bars are the standard deviation. Two sample t-tests returned p-values of 0.496, 0.635 and 0.231 for the three siRNA treatments respectively. The combined p-value for the gene was 0.513 (no EGF treatment) which was not significant after Benjamini-Hochberg correction. (c) Mean percentage EGFR signal across all banded regions for siRNA targeting TBC1D5 (EGF treated). (d) Plot of individual replicate means for band 2. Two sample t-tests returned p-values of 0.130, 0.028 and 0.002 for the three siRNA treatments respectively. The combined p-value for the gene was 0.001 (EGF treated) which was significant after Benjamini-Hochberg correction.

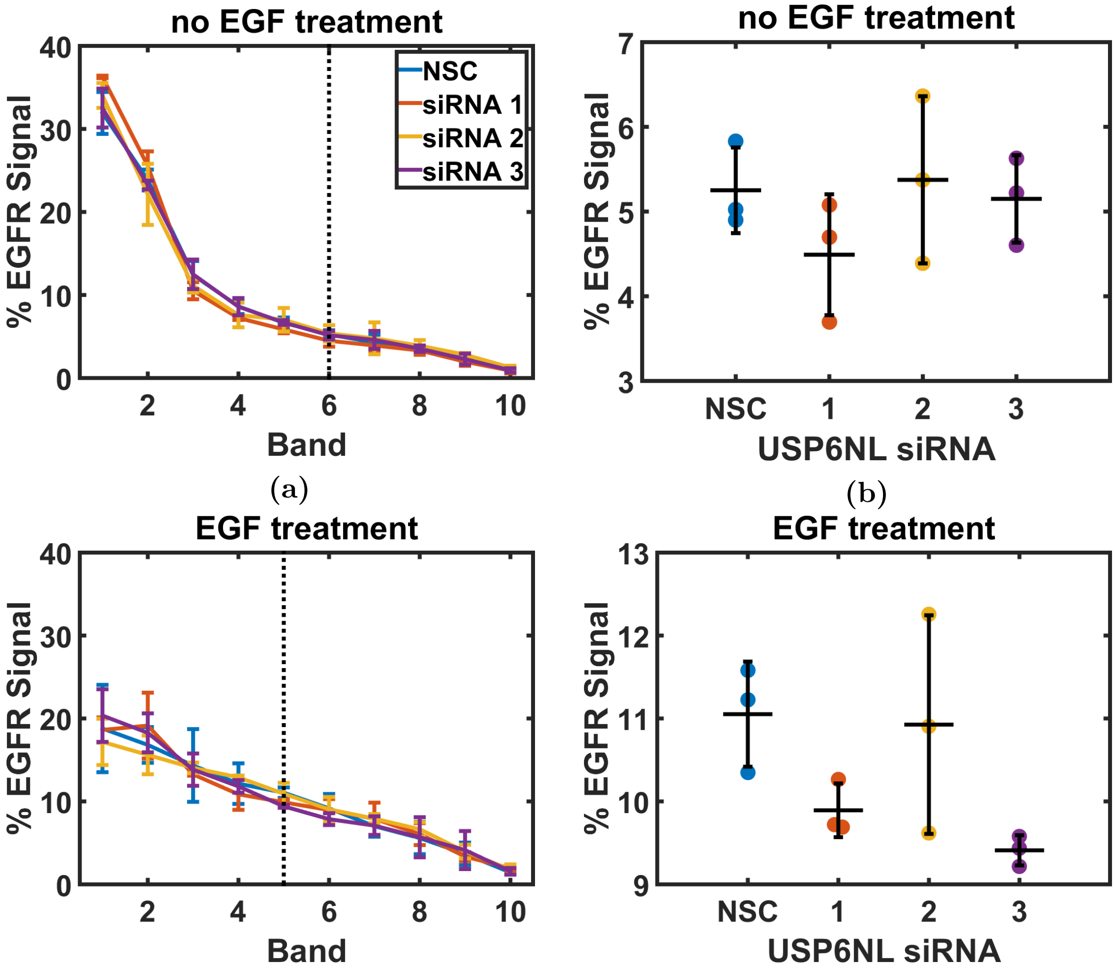

(a) (b) (c) (d)

Figure 4.11: USP6NL is a screen hit. (a) Mean percentage EGFR signal across all banded regions for siRNA targeting USP6NL (no EGF treatment). Band 1 is the outermost and band 10 is the innermost. Dotted line indicates the band chosen for further statistical analysis (band 6). Error bars are the standard deviation across the replicates. (b) Plot of individual replicate means for band 6. Central band represents the mean and the error bars are the standard deviation. Two sample t-tests returned p-values of 0.206, 0.856 and 0.820 for the three siRNA treatments respectively. The combined p-value for the gene was 0.695 (no EGF treatment) which was not significant after Benjamini-Hochberg correction. (c) Mean percentage EGFR signal across all banded regions for siRNA targeting USP6NL (EGF treated). (d) Plot of individual replicate means for band 5. Two sample t-tests returned p-values of 0.048, 0.889 and 0.013 for the three siRNA treatments respectively. The combined p-value for the gene was 0.020 (EGF treated) which was significant after Benjamini-Hochberg correction.

surement of sub-cellular receptor distribution is derived solely from the EGFR-EGFP signal. This is advantageous, as using additional fluorescent markers, for example nuclear and cytoplasm stains, increase the experimental complexity and cost of the screen.

Secondly, the band based measure of sub-cellular receptor distribution introduced (section 4.5.3) is able to quantify, not only changes to plasma membrane receptor levels, but also variation in the intracellular distribution. It is advantageous to choose as few measures as possible prior to analysing the screen data. This is because every measure used will double the number of hypotheses tested. If multiple hypothesis corrections are employed this will lead to loss of statistical power, and a corresponding increase in false negatives.

After blind and semi-automated selection of non-mitotic cells, the entire workflow, from pre-processing to statistical analysis and hit detection, is fully automated. The key advantage of an automated process is the removal of user bias and error often present in manually analysed data. It also facilitates the analysis of larger data-sets than are feasible with manual approaches. The experimental simplicity of the presented approach can enable the use of an siRNA screening approach, where lack of resources (equipment, budget and time) are often the limiting factor. However the described image analysis workflows could be applied to screens of arbitrary size without modification.

A potential avenue for future work could be the development of visual approaches for the presentation of screen results. Tools such as ScreenSifter allow for dynamic visualisation of siRNA screen results through protein-protein interaction analyses and gene ontology [255]. An alternative approach could be the visualisation of representative images from hit genes. These images could be annotated with the cellular segmentation and band positions and displayed alongside plots of the sub-cellular receptor distibution (figure 4.6). This would allow the researcher to visually inspect the raw data and correlate this to the outputs of the statistical analysis.

Before discussing the hits it is worth noting that, although the described statistical analysis for hit detection is thorough, it is not recommended to draw definite conclusions using only the results of this workflow. There are several reasons for this; firstly the significance level for hit detection was set to $p < 0.1$ (in non screening approaches $p < 0.05$ is conventional). Moreover, parametric hypothesis tests are used when the assumption of normality is not well validated. Finally, it is appropriate to perform follow up studies in live cells and in 3D. This is discussed in more detail in chapter 5. Note also that negative results (genes which are not hits) should not be assigned any meaning. This is the case in general when using hypothesis tests such at the Student's t test, but even more true here, where the knock-down efficiency of each siRNA is not verified.

4.7.1 Screen Hits in Context of the Literature

In this section the relevant literature for each of the screen hits is discussed. First note, all of the hits, with the exception of TBC1D5, are also identified as regulators of endocytosis and/or trafficking in at least one of three imaging based RNAi depletion screens (table 4.5) [3, 256, 2]. This overlap with similar screening approaches adds confidence to our protocol and the corresponding hits.

IQSEC1

IQSEC1 (also known as GEP100 and BRAG2) has well established GEF activity for ARF6. Recall, from section 2.3.2, that ARF6 is a member of the Ras super-family of small G-proteins and is heavily implicated in the regulation of endosomal trafficking [115]. Also recall from section 2.3.3 that IQSEC1, together with EGFR signalling, is implicated in the invasion of breast cancer [257]. Specifically, EGF induced, direct binding of EGFR to IQSEC1 triggers activation of ARF6 and its effector AMAP1 [123, 122]. Interestingly, Morishige *et al.* (2008) demonstrate that invasive activity of a breast cancer cell line is dependent on IQSEC1, but not any of the other 9 ARF6 GEFs expressed in cell line [122].

	Screen		
Gene	**Collinet *et al.***	**Kozik *et al.***	**Liberali *et al.***
IQSEC1	Hit	No hit	Not tested
VAV2	Hit	No hit	Hit ($\|z\| \geqslant 1$)
TBC1D10B	Hit	No hit	Not tested
TBC1D5	No hit	No hit	Not tested
USP6NL	Hit	No hit	Hit ($\|z\| \geqslant 1$)

Table 4.5: Comparison of hits with the results of other imaging based RNAi screens. The 5 hits from the screen presented in this chapter were compared to the results of three large scale screens. Collinet *et al.* (2010) performed a genome wide screen for regulators of EGFR and transferrin endocytosis and trafficking [3]. Kozik *et al.* (2013) performed a genome wide screen for regulators of clathrin mediated endocytosis [256]. Liberali *et al.* (2014) performed 13 parallel screens for regulators of endocytois and trafficking [2]. VAV2 depletion returned absolute z-scores ($|z|$) of greater than 1 for the EGF uptake (HeLa) and GM1 staining (A431) screens. Similarly, USP6NL depletion returned $|z| \geqslant 1$ for the EGF uptake (A431), EGF stimulated macropinocytosis (A431) and dextran uptake (A431) screens.

IQSEC1 is also implicated in the endocytosis and trafficking of $\beta 1$ integrins. Dunphy *et al.* (2006) demonstrate that knockdown of IQSEC1 leads to accumulation of integrins on the plasma membrane [258]. In a follow up study, Morvavec *et al.* (2012) show that IQSEC1 is also a GEF for ARF5 and ARF4 [259]. Moreover it is suggested that the IQSEC1 mediated activation of ARF5, not ARF6, is responsible for the selective inhibition of integrin endocytosis (transferrin uptake is unaffected). Also note IQSEC1 is shown to bind AP2 and clathrin, both key components of clathrin mediated endocytosis.

Clearly IQSEC1 is implicated heavily in both EGFR signalling and endocytic function [257, 260]. However, to the best of our knowledge, there is no study that demonstrates a perturbation to EGFR endocytosis or trafficking in response to IQSEC1 knockdown, hence this screen provides the first evidence for this. Due to the specificity of IQSEC1 for inhibition of integrin, but not transferrin endocytosis, and the strong links to cancer, it will be of particular interest to validate and further investigate this hit in future work.

VAV2

VAV2 is a GEF for the Rho sub-family of Ras small G-proteins (section 2.3.2). Recall from section 2.3.3 that VAV2 is implicated in several cancers [124, 104] and also EGFR signalling [125]. Also recall that Thalappilly *et al.* (2010) demonstrated VAV2 knockdown in HeLa cells increased the rate of, EGF induced, EGFR degradation and net internalisation [126]. Therefore this hit is in direct agreement with the literature and provides a degree of validation for our approach.

Interestingly Cowen *et al.* (2003) demonstrate a role for VAV2 in the regulation of endocytosis for Eph family receptor tyrosine kinases in neurons. This implies that VAV2 regulation of receptor trafficking is not restricted to EGFR [261]. Note also that VAV2 is known to form a complex with EGFR and its binding partner Grb2 [244].

Although Thalappilly *et al.* (2010) demonstrate colocalization of EGFR, VAV2 and rab5 in early endosomes, the analysis is not quantitative. Future work could further investigate the effect of VAV2 knockdown, or over-expression, on the trafficking of EGFR. This could be done quantifying the colocalization with various sub-endosome populations over time, post EGF treatment (chapter 5).

TBC1D10B

TBC1D10B (also known as EP164B) is a member of the EP164 family, which has GAP activity for both the Rab and Ras sub-families of Ras small G-proteins (section 2.3.2) [262]. Interestingly Negai *et al.* (2013) propose that the EP164 family predominantly deactivates Rab and Ras targets at the cellular periphery, implying roles in endocytosis and trafficking [262]. Fuchs *et al.* (2007) used a epi-fluorescence based microscopy screen to identify TBC1D10B as a regulator of Shiga toxic uptake in HeLa cells, but did not detect any change in EGF uptake [263]. The authors imply that EGF uptake is not modulated by TBC1D10B because they cannot detect any change with their measure, but such an assertion is unsubstantiated. Moreover the measure used is simply the percentage of cells which take up EGF. Therefore any variation to the endocytosis, or trafficking, of EGFR which does not completely block the EGF uptake is not considered.

TBC1D10B is a GAP for rab35 and also an effector for ARF6. Interestingly Chesneau *et al.* (2012) demonstrate that over-expression of mutated active (GTP bound) ARF6, or over-expression of mutated inactive (GDP bound) rab35, both inhibit recycling of transferrin receptor [264]. Moreover it is demonstrated that ARF6 negatively regulates rab35 activation through TBC1D10B. Allaire *et al.* (2013) suggest that the ability of ligand stimulated EGFR to activate ARF6, and regulate receptor recycling rate, is mediated through TBC1D10B dependent rab35 deactivation [117]. This screen provides evidence to support this hypothesis and provides an interesting platform for further research. Finally note that ARF6 hyper-activity and rab35 depletion is often observed in malignant tumours [123, 117].

TBC1D5

TBC1D5 is a rab GAP with known activity for rab7a. Seaman *et al.* (2009) demonstrated that rab7 dependent recruitment of retromer to endosomes is facilitated by TBC1D5 [265]. Moreover this TBC1D5 mediated recruitment is heavily implicated in endosomal sorting [266, 267, 268].

TBC1D5 is also implicated in the formulation and regulation of autophagosomes [269]. A recent study by Popovic and Dikic (2014) demonstrated that TBC1D5 interacts with both AP2 and clathrin. Moreover it was shown that clathrin mediated endocytosis and TBC1D5 were necessary for the trafficking of ATG9, a membrane spanning protein necessary for autophagy [270].

Importantly, rab7 is heavily implicated in EGFR trafficking [271, 272, 273]. However there is, to the best of our knowledge, no established (direct) link between TBC1D5 and abnormal RTK trafficking. Note TBC1D5 is a GAP for Rab7a and will therefore facilitate the hydrolysis of bound GTP and the deactivation of rab7 [265]. Reduced expression of TBC1D5 though siRNA treatment could lead to an increased level of active GTP bound Rab7. This could promote EGFR trafficking to lysosomes and receptor degradation, thus potentially decreasing the level of EGFR in the cellular interior [274]. The screen results indicate a decreased percentage of EGFR in the interior and in increase at, or near, the plasma membrane which correlates well with this hypothesis (figure 4.10). However this conclusion is speculative as compensatory responses and the biosynthetic secretory system could play an important role. Also note that TBC1D5 was not classified as either a strong, or mild, phenotype in the genome wide screen performed by Collinet *et al.* (2010) [3]. Clearly more work is needed to elucidate the role of TBC1D5 in EGFR trafficking.

USP6NL

USP6NL (also known as Rn-Tre) is a GAP, with activity for the Rab sub-family of Ras small G-proteins (section 2.3.2). Lanzetti *et al.* (2000) demonstrated that USP6NL is a GAP for rab5 and a binding partner for the EGFR substrate, Eps8 [275]. Recall, from section 2.3.2, that rab5 is heavily implicated in the endocytosis and trafficking of EGFR [276]. Moreover, it was shown that USP6NL over-expression inhibited internalisation of both EGFR and transferrin receptor. Interestingly, Esp8 was shown to be required for USP6NL mediated inhibition of EGFR, but not transferrin, internalisation. Martinu *et al.* (2002) demonstrated that the EGFR binding partner, Grb2, also binds USP6NL [277]. Moreover binding of USP6NL to Grb2 was required for, USP6NL dependent, inhibition of EGFR internalisation.

A recent study by Palamidessi *et al.* (2013) demonstrated that USP6NL inhibits internalisation of $\beta1$, but not $\beta2$, integrins. This was shown to have consequences for focal adhesion formation and cell migration, and provides further evidence that USP6NL can mediate endocytosis for specific receptors [278].

Finally, note that USP6NL has demonstrated activity for other rabs including rab41

[279], and also functions as a rab5 effector to mediate actin remodelling through RTK signalling [280]. In the context of this screen, the hit is further evidence that USP6NL can regulate EGFR trafficking.

4.8 Conclusion

In this chapter 16 GEFs and GAPs were selected from the results of a SILAC proteomics screen. The expression levels for each of the 16 genes was depleted using a siRNA library and screened with confocal microscopy in a HeLa cell line, expressing EGFR-EGFP. This was done both with and without EGF treatment. Using only the EGFR-EGFP signal, cells were segmented, and a novel measure was used to quantify the sub-cellular distribution of EGFR. Using an automated protocol for hit detection, 5 of the GEFs and GAPs were identify as hits, demonstrating abnormally distributed EGFR post EGF treatment. There we no hits for the untreated data-set. The 5 hits from the screen were IQSEC1, VAV2, TBC1D14, TBC1D5 and USP6NL. Either over-expression, or knockdown, of VAV2 and USP6NL are known to perturb EGFR internalisation post ligand treatment so this screen provides further evidence to support these studies [126, 276]. The role of IQSEC1, TBC1D14 and TBC1D5 in the regulation of EGFR trafficking isn't as well defined. This is discussed in detail in section 4.7.1. All of hits present interesting opportunities for future research. Due to time constraints follow up studies for screen hits were not carried out. However the protocols defined in the next chapter are ideally suited to do this.

In summary, we have presented a microscopy based platform to screen for regulators of receptor trafficking. The presented approach is experimentally simple, and the analysis is fully automated and robust. It is well suited to secondary screening of larger primary (proteomics or microscopy based) screens.

Chapter 5

Workflows to Quantify Receptor Trafficking in 4D

5.1 Introduction

Many studies employ image analysis workflows to quantify the endocytosis and trafficking of cellular receptors using live cell time-lapse microscopy data. In this chapter novel protocols are introduced to do this for 4D data. First, some of the approaches used in the literature are discussed. This is done to highlight both good and bad practice.

Live cell time-lapse microscopy can be performed in either 2, or 3, spatial dimensions. For example, Fortian and Sorkin (2014) used spinning disk confocal microscopy to quantify EGFR internalisation and colocalization with Grb2 in 4D (3D time-lapse) [6]. Conversely, Yamazaki *et al.* (2002) used 2D time-lapse data to quantify EGFR internalisation and colocalization with Grb2 [281]. 3D time-lapse data is inherently superior as the spatio-temporal dynamics of receptor internalisation and colocalization can be measured for the entire cellular volume. With 2D time-lapse data, only a single axial slice is recorded. As the spatial distribution of the receptor and/or endosomes can vary dramatically through the cellular volume, 2D acquisition can lead to high levels of variation in the data and/or biased conclusions. For example, receptor dynamics near the membrane-coverslip interface can be dramatically different to those for a plane which dissects the nucleus (figure 5.13). This variation can be minimised by an unbiased and consistent procedure for selection of the axial position. For example Hsu *et al.* (2011) always choose the middle nuclear plane [282], whereas in chapter 4 a set distance from the coverslip is selected. Note computer aided microscopy (CAM) scripts can be used to automate plane selection [283]. However, in many cases, no plane selection criteria are used and a 3D time-lapse approach will always be superior.

Time-lapse microscopy can be used to measure changes in receptor levels at the membrane and/or cellular interior over time. To do this, Perera *et al.* (2007) manually drew regions of interest (ROIs) corresponding to the membrane (rectangular or circular) and calculated the mean pixel intensity within those regions [284]. This typical approach has several important limitations; firstly, the manual selection of ROIs introduces (conscious or un-conscious) user bias. Secondly, only a very small percentage of the plasma membrane is contained within the ROIs, this can lead to sampling errors. Finally, the mean intensity is an inappropriate measure to use in this procedure. To see this, note that the ROIs will contain pixels originating from both *signal* and *background.* Without isolating the signal containing pixels, the presence of background pixels in the ROI will distort the mean.

Holleran *et al.* (2013) use ROIs for the peri-nuclear region (and the whole cell) to quantify internalisation [285]. The ratio of peri-nuclear signal to total cellular signal is recorded over time. It isn't explicitly stated how these ROIs where generated, but manual selection is implied. Moreover no pre-processing to remove background signal or noise is used.

Fortian and Sorkin (2014) used background subtraction, and a 3D edge based method, to segment cells using Grb2-YFP signal [6]. This was followed by image erosion (5 pixels) to identify the interior (and membrane). Finally, the percentage of the total cellular Grb2 signal localised to membrane, was calculated over time. This excellent approach has strong similarities to the methods presented in this chapter, but we note it was developed independently. The main limitation of their approach is that insufficient technical details are provided to reproduce and test the protocols.

Fluorescent probes sensitive to pH can also be used to quantify receptor internalisation. Adie *et al.* (2002) introduce a novel probe which only fluoresces under acidic conditions. This probe is tagged to G protein coupled receptors and is used to quantify internalisation into acidic endosomes [286]. This is a powerful approach, however it requires the modification of receptors to incorporate epitote tags, preventing the use of existing fluorescent constructs.

In section 5.5 protocols for quantifying the spatio-temporal colocalization between receptors and sub-endosome populations are introduced. Section 2.6 provides an introduction to common methods used to measure colocalization.

It is worth noting that colocalization is often not quantified when studying receptor trafficking in endosomes [77, 87]. Miaczynska *et al.* (2004) simply use the abundance of *yellow* pixels as proof of colocalization [88]. The number (and definition) of yellow pixels required for colocalization is chosen arbitrarily to suit the authors' conclusions, and is an example of particularly bad practice.

The Pearson's coefficient, the Manders' coefficient and the Manders' overlap coefficients are typically used for quantification (section 2.6.1) [95, 78, 287]. However, it is unusual for more than one measure to be used or the choice of measure to be justified. ROIs are typically drawn manually and do not account for the all of the biologically relevant signal. Moreover pre-processing, signal isolation and statistical significance are often not considered.

5.2 Chapter Aims

The aims for this chapter can be summarised as follows:

1. Implement the 4D level set methods from chapter 3 to identify regions of interest (the plasma membrane and nucleus) for internalisation and colocalization analysis.
2. Develop automated protocols to quantify sub-cellular receptor distribution in response to ligand (for 4D data).
3. Develop automated protocols to quantify receptor colocalization with sub-endosome populations (for 4D data).
4. Discuss and develop appropriate techniques for the visualisation of sub-cellular colocalization.
5. Validate all approaches on a real biological system. Explicitly, pertubation of EGFR trafficking, and colocalization with rab5 positive endosomes, in the presence of dynasore (dynamin inhibitor), AG1478 (EGFR kinase inhibitor) and dasatinib, should be quantified.

The aim is to develop automated, justified and robust protocols. Image pre-processing (noise removal and background subtraction) and statistical testing should be considered. Importantly, the steps in all protocols should be explained in sufficient detail as to be reproducible. As already mentioned this is often not the case in the literature. This will provide an important toolbox for the community, facilitating the use of state of the art image analysis workflows to quantity receptor trafficking.

5.3 Cellular and Nuclear Segmentation

The workflows presented in this chapter for quantifying the sub-cellular distribution of receptor (section 5.5), and colocalization with sub-endosome populations (section 5.4), both require accurate and reliable cellular segmentation protocols. It is also advantageous to segment the nucelus such that a ROI can be defined which includes the plasma membrane and cytoplasm, but excludes the nucleus. This is done because the vast majority of receptor is either localized at the plasma membrane, or internalised in endosomal structures (including lysosomes) within the cytoplasm (figure 2.3).

Note that for all the experiments presented in this chapter, HeLa cells were transfected with both EGFR-EGFP and rab5-mRFP. Recall, from sections 2.2.2 and 2.3.2, that rab5 is an established marker for a sub-population of early endosomes, and heavily implicated in the regulation of EGFR signalling and trafficking. Ideally, segmentation of both the plasma membrane and the nucleus should be performed with only these two labels (section 5.7).

To segment the plasma membrane a 4D edge based DRLSE approach, with a constant volume term, was used (Matlab) (equations 3.6.9 and 3.7.1). This was done using only the EGFR-EGFP signal. This approach was extensively validated (figure 3.10), and demonstrated superior performance over the other methods presented, in section 3.7 (figure 3.13). Moreover it was shown to be superior to equivalent 2D and 3D segmentation protocols. Table 3.4 lists the parameters used to implement to the DRLSE segmentation. Note the edge constant was fixed at $\lambda = 8$, and the temporal constraint constant was fixed at $c_0 = 1$.

To segment the nucleus, information from both the EGFR-EGFP, and rab5-mRFP channels were combined, but importantly no nuclear stain was used. The strategy is to identify the nuclear region by the absence of background signal in the EGFR and rab5 channels (figure 5.1c). Such an approach is clearly more difficult to implement than segmentation with a nuclear stain, and will require a powerful and reliable segmentation protocol. To do this, 4D region based DRLSE approaches were tested (equation 3.6.10). Region based approaches were chosen over edge based approaches as the nuclear boundary is often not well defined, hence edge based level set evolution will tend to bleed-through into the cytoplasm.

To accurately segment the nucleus for each cell it is necessary to initialise the level set function (LSF) as a contour entirely contained within the nucleus. The LSF will then evolve, expanding the segmentation contour, to refine and locate the nuclear boundary. The protocol used to find an initial segmentation estimate of the nucleus was K-means based, and is similar to those used for the cellular segmentation as described in sections 3.6.6 and 4.5.2. The details are as follows and are illustrated in figure 5.1;

1. The 3D data for each time-point was de-noised with a PURE-LET scheme (section 2.5.4) [166]. Parameters were estimated automatically from the image. MIJ was used to run ImageJ within Matlab and keep the workflow fully automated [251].

2. The data was further processed with 3D Gaussian blurring (section 2.5.1) (radius $= 200nm$). This was done to smooth features such as endosomes, and the membrane localised receptors, as these features are of no interest for nuclear segmentation.

3. Multi-variate K-means clustering was performed using both the EGFR and rab5 channels. Note only pixels within the cellular segmentation (after 3D erosion with spherical structural element of $1\mu m$ radius, and exclusion of extremal planes) were considered. The cluster with the lowest mean (averaged across both channels) was selected. This is done under the assumption that, within the nucleus, the background fluorescence will be low in both channels. A large number of clusters (15) was used to ensure that the estimate is inside the nucleus. Note however, that the estimate is not particularly sensitive to the number of clusters.

4. Finally, the selected cluster was processed, by erosion, filling and dilation ($1\mu m$ radius). The largest single object (by volume, 4-connectivity in 3D) in every time-point was then selected and used to initialise the 4D LSF as a binary step function

(section 3.6.4).

To test the accuracy of both the initial and level set based segmentation protocols, the nucleus was manually segmented for 10 4D movies. This was done using an overlay of the fluorescent (EGFR-EGFP and rab5-mRFP) and bright-field channels, within a semi-automated custom Matlab script. The manual segmentation was performed for every time-point (4 total) and every 3rd axial slice. The performance of each segmentation algorithm was quantified, with respect to the manual segmentation, using the Jaccard index (equation 3.6.13). The region based 4D DRLSE approach was first tested without a volume constraint, and with varying region constant, β. Note, the data term, I, from equation 3.6.10 was constructed as the sum of the two fluorescent channels. The results of this analysis are shown in figure 5.2a. Note that for all β, the 4D DRLSE approach demonstrated higher mean performance than the K-Means estimate. A constant volume temporal constraint was then introduced and tested (figure 5.2b) (equation 3.7.1). There was no significant improvement in (or loss of) maximal performance with the introduction of the constant volume constraint. Despite this, we choose to use the restraint as it provides greater capacity for recovery if the segmentation protocol under-performs for a single time-point. Note, from figure 5.2c, that there is an outlier for which the initial segmentation estimate is poor (Jaccard index < 0.4). Importantly, the 4D DRLSE protocol recovers the segmentation performance for this movie (both with, and without a temporal constraint).

The maximal segmentation performance was obtained, with a constant volume constraint, when $\beta = 40$ and $c_0 = 0.8$. Therefore these values were used for the nuclear segmentation in the remainder of this chapter. A full list of segmentation parameters for the 4D DRLSE nuclear segmentation is listed in table 5.1. With these parameters a mean Jaccard index of 0.82 ± 0.07 was calculated across the manually annotated data. We consider this to be impressive, considering there is no nuclear stain, and sufficiently

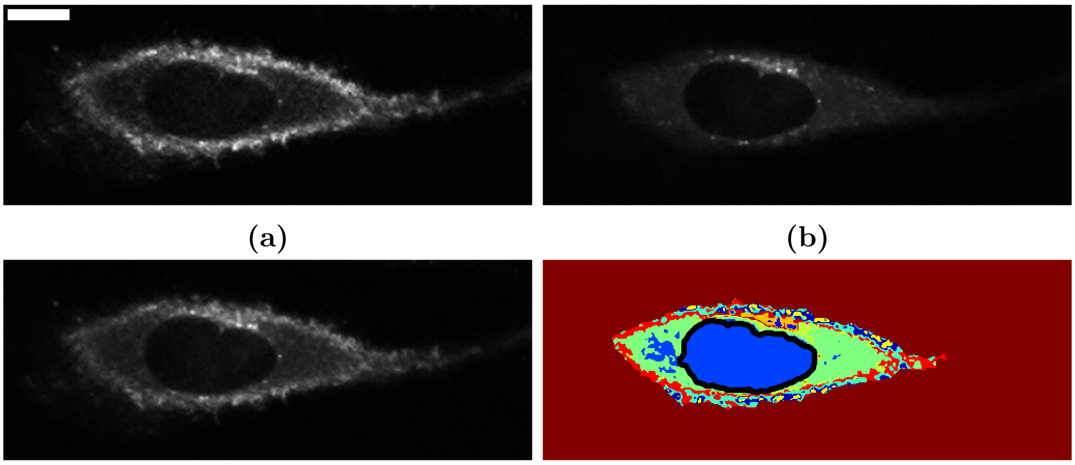

(a) (b) (c) (d)

Figure 5.1: Initial estimate for the label free nuclear segmentation with a K-means clustering approach. (a)-(b) For each time-point, de-noised (PURE-LET scheme) data for both the EGFR-EGFP and rab5-mRFP channels were blurred with a 3D Gaussian profile (radius = $200nm$). Scale bar set at $10\mu m$. (c) Data from both channels summed together. Note the location of the nucleus is visible from the lack of auto/background fluorescence. (d) K-means clustering (15 clusters, each cluster represented by a different colour) was performed in 3D across both channels simultaneously and for each time point separately. Note, only pixels within the cellular segmentation were clustered. The cluster with the lowest mean was used to construct the initial estimate. Post-processing by erosion, filling and dilation ($1\mu m$ radius) was performed to produce the final estimate (black contour).

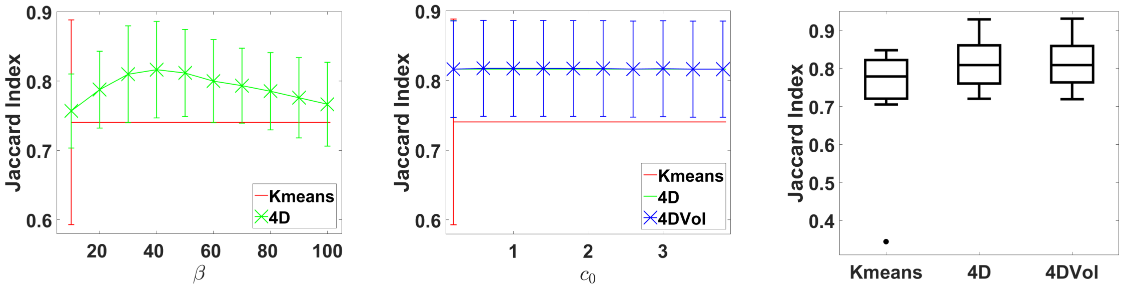

(a) **(b)** **(c)**

Figure 5.2: Validation of the 4D region based DRLSE nuclear segmentation protocol. (a) Mean performance of the K-means based initialisation protocol (red) and 4D region based DRLSE algorithm (green) across all 10 manually annotated movies, with varying values for the region constant, β. Error bars are given by the standard deviation. The mean Jaccard index for the K-means initialisation was 0.74 ± 0.15. The maximal (mean) Jaccard index for 4D region based level set segmentation was 0.82 ± 0.07 ($\beta = 40$). (c) The introduction of a constant volume term to the level set energy function was tested for $\beta = 40$, and varying values for the constant, c_0. The maximal (mean) Jaccard index for 4D region based level set segmentation with a constant volume constraint was 0.82 ± 0.07 ($c_0 = 0.8$). (d) Summary box-plot, showing the performance of the initialisation and the maximal performance of the 4D region based DRLSE, with and without a constant volume constraint term. Note that Friedman's test returned $p = 0.07$, hence we cannot conclude that there is a statistically significant difference in performance between the algorithms. Central mark on box-plot represents the median, and the edges of the box are the 25th and 75th percentiles. Outliers are shown separately.

Parameter	Value	Reference
Constant force term; c	0	equation 3.6.9 & 3.6.10
Constant volume factor; c_0	0.8	equation 3.7.1
Lateral scaling factors; Δx, Δy	1	section 3.6.2
Axial scaling factor; Δz	variable	equation 3.6.7
Temporal scaling factor; Δt	variable	figure 3.4
Update step; $\Delta\tau$	1	equation 3.6.1
DRLSE factor; μ	variable	equation 3.6.4
Binary step size; h	2	equation 3.6.4
Dirac-delta function width; α	1.5	equation 3.6.12
Stopping constant; s	0.01%	algorithm 1
Maximum number of iterations	50	section 3.6.1
Smoothing term; λ	1	equations 3.6.9 & 3.6.10
Region term; β	40	equation 3.6.10

Table 5.1: Segmentation parameters for region based 4D DRLSE nuclear segmentation. Note a constant volume constraint was used.

accurate for the analysis workflows presented.

It can be informative to visualise the segmentation results of both the plasma membrane, and nucleus using 3D surface rendering (Matlab). In figure 5.3 this is done for a representative cell, which has been treated with $2ng/ml$ EGF and imaged for 30 minutes. Note, over this time-period, neither the shape or volume of both the cell and nucleus change significantly. This demonstrates why 4D level set approaches and constant volume temporal constraints are well suited to this application.

5.4 Workflow to Quantify the Sub-cellular Receptor Distribution

In this section, a band based analysis workflow to quantify the sub-cellular distribution of EGFR is defined. This can thought of as an extension, to 3D time-lapse data, of the analysis protocols described in section 4.5.3.

In this chapter the data-set consists of live cell confocal microscopy movies (3D time-lapse) of HeLa cells, expressing both EGFR-EGFP and rab5-mRFP. Note low EGF con-

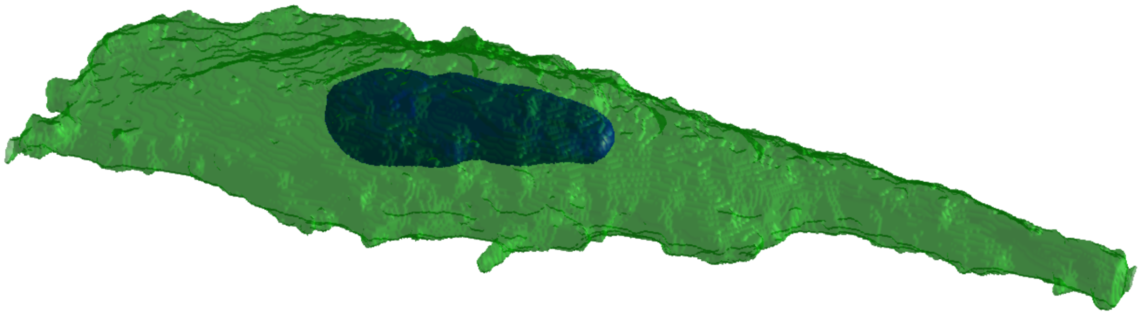

(a) pre EGF treatment

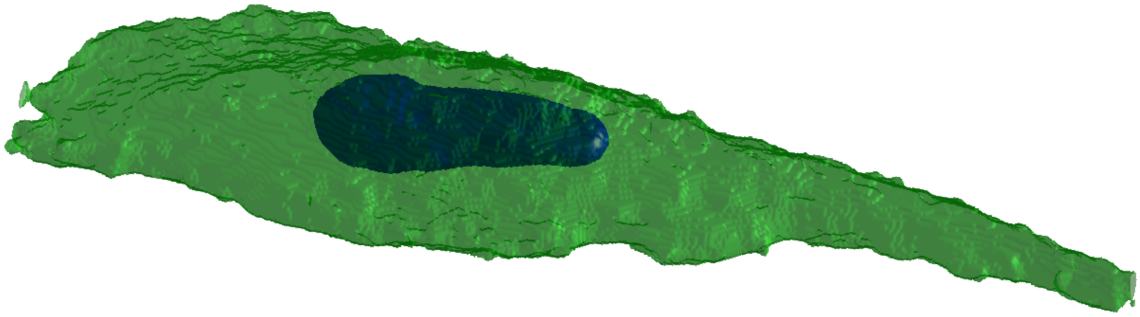

(b) 10 minutes post EGF treatment

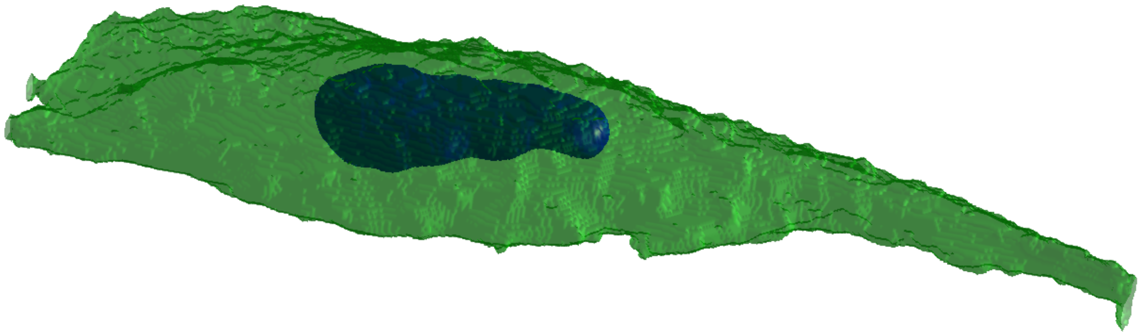

(c) 20 minutes post EGF treatment

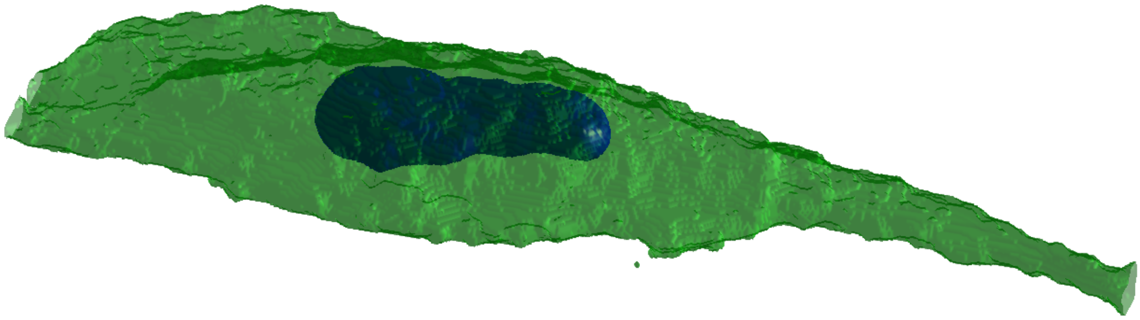

(d) 30 minutes post EGF treatment

Figure 5.3: Segmentation results can be visualised in 3D by surface rendering. Representative HeLa cell which has been treated with $2ng/ml$ EGF and imaged for 30 minutes (confocal microscopy). The cellular segmentation is shown in green the nuclear in blue. Note the surface rendering of the cellular segmentation is partially transparent.

centration ($2ng/ml$) was used to stimulate the cells, as opposed to the $100ng/ml$ used in chapter 4. This is done to better represent physiological EGF levels, and to demonstrate that the proposed workflows are capable of detecting perturbations, to endocytosis and receptor trafficking, under such conditions. The cells were treated with EGF immediately prior to imaging. This was done in the presence of one of three drug treatments; AG1478, dynasore and dasatinib (and a DMSO treated control). Briefly, AG1478 is a well established EGFR kinase inhibitor [288]. Treatment with AG148 has been shown to inhibit EGF internalisation [289], but recent studies suggest that EGFR kinase activity is not necessary for endocytosis [290]. These contradictory reports are discussed, alongside the results presented in this chapter, in section 5.7. Dynasore is a small molecule inhibitor of dynamin, a key component of endocytosis (section 2.2.1). Note, dynasore treatment has been shown to inhibit dynamin dependent endocytosis of EGFR [291, 292]. Finally, dasatinib is an inhibitor of both Src family and Abl kinases [293], and is heavily implicated in EGFR signalling [294, 295].

The raw-data was pre-processed by semi-automated blind selection of cells (Matlab), followed by de-noising (PURE-LET, parameters estimated from image). The de-noised data was then further processed with rolling ball background subtraction. This was implemented in 3D using a spherical structural element, with radius $1\mu m$ (features larger than this considered background). These processing steps were applied to both channels. Finally, the plasma membrane and nucleus of each cell were segmented with the 4D level set protocols described in section 5.3.

The cellular interior (the area contained by the membrane segmentation, excluding the nuclear region) of each cell was split into 10 banded regions (figure 5.4). This was done based on either distance from the membrane, or distance from the nucleus. Note, distance transforms were calculated in 3D, and weighted with the axial and lateral dimensions of each voxel. Having split the ROI into banded sub-regions, the percentage of each cell's

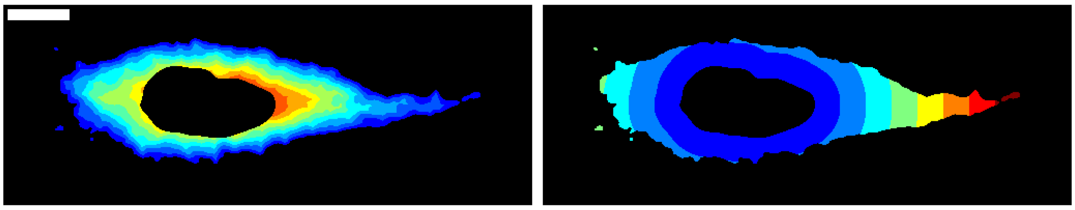

(a) (b)

Figure 5.4: Band based analysis for sub-cellular receptor distribution in 4D. After preprocessing (de-noising and background subtraction) the cellular region, excluding the nucleus), is binned into 10 bands based on either distance from (a) the cellular membrane or (b) the nucleus. The process is performed fully in 3D. The percentage of the cell's total EGFR-EGFP signal in each band can be calculated, and used to characterise the sub-cellular receptor distribution over time.

total EGFR signal in each band, at each time-point, was calculated. This intensity was normalised, for each cell, using the distribution of the receptor signal at the first time-point. Specifically, for every time-point (and every band) the percentage EGFR signal at the first time-point (for the same cell and band) was subtracted.

Figures 5.5a and 5.6a show the results of the described band based analysis, using distance from the plasma membrane and the nucleus respectively. Note that the data-set consists of at least 10 cells per treatment. Individual cells are considered technical replicates for the purpose of statistical testing. This is valid because only a single cell (per treatment) was acquired for each experiment (and cell passage). It is desirable to design a statistical testing protocol to determine if the variation in sub-cellular distribution of receptor, as measured by the band analysis, is statistically significant relative to the control. To do this, parametric analysis of variance tests, such as a two way repeated measures ANOVA, were considered. However, when the distributions consist of single cell measurements, the assumptions of normality and absence of outliers do not hold. Non-parametric tests equivalent to two-way ANOVA are not well established. Therefore, for each cell, the normalised percentage EGFR signal of each treatment was averaged over time and all bands (figures 5.5b and 5.6b). This gives a measure of each cell's total change to the sub-cellular receptor distribution in response to ligand. A non-parametric Kruskal-Wallis one-way analysis of variance was used to determine if there were significant differences between treatments [296]. This was followed by post-hoc testing of each treatment, relative to the control, with the Mann-Whitney U test [297]. Finally, p-values from the pairwise corrections were corrected for multiple comparisons with the Bonferroni method ($n = 3$) (equation 3.6.14).

With the described statistical analysis workflow, and when bands are defined by the distance from the plasma membrane, the overall effect of EGF stimulated EGFR trafficking is statistically significant when treated with either AG1478 or dynasore (figure 5.5b). When the bands are defined by the distance from the nucleus only the dynasore treatment is significant (figure 5.6b).

Note the measured perturbation to EGFR trafficking for each treatment, in each band, can be seen in figures 5.5a and 5.6a. However, these plots contain a lot of information which can be difficult to interpret. Therefore, it can be instructive to reformulate the information contained within these plots using heat-maps (figures 5.7 and 5.8). To do this, each band, b, and each time-point, t, was assigned a value, $H(b,t)$, and a position on the heat-map. This value was defined as the (mean) difference of the normalised percentage EGFR signals between the treatment, S_T, and control, S_C, divided by the error in this measurement;

$$H(b,t) = \frac{S_T(b,t) - S_C(b,t)}{\sqrt{\sigma_T(b,t)^2 + \sigma_C(b,t)^2}} \tag{5.4.1}$$

where $\sigma_T(b,t)$ and $\sigma_C(b,t)$ are the standard deviations for the mean normalised percentage EGFR signals of the treatment and control respectively. Note the absolute value of the heat-map, $|H(b,t)|$, gives an indication of the effect size relative to the error in the effect. Therefore, the larger $|H(b,t)|$, the greater the confidence that the effect is real and not an artefact of the data. The sign of $H(b,t)$ determines if the effect is positive or

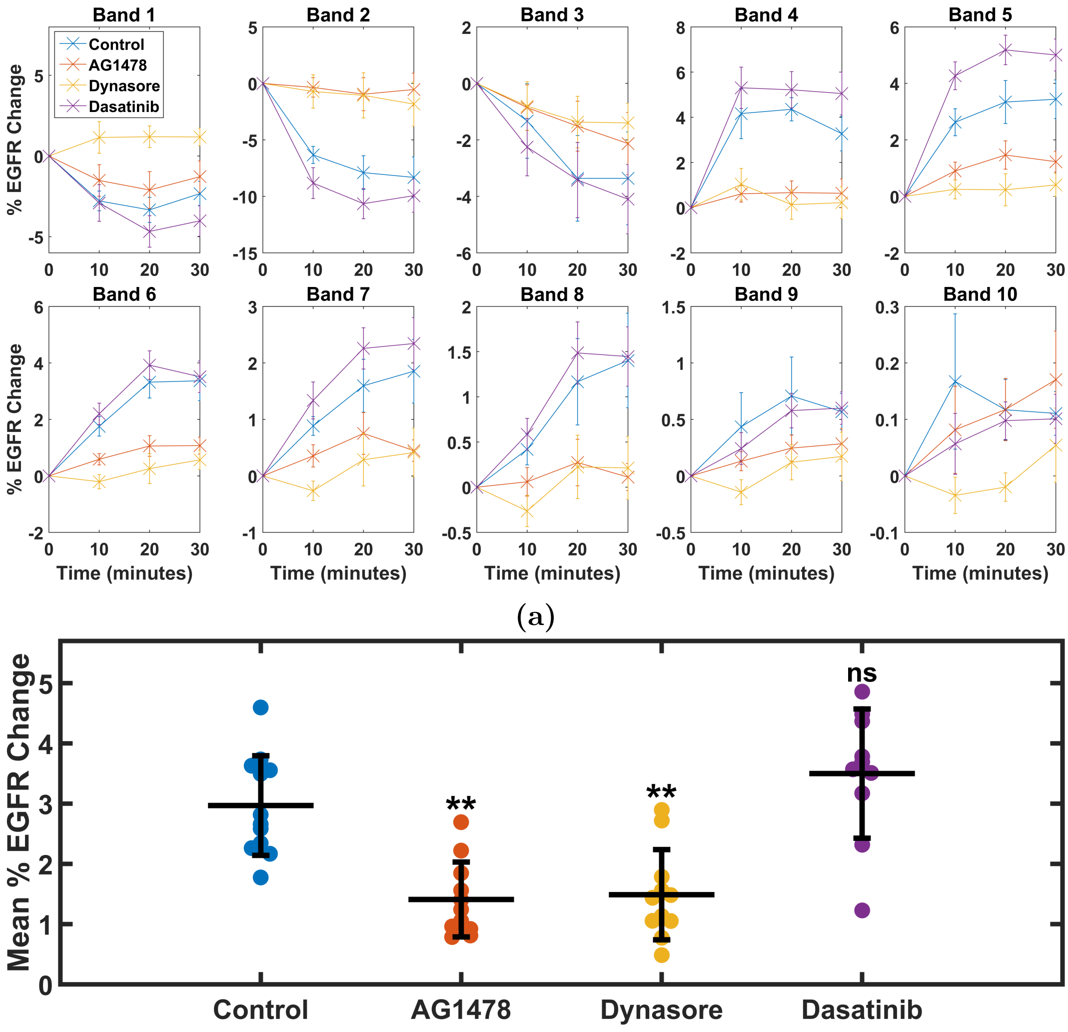

(a)

(b)

Figure 5.5: Band based analysis results (membrane distance). (a) Distance from the cellular membrane was used to separate each cell into 10 banded regions. The mean percentage EGFR signal (normalised for each cell by subtracting the percentage pre-EGF treatment) in each band, over time, and post $2ng/ml$ EGF treatment is shown. This analysis was performed for a DMSO control and 3 drug treatments; AG1478, dynasore and dasatinib. There are at least 10 cells per treatment, and errors bars are given by the standard error. (b) Plot of the mean change in normalised percentage EGFR signal, across all bands and time-points, for each treatment. A Kruskal-Wallis one-way analysis of variance returned, $p = 3 \times 10^{-5}$. This indicates that there are significant differences between treatments. Post-hoc testing of all treatments relative to the control, by the Mann-Whitney U test (corrected by the Bonferroni method), returned $p = 0.002$, $p = 0.005$ and $p = 0.5$ for the AG1478, dynasore and dasatinib treatments respectively. Central band represents the mean, and the error bars are the standard deviation.

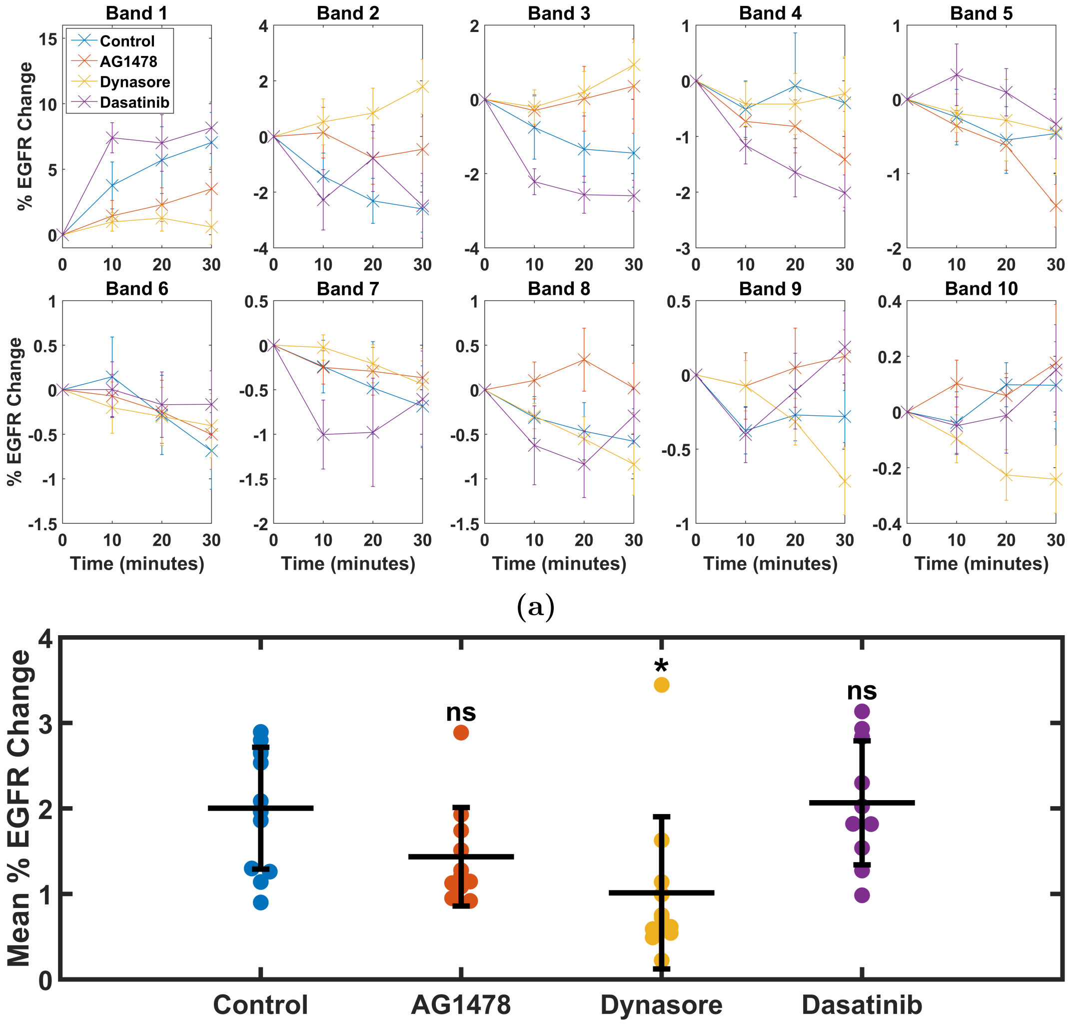

(a)

(b)

Figure 5.6: Band based analysis results (nuclear distance). (a) Distance from the nucleus was used to separate each cell into 10 banded regions. The mean percentage EGFR signal (normalised for each cell by subtracting the percentage pre-EGF treatment) in each band, over time, and post $2ng/ml$ EGF treatment is shown. This analysis was performed for a DMSO control and 3 drug treatments; AG1478, dynasore and dasatinib. There are at least 10 cells per treatment, and errors bars are given by the standard error. (b) Plot of the mean change in normalised percentage EGFR signal, across all bands and time-points, for each treatment. A Kruskal-Wallis one-way analysis of variance returned, $p = 0.002$. This indicates that there are significant differences between treatments. Post-hoc testing of all treatments relative to the control, by the Mann-Whitney U test (corrected by the Bonferroni method), returned $p = 0.2$, $p = 0.01$ and $p = 2.4$ for the AG1478, dynasore and dasatinib treatments respectively. Central band represents the mean, and the error bars are the standard deviation.

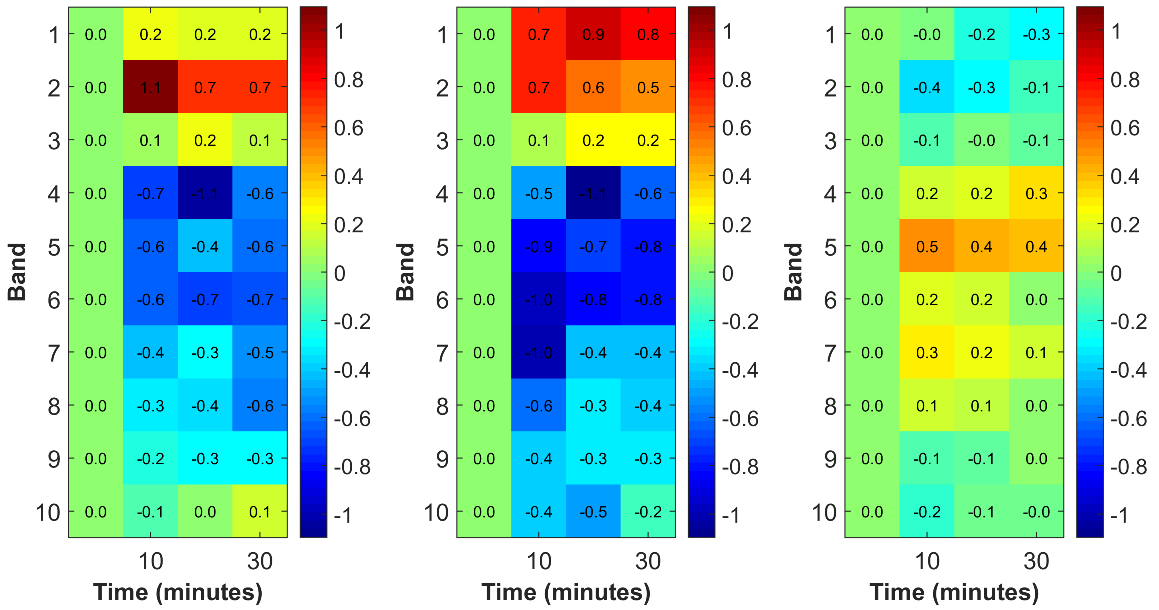

(a) AG1478 **(b)** Dynasore **(c)** Dasatinib

Figure 5.7: Heat map representation of band analysis (membrane distance). Cells were treated with either (a) AG1478, (b) dynasore or (c) dasatinib and compared to a DMSO control. The value of the heat map at a given band, and time-point, was calculated by the (mean) difference in normalised percentage EGFR signal between the control and drug treatments, divided by the associated error (sum of standard deviations).

negative relative to the control.

To conclude, a 4D band based analysis protocol has been presented to quantify changes in receptor distribution, over time and post ligand treatment. The use of heat-maps to visualise perturbations in receptor trafficking with different treatments has been introduced. The implications of both the methods and analysis results presented are discussed, in the context of relevant literature, in section 5.7.

5.5 Workflow to Quantify Colocalization

In this section a workflow is presented to quantify colocalization, between receptor and sub-endosome populations, for 4D data. Three drug treatments are used to perturb the system, and strategies to identify statistically significant changes to the ligand induced colocalization response are discussed. Note that the data was pre-processed, as in the

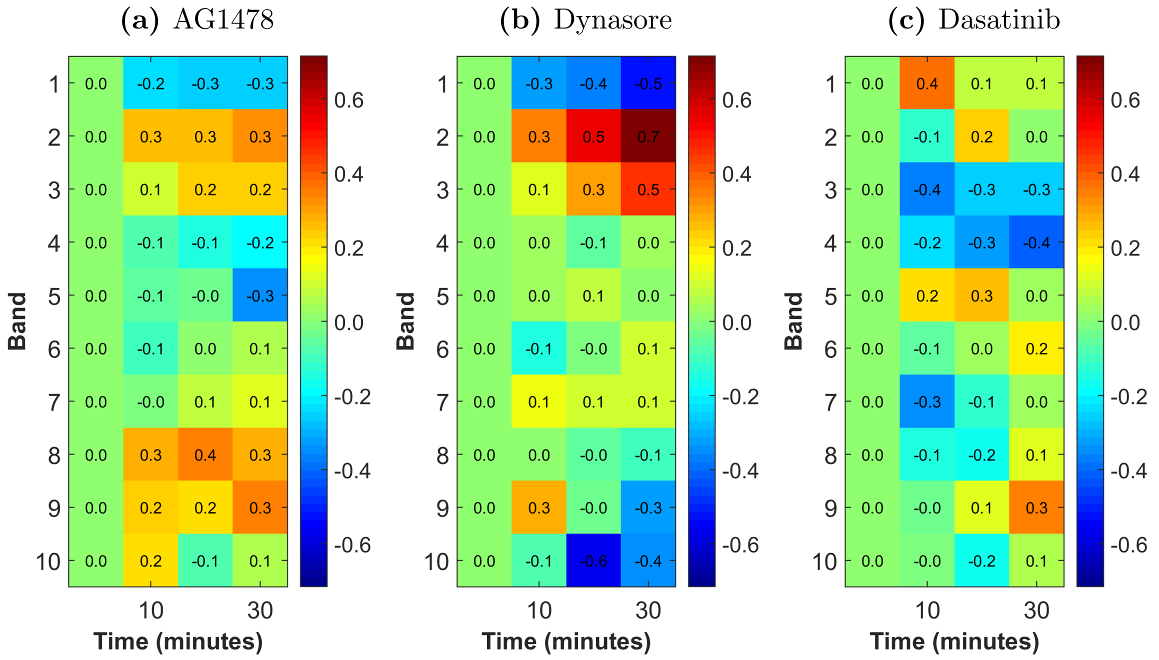

Figure 5.8: Heat map representation of band analysis (nuclear distance). Cells were treated with either (a) AG1478, (b) dynasore or (c) dasatinib and compared to a DMSO control. The value of the heat map at a given band, and time-point, was calculated by the (mean) difference in normalised percentage EGFR signal between the control and drug treatments, divided by the associated error (sum of standard deviations).

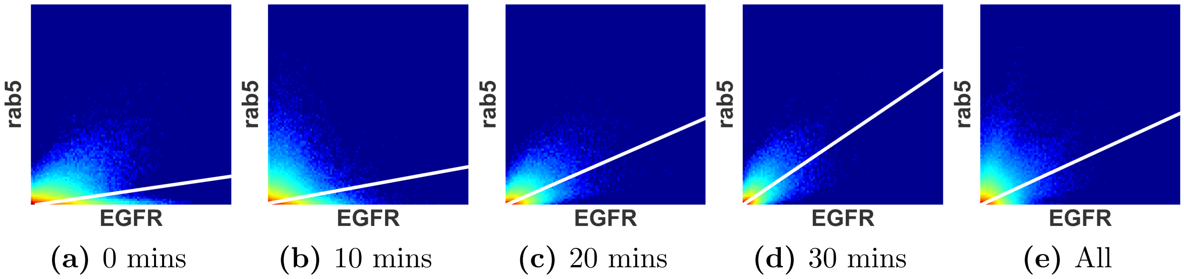

(a) 0 mins **(b)** 10 mins **(c)** 20 mins **(d)** 30 mins **(e)** All

Figure 5.9: Joint histograms to visualise colocalization. (a)-(d) Joint histograms, for a single representative cell, showing the correlation between EGFR and rab5, at various time-points, post $2ng/ml$ EGF stimulation. Only the region inside the cellular segmentation, and outside the nucleus, was included in the plots. (e) Joint histogram for the combined data across all time-points. A linear fit (white) is shown for all plots. Note this fit only well represents the data for the later time-points, where the colocalized voxels dominate the distribution. The data was pre-processed by PURE-LET de-noising and rolling ball background subtraction.

previous section, by de-noising and background subtraction. Similarly, cellular and nuclear segmentation was performed using the workflows introduced in section 5.3. These segmentation protocols are a vital component of the workflows presented in this section.

Recall, from section 2.6, that the use of colour merges to visualise colocalization is uninformative and commonly miss-leading. Therefore, no *representative* colour merges of single images are presented in this work. Instead the colocalization is visualised using joint histograms of the data (figure 5.9). This approach is particularly useful for 4D data, as plots for each time-point can be used to visualise the change in correlation over time (figure 5.9a - 5.9d). Note, for the representative movie shown, there is an increase in the correlation between the two channels post EGF treatment. This is indicative of in increase in colocalization. In a joint histogram approach all the data, from each point, is used, as opposed to just the single 2D plane shown in colour merges. Note only pixels from inside the ROI (inside the cellular segmentation, excluding the nucleus) were included in the plots.

In this work, pixel based (section 2.6.1), rather than object based, colocalization measures are used (section 2.6.2). This is done because the resolution (and sampling rate) of the data is such that overlap based measures are sufficient to quantify the endosomal colocalization. Moreover, pixel based measures are simpler to apply and interpret.

Recall, from section 2.6.1, that we consider it best practice to calculate both the Manders' coefficients, and the Pearson coefficient. To calculate the Manders' coefficients it is necessary to isolate the biologically relevant signal. This is also considered best practice for the Pearson coefficient, where only pixels containing isolated signal from both channels should be considered [8]. Also recall, the standard approach for signal isolation in colocalization analysis is Costes' thresholding (figure 2.12) [182]. Figures 5.10a and 5.10b show representative, pre-processed, images (from a 4D movie) for the EGFR-EGFP and rab5-mRFP channels respectively. Figures 5.10c and 5.10d show the corresponding binary images after Costes' thresholding (only pixels within the ROI were included in the calculations), with a tolerance threshold of 0.01 for the Pearson coefficient. Note the Costes' approach has over-segmented the data, and failed to isolate the biologically relevant signal. The reasons for this are discussed in detail in section 5.7, but note a different approach is clearly required.

The pre-processing of the data (de-noising and background subtraction) enabled the use of a reasonably simple, and automated, global thresholding approach. A minimum cross entropy (MCE) approach, as described by Li and Lee (1993), was found to accurately isolate the endosomes and membrane (figures 5.10e and 5.10f) [298, 299]. In a MCE approach, the cross entropy, D, between two distributions, q and p, is defined such that;

$$D(q,p) = \sum_{i=1}^{N} q(i) \log \frac{q(i)}{p(i)} \tag{5.5.1}$$

where N is the number of elements in each distribution. When applied to image thresholding the cross-entropy between the histogram of the input data, and the thresholded data, is minimised [300].

Having isolated the cellular ROI, and also the biologically relevant signal for both

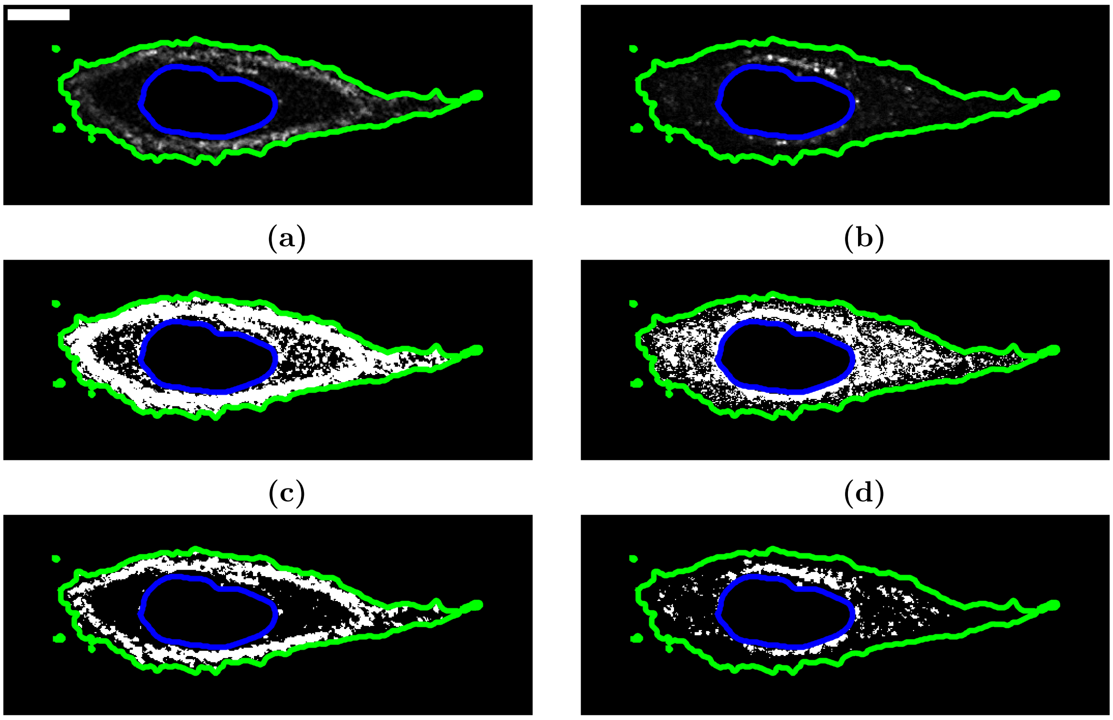

(a) **(b)**

(c) **(d)**

(e) **(f)**

Figure 5.10: Thresholding approaches for colocalization analysis. (a)-(b) Representative slices, from a 4D movie, showing the EGFR and rab5 signal after pre-processing. A threshold should be applied to this data to isolate the biologically relevant signal, necessary for calculation of colocalization statistics. The contrast has been enhanced in both channels by scaling between 0 and half the maximum value. Scale bar set at $10\mu m$. (c)-(d) A Costes' threshing approach returns a threshold value which is far too low. This is the case even with a small tolerance for the Pearson threshold (0.01). (e)-(f) A minimum cross entropy (MCE) thresholding approach produces a result which better segments the biologically relevant signal. Both the Costes' and MCE threshold values were calculated globally across all time-points simultaneously. Only voxels within the ROI, inside the cellular segmentation and outside the nucleus, were considered in the calculations.

channels, the Manders' coefficients, $M1$ and $M2$, were calculated for each cell in every treatment and time-point (equation 2.6.3). This was done in 3D. Note $M1$ can be interpreted as the percentage of total (isolated) EGFR signal overlapping with (isolated) rab5 signal. Similarly, $M2$ is the percentage of total rab5 signal overlapping with EGFR signal. To normalise the Manders' coefficients, the value at the first time-point (for each cell) was subtracted. With this normalisation the change in colocalization over time, not simply the existence of colocalization, in response to ligand is analysed. Figures 5.11a and 5.11c show the results of this analysis.

It is advantageous to implement a statistical testing protocol to determine if the perturbation to colocalization, induced by a specific drug treatment, is statistically significant relative to the control. The same approach is taken as for the quantification of sub-cellular receptor distribution in section 5.4. Specifically, for each treatment, the normalised coefficients were averaged across all time-points and analysed for variation with a Kruskal-Wallis one-way analysis of variance. If significant ($p < 0.05$), this was followed by pairwise comparison (Mann-Whitney U test) relative to the control, and a correction for multiple hypothesis testing was applied (Bonferroni). With this approach, the distributions of colocalization measures across a number of cells have been compared, with well established hypothesis tests, to determine differences in treatments [10]. This is unconventional approach which is justified, and discussed, in more detail in section 5.7. Figure 5.11b demonstrates a statistically significant variation in the colocalization response (EGF induced) for the AG1478 and dynasore treatments, as measured by $M1$. Note, from figure 5.11d, that no statistically significant variation is found for any of the drug treatments when $M2$ is used as the measure.

The described analysis was repeated, but with the Pearson coefficient as the measure of colocalization. This was done both without (figure 5.12a), and with (figure 5.12c), signal isolation. In the later case only the voxels which contained isolated signal from both

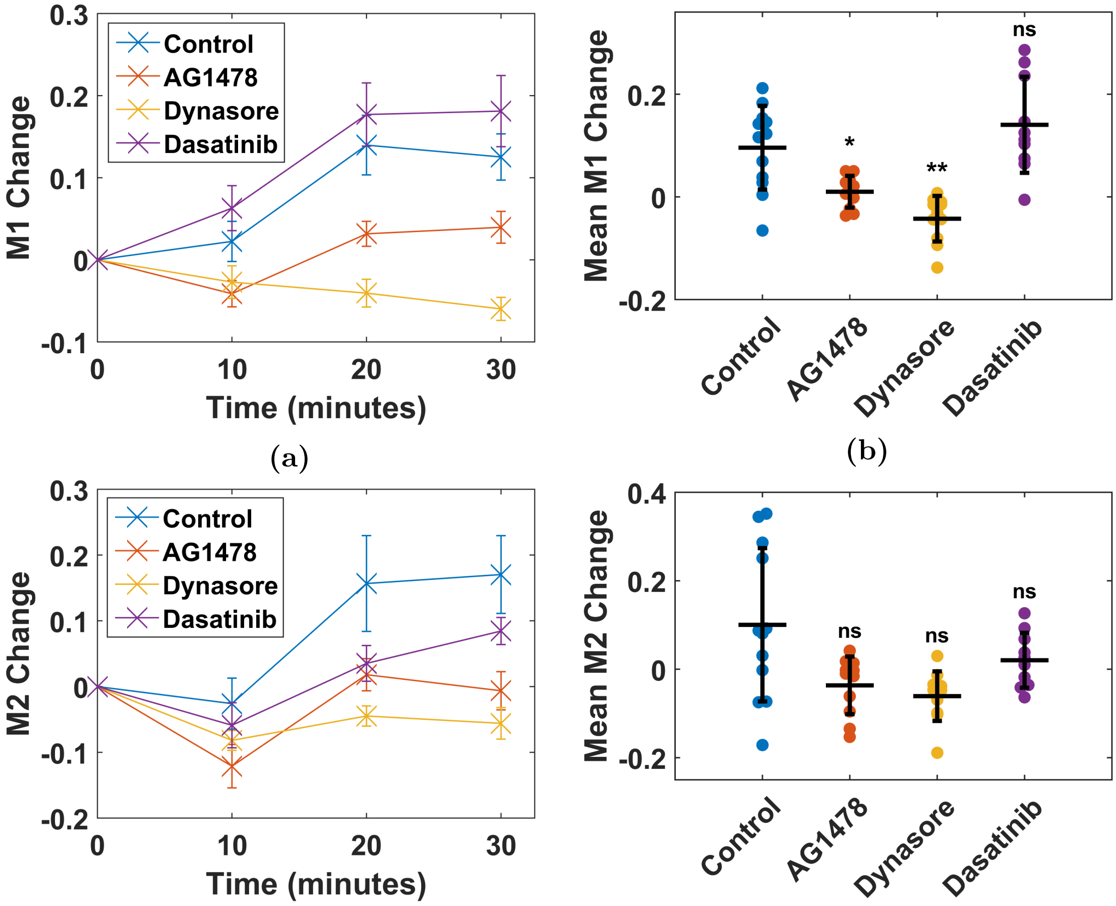

(a) (b)

(c) (d)

Figure 5.11: Quantifying the, ligand induced, colocalization response with the Manders' coefficients. For each cell the Manders' coefficients ($M1$ and $M2$) were calculated using the pre-processed and isolated signal. This analysis was performed for a DMSO control and 3 drug treatments; AG1478, dynasore and dasatinib. (a) Mean $M1$ coefficient, across all cells, over time. The coefficients have been normalised on a per cell basis by subtracting the value of the coefficient for the first time-point ($M1$ change). There are at least 10 cells per treatment and errors bars are given by the standard error. (b) Box-plot of the mean normalised $M1$ coefficient across all time-points. A Kruskal-Wallis one-way analysis of variance returned $p = 1 \times 10^{-5}$, indicating that there are significant differences between treatments. Post-hoc testing of all treatments relative to the control, by the Mann-Whitney U test (corrected by Bonferroni method), returned $p = 0.03$, $p = 0.002$ and $p = 0.73$ for the AG1478, dynasore and dasatinib treatments respectively. Central band represents the mean, and the error bars are the standard deviation. (c) Mean normalised $M2$ coefficient, across all cells, over time ($M2$ change). (d) Box-plot of the mean normalised $M2$ coefficient across all time-points. A Kruskal-Wallis one-way analysis of variance returned $p = 0.01$, indicating that there are significant differences between treatments. Post-hoc testing of all treatments relative to the control returned $p = 0.1$, $p = 0.053$ and $p = 1.1$ for the AG1478, dynasore and dasatinib treatments respectively.

channels were included in the calculation. In the former case, all pixels within the cellular ROI were included. With signal isolation, the Pearson coefficient can be interpreted as a measure of the linear correlation in endosomes positive for both EGFR and rab5. Without signal isolation, the Pearson coefficient is difficult to interpret. Figure 5.12b demonstrates that, without signal isolation, only the net effect of the dynasore treatment is statistically significant to the control. With signal isolation none of the drug treatments are observed to be significant (figure 5.12d).

To conclude, a protocol has been presented to quantify perturbations to the spatio-temporal dynamics of ligand stimulated colocalization, between receptor and sub-endosome populations, in response to various treatments. This protocol was implemented on 4D (3D time-lapse) data. Moreover, non-parametric statical tests were incorporated into the workflow to determine statistically significant changes in the, ligand induced, colocalization response.

5.6 Visualising colocalization in 4D

In the previous section, joint histograms were used to visualise colocalization in 4D (figure 5.9). We consider this to be the best way to visualise a change in colocalization over time. However, there is no spatial information in a joint-histogram. It can be useful to visualise the spatial distribution of the colocalization response at a particular time-point (or time-points). This is conventionally done with 2D colour merges but, as discussed in section 2.6, this has many draw-backs. In this section, an unbiased visualisation strategy for colocalization studies is presented.

In the presented approach, the contribution of each voxel to either the first, or second, Manders' coefficient is visualised (equation 2.6.3). First, the voxels containing signal from both channels are isolated. This is done using the protocols described in the previous section. After pre-processing the data (section 5.4), the intensities of the isolated voxels

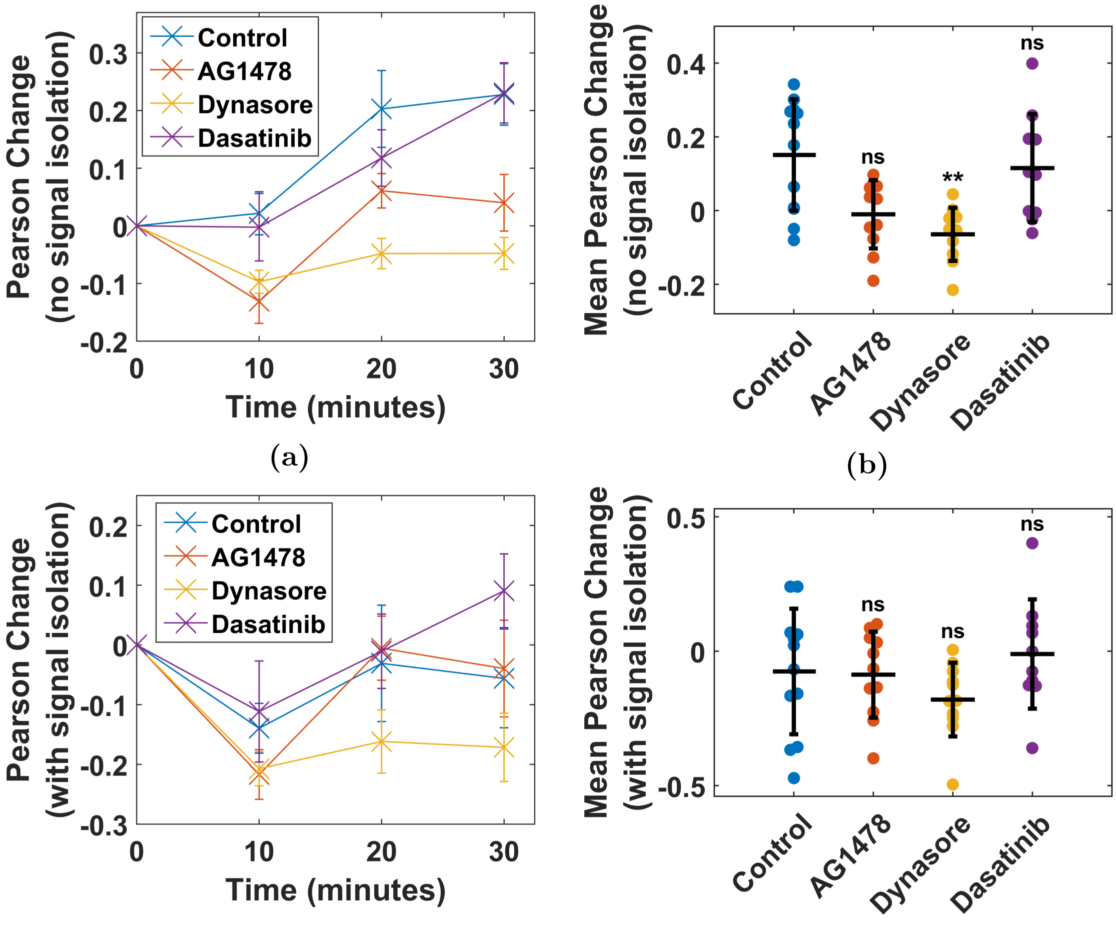

(a) (b) (c) (d)

Figure 5.12: Quantifying the, ligand induced, colocalization response with the Pearson coefficient. For each cell the Pearson coefficients were calculated using the pre-processed and isolated signal. This analysis was performed for a DMSO control and 3 drug treatments; AG1478, dynasore and dasatinib. (a) Mean Pearson coefficient (without signal isolation), across all cells, over time. The coefficients have been normalised on a per cell basis by subtracting the value of the coefficient for the first time-point (Pearson change). There are at least 10 cells per treatment and errors bars are given by the standard error. (b) Box-plot of the mean normalised Pearson coefficient (without signal isolation) across all time-points. A Kruskal-Wallis one-way analysis of variance returned $p = 0.002$, indicating that there are significant differences between treatments. Post-hoc testing of all treatments relative to the control, by the Mann-Whitney U test (corrected by Bonferroni method), returned $p = 0.1$, $p = 0.004$ and $p = 1.3$ for the AG1478, dynasore and dasatinib treatments respectively. Central band represents the mean, and the error bars are the standard deviation. (c) Mean normalised Pearson coefficient (with signal isolation), across all cells, over time (Pearson change). (d) Box-plot of the mean normalised Pearson coefficient (with signal isolation) across all time-points. A Kruskal-Wallis one-way analysis of variance returned $p = 0.2$, indicating that there are no significant differences between treatments.

are normalised across either, the entire movie, or a 3D time-point. If visual comparisons are to be made over time, then it is important to normalise across the entire movie. Note either the intensities of the first (EGFR), or second (rab5), channel are used. The choice of channel is context dependent. In the case of EGFR and rab5, $M1$ is a more biologically relevant parameter, hence the EGFR channel should be used. The normalised voxels, positive for both EGFR and rab5, can then be visualised with volume rendering techniques in 3D (Matlab[1]). Moreover, the colocalization can be visualised in parallel with (semi-transparent) surface renderings of the cellular and nuclear segmentations (section 5.3). This provides a powerful tool for researchers, allowing real-time rotation and inspection of the spatial colocalization response, in 3D, and without bias. An example of such a visualisation is shown in figure 5.13.

Note, when using 3D rendering approaches, only *snapshots* can be used for (2D) figures (figure 5.13). Therefore, under some circumstances, it is appropriate to visualise the colocalization in individual 2D slices (figure 5.14). The same approach, where the contribution of each voxel to a Manders' coefficient is visualised, can be used. To gain sufficient contrast, for display and printing, it can be necessary to normalise the data using only the 2D image (as opposed to the 3D time-point, or 4D movie). However, when this is done, the image should not be directly compared to any other slices within the movie. Note, when comparing figures 5.14 and 5.13, how little of the total colocalization response is captured by a single slice. This emphasises the need for 3D approaches in receptor trafficking studies.

The visualisation strategies, presented in this chapter, should not be used to confirm the presence of colocalization. This can be done with the various statistical strategies discussed in section 2.6.1. Similarly, visualisations cannot be used to determine if two treatments, or two time-points, have different levels of colocalization. To do this, quanti-

---

[1] http://www.mathworks.com/matlabcentral/fileexchange/22940-vol3d-v2

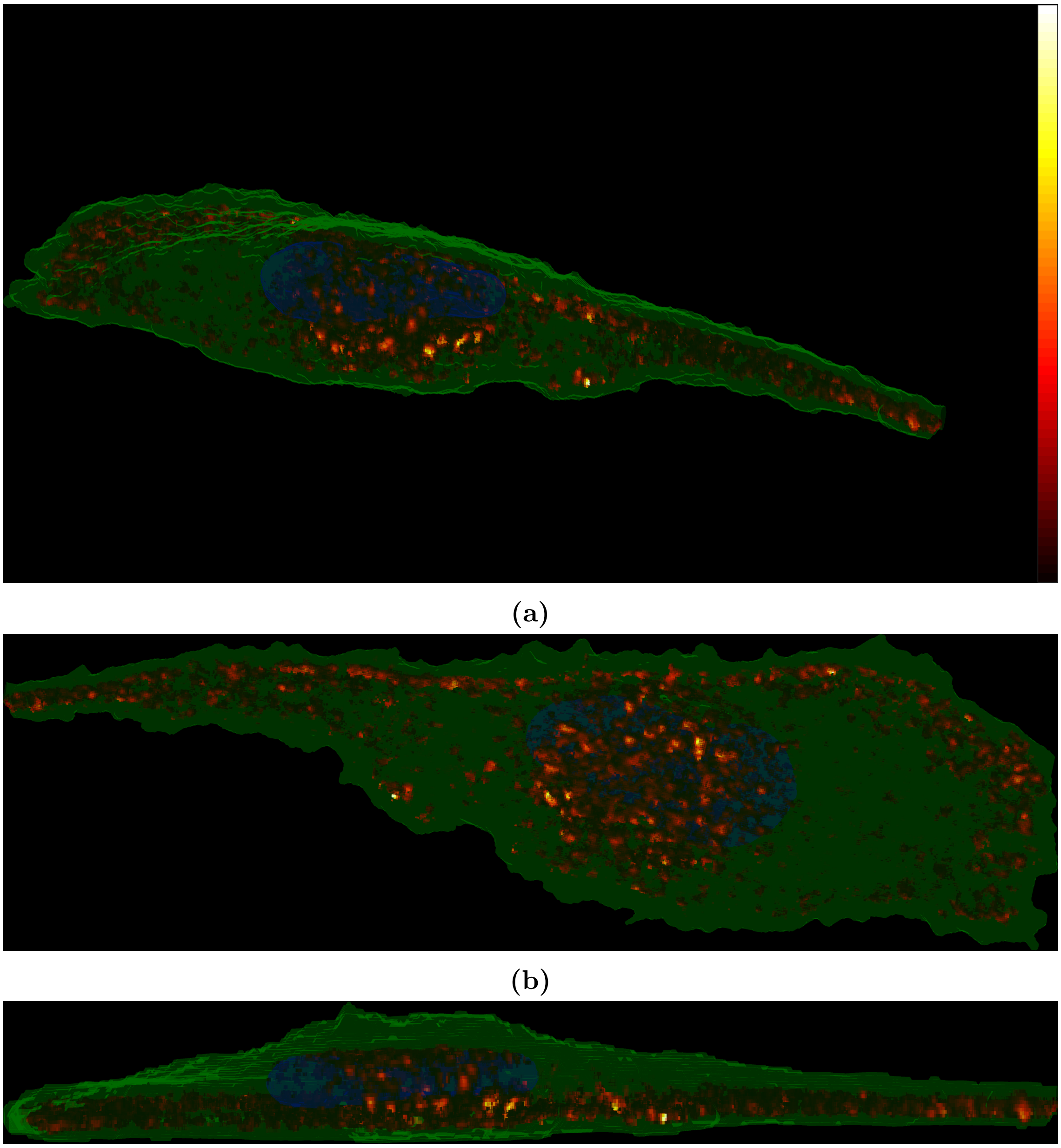

(a)

(b)

(c)

Figure 5.13: Visualising colocalization for a 3D time-point. A single time-point, from a 4D movie, of a HeLa cell expressing EGFR-EGFP and rab5-mRFP. The time-point was acquired 10 minutes post $2ng/ml$ EGF treatment. (a)-(c) Three different views of the cell. The cellular and nuclear segmentations are shown in green and blue respectively. The intra-cellular heat-map represents the colocalization between EGFR and rab5. It is non-zero for all voxels positive for both EGFR and rab5. The intensity of the heat-map is proportional to the normalised (across this time-point) EGFR intensity. This is analogous to visualising the contribution of each voxel to the Manders' coefficient; $M1$.

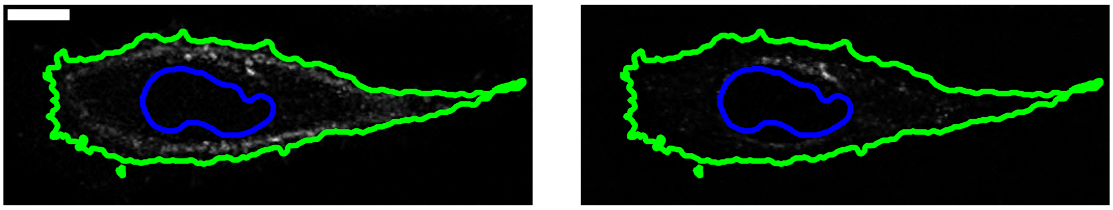

(a) EGFR

(b) rab5

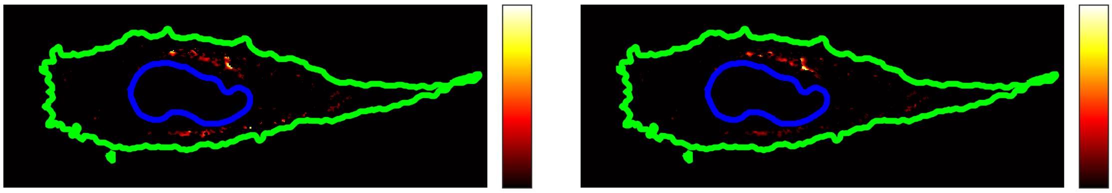

(c) Colocalization (EGFR weighted)

(d) Colocalization (rab5 weighted)

Figure 5.14: Visualising colocalization for a 2D plane. A single axial slice, from a 4D movie, of a HeLa cell expressing (a) EGFR-EGFP and (b) rab5-mRFP. The images are from a time-point acquired 10 minutes post $2ng/ml$ EGF treatment. Images have been pre-processed with PURE-LET de-noising and rolling ball background subtraction ($1\mu m$ radius). The contrast has been enhanced in both channels by scaling between 0 and half the maximum value. The green and blue contours show the outline of the automated segmentations for the plasma membrane and nucleus respectively. Scale bar set at $10\mu m$. (c) Intra-cellular heat-map representing the colocalization between EGFR and rab5. It is non-zero for all voxels positive for both EGFR and rab5. The intensity of the heat-map is proportional to the normalised (across this slice) EGFR intensity. (d) Colocalization heat-map for EGFR and rab5. The intensity of the heat-map is proportional to the normalised rab5 intensity. Note (c) and (d) are analogous to the contribution of each pixel to the Manders' coefficients; $M1$ and $M2$ respectively.

tative methods, such as those introduced in the previous section, should be used. Instead, the discussed visualisation strategies provide a useful tool for unbiased inspection of the intra-cellular spatial distribution of a colocalization response, which has already been quantified.

5.7 Discussion

The key outputs of this chapter are methodological, and are discussed in section 5.7.1. The use of these novel protocols was demonstrated, by quantifying perturbation to EGFR trafficking, for three drug treatments (AG1478, dynasore and dasatinib). There are some interesting points for discussion based on this data, which is discussed in section 5.7.2.

5.7.1 Protocols

In section 5.3, protocols were introduced to segment the plasma membrane, and nucleus, of individual cells in 4D. This was done using only the signal from a fluorescently labelled receptor (EGFR-EGFP) and an endosome sub-population (rab5-mRFP). These protocols were built around a 4D DRLSE approach, with a constant volume temporal constraint, as introduced in chapter 3. A key advantage of these protocols is that accurate segmentations are produced without the need for membrane (or cytoplasmic) and nuclear staining (figures 3.10 and 5.2). This is advantageous for several reasons; firstly, it limits the experimental complexity and cost of experiments. Secondly, it dramatically reduces the light exposure to the sample and also the acquisition time. To see this note, if independent stains are used for the membrane and nucleus, then four fluorescent channels (as opposed to two) will be needed. Hence the sample will be exposed to, approximately, twice the amount of light, and the data for each time-point will take longer to acquire. This is particularly important for live cell 3D time-lapse, where photo-toxic effects and the acquisition time will limit both the spatial, and temporal, sampling rate. Finally, note that the labelling of proteins with fluorescent markers can be toxic, or interfere with the function of the target. Therefore it is always good practice to minimise the number of markers used for live imaging.

In a recent study, Lukinavivcius *et al.* (2015) introduced a novel far-red (less phototoxic) DNA stain; sir-Hoechst [301]. The stain was demonstrated to have high specificity and low toxicity and is therefore ideal for live cell imaging. Note, that for the reasons given above, no stain will always be superior if the required measurements can be reliably made without it. However, if the density (confluency) of the sample is such that isolation of individual cells is difficult, our protocols will not be reliable, and a stain such as sir-Hoechst should be used.

In sections 5.4 and 5.5, workflows were introduced to quantify both, the sub-cellular distribution, and colocalization with sub-endosome populations, of receptors in response to ligand treatment. These workflows offer several important improvements over the protocols typically used in the literature (section 5.1). Firstly, the data is acquired and processed is 4D (3D time-lapse). Therefore, the entire cellular volume is imaged, and no bias is introduced by the selection of a single 2D plane. Secondly, the protocols are fully automated. After (blindly) selecting cells for analysis (only dead and mitotic cells removed) the entire workflow, including the statistical analysis and production of figures, is automated within Matlab. This eliminates problems associated with user error and bias, as well as dramatically reducing the time needed to analyse the data. Moreover the workflows, in particular the segmentation protocols, are fully validated and were tested on a subset of manually annotated data. Finally, the protocols are described in the extensive detail necessary to be completely reproducible.

In section 5.4 a band-based analysis, for quantifying the change in sub-cellular receptor distribution over time, was introduced. This protocol provides a large amount of information; specifically a temporal response curve for each band (figures 5.5a and 5.6a). This is advantageous because it allows the trafficking response to be analysed for the whole cell (based on either distance from the plasma membrane or nucleus), not just the surface. However, this information can be difficult to interpret and process. To counter this, two strategies were devised. In the first the *total* response of each cell, to ligand treatment, over the whole time-course is reduced to a single measurement; the mean change in normalised (relative to the first time-point) percentage receptor signal, over all time-points, and all bands (figures 5.5b and 5.6b). This approach is advantageous as non-parametric statistical tests can be used to determine if a perturbation to receptor trafficking, for a specific treatment, is statistically significant relative to a control distribution. However, by reducing the data to a single measurement per cell, a lot of potentially informative information is lost, and the statistical testing is therefore harsh.

In the second approach, a heat-map is used to visualise the temporal response curves of a specific treatment, relative to a control. The heat-maps are normalised using the error in the measurement (equation 5.4.1). Therefore, the heat-maps provide a visualisation of the confidence in the measured perturbation, for every band, and every time-point. This approach is advantageous as it provides an intuitive way to visualise the effects of a treatment relative to a control, without any reduction of the measurement variables. However, although the heat-maps can be used to assess the confidence for a measured effect, there is no formal procedure to reject the null hypothesis that the treatment has no effect on the sub-cellular receptor distribution. Therefore, the two approaches are complementary, and together provide a powerful tool to study receptor trafficking.

In section 5.5 workflows to quantify the change, over time, in the colocalization between receptor and sub-endosome populations were introduced. There are several important points for discussion arising from the development of these protocols. Firstly, recall from section 2.6, that Costes' thresholding is a well established technique for signal isolation in colocalization analysis [182]. It is implemented in popular image analysis software, and is cited as good practice in several review papers (figure 2.12) [170, 9, 177]. With a Costes' thresholding approach there is an assumption that the dominant component of the data has positive correlation (the colocalized pixels). Adler and Parmryd (2013) note that a Costes' thresholding approach will fail if the two signals have no correlation [177]. Therefore, the Costes' approach assumes that there is both colocalized and correlated signal present in the data. We consider this an inappropriate assumption for the majority of colocalization studies, where the purpose is to test for the existence of colocalization, so clearly correlation should not be assumed.

Moreover, Dunn *et al.* (2011) note that a Costes' thresholding approach may fail if the SNR is too low, the labelling density is too high, or if there are too many *structures* in one channel [9]. When the Costes' approach fails it will often over-segment the signal as seen in figures 5.10c and 5.10d. We note that if the data has multiple components, with different levels of correlation, then a Costes' thresholding approach is not applicable. This is the case for our work where EGFR has three distinct components (relative to rab5); membrane localised receptor, receptor in rab5 positive endosomes and receptor in rab5 negative intracellular structures (eg lysosomes). It is reasonable to expect each of these components to have different levels of correlation, and moreover these levels will change over time in response to ligand treatment. To fit a single linear relationship to multi-component data, as is done in a Costes' approach, is completely inappropriate. To see this, note from figure 5.9 that a linear fit does not well represent the data from the earlier time-points, or all the time-points combined. This is because the membrane bound receptor will have low correlation (relative to rab5 signal), and will distort the linear fit and the corresponding Costes' threshold values.

Therefore, we conclude that Costes' thresholding is only applicable if it can be assumed (before the analysis) that the signal is both correlated, and well represented by only one component. We note that these assumptions are not met in the majority of colocalization studies. Therefore a different approach is required. The approach needed will be application dependent, but should accurately segment the biologically relevant signal in both channels and be automated. Dunn *et al.* suggest background subtraction, using a median filter, followed by a manually selected global threshold. We use a similar approach for background subtraction (rolling ball mean filter), but use an automated MCE approach to select the global threshold. The selection of the global threshold value should be automated to remove any user bias, and also to allow for adaptability for different levels of construct expression.

In section 5.5 the distributions of colocalization measures over time (Manders' and Pearson) were reduced to a single statistic per cell, and processed with standard statistical tests (figures 5.11 and 5.12). This was done to test the null hypothesis that the trafficking of EGFR to rab5 positive endosomes, in response to EGF treatment and relative to a control, was not affected by a specific drug treatment. In the described approach, a Kruskal-Walis one-way analysis of variance, with post-hoc testing by the Mann-Whitney U test (Bonferroni correction) was used. McDonald *et al.* (2013) validated the use of the two way Student t-tests to compare distributions of either the Pearson or Manders' coefficients [10]. It is concluded that (quotation);

> *One can imagine experiments in which more complicated statistical tests could be applied to measures of colocalization, such as analysis of variance (anova) and regression. Although we have not simulated the broad variety of possible experimental designs, our results here suggest that treating PCC or* MCC_{diff} *as a variable to be analyzed like any other measurement variable is a promising approach that may not suffer from obvious statistical artefacts.*

where PCC is the Pearson coefficient, and MCC_{diff} are the Manders' coefficients (difference between treatments or relative to an expected value). Note in our approach we choose not to assume normality. However, the use of a two-way Student t-test for individual comparisons is also a reasonable choice, as it is typically robust to violation of the normality assumption if the distributions are the same size [302].

The key advantage of the described approach is it allows for comparisons between multiple conditions, relative to a colocalization measure, and is very simple to implement. In other strategies for statistical testing, each cell is individually tested against the null hypothesis; typically the presence of colocalization (section 2.6.1). This approach isn't particular useful for this work as populations, not individuals, need to be analysed. Furthermore, these approaches are confounded by auto-correlation within the data which is technically difficult to account for. In our approach, differences between conditions are analysed, hence auto-correlation need not be considered. Future work should further justify the use of the Kruskal-Walis one-way analysis of variance, and the Mann-Whitney U test, for distributions of colocalization measures using simulated data.

Although it was not performed in this work, treatment with a protein synthesis inhibitor such as cycloheximide could have been used to quantify the rate of EGFR degradation [303]. However Oksvold *et al.* (2012) provide evidence that cycloheximide treatment can trigger ligand independent internalisation of EGFR so the interpretation of such experiments should perhaps be treated with caution [304].

All of the approaches described in this chapter for live cell imaging, and in chapter 4 for fixed sample screening, use labelled receptor. An alternative approach is to use labelled ligand [3]. There are advantages to each approach. The use of labelled ligand avoids quantification of the entire receptor population, isolating the ligand induced response. In the live-experiments presented in this chapter a similar quantification is achieved with labelled receptor by subtracting the measurements from the first time-point. The use of labelled ligand would also avoid over-expression of the receptor. An advantage of labelled receptor is that it allows for the quantification of any abnormalities in the sub-cellular distribution, or colocalization, of receptor prior to ligand treatment. Labelled receptor also ensures that the localization of the receptor is correctly quantified after ligand dissociation. In the presented workflows the labelled receptor signal is used to segment the cellular and nuclear boundaries. This would not be feasible using labelled ligand so additional membrane, or cytoplasmic, and nuclear labels would be required. Finally, note that after segmenting regions of interest, all of the workflows presented in both this chapter, and chapter 4, would be equally applicable with labelled ligand.

5.7.2 Data from Drug Treatments

The implementation of the protocols introduced in this chapter were demonstrated using data with one of three drug treatments; dynasore, AG1478 and dasatinib, with comparison to a DMSO control. In this sub-section, the results of this analysis are discussed. This is done to demonstrate how to interpret the output of the novel protocols introduced, and also because the results have some interesting biological implications.

First note the band based analysis, of sub-cellular receptor distribution, was based on either distance from the plasma membrane, or distance from the nucleus (section 5.4). In the case of the three drug treatments, the results based on plasma membrane distance are easier to interpret. Note band 1 corresponds to the plasma membrane itself. Therefore we restrict our discussion to the results based on plasma membrane distance (figures 5.5 and 5.7).

In section 5.5 both Manders' coefficients are calculated (figure 5.11). $M1$ corresponds to the percentage of (isolated) EGFR signal overlapping with rab5 signal. $M2$ corresponds to the percentage of rab5 signal overlapping with EGFR signal. Clearly, in the context of receptor trafficking, $M1$ is the more meaningful measurement. Therefore the discussion of colocalization is restricted to the first Manders' coefficient.

The Pearson coefficient was calculated for all the pixels in the cellular ROI, and also only the pixels containing (isolated) signal in both channels (figures 5.12a and 5.12c). The former is difficult to interpret, but the later is a measure of the (linear) correlation between EGFR and rab5 in endosomes positive for both constructs. Note, from figures 5.12c and 5.12d, that there is no significant change to this correlation, for the control distribution, in response to EGF treatment. Also note that none of the drug treatments induce a significant change in the correlation (averaged across time-points) relative to the control. This is interesting because although there is a increase in overlap, as measured by the Manders' coefficients (figure 5.11) , there is no increase in correlation. This illustrates the advantage of using separate colocalization measures for overlap and correlation.

Dynasore

Figure 5.5a shows the temporal response curves quantifying the change in sub-cellular EGFR distribution, in response to EGF treatment, with and without dynasore treatment. Note from figure 5.5b that the net perturbation to EGFR trafficking, in response to dynasore treatment, is significant. Also consider the corresponding heat-map representation, shown in figure 5.7b. Recall, the heat-map illustrates the confidence in the significance of the perturbation to EGFR trafficking (relative to the control) for each band and each time-point. Note the bands closest to the membrane (1-2) have a strong positive effect (increase in signal) for all time-points (excluding time-zero). The bands corresponding to the cellular interior (4-10) have a strong negative effect. Now re-consider the temporal response curves (figure 5.5a). It is clear that the response to EGF stimulation is small across all bands and all time-points. Also note, from figure 5.11a, that relative to the control, there is a decrease over-time in the colocalization between EGFR and rab5 as measured by the first Manders' coefficient. Finally note, from figure 5.11b, that relative to the control, this effect is significant. Together these results indicate that dynasore treatment blocks all EGFR internalisation (as detectable with our protocols) and correspondingly no increase in EGFR, localised to rab5 positive endosomes, is observed.

Recall dynasore is an inhibitor of dynamin, a key component of endocytosis [305]. Therefore our results support the widely excepted hypothesis that, at low EGF concentrations ($2ng/ml$), the dominant endocytic routes for EGFR internalisation are dynamin dependent [65].

AG1478

Recall AG1478 is a EGFR kinase inhibitor. It has been demonstrated, in-vitro, to have higher affinity for EGFR than for ERBB2. However the effects of AG478 on ERRB2 and ERBB4 kinase activity are not well characterised [306, 307]. First note, from figure 5.5b, that the net perturbation to EGFR trafficking, relative to the control, in response to AG1478 treatment is significant. From the corresponding heat-map (figure 5.7b), it is clear that there is a large positive effect (increase in receptor signal) in band 2 (across all time points), and a large negative effect for bands 4-8. Interestingly, the effect confidence is small for band 1, which is associated with the (outermost) plasma membrane. Now consider the temporal response curves shown in figure 5.5a. For the intracellular bands, the receptor distribution closely matches the profile induced by dynasore treatment (inhibition of endocytosis).

Figure 5.11a demonstrates, that for AG1478 treated cells, there is a substantial reduction in the colocalization between EGFR and rab5 (relative to the control), as measured by the first Manders' coefficient. Also note, from figure 5.11b, that this effect is significant. Together, these results demonstrate that EGFR kinase inhibition (through AG1478 treatment) significantly reduces the net internalisation of EGFR and trafficking to early endosomes.

In the literature the relationship between EGFR kinase activity and EGFR internalisation is a controversial issue [308]. It was originally thought that EGFR kinase activity was necessary for, EGF induced, EGFR internalisation [309, 289]. Huang and Sorkin (2005) show that recruitment of the ubiquitin ligase Cbl RING domain to EGFR (Grb-2 mediated) is necessary for clathrin mediated endocytosis [310]. This strongly supports the hypothesis that EGFR kinase activity is necessary for EGFR internalisation. However Wang *et al.* (2002, 2005, 2015) have demonstrated, in a series of studies, that receptor dimerisation, but not kinase activity, is necessary for internalisation [311, 290, 312]. Our results indicate that both net EGFR internalisation to the central regions of the cell and trafficking to early endosomes (rab5 positive) is dramatically reduced by EGFR kinise inhibition. However, we do not account for rapid recycling of EGFR back to the plasma membrane, or for inhibited post endocytic trafficking and fusion to early endosomes. Therefore we cannot conlude that kinase activity is essential for endocytosis. A particularly interesting experiment would be to label recycling endosomes in AG1478 treated cells and repeat the analysis presented in this chapter.

Dasatinib

Recall dasatinib is an inhibitor of both Src family, and Abl kinases [293]. Figures 5.5a and 5.7c show a small increase in EGFR trafficking to the interior of the cell. Moreover, figure 5.11a shows an increase in, EGF induced, colocalization between EGFR and rab5, relative to the control, for all time-points. However, the net effect of either of these analyses was not significant (relative to the control) so no conclusions can be made from these results (figures 5.5b and 5.11b).

Lin *et al.* (2012) demonstrated that EGFR was down-regulated, and Cbl activity was increased, by dasatinib treatment [295]. It was suggested that Cbl mediated trafficking of EGFR to lysosomes could be increased by dasatinib treatment. Therefore a very interesting set of experiments would be to repeat the protocols presented but with lysosome (as opposed to early endosome) labelling.

5.8 Conclusion

In this chapter state of the art, and fully automated, workflows were introduced to quantify perturbation to receptor trafficking, in 4D, using confocal microscopy. This was done by quantifying the change to the sub-cellular distribution of receptor, and also the colocalization with a sub-population of endosomes, over time, and in response to ligand stimulation.

Novel 4D level set based segmentation protocols were used to segment the plasma membrane and nucleus, using only the receptor and endosomal labels. This minimised the number of labels needed. A band-band analysis was introduced to quantify the sub-cellular distribution of receptor. Importantly, both the membrane bound and intracellular receptor were analysed. Heat-map representations of the analysis were used to visualise the perturbation to receptor trafficking, and statistical tests were used to determine if the net perturbation was statistically significant.

Quantitative colocalization protocols to quantify the change in colocalization over time, and between different treatments, were introduced. Pre-processing and signal isolation strategies were discussed. A statistical testing protocol to compare the, ligand induced, response between conditions was presented. Moreover, unbiased strategies to visualise the colocalization response in 4D were developed.

These protocols were demonstrated on a test system; HeLa cells expressing both EGFR-EGFP and rab5-mRFP were imaged in 4D using confocal microscopy, and stimulated with EGF. This was done in the presence of one of three drug treatments, or a DMSO treated control.

In conclusion, these protocols provide a valuable toolbox of reproducible, automated and unbiased methods. Paired with the screening approaches introduced in the previous chapter, they provide a valuable resource for researchers studying receptor trafficking.

CHAPTER 6

CONCLUSION AND FUTURE DIRECTIONS

6.1 Conclusion

The networks regulating the endoyctosis, trafficking and signalling of cellular receptors are highly interlinked. Aberrant crosstalk between the regulatory mechanisms of these networks is heavily implicated in disease. There is increasing evidence for the existence and importance of signalling endosomes (section 2.2.3) [1]. Importantly, the signalling response can be dependent on receptor location within the endocytic network. This highlights the role of endocytic trafficking as a regulator of signalling outcome, not only signal attenuation. It is clear that much remains to be understood about the role of trafficking in regulating receptor signalling.

Fluoresence microscopy is a powerful tool for the quantification of the spatial-temporal dynamics of receptor trafficking and endocytosis. The analysis of the data is a crucial aspect of imaging based studies. However, within the literature, there are frequent examples of poorly designed or described image analysis protocols (section 5.1). To design and report an image analysis protocol, two important elements should always be considered. Firstly, the protocol should be described in sufficient detail as to be reproducible. Secondly, it should not be open to user bias. Ideally, the process should be fully automated, but any manual analysis should be done blindly. It is striking that in many publications, great care is taken to fully describe the experimental methodologies, but the details of the image analysis are absent or insufficient. The aim of this thesis was to report and develop workflows to quantify the spatio-temporal dynamics of receptor trafficking and colocalization using (confocal) florescence microscopy. Importantly, the workflows should be reproducible and unbiased, as well as automated and accurate.

The development of the 4D level set segmentation protocols presented in chapter 3 was motivated by the problem of cellular segmentation. Specifically, for live cell 4D (3D+time) confocal microscopy data, using only the signal from a fluorescently labelled receptor (EGFR-EGFP). For this application, accurate segmentation is required to quantify the membrane bound receptor. However, this is a difficult problem for live cell applications where the signal to noise ratio is typically low (the sample should be exposed to a minimal amount of light). Deformable model (including level set based) segmentation approaches are well established in the literature (section 3.3). The conventional approach is to use at least one level to segment the data from each time-point. We hypothesised that by constructing the dataset as a single 4D array, and using a single level set function to find a globally optimum solution, greater segmentation performance could be achieved. It is important to note that the potential applications of such a framework are not limited to cellular segmentation.

The presented approach to 4D level set segmentation is sufficiently novel as to require extensive documentation and validation. We described an extension of the distance regularized level set evolution (DRLSE) framework to 4D [225]. Both edge [13] and region [14] based implementations were introduced. Strategies for the scaling of the temporal derivatives with respect to spatial dimensions were described, as were efficient protocols for the initialisation of the level set function. These 4D level set frameworks were validated on both real and synthetic confocal microscopy test data. Importantly, for both the synthetic and real test datasets, a statistically significant increase in maximal performance was seen, over equivalent 3D and 2D implementations, thus confirming our hypothesis (figures 3.6, 3.7 and 3.9). Finally, we introduced adaptations to the level set equation to take advantage of temporal assumptions and improve segmentation performance. For example, for the real test dataset, we demonstrated that an assumption of constant volume over time could be used to introduce a constraint to the level set equation. This constraint was shown to further increase the maximal segmentation performance of the 4D level set algorithm (figure 3.13).

In chapter 4, we presented a microscopy based screening framework. This was used to screen for genes involved in the regulation of receptor endocytosis and trafficking. To demonstrate the use of this framework, 16 GEFs and GAPs were selected from the results of a SILAC proteomics screen (Debbie Cunningham, University of Birmingham). A detailed workflow for data pre-processing, cellular segmentation and hit detection (using only the EGFR-EGP signal) was provided. Hit detection was performed using a band based measure which quantifies the distribution of receptor, based on distance from the plasma membrane. Using this framework we identified 5 hits for regulators of EGFR endocytosis and/or trafficking (figures 4.7 - 4.11). Note, 4 of these hits have been identified by previous screens in the literature as regulators of endocytosis and trafficking. The key advantages of our screening approach is the detailed, validated and unbiased image analysis protocols, alongside experimental simplicity. It is well suited to the secondary screening of large non-imaging based screens.

The confocal microscopy screen was performed in 2D, and on fixed cells. This was done due to equipment and budget limitations, and is a typical strategy for the identification of (potential) phenotypes. Note, it is best practice to validate such hits using live cell 3D microscopy. In chapter 5 we presented workflows to analyse and quantify receptor trafficking for the 4D datasets generated from such validation experiments. After pre-processing the data, both the cellular and nuclear boundaries were segmented using the 4D level set approaches described in chapter 3. Importantly, only signal from the receptor (EGFR-EGFP) and early endosome marker (rab5-mRFP) were used to do this. Using the results of these segmentation algorithms, we adapted the band based measure introduced in chapter 4 to characterise the sub-cellular distribution of receptor in 4D. Drug induced perturbations to the, EGF stimulated, trafficking response were quantified using three different treatments; AG1478, dynasore and dasatinib. Relative to the control, the spatial-temporal dynamics of EGFR was shown to be distinct for the AG1478 and dynsore treated populations (figure 5.5). A heat map visualisation of the 4D receptor distribution was introduced to aid the interpretation of the results (figure 5.7).

Fluorescently labelled markers for sub-endosome populations can be used to quantify the colocalization between receptor and different components of the endocytic network. However, despite several excellent reviews, colocalization analysis is still often poorly understood and implemented. In section 2.6 we provided a thorough review of best practice in colocalization analysis, focusing on overlap, over object based measures. In chapter 5 we implemented and adapted existing colocalization methods to quantify the spatial-temporal dynamics of colocalization in 4D data. Using these workflows, we were able to identify (relative to the control) perturbations, to the (EGF induced) colocalization response between EGFR and rab5, for AG1478 and dynasore treated samples (figure 5.11). The drug treatments presented in this chapter are intended to provide an illustrative example of the application of the proposed protocols. It is worth noting that we challenged the use of Costes' thresholding, which is often referenced as best practice [170, 9], for any colocalization analysis where linear correlation cannot be assumed.

Finally, we considered the visualisation of colocalization. Colour overlays are easily manipulated or mis-interpreted. Joint histograms provide a simple and unbiased way to visualise the correlation in an image but all spatial information is lost. We presented a strategy where the relative contribution of each voxel to either of the Manders' coefficients is used to define a heat-map for spatial visualisation (figure 5.13). This approach provides both an unbiased, and automated strategy to visualise the spatial distribution of colocalization.

6.2 Future Directions

Avenues for the further development of the 4D level set algorithms are discussed in detail in section 3.8. In summary, there is extensive potential to develop sophisticated and customised temporal constraints. For example, shape classifiers, or tracking of multiple targets, could be introduced. Alternatively, strategies to reduce the computational time such as implementation on the GPU, or a discrete representation, could be tested.

In chapter 4, only a small subset of the hits from the SILAC study were screened with our imaging based strategy. Therefore, an interesting study would be to perform an imaging based secondary screen of the remaining SILAC hits using the presented methods. The 5 hits identified should be validated in live cells using 3D time-lapse microscopy, and the analysis methods described in chapter 5. Of particular interest is the validation of TBC1D5 which has no established role in the regulation of EGFR endocytosis and trafficking.

The analysis of the spatio-temporal dynamics of EGFR in response to EGF stimulation with drug treatments (chapter 5) could be repeated, but with alternative sub-cellular markers for colocalization analysis. In particular, a marker of recycling endosomes for the AG1478 treatment could help to clarify the dependency of EGFR kinase activity for endocytosis. To see this recall, from section 2.2.2, that recycling of EGFR can be seen as the default option when receptor is not ubiquitinated [66]. Moreover EGFR kinase activity (through ubiquitin ligase Cbl) is thought to be necessary for ubiquitination of receptors and the subsequent diversion from a recycling pathway [308]. Therefore it is essential to account for the recycling component before making conclusions about the endocytic rate. Alternately, a lysosomal marker for the dasatinib treatment would be interesting and could reveal if there is increased trafficking of EGFR to lysosomes.

In conclusion, we have presented a series of workflows which use confocal microscopy to quantify perturbations to the trafficking and endocytosis of cellular receptor. These unbiased workflows are defined in sufficient detail as to be reproducible and adaptable for a range of applications. It is hoped that there will be substantial future work which takes advantage of these tools to elucidate novel aspects of receptor signalling and trafficking.

CHAPTER 7

MATERIALS AND EXPERIMENTAL METHODS

7.1 Solutions

Cell Culture Media

Pre-made Dulbeccos Modified Eagle Medium (DMEM) (supplemented with $4.5g/l$ L- glutamine (Invitrogen)) was sterile filtered using a $500ml$, $0.1\mu m$ pore vacuum filter system (Corning). Unless otherwise stated 1% Penicillin-Streptomycin solution (100x) (Invitrogen) and 10% Fetal Bovine Serum (FBS) (Biosera) were added before filtering. Stored at 4 °C.

Cell Imaging Media (CIM)

$2.38g$ HEPES (Fisher) and $9.7g$ Hanks Balanced Salt (without phenol red and sodium bicarbonate) (Sigma) were dissolved in $1l$ distilled water. NaOH was added dropwise to increase the pH to 7.5 (Delver instruments pH meter). Solution was subsequently sterile filtered using a $500ml$, $0.1\mu m$ pore vacuum filter system (Corning) and stored at 4 °C.

Luria Bertani (LB) broth

10*g* of pre-made LB Broth (Sigma) was dissolved in 500*ml* distilled water. Subsequently autoclaved at 121 °C for 20 minutes.

Lysis Buffer

100*μl* of 100% Triton X-100 (Sigma) added to 10*ml* DPBS (Lonza). Stored at 4 °C. 24 hours prior to use 1 EDTA free protease inhibitor cocktail tablet (Roche) was added and solution vortexed.

0.5, 1 and 1.5M Tris-HCl, various pH

Either 60.57*g* (0.5M), 121.14*g* (1M) or 181.71*g* (1.5M) of Tris (Fisher Scientific) was dissolved in 1*l* distilled H_2O. 1M HCl added dropwise until the desired pH was reached (Denver instruments pH meter).

Sample Buffer (3X)

100*ml* distilled H_2O, 30*ml* glycerol, 18.8*ml* of 1M Tris pH 6.8, 15*ml* beta-mercaptoethanol (Sigma), 18.8*ml* of 1M Tris pH 6.8 and 6*g* Sodium dodecyl sulphate (SDS) (Sigma) mixed. Stored at room temperature.

10% **Set Acrylamide Gel**

10% stacking and resolving gel solutions made by mixing 20*ml* distilled H_2O, 12.5*ml* Tris-HCl, 16.5*ml* Bis Acrylamide (Protogel) and 0.5*ml* 10% SDS (Sigma). Stored at 4 °C. 0.5M pH 6.8 Tris-HCl and 1.5M pH 8.8 Tris-HCl were used for the stacking and resolving gels respectively. 500*μl* 10% APS (BIO-RAD) and 75*μl* TEMED (Sigma) added immediately before use. Resolving gel was used to fill a Novex 1.5*ml* cassette (Life Technologies) and set for 30 minutes. Stacking gel and 10 well comb then added and left to set for a further 30 minutes before use.

Running Buffer

10× running buffer made by dissolving 144*g* Glycine (Fisher Scientific), 30*g* Tris (Fisher Scientific), 4*g* SDS (Sigma) in 1*l* of distilled H_2O. 1× running buffer made by mixing 100*ml* 10× running buffer and 900*ml* distilled H_2O.

Transfer Buffer

10× transfer buffer made by dissolving 144*g* Glycine (Fisher Scientific) and 30*g* Tris (Fisher Scientific) in 1*l* of distilled H_2O. 1× transfer buffer made by mixing 100*ml* 10× transfer buffer, 200*ml* methanol and 700*ml* distilled H_2O.

TBST and high salt TBST

10× TBST made by mixing 500*ml* distilled H_2O, 300*ml* 5M NaCl and 200*ml* 1M Tris-HCl pH 7.5. 1× TBST made by mixing 100*ml* 10× TBST and 900*ml* distilled H_2O. High salt TBST made by mixing 145*ml* NaCl, 100*ml* 10× TBST and 755*ml* distilled H_2O.

Milk TBST

Milk TBST made by dissolving 10*g* skimmed milk powder (Marvil) in 200*ml* 1× TBST.

7.2 Plasmid Constructs

The EGFR-EGFP construct was a gift from Alexander Sorkin (University of Pittsburgh, USA). The rab5-mRFP construct was a gift from Ari Helenius (Institute of Biochemistry, ETH Zurich).

7.2.1 Preparation

Bacteria Transformation by Heat Shock

1μg of plasmid DNA was added to 50 μl of DH5α E.coli competent cells (Invitrogen). After 30 minutes of incubation on ice, the bacteria was transferred to a water bath at

45 °C for 45 seconds (heat shock) before a further 2 minutes of incubation on ice. $500\mu l$ of LB broth (section 7.1) was added to the bacteria before incubating at 37 °C (with agitation) for 1 hour. $125\mu l$ of the bacteria culture was transferred to a $13cm$ LB agar plate (Sigma) containing the appropriate antibiotic (under a flame). After approximately 12 hours intubation at 37 °C two distinct colonies where removed (with a pipette tip) and each was placed in $2ml$ of LB broth containing either $50\mu g/ml$ of kanamycin or $100\mu g/ml$ of ampicillin as appropriate (using 14ml dual-position snap cap round bottomed tube (Falcon)). Each bacteria colony then incubated for 4 hours at 37 °C (with agitation). $100\mu l$ of each bacteria culture transferred to conical flask containing $100ml$ of LB broth with preserved concentration of antibiotics before incubation at 37 °C (with agitation) for approximately 12 hours. Cultures were split into two $50ml$ ultracentrifuge tubes (falcon) and centrifuged at $5000rmp$, 4 °C for 15 minutes. Supernatant removed and pellets stored at −20 °C, ready for purification as described below.

Purification and Isolation of Plasmid DNA

A QIAGEN Plasmid Maxi Kit was used to purify plasmid DNA according to the manufacturer's instructions. After purification, DNA was washed with 70% ethanol and redissolved in ultra-purified water and stored at −20 °C. Concentration was determined by UV spectrophotometry using a NanoDrop spectrometer (according to manufacturer's instructions).

7.3 Cell Biology Methods

7.3.1 HeLa cell culture

HeLa cell line was cultured in cell culture media (section 7.1) in plastic T75 flasks (Corning) at 37 °C and 5% CO_2. At $80 - 90\%$ confluency, cells were passaged as follows; media removed and cells washed twice with $5ml$ DPBS (Lonza) before addition of $1ml$

1% trypsin solution (Gibco). Cells incubated in trypsin solution at 37 °C for 2 minutes (or until detached) before re-suspension in cell culture media and transfer to new flasks. Cells were used for a maximum of 20 passage cycles.

The stably expressing EGFR-EGFP HeLa cell line was kindly produced by Debbie Cunningham (School of Biosciences, University of Birmingham). The stable cell line was cultured as above with but with addition of $400\mu g/ml$ G418 disulfate salt (Sigma) to the cell culture media.

7.3.2 Transient Transfection with Plasmid Constructs

Cells were plated onto either $35mm$ glass bottomed dishes (MaTek) or 6 well glass/plastic bottomed dishes (MaTek/Corning) in cell culture media without antibiotics (section 7.1). Unless otherwise stated, 2×10^6 cells/well were seeded into each $35mm$ diameter well. 24 hours after plating, cells were transfected with the relevant plasmid using Lipofectamine 2000 (Invitrogen) according to the manufacturer's instructions. Note, for rab5-RFP transfections, $6\mu l$ of Lipofectamine 2000 and $0.5\mu g$ of cDNA per well was found to be optimal. For EGFR-EGFP, $10\mu l$ of Lipofectamine 2000 and $4\mu g$ per well was used. For transient dual transfection, $10\mu l$ of Lipofectamine 2000 and $2\mu g$ of both constructs was used. 3 hours after addition of the constructs, the media was changed (without antibiotics). Cells were imaged after 24 hours expression.

7.3.3 Transient siRNA Knockdown

siRNA knockdowns were performed with a reverse transfection approach using the Lipofectamine RNAiMAX reagent (Invitrogen) according to the manufacturer's instructions. $2\mu l$ of RNAiMAX reagent was used per well. Cells were plated onto siRNA in 24 well glass/plastic bottomed dishes (MaTek/Corning) in cell culture media without antibiotics (section 7.1). Unless otherwise stated 5×10^4 cells were seeded. siRNA targeting the alpha-adaptin subunit of AP2 (sequence GAGCAUGUGCACGCUGGCCAdTdT) was

Gene	Product Codes		
ARFGEF2	s20728	s20729	s20730
FGD1	s5121	s5122	s5123
IQSEC1	s19245	s19246	s19247
HERC1	s17065	s17066	s17067
PSD3	s23653	s23654	s23655
SOS1	s13285	s13286	s13287
VAV2	s14753	s14754	s14755
ASAP2	s16903	s16904	s16905
TBC1D2	s30819	s30820	s30821
TBC1D4	s19140	s19141	s19142
TBC1D5	s229656	s229657	s229658
TBC1D10B	s24904	s24905	s24906
TBC1D14	s33244	s33245	s33246
TBC1D15	s34944	s34945	s34946
USP6NL	s18719	s18720	s18721
TSC2	s14436	s14437	s14438

Table 7.1: siRNA library details. Product codes for siRNA library from the Silencer Select product range (Ambion)

from (Dharmacon RNAi) [248]. All other siRNA was from the Silencer Select range (Ambion) and is listed in table 7.1. A final siRNA concentration of $5nM$ was used. Cells were imaged after 48 hours expression.

7.4 Imaging Protocols

7.4.1 Fixed Cell Experiments for siRNA screen

In fixed cell imaging experiments, cells were prepared in 24 well glass bottomed dished (MaTek). For EGF stimulation experiments, cells were washed with with $500\mu l$ DPBS (Lonza) and serum starved in serum/antibiotic free cell culture media for 30 minutes (37 °C, 5% CO_2). Cells then treated with EGF ($100ng/ml$) (Bachem)(stock at $1mg/ml$ in DPBS) as appropriate (typically $100ng/ml$) and incubated for a further 30 minutes. To fix, cells where washed twice with $500\mu l$ DPBS before adding $250\mu l$ of 4% Paraformaldehyde (PFA) (Electron Microscopy Sciences) (16% stock diluted with DPBS). After 10 minutes incubation at room temperature, cells were washed a further two times with DPBS and left in $500\mu l$ DPBS at $4\,°C$ for a maximum of 6 hours before imaging.

7.4.2 Live Cell Time-lapse Experiments with Drug Treatments

Cells were prepared in $35mm$ glass bottomed dishes (MaTek). Prior to imaging, cells were washed with $1ml$ DPBS (Lonza) and serum starved in $2ml$ serum/antibiotic free cell culture media for 30 minutes ($37\,°C$, 5% CO_2). Media replaced with $2.5ml$ CIM (section 7.1) and treated with either $5\mu g/ml$ AG1478 (Sigma) ($1\mu l/ml$ DMSO:MeOH $1:1$ vehicle), $80\mu M$ dynasore hydrate (Sigma) ($1\mu l/ml$ DMSO vehicle) or $50nM$ Dasatinib (Sellek Chemicals) ($1\mu l/ml$ DMSO vehicle). Control cells were treated with $1\mu l/ml$ dimethyl sulfoxide (DMSO) (Sigma). Cells were incubated for a further 30 minutes before transfer to the microscope, where the cells were treated with EGF ($2ng/ml$) immediately prior to beginning the time-lapse.

7.4.3 Confocal Microscopy

Confocal images acquired using a Eclipse Ti, Nikon A1R inverted microscope. An Argon-Ion 457-514nm laser was used to excite the EGFR-EGFP construct and a Green Diode 561 nm laser was used for the rab5-mRFP construct. Images were captured using a 100x 1.49 NA oil immersion objective and an Andor iXon 885 EMCCD camera. For live cell imaging and multi-point fixed cell, the Nikon Perfect Focus system was used to minimise axial focus drift. For live cell imaging, the samples were kept at $37\,°C$ and 5% CO_2. Singly labelled controls were used to confirm the lack of bleed-through between the EGFR-EGFP and rab5-mRFP channels under this setup.

7.5 Biochemistry Methods

7.5.1 Whole Cell Lysis

Cells were plated and treated as appropriate in plastic dishes (Corning). Cells were then washed twice with $1ml$ DPBS (Lonza) before adding a further $1ml$ DPBS and placing the plate on ice. In each well, cells were detached from the plate mechanically using a scraper and transferred to $1.5ml$ ependorfs (on ice). Samples were then centrifuged for 3 minutes at 4 °C and 5000RPM. Approximately 90% of supernatant was aspirated and the samples were centrifuged again under the same conditions. The remainder of the supernatant was then aspirated before adding $50\mu l$ of lysis buffer (section 7.1) and vortexing. Lysates were then incubated on ice for 1 hour, vortexing every 15 minutes. Lysates were then centrifuged for 10 minutes at 4 °C and 14000RPM. $50\mu l$ supernatant was then aspirated and added to $25\mu l$ of sample buffer (3X) (section 7.1). Lysates were stored at -20 °C.

7.5.2 Western Blotting

Whole cell lysate samples (section 7.5.1) were denatured by heating to 95 °C for 5 minutes. Samples were then separated by running through 10% polyacrylamide gels (section 7.1). $15\mu l$ of each sample was loaded per well. $15\mu l$ of Prestained Protein Marker, Broad Range ($7-175kDa$, BioLabs) was loaded in at least one empty well. Samples were run at $125V$ in 1× of running buffer (section 7.5.1) until the gel front was at the bottom of the cassette (approximately 2 hours). Protein was then transferred to Immobilon FL transfer membrane (activated in methanol) (Merck Millipore) in 1× transfer buffer (section 7.1) at $30V$ for 90 minutes. The membrane was then blocked in milk TBST (section 7.1) for 1 hour at room temperature. The membrane was then incubated with primary antibodies (in milk TBST) for 12-16 hours at 4 °C. The membrane was then washed 4 times (5 minutes) with $15ml$ high salt TBST (section 7.1). The membrane was then incubated with secondary antibodies as appropriate ($1\mu l$ in $15ml$ milk TBST) for 2 hours at room temperature. The membrane was then washed again, 4 times (5 minutes) with $15ml$ high salt TBST. The membrane was imaged using a Odyssey scanner (LI-COR biosciences) according to the manufacturer's instructions.

7.5.3 Antibodies

The anti-α-adaptin (Santa Cruz) and anti-α-tubulin (Sigma) primary antibodies were used at dilutions of 1:1000 and 1:10000 respectively. Mouse IgG IRDye800CW (LI-COR) and Rabbit IgG IRDye680CW (LI-COR) secondary antibodies were used at a dilution of 1:15000.

LIST OF REFERENCES

[1] Alexander Sorkin and Mark von Zastrow. Endocytosis and signalling: intertwining molecular networks. *Nature reviews Molecular cell biology*, 10(9):609–622, 2009.

[2] Prisca Liberali, Berend Snijder, and Lucas Pelkmans. A hierarchical map of regulatory genetic interactions in membrane trafficking. *Cell*, 157(6):1473–1487, 2014.

[3] Claudio Collinet, Martin Stöter, Charles R Bradshaw, Nikolay Samusik, Jochen C Rink, Denise Kenski, Bianca Habermann, Frank Buchholz, Robert Henschel, Matthias S Mueller, et al. Systems survey of endocytosis by multiparametric image analysis. *Nature*, 464(7286):243–249, 2010.

[4] Thierry Galvez, Mary N Teruel, Won Do Heo, Joshua T Jones, Man Lyang Kim, Jen Liou, Jason W Myers, and Tobias Meyer. sirna screen of the human signaling proteome identifies the ptdins (3, 4, 5) p. *Genome Biol*, 8:R142, 2007.

[5] Lucas Pelkmans, Eugenio Fava, Hannes Grabner, Michael Hannus, Bianca Habermann, Eberhard Krausz, and Marino Zerial. Genome-wide analysis of human kinases in clathrin-and caveolae/raft-mediated endocytosis. *Nature*, 436(7047):78–86, 2005.

[6] Arola Fortian and Alexander Sorkin. Live-cell fluorescence imaging reveals high stoichiometry of grb2 binding to the egf receptor sustained during endocytosis. *Journal of cell science*, 127(2):432–444, 2014.

[7] Giulio Auciello, Debbie L Cunningham, Tulin Tatar, John K Heath, and Joshua Z Rappoport. Regulation of fibroblast growth factor receptor signalling and trafficking by src and eps8. *Journal of cell science*, 126(2):613–624, 2013.

[8] Jeremy Adler and Ingela Parmryd. Quantifying colocalization by correlation: the pearson correlation coefficient is superior to the mander's overlap coefficient. *Cytometry Part A*, 77(8):733–742, 2010.

[9] Kenneth W Dunn, Malgorzata M Kamocka, and John H McDonald. A practical guide to evaluating colocalization in biological microscopy. *American Journal of Physiology-Cell Physiology*, 300(4):C723–C742, 2011.

[10] John H McDonald and Kenneth W Dunn. Statistical tests for measures of colocalization in biological microscopy. *Journal of microscopy*, 252(3):295–302, 2013.

[11] Timo Kohlberger, Daniel Cremers, Mikaël Rousson, Ramamani Ramaraj, and Gareth Funka-Lea. 4d shape priors for a level set segmentation of the left myocardium in spect sequences. In *Medical Image Computing and Computer-Assisted Intervention–MICCAI 2006*, pages 92–100. Springer, 2006.

[12] Amer Abufadel, Tony Yezzi, and Ronald W Schafer. *4D segmentation of cardiac data using active surfaces with spatiotemporal shape priors*. Springer, 2008.

[13] Vicent Caselles, Ron Kimmel, and Guillermo Sapiro. Geodesic active contours. *International journal of computer vision*, 22(1):61–79, 1997.

[14] Tony F Chan, Luminita Vese, et al. Active contours without edges. *Image processing, IEEE transactions on*, 10(2):266–277, 2001.

[15] Rita Levi-Montalcini, Hertha Meyer, and Viktor Hamburger. In vitro experiments on the effects of mouse sarcomas 180 and 37 on the spinal and sympathetic ganglia of the chick embryo. *Cancer research*, 14(1):49–57, 1954.

[16] Stanley Cohen. Isolation of a mouse submaxillary gland protein accelerating incisor eruption and eyelid opening in the new-born animal. *Journal of Biological Chemistry*, 237(5):1555–1562, 1962.

[17] S Cohen, G Carpenter, and L King Jr. Epidermal growth factor-receptor-protein kinase interactions. *Progress in clinical and biological research*, 66:557–567, 1980.

[18] Graham Carpenter. The biochemistry and physiology of the receptor-kinase for epidermal growth factor. *Molecular and cellular endocrinology*, 31(1):1–19, 1983.

[19] Dan R Robinson, Yi-Mi Wu, and Su-Fang Lin. The protein tyrosine kinase family of the human genome. *Oncogene*, 19(49):5548–5557, 2000.

[20] Hans-Dietmar Beer, Michael T Longaker, and Sabine Werner. Reduced expression of pdgf and pdgf receptors during impaired wound healing. *Journal of Investigative Dermatology*, 109(2):132–138, 1997.

[21] Heather M Bill, Beatrice Knudsen, Sheri L Moores, Senthil K Muthuswamy, Vikram R Rao, Joan S Brugge, and Cindy K Miranti. Epidermal growth factor receptor-dependent regulation of integrin-mediated signaling and cell cycle entry in epithelial cells. *Molecular and cellular biology*, 24(19):8586–8599, 2004.

[22] Guo-Hua Fong, Janet Rossant, Marina Gertsenstein, and Martin L Breitman. Role of the flt-1 receptor tyrosine kinase in regulating the assembly of vascular endothelium. *Nature*, 376(6535):66–70, 1995.

[23] Hidenori Ichijo, Eisuke Nishida, Kenji Irie, Peter ten Dijke, Masao Saitoh, Tetsuo Moriguchi, Minoru Takagi, Kunihiro Matsumoto, Kohei Miyazono, and Yukiko Gotoh. Induction of apoptosis by ask1, a mammalian mapkkk that activates sapk/jnk and p38 signaling pathways. *Science*, 275(5296):90–94, 1997.

[24] Dipa Natarajan, Camelia Marcos-Gutierrez, Vassilis Pachnis, and Esther de Graaff. Requirement of signalling by receptor tyrosine kinase ret for the directed migration of enteric nervous system progenitor cells during mammalian embryogenesis. *Development*, 129(22):5151–5160, 2002.

[25] Ren-He Xu, Ruthann M Peck, Dong S Li, Xuezhu Feng, Tenneille Ludwig, and James A Thomson. Basic fgf and suppression of bmp signaling sustain undifferentiated proliferation of human es cells. *Nature methods*, 2(3):185–190, 2005.

[26] Peter Blume-Jensen and Tony Hunter. Oncogenic kinase signalling. *Nature*, 411(6835):355–365, 2001.

[27] Stevan R Hubbard and Jeffrey H Till. Protein tyrosine kinase structure and function. *Annual review of biochemistry*, 69(1):373–398, 2000.

[28] Mark A Lemmon and Joseph Schlessinger. Cell signaling by receptor tyrosine kinases. *Cell*, 141(7):1117–1134, 2010.

[29] Rong-Hua Tao and Ichi N Maruyama. All egf (erbb) receptors have preformed homo- and heterodimeric structures in living cells. *Journal of cell science*, 121(19):3207–3217, 2008.

[30] AM Honegger, RM Kris, A Ullrich, and J Schlessinger. Evidence that autophosphorylation of solubilized receptors for epidermal growth factor is mediated by intermolecular cross-phosphorylation. *Proceedings of the National Academy of Sciences*, 86(3):925–929, 1989.

[31] Cristina M Furdui, Erin D Lew, Joseph Schlessinger, and Karen S Anderson. Autophosphorylation of fgfr1 kinase is mediated by a sequential and precisely ordered reaction. *Molecular cell*, 21(5):711–717, 2006.

[32] Kathryn M Ferguson, Paul J Darling, Mohita J Mohan, Timothy L Macatee, and Mark A Lemmon. Extracellular domains drive homo-but not hetero-dimerization of erbb receptors. *The EMBO journal*, 19(17):4632–4643, 2000.

[33] Mark A Lemmon, Joseph Schlessinger, and Kathryn M Ferguson. The egfr family: not so prototypical receptor tyrosine kinases. *Cold Spring Harbor perspectives in biology*, 6(4):a020768, 2014.

[34] Nancy E Hynes and Heidi A Lane. Erbb receptors and cancer: the complexity of targeted inhibitors. *Nature Reviews Cancer*, 5(5):341–354, 2005.

[35] Eldad Tzahar, Hadassa Waterman, Xiomei Chen, Gil Levkowitz, Devarajan Karunagaran, Sara Lavi, Barry J Ratzkin, and Yosef Yarden. A hierarchical network of interreceptor interactions determines signal transduction by neu differentiation factor/neuregulin and epidermal growth factor. *Molecular and cellular biology*, 16(10):5276–5287, 1996.

[36] Ami Citri and Yosef Yarden. Egf–erbb signalling: towards the systems level. *Nature reviews Molecular cell biology*, 7(7):505–516, 2006.

[37] Thomas PJ Garrett, Neil M McKern, Meizhen Lou, Thomas C Elleman, Timothy E Adams, George O Lovrecz, Hong-Jian Zhu, Francesca Walker, Morry J Frenkel, Peter A Hoyne, et al. Crystal structure of a truncated epidermal growth factor receptor extracellular domain bound to transforming growth factor α. *Cell*, 110(6):763–773, 2002.

[38] Antony W Burgess, Hyun-Soo Cho, Charles Eigenbrot, Kathryn M Ferguson, Thomas PJ Garrett, Daniel J Leahy, Mark A Lemmon, Mark X Sliwkowski, Colin W Ward, and Shigeyuki Yokoyama. An open-and-shut case? recent insights into the activation of egf/erbb receptors. *Molecular cell*, 12(3):541–552, 2003.

[39] Natalia Jura, Nicholas F Endres, Kate Engel, Sebastian Deindl, Rahul Das, Meindert H Lamers, David E Wemmer, Xuewu Zhang, and John Kuriyan. Mechanism for activation of the egf receptor catalytic domain by the juxtamembrane segment. *Cell*, 137(7):1293–1307, 2009.

[40] Xuewu Zhang, Jodi Gureasko, Kui Shen, Philip A Cole, and John Kuriyan. An allosteric mechanism for activation of the kinase domain of epidermal growth factor receptor. *Cell*, 125(6):1137–1149, 2006.

[41] Waltraud X Schulze, Lei Deng, and Matthias Mann. Phosphotyrosine interactome of the erbb-receptor kinase family. *Molecular systems biology*, 1(1), 2005.

[42] Robert N Jorissen, Francesca Walker, Normand Pouliot, Thomas PJ Garrett, Colin W Ward, and Antony W Burgess. Epidermal growth factor receptor: mechanisms of activation and signalling. *Experimental cell research*, 284(1):31–53, 2003.

[43] Henryk Dudek, Sandeep Robert Datta, Thomas F Franke, Morris J Birnbaum, Ryoji Yao, Geoffrey M Cooper, Rosalind A Segal, David R Kaplan, and Michael E Greenberg. Regulation of neuronal survival by the serine-threonine protein kinase akt. *Science*, 275(5300):661–665, 1997.

[44] Sandeep Robert Datta, Henryk Dudek, Xu Tao, Shane Masters, Haian Fu, Yukiko Gotoh, and Michael E Greenberg. Akt phosphorylation of bad couples survival signals to the cell-intrinsic death machinery. *Cell*, 91(2):231–241, 1997.

[45] Kevin M Pumiglia and Stuart J Decker. Cell cycle arrest mediated by the mek/mitogen-activated protein kinase pathway. *Proceedings of the National Academy of Sciences*, 94(2):448–452, 1997.

[46] Gilles Pagès, Sandrine Guérin, Dominique Grall, Frédéric Bonino, Austin Smith, Fabienne Anjuere, Patrick Auberger, and Jacques Pouysségur. Defective thymocyte maturation in p44 map kinase (erk 1) knockout mice. *Science*, 286(5443):1374–1377, 1999.

[47] Kanae Oda, Yukiko Matsuoka, Akira Funahashi, and Hiroaki Kitano. A comprehensive pathway map of epidermal growth factor receptor signaling. *Molecular systems biology*, 1(1), 2005.

[48] Roi Avraham and Yosef Yarden. Feedback regulation of egfr signalling: decision making by early and delayed loops. *Nature reviews Molecular cell biology*, 12(2):104–117, 2011.

[49] Sven Zimmermann and Karin Moelling. Phosphorylation and regulation of raf by akt (protein kinase b). *Science*, 286(5445):1741–1744, 1999.

[50] Michele K Dougherty, Jürgen Müller, Daniel A Ritt, Ming Zhou, Xiao Zhen Zhou, Terry D Copeland, Thomas P Conrads, Timothy D Veenstra, Kun Ping Lu, and Deborah K Morrison. Regulation of raf-1 by direct feedback phosphorylation. *Molecular cell*, 17(2):215–224, 2005.

[51] Maria Sörby et al. Protein-tyrosine phosphatase-mediated decrease of epidermal growth factor and platelet-derived growth factor receptor tyrosine phosphorylation in high cell density cultures. *Journal of Biological Chemistry*, 271(18):10963–10966, 1996.

[52] Yun Soo Bae, Sang Won Kang, Min Seok Seo, Ivan C Baines, Ephrem Tekle, P Boon Chock, and Sue Goo Rhee. Epidermal growth factor (egf)-induced generation of hydrogen peroxide role in egf receptor-mediated tyrosine phosphorylation. *Journal of Biological Chemistry*, 272(1):217–221, 1997.

[53] Andrew R Reynolds, Christian Tischer, Peter J Verveer, Oliver Rocks, and Philippe IH Bastiaens. Egfr activation coupled to inhibition of tyrosine phosphatases causes lateral signal propagation. *Nature cell biology*, 5(5):447–453, 2003.

[54] Rebecca J Webster, Keith M Giles, Karina J Price, Priscilla M Zhang, John S Mattick, and Peter J Leedman. Regulation of epidermal growth factor receptor signaling in human cancer cells by microrna-7. *Journal of Biological Chemistry*, 284(9):5731–5741, 2009.

[55] Xin Li and Richard W Carthew. A microrna mediates egf receptor signaling and promotes photoreceptor differentiation in the drosophila eye. *Cell*, 123(7):1267–1277, 2005.

[56] Steven M Johnson, Helge Grosshans, Jaclyn Shingara, Mike Byrom, Rich Jarvis, Angie Cheng, Emmanuel Labourier, Kristy L Reinert, David Brown, and Frank J Slack. Ras is regulated by the let-7 microrna family. *Cell*, 120(5):635–647, 2005.

[57] Roi Avraham, Aldema Sas-Chen, Ohad Manor, Israel Steinfeld, Reut Shalgi, Gabi Tarcic, Noa Bossel, Amit Zeisel, Ido Amit, Yaara Zwang, et al. Egf decreases the abundance of micrornas that restrain oncogenic transcription factors. *Sci Signal*, 3(124):ra43, 2010.

[58] Amandio V Vieira, Christophe Lamaze, and Sandra L Schmid. Control of egf receptor signaling by clathrin-mediated endocytosis. *Science*, 274(5295):2086–2089, 1996.

[59] Lai Kuan Goh and Alexander Sorkin. Endocytosis of receptor tyrosine kinases. *Cold Spring Harbor perspectives in biology*, 5(5):a017459, 2013.

[60] Satyajit Mayor and Richard E Pagano. Pathways of clathrin-independent endocytosis. *Nature reviews Molecular cell biology*, 8(8):603–612, 2007.

[61] Sara Sigismund, Tanja Woelk, Claudia Puri, Elena Maspero, Carlo Tacchetti, Pietro Transidico, Pier Paolo Di Fiore, and Simona Polo. Clathrin-independent endocytosis of ubiquitinated cargos. *Proceedings of the National Academy of Sciences of the United States of America*, 102(8):2760–2765, 2005.

[62] Sara Sigismund, Elisabetta Argenzio, Daniela Tosoni, Elena Cavallaro, Simona Polo, and Pier Paolo Di Fiore. Clathrin-mediated internalization is essential for sustained egfr signaling but dispensable for degradation. *Developmental cell*, 15(2):209–219, 2008.

[63] Sara Sigismund, Veronica Algisi, Gilda Nappo, Alexia Conte, Roberta Pascolutti, Alessandro Cuomo, Tiziana Bonaldi, Elisabetta Argenzio, Lisette GGC Verhoef, Elena Maspero, et al. Threshold-controlled ubiquitination of the egfr directs receptor fate. *The EMBO journal*, 32(15):2140–2157, 2013.

[64] Harvey T McMahon and Emmanuel Boucrot. Molecular mechanism and physiological functions of clathrin-mediated endocytosis. *Nature reviews Molecular cell biology*, 12(8):517–533, 2011.

[65] Lasse Henriksen, Michael Vibo Grandal, SL Knudsen, Bo van Deurs, and Lene Melsaether Grovdal. Internalization mechanisms of the epidermal growth factor receptor after activation with different ligands. *PloS one*, 8(3), 2013.

[66] Alejandra Tomas, Clare E Futter, and Emily R Eden. Egf receptor trafficking: consequences for signaling and cancer. *Trends in cell biology*, 24(1):26–34, 2014.

[67] Alina De Donatis, Giusy Comito, Francesca Buricchi, Maria C Vinci, Astrid Parenti, Anna Caselli, Guido Camici, Giampaolo Manao, Giampietro Ramponi, and Paolo Cirri. Proliferation versus migration in platelet-derived growth factor signaling the key role of endocytosis. *Journal of Biological Chemistry*, 283(29):19948–19956, 2008.

[68] Barth D Grant and Julie G Donaldson. Pathways and mechanisms of endocytic recycling. *Nature reviews Molecular cell biology*, 10(9):597–608, 2009.

[69] Graham Carpenter and Hong-Jun Liao. Trafficking of receptor tyrosine kinases to the nucleus. *Experimental cell research*, 315(9):1556–1566, 2009.

[70] Michelle L Demory, Julie L Boerner, Robert Davidson, William Faust, Tsuyoshi Miyake, Icksoo Lee, Maik Hüttemann, Robert Douglas, Gabriel Haddad, and Sarah J Parsons. Epidermal growth factor receptor translocation to the mitochondria regulation and effect. *Journal of Biological Chemistry*, 284(52):36592–36604, 2009.

[71] Michael J Clague, Han Liu, and Sylvie Urbé. Governance of endocytic trafficking and signaling by reversible ubiquitylation. *Developmental cell*, 23(3):457–467, 2012.

[72] Senthil K Muthuswamy, Michael Gilman, and Joan S Brugge. Controlled dimerization of erbb receptors provides evidence for differential signaling by homo-and heterodimers. *Molecular and cellular biology*, 19(10):6845–6857, 1999.

[73] Anne EG Lenferink, Ronit Pinkas-Kramarski, Monique LM van de Poll, Marianne JH van Vugt, Leah N Klapper, Eldad Tzahar, Hadassa Waterman, Michael Sela, Everardus JJ van Zoelen, and Yosef Yarden. Differential endocytic routing of homo-and hetero-dimeric erbb tyrosine kinases confers signaling superiority to receptor heterodimers. *The EMBO journal*, 17(12):3385–3397, 1998.

[74] Kirstine Roepstorff, Michael Vibo Grandal, Lasse Henriksen, Stine Louise Jeppe Knudsen, Mads Lerdrup, Lene Grøvdal, Berthe Marie Willumsen, and Bo Van Deurs. Differential effects of egfr ligands on endocytic sorting of the receptor. *Traffic*, 10(8):1115–1127, 2009.

[75] Anthony R French, Douglas K Tadaki, Salil K Niyogi, and Douglas A Lauffenburger. Intracellular trafficking of epidermal growth factor family ligands is directly influenced by the ph sensitivity of the receptor/ligand interaction. *Journal of Biological Chemistry*, 270(9):4334–4340, 1995.

[76] Emily R Eden, Fangtian Huang, Alexander Sorkin, and Clare E Futter. The role of egf receptor ubiquitination in regulating its intracellular traffic. *Traffic*, 13(2):329–337, 2012.

[77] David D Tran, Helen R Russell, Shari L Sutor, Jan van Deursen, and Richard J Bram. Caml is required for efficient egf receptor recycling. *Developmental cell*, 5(2):245–256, 2003.

[78] Susan Chi, Hong Cao, Yu Wang, and Mark A McNiven. Recycling of the epidermal growth factor receptor is mediated by a novel form of the clathrin adaptor protein eps15. *Journal of Biological Chemistry*, 286(40):35196–35208, 2011.

[79] Jiefei Tong, Yaroslav Sydorskyy, Jonathan R St-Germain, Paul Taylor, Ming S Tsao, Michael F Moran, et al. Odin (anks1a) modulates egf receptor recycling and stability. *PloS one*, 8(6), 2013.

[80] Ulrich Marti, Susan Jo Burwen, Alan Wells, Mary E Barker, Sandra Huling, Anna M Feren, and Albert L Jones. Localization of epidermal growth factor receptor in hepatocyte nuclei. *Hepatology*, 13(1):15–20, 1991.

[81] YN Wang, H Yamaguchi, JM Hsu, and MC Hung. Nuclear trafficking of the epidermal growth factor receptor family membrane proteins. *Oncogene*, 29(28):3997–4006, 2010.

[82] Xinyu Cao, Hu Zhu, Francis Ali-Osman, and Hui-Wen Lo. Egfr and egfrviii undergo stress-and egfr kinase inhibitor-induced mitochondrial translocalization: a potential mechanism of egfr-driven antagonism of apoptosis. *Mol Cancer*, 10(26):2499–2513, 2011.

[83] GM Di Guglielmo, PC Baass, WJ Ou, BI Posner, and JJ Bergeron. Compartmentalization of shc, grb2 and msos, and hyperphosphorylation of raf-1 by egf but not insulin in liver parenchyma. *The EMBO journal*, 13(18):4269, 1994.

[84] Mark L Grimes, Eric Beattie, and William C Mobley. A signaling organelle containing the nerve growth factor-activated receptor tyrosine kinase, trka. *Proceedings of the National Academy of Sciences*, 94(18):9909–9914, 1997.

[85] Charles L Howe and William C Mobley. Signaling endosome hypothesis: A cellular mechanism for long distance communication. *Journal of neurobiology*, 58(2):207–216, 2004.

[86] Roshanak Irannejad, Nikoleta G Tsvetanova, Braden T Lobingier, and Mark von Zastrow. Effects of endocytosis on receptor-mediated signaling. *Current opinion in cell biology*, 35:137–143, 2015.

[87] David Teis, Nicole Taub, Robert Kurzbauer, Diana Hilber, Mariana E de Araujo, Miriam Erlacher, Martin Offterdinger, Andreas Villunger, Stephan Geley, Georg Bohn, et al. p14–mp1-mek1 signaling regulates endosomal traffic and cellular proliferation during tissue homeostasis. *The Journal of cell biology*, 175(6):861–868, 2006.

[88] Marta Miaczynska, Savvas Christoforidis, Angelika Giner, Anna Shevchenko, Sandrine Uttenweiler-Joseph, Bianca Habermann, Matthias Wilm, Robert G Parton, and Marino Zerial. Appl proteins link rab5 to nuclear signal transduction via an endosomal compartment. *Cell*, 116(3):445–456, 2004.

[89] Roberto Villaseñor, Hidenori Nonaka, Perla Del Conte-Zerial, Yannis Kalaidzidis, and Marino Zerial. Regulation of egfr signal transduction by analogue-to-digital conversion in endosomes. *eLife*, 4:e06156, 2015.

[90] Nancy E Hynes and Gwen MacDonald. Erbb receptors and signaling pathways in cancer. *Current opinion in cell biology*, 21(2):177–184, 2009.

[91] Dennis J Slamon, Gary M Clark, Steven G Wong, Wendy J Levin, Axel Ullrich, and William L McGuire. Human breast cancer: correlation of relapse and survival with amplification of the her-2/neu oncogene. *Science*, 235(4785):177–182, 1987.

[92] Jeffrey A Engelman, Pasi A Jänne, Craig Mermel, Joseph Pearlberg, Toru Mukohara, Christina Fleet, Karen Cichowski, Bruce E Johnson, and Lewis C Cantley. Erbb-3 mediates phosphoinositide 3-kinase activity in gefitinib-sensitive non-small cell lung cancer cell lines. *Proceedings of the National Academy of Sciences of the United States of America*, 102(10):3788–3793, 2005.

[93] Julie L Boerner, Andrew Danielsen, and Nita J Maihle. Ligand-independent oncogenic signaling by the epidermal growth factor receptor: v-erbb as a paradigm. *Experimental cell research*, 284(1):111–121, 2003.

[94] K Shtiegman, BS Kochupurakkal, Y Zwang, G Pines, A Starr, A Vexler, A Citri, M Katz, S Lavi, Y Ben-Basat, et al. Defective ubiquitinylation of egfr mutants of lung cancer confers prolonged signaling. *Oncogene*, 26(49):6968–6978, 2007.

[95] Byung M Chung, Srikumar M Raja, Robert J Clubb, Chun Tu, Manju George, Vimla Band, and Hamid Band. Aberrant trafficking of nsclc-associated egfr mutants through the endocytic recycling pathway promotes interaction with src@. *BMC cell biology*, 10(1):84, 2009.

[96] Byung Min Chung, Manjari Dimri, Manju George, Alagarsamy Lakku Reddi, Gengsheng Chen, Vimla Band, and Hamid Band. The role of cooperativity with src in oncogenic transformation mediated by non-small cell lung cancer-associated egf receptor mutants. *Oncogene*, 28(16):1821–1832, 2009.

[97] Meiling Gao, Rachana Patel, Imran Ahmad, Janis Fleming, Joanne Edwards, Stuart McCracken, Kanagasabai Sahadevan, Morag Seywright, Jim Norman, Owen Sansom, et al. Spry2 loss enhances erbb trafficking and pi3k/akt signalling to drive human and mouse prostate carcinogenesis. *EMBO molecular medicine*, 4(8):776–790, 2012.

[98] Yaara Zwang and Yosef Yarden. p38 map kinase mediates stress-induced internalization of egfr: implications for cancer chemotherapy. *The EMBO journal*, 25(18):4195–4206, 2006.

[99] Ana Markovic and Christine H Chung. Current role of egf receptor monoclonal antibodies and tyrosine kinase inhibitors in the management of head and neck squamous cell carcinoma. *Expert review of anticancer therapy*, 12(9):1149–1159, 2012.

[100] Jacqueline Cherfils and Mahel Zeghouf. Regulation of small gtpases by gefs, gaps, and gdis. *Physiological reviews*, 93(1):269–309, 2013.

[101] Christian Lenzen, Robbert H Cool, Heino Prinz, Jürgen Kuhlmann, and Alfred Wittinghofer. Kinetic analysis by fluorescence of the interaction between ras and the catalytic domain of the guanine nucleotide exchange factor cdc25mm. *Biochemistry*, 37(20):7420–7430, 1998.

[102] Johannes L Bos, Holger Rehmann, and Alfred Wittinghofer. Gefs and gaps: critical elements in the control of small g proteins. *Cell*, 129(5):865–877, 2007.

[103] Petra Gideon, Jacob John, Matthias Frech, Alfred Lautwein, Robin Clark, Julie E Scheffler, and Alfred Wittinghofer. Mutational and kinetic analyses of the gtpase-activating protein (gap)-p21 interaction: the c-terminal domain of gap is not sufficient for full activity. *Molecular and Cellular Biology*, 12(5):2050–2056, 1992.

[104] Dominico Vigil, Jacqueline Cherfils, Kent L Rossman, and Channing J Der. Ras superfamily gefs and gaps: validated and tractable targets for cancer therapy? *Nature Reviews Cancer*, 10(12):842–857, 2010.

[105] Harald Stenmark. Rab gtpases as coordinators of vesicle traffic. *Nature reviews Molecular cell biology*, 10(8):513–525, 2009.

[106] Julie G Donaldson and Catherine L Jackson. Arf family g proteins and their regulators: roles in membrane transport, development and disease. *Nature reviews Molecular cell biology*, 12(6):362–375, 2011.

[107] Sophia Semerdjieva, Barry Shortt, Emma Maxwell, Sukhdeep Singh, Paul Fonarev, Jonathan Hansen, Giampietro Schiavo, Barth D Grant, and Elizabeth Smythe. Coordinated regulation of ap2 uncoating from clathrin-coated vesicles by rab5 and hrme-6. *The Journal of cell biology*, 183(3):499–511, 2008.

[108] Jean-Pierre Gorvel, Philippe Chavrier, Marino Zerial, and Jean Gruenberg. rab5 controls early endosome fusion in vitro. *Cell*, 64(5):915–925, 1991.

[109] Harald Stenmark, Robert G Parton, Olivia Steele-Mortimer, A Lütcke, Jean Gruenberg, and M Zerial. Inhibition of rab5 gtpase activity stimulates membrane fusion in endocytosis. *The EMBO journal*, 13(6):1287, 1994.

[110] Erik Nielsen, Fedor Severin, Jonathan M Backer, Anthony A Hyman, and Marino Zerial. Rab5 regulates motility of early endosomes on microtubules. *Nature Cell Biology*, 1(6):376–382, 1999.

[111] Annette Schenck, Livia Goto-Silva, Claudio Collinet, Muriel Rhinn, Angelika Giner, Bianca Habermann, Michael Brand, and Marino Zerial. The endosomal protein appl1 mediates akt substrate specificity and cell survival in vertebrate development. *Cell*, 133(3):486–497, 2008.

[112] Gregory G Tall, M Alejandro Barbieri, Philip D Stahl, and Bruce F Horazdovsky. Ras-activated endocytosis is mediated by the rab5 guanine nucleotide exchange activity of rin1. *Developmental cell*, 1(1):73–82, 2001.

[113] Pin-I Chen, Chen Kong, Xiong Su, and Philip D Stahl. Rab5 isoforms differentially regulate the trafficking and degradation of epidermal growth factor receptors. *Journal of Biological Chemistry*, 284(44):30328–30338, 2009.

[114] Kavitha Balaji, Chelsea Mooser, Christine M Janson, Joanne M Bliss, Houmehr Hojjat, and John Colicelli. Rin1 orchestrates the activation of rab5 gtpases and abl tyrosine kinases to determine the fate of egfr. *Journal of cell science*, 125(23):5887–5896, 2012.

[115] Crislyn D'Souza-Schorey and Philippe Chavrier. Arf proteins: roles in membrane traffic and beyond. *Nature reviews Molecular cell biology*, 7(5):347–358, 2006.

[116] Jill Kuglin Schweitzer, Alanna E Sedgwick, and Crislyn D'Souza-Schorey. Arf6-mediated endocytic recycling impacts cell movement, cell division and lipid homeostasis. In *Seminars in cell & developmental biology*, volume 22, pages 39–47. Elsevier, 2011.

[117] Patrick D Allaire, Mohamed Seyed Sadr, Mathilde Chaineau, Emad Seyed Sadr, Sarah Konefal, Maryam Fotouhi, Deborah Maret, Brigitte Ritter, Rolando F Del Maestro, and Peter S McPherson. Interplay between rab35 and arf6 controls cargo recycling to coordinate cell adhesion and migration. *Journal of cell science*, 126(3):722–731, 2013.

[118] Aimee M Powelka, Jianlan Sun, Jian Li, Minggeng Gao, Leslie M Shaw, Arnoud Sonnenberg, and Victor W Hsu. Stimulation-dependent recycling of integrin $\beta1$ regulated by arf6 and rab11. *Traffic*, 5(1):20–36, 2004.

[119] Felipe Palacios, Jogender S Tushir, Yasuyuki Fujita, and Crislyn D'Souza-Schorey. Lysosomal targeting of e-cadherin: a unique mechanism for the down-regulation of cell-cell adhesion during epithelial to mesenchymal transitions. *Molecular and cellular biology*, 25(1):389–402, 2005.

[120] Shigeru Hashimoto, Yasuhito Onodera, Ari Hashimoto, Miwa Tanaka, Michinari Hamaguchi, Atsuko Yamada, and Hisataka Sabe. Requirement for arf6 in breast cancer invasive activities. *Proceedings of the National Academy of Sciences of the United States of America*, 101(17):6647–6652, 2004.

[121] Vandhana Muralidharan-Chari, Holly Hoover, James Clancy, Jill Schweitzer, Mark A Suckow, Valerie Schroeder, Francis J Castellino, Jeffrey S Schorey, and Crislyn D'Souza-Schorey. Adp-ribosylation factor 6 regulates tumorigenic and invasive properties in vivo. *Cancer research*, 69(6):2201–2209, 2009.

[122] Masaki Morishige, Shigeru Hashimoto, Eiji Ogawa, Yoshinobu Toda, Hirokazu Kotani, Mayumi Hirose, Shumei Wei, Ari Hashimoto, Atsuko Yamada, Hajime Yano, et al. Gep100 links epidermal growth factor receptor signalling to arf6 activation to induce breast cancer invasion. *Nature cell biology*, 10(1):85–92, 2008.

[123] Hisataka Sabe, Shigeru Hashimoto, Masaki Morishige, Eiji Ogawa, Ari Hashimoto, Jin-Min Nam, Koichi Miura, Hajime Yano, and Yasuhito Onodera. The egfr-gep100-arf6-amap1 signaling pathway specific to breast cancer invasion and metastasis. *Traffic*, 10(8):982–993, 2009.

[124] Dana M Brantley-Sieders, Guanglei Zhuang, David Vaught, Tanner Freeman, Yoonha Hwang, Donna Hicks, and Jin Chen. Host deficiency in vav2/3 guanine nucleotide exchange factors impairs tumor growth, survival, and angiogenesis in vivo. *Molecular Cancer Research*, 7(5):615–623, 2009.

[125] Vyomesh Patel, Hans M Rosenfeldt, Ruth Lyons, Joan-Marc Servitja, Xosé R Bustelo, Mary Siroff, and J Silvio Gutkind. Persistent activation of rac1 in squamous carcinomas of the head and neck: evidence for an egfr/vav2 signaling axis involved in cell invasion. *Carcinogenesis*, 28(6):1145–1152, 2007.

[126] S Thalappilly, P Soubeyran, JL Iovanna, and NJ Dusetti. Vav2 regulates epidermal growth factor receptor endocytosis and degradation. *Oncogene*, 29(17):2528–2539, 2010.

[127] Elena Mossessova, Richard A Corpina, and Jonathan Goldberg. Crystal structure of arf1 sec7 complexed with brefeldin a and its implications for the guanine nucleotide exchange mechanism. *Molecular cell*, 12(6):1403–1411, 2003.

[128] Julien Viaud, Mahel Zeghouf, Hélène Barelli, Jean-Christophe Zeeh, André Padilla, Bernard Guibert, Pierre Chardin, Catherine A Royer, Jacqueline Cherfils, and Alain Chavanieu. Structure-based discovery of an inhibitor of arf activation by sec7 domains through targeting of protein–protein complexes. *Proceedings of the National Academy of Sciences*, 104(25):10370–10375, 2007.

[129] William Herschel. On a case of superficial colour presented by a homogeneous liquid internally colourless. *Philosophical Transactions of the Royal Society of London*, pages 143–145, 1845.

[130] Gabriel Stokes. On the change of refrangibility of light. *Philosophical Transactions of the Royal Society of London*, pages 463–562, 1852.

[131] A Jaboski. Efficiency of anti-stokes fluorescence in dyes. *Nature*, 131(839-840):21, 1933.

[132] Oskar Heimstädt. Das fluoreszenzmikroskop. *Z Wiss Mikrosk*, 28:330–337, 1911.

[133] August Köhler. Ein neues beleuchtungsverfahren für mikrophotographische zwecke. *Zeitschrift für wissenschaftliche Mikroskopie und für mikroskopische Technik*, 10(4):433–440, 1893.

[134] Hagai Kirshner, Franois Aguet, Daniel Sage, and Michael Unser. 3-d psf fitting for fluorescence microscopy: implementation and localization application. *Journal of microscopy*, 249(1):13–25, 2013.

[135] Max Born and Emil Wolf. *Principles of optics: electromagnetic theory of propagation, interference and diffraction of light*. Cambridge university press, 1999.

[136] William Thomas Eric Pitkeathly. *Four dimensional analysis of vesicle dynamics during directed cell migration*. PhD thesis, University of Birmingham, 2016.

[137] Robert H Webb. Confocal optical microscopy. *Reports on Progress in Physics*, 59(3):427, 1996.

[138] James B Pawley. Sources of noise in three-dimensional microscopical data sets. *Three-Dimensional Confocal Microscopy: Volume Investigation of Biological Specimens*, pages 47–94, 2012.

[139] Colin JR Sheppard, Xiaosong Gan, Min Gu, and Maitreyee Roy. Signal-to-noise ratio in confocal microscopes. In *Handbook of biological confocal microscopy*, pages 442–452. Springer, 2006.

[140] Florian Luisier, Thierry Blu, and Michael Unser. Image denoising in mixed poisson–gaussian noise. *Image Processing, IEEE Transactions on*, 20(3):696–708, 2011.

[141] Nathan C Shaner, Paul A Steinbach, and Roger Y Tsien. A guide to choosing fluorescent proteins. *Nature methods*, 2(12):905–909, 2005.

[142] Alison J North. Seeing is believing? a beginners' guide to practical pitfalls in image acquisition. *The Journal of cell biology*, 172(1):9–18, 2006.

[143] Jeremy Sanderson. Fluorescence bleed-through. Accessed: 13-07-2015.

[144] K David Wegner and Niko Hildebrandt. Quantum dots: bright and versatile in vitro and in vivo fluorescence imaging biosensors. *Chemical Society Reviews*, 2015.

[145] Ben NG Giepmans, Stephen R Adams, Mark H Ellisman, and Roger Y Tsien. The fluorescent toolbox for assessing protein location and function. *Science*, 312(5771):217–224, 2006.

[146] Osamu Shimomura, Frank H Johnson, and Yo Saiga. Extraction, purification and properties of aequorin, a bioluminescent protein from the luminous hydromedusan, aequorea. *Journal of cellular and comparative physiology*, 59(3):223–239, 1962.

[147] Roger Y Tsien. The green fluorescent protein. *Annual review of biochemistry*, 67(1):509–544, 1998.

[148] Mikhail V Matz, Arkady F Fradkov, Yulii A Labas, Aleksandr P Savitsky, Andrey G Zaraisky, Mikhail L Markelov, and Sergey A Lukyanov. Fluorescent proteins from nonbioluminescent anthozoa species. *Nature biotechnology*, 17(10):969–973, 1999.

[149] Antoni Buades, Bartomeu Coll, and Jean-Michel Morel. A review of image denoising algorithms, with a new one. *Multiscale Modeling & Simulation*, 4(2):490–530, 2005.

[150] George L Turin. An introduction to digitial matched filters. *Proceedings of the IEEE*, 64(7):1092–1112, 1976.

[151] Bo Zhang, Josiane Zerubia, and Jean-Christophe Olivo-Marin. Gaussian approximations of fluorescence microscope point-spread function models. *Applied Optics*, 46(10):1819–1829, 2007.

[152] Ihor Smal, Marco Loog, Wiro Niessen, and Erik Meijering. Quantitative comparison of spot detection methods in fluorescence microscopy. *Medical Imaging, IEEE Transactions on*, 29(2):282–301, 2010.

[153] Daniel Sage, Franck R Neumann, Florence Hediger, Susan M Gasser, and Michael Unser. Automatic tracking of individual fluorescence particles: application to the study of chromosome dynamics. *Image Processing, IEEE Transactions on*, 14(9):1372–1383, 2005.

[154] Antoine Basset, Jérôme Boulanger, Patrick Bouthemy, Charles Kervrann, and Jean Salamero. Slt-log: A vesicle segmentation method with automatic scale selection and local thresholding applied to tirf microscopy. In *Biomedical Imaging (ISBI), 2014 IEEE 11th International Symposium on*, pages 533–536. IEEE, 2014.

[155] Stéphane Mallat. *A wavelet tour of signal processing.* Academic press, 1999.

[156] David L Donoho. De-noising by soft-thresholding. *IEEE transactions on information theory*, 41(3):613–627, 1995.

[157] Jean-Luc Starck, Jalal Fadili, and Fionn Murtagh. The undecimated wavelet decomposition and its reconstruction. *Image Processing, IEEE Transactions on*, 16(2):297–309, 2007.

[158] Aglika Gyaourova, Chandrika Kamath, and Imola K Fodor. Undecimated wavelet transforms for image de-noising. *Report, Lawrence Livermore National Lab., CA*, 18, 2002.

[159] Matthias Holschneider, Richard Kronland-Martinet, Jean Morlet, and Ph Tchamitchian. A real-time algorithm for signal analysis with the help of the wavelet transform. In *Wavelets*, pages 286–297. Springer, 1989.

[160] Jean-Luc Starck, Fionn D Murtagh, and Albert Bijaoui. *Image processing and data analysis: the multiscale approach.* Cambridge University Press, 1998.

[161] Jean-Luc Starck, Fionn Murtagii, and Albert Bijaoui. Multiresolution support applied to image filtering and restoration. *Graphical models and image processing*, 57(5):420–431, 1995.

[162] Francis J Anscombe. The transformation of poisson, binomial and negative-binomial data. *Biometrika*, pages 246–254, 1948.

[163] Bo Zhang, Jalal M Fadili, and Jean-Luc Starck. Wavelets, ridgelets, and curvelets for poisson noise removal. *Image Processing, IEEE Transactions on*, 17(7):1093–1108, 2008.

[164] Robert D Nowak and Richard G Baraniuk. Wavelet-domain filtering for photon imaging systems. *Image Processing, IEEE Transactions on*, 8(5):666–678, 1999.

[165] Bo Zhang, MJ Fadili, J-L Starck, and Seth W Digel. Fast poisson noise removal by biorthogonal haar domain hypothesis testing. *Statistical Methodology*, 5(4):387–396, 2008.

[166] Florian Luisier, Cédric Vonesch, Thierry Blu, and Michael Unser. Fast interscale wavelet denoising of poisson-corrupted images. *Signal Processing*, 90(2):415–427, 2010.

[167] Thierry Blu and Florian Luisier. The sure-let approach to image denoising. *Image Processing, IEEE Transactions on*, 16(11):2778–2786, 2007.

[168] Thibault Lagache, Nathalie Sauvonnet, Lydia Danglot, and Jean-Christophe Olivo-Marin. Statistical analysis of molecule colocalization in bioimaging. *Cytometry Part A*, 2015.

[169] Yong Wu, Vadim Zinchuk, Olga Grossenbacher-Zinchuk, and Enrico Stefani. Critical evaluation of quantitative colocalization analysis in confocal fluorescence microscopy. *Interdisciplinary Sciences: Computational Life Sciences*, 4(1):27–37, 2012.

[170] S Bolte and FP Cordelieres. A guided tour into subcellular colocalization analysis in light microscopy. *Journal of microscopy*, 224(3):213–232, 2006.

[171] Mats GL Gustafsson. Surpassing the lateral resolution limit by a factor of two using structured illumination microscopy. *Journal of microscopy*, 198(2):82–87, 2000.

[172] Stefan W Hell and Jan Wichmann. Breaking the diffraction resolution limit by stimulated emission: stimulated-emission-depletion fluorescence microscopy. *Optics letters*, 19(11):780–782, 1994.

[173] Michael J Rust, Mark Bates, and Xiaowei Zhuang. Sub-diffraction-limit imaging by stochastic optical reconstruction microscopy (storm). *Nature methods*, 3(10):793–796, 2006.

[174] Eric Betzig, George H Patterson, Rachid Sougrat, O Wolf Lindwasser, Scott Olenych, Juan S Bonifacino, Michael W Davidson, Jennifer Lippincott-Schwartz, and Harald F Hess. Imaging intracellular fluorescent proteins at nanometer resolution. *Science*, 313(5793):1642–1645, 2006.

[175] Rajesh Babu Sekar and Ammasi Periasamy. Fluorescence resonance energy transfer (fret) microscopy imaging of live cell protein localizations. *The Journal of cell biology*, 160(5):629–633, 2003.

[176] Kirsten Bacia, Sally A Kim, and Petra Schwille. Fluorescence cross-correlation spectroscopy in living cells. *Nature methods*, 3(2):83–89, 2006.

[177] Jeremy Adler and Ingela Parmryd. Colocalization analysis in fluorescence microscopy. In *Cell Imaging Techniques*, pages 97–109. Springer, 2013.

[178] EM Manders, J Stap, GJ Brakenhoff, R Van Driel, and JA Aten. Dynamics of three-dimensional replication patterns during the s-phase, analysed by double labelling of dna and confocal microscopy. *Journal of cell science*, 103(3):857–862, 1992.

[179] EMM Manders, FJ Verbeek, and JA Aten. Measurement of co-localization of objects in dual-colour confocal images. *Journal of microscopy*, 169(3):375–382, 1993.

[180] Vasanth R Singan, Thouis R Jones, Kathleen M Curran, and Jeremy C Simpson. Dual channel rank-based intensity weighting for quantitative co-localization of microscopy images. *BMC bioinformatics*, 12(1):407, 2011.

[181] Fabian Humpert, Idir Yahiatene, Martina Lummer, Markus Sauer, and Thomas Huser. Quantifying molecular colocalization in live cell fluorescence microscopy. *Journal of biophotonics*, 8(1-2):124–132, 2015.

[182] Sylvain V Costes, Dirk Daelemans, Edward H Cho, Zachary Dobbin, George Pavlakis, and Stephen Lockett. Automatic and quantitative measurement of protein-protein colocalization in live cells. *Biophysical journal*, 86(6):3993–4003, 2004.

[183] Mehul Shah, Kirit Patel, Somshuvra Mukhopadhyay, Fang Xu, Gary Guo, and Pravin B Sehgal. Membrane-associated stat3 and py-stat3 in the cytoplasm. *Journal of Biological Chemistry*, 281(11):7302–7308, 2006.

[184] Rafal Robert Nazarewicz, Gloria Salazar, Nikolay Patrushev, Alejandra San Martin, Lula Hilenski, Shiqin Xiong, and R Wayne Alexander. Early endosomal antigen 1 (eea1) is an obligate scaffold for angiotensin ii-induced, pkc-α-dependent akt activation in endosomes. *Journal of Biological Chemistry*, 286(4):2886–2895, 2011.

[185] Loredana Petecchia, Federica Sabatini, Cesare Usai, Emanuela Caci, Luigi Varesio, and Giovanni A Rossi. Cytokines induce tight junction disassembly in airway cells via an egfr-dependent mapk/erk1/2-pathway. *Laboratory Investigation*, 92(8):1140–1148, 2012.

[186] Johannes Schindelin, Ignacio Arganda-Carreras, Erwin Frise, Verena Kaynig, Mark Longair, Tobias Pietzsch, Stephan Preibisch, Curtis Rueden, Stephan Saalfeld, Benjamin Schmid, et al. Fiji: an open-source platform for biological-image analysis. *Nature methods*, 9(7):676–682, 2012.

[187] Clifford M Babbey, Nahid Ahktar, Exing Wang, Carlos Chih-Hsiung Chen, Barth D Grant, and Kenneth W Dunn. Rab10 regulates membrane transport through early endosomes of polarized madin-darby canine kidney cells. *Molecular biology of the cell*, 17(7):3156–3175, 2006.

[188] Jonathan WD Comeau, Santiago Costantino, and Paul W Wiseman. A guide to accurate fluorescence microscopy colocalization measurements. *Biophysical journal*, 91(12):4611–4622, 2006.

[189] Jorge Ignacio Villalta, Soledad Galli, María Florencia Iacaruso, VG Antico Arciuch, Juan José Poderoso, Elizabeth Andrea Jares-Erijman, and Lía Isabel Pietrasanta. New algorithm to determine true colocalization in combination with image restoration and time-lapse confocal microscopy to map kinases in mitochondria. *PloS one*, 6(4):e19031–e19031, 2011.

[190] O Ramirez, A Garcia, R Rojas, A Couve, and S Härtel. Confined displacement algorithm determines true and random colocalization in fluorescence microscopy. *Journal of microscopy*, 239(3):173–183, 2010.

[191] Mark RT Dale and Marie-Josée Fortin. *Spatial analysis: a guide for ecologists.* Cambridge University Press, 2014.

[192] Jean-Christophe Olivo-Marin. Extraction of spots in biological images using multiscale products. *Pattern recognition*, 35(9):1989–1996, 2002.

[193] Fabrice De Chaumont, Stéphane Dallongeville, Nicolas Chenouard, Nicolas Hervé, Sorin Pop, Thomas Provoost, Vannary Meas-Yedid, Praveen Pankajakshan, Timothée Lecomte, Yoann Le Montagner, et al. Icy: an open bioimage informatics platform for extended reproducible research. *Nature methods*, 9(7):690–696, 2012.

[194] Philip J Clark and Francis C Evans. Distance to nearest neighbor as a measure of spatial relationships in populations. *Ecology*, pages 445–453, 1954.

[195] Brian D Ripley. The second-order analysis of stationary point processes. *Journal of applied probability*, pages 255–266, 1976.

[196] Philip M Dixon. Ripley's k function. *Encyclopedia of environmetrics*, 2002.

[197] George LW Perry, Ben P Miller, and Neal J Enright. A comparison of methods for the statistical analysis of spatial point patterns in plant ecology. *Plant Ecology*, 187(1):59–82, 2006.

[198] E Lachmanovich, DE Shvartsman, Y Malka, C Botvin, YI Henis, and AM Weiss. Co-localization analysis of complex formation among membrane proteins by computerized fluorescence microscopy: application to immunofluorescence co-patching studies. *Journal of microscopy*, 212(2):122–131, 2003.

[199] Thibault Lagache, Vannary Meas-Yedid, and Jean-Christophe Olivo-Marin. A statistical analysis of spatial colocalization using ripley's k function. In *ISBI*, pages 896–901, 2013.

[200] Jo A Helmuth, Grégory Paul, and Ivo F Sbalzarini. Beyond co-localization: inferring spatial interactions between sub-cellular structures from microscopy images. *BMC bioinformatics*, 11(1):372, 2010.

[201] Ivo F Sbalzarini. Seeing is believing: Quantifying is convincing: Computational image analysis in biology. In *Focus on Bio-Image Informatics*, pages 1–39. Springer, 2016.

[202] Pierre Soille and Luc M Vincent. Determining watersheds in digital pictures via flooding simulations. In *Lausanne-DL tentative*, pages 240–250. International Society for Optics and Photonics, 1990.

[203] Grégory Paul, Janick Cardinale, and Ivo F Sbalzarini. Coupling image restoration and segmentation: a generalized linear model/bregman perspective. *International Journal of Computer Vision*, 104(1):69–93, 2013.

[204] Aurélien Rizk, Grégory Paul, Pietro Incardona, Milica Bugarski, Maysam Mansouri, Axel Niemann, Urs Ziegler, Philipp Berger, and Ivo F Sbalzarini. Segmentation and quantification of subcellular structures in fluorescence microscopy images using squassh. *Nature protocols*, 9(3):586–596, 2014.

[205] Janick Cardinale, Grégory Paul, and Ivo F Sbalzarini. Discrete region competition for unknown numbers of connected regions. *IEEE Transactions on Image Processing*, 21(8):3531–3545, 2012.

[206] Fernando Amat, William Lemon, Daniel P Mossing, Katie McDole, Yinan Wan, Kristin Branson, Eugene W Myers, and Philipp J Keller. Fast, accurate reconstruction of cell lineages from large-scale fluorescence microscopy data. *Nature methods*, 2014.

[207] Gang Lin, Umesh Adiga, Kathy Olson, John F Guzowski, Carol A Barnes, and Badrinath Roysam. A hybrid 3d watershed algorithm incorporating gradient cues and object models for automatic segmentation of nuclei in confocal image stacks. *Cytometry Part A*, 56(1):23–36, 2003.

[208] Christoph Sommer and Daniel W Gerlich. Machine learning in cell biology–teaching computers to recognize phenotypes. *J Cell Sci*, 126(24):5529–5539, 2013.

[209] Michael Held, Michael HA Schmitz, Bernd Fischer, Thomas Walter, Beate Neumann, Michael H Olma, Matthias Peter, Jan Ellenberg, and Daniel W Gerlich. Cellcognition: time-resolved phenotype annotation in high-throughput live cell imaging. *Nature methods*, 7(9):747–754, 2010.

[210] Bernhard E Boser, Isabelle M Guyon, and Vladimir N Vapnik. A training algorithm for optimal margin classifiers. In *Proceedings of the fifth annual workshop on Computational learning theory*, pages 144–152. ACM, 1992.

[211] Yoav Freund and Robert E Schapire. A desicion-theoretic generalization of on-line learning and an application to boosting. In *European conference on computational learning theory*, pages 23–37. Springer, 1995.

[212] Leo Breiman. Random forests. *Machine learning*, 45(1):5–32, 2001.

[213] Christoph Sommer, Christoph Straehle, Ullrich Köthe, and Fred A Hamprecht. Ilastik: Interactive learning and segmentation toolkit. In *2011 IEEE international symposium on biomedical imaging: From nano to macro*, pages 230–233. IEEE, 2011.

[214] Stanley Osher and James A Sethian. Fronts propagating with curvature-dependent speed: algorithms based on hamilton-jacobi formulations. *Journal of computational physics*, 79(1):12–49, 1988.

[215] Chenyang Xu, Dzung L Pham, and Jerry L Prince. Image segmentation using deformable models. *Handbook of medical imaging*, 2:129–174, 2000.

[216] Tim McInerney and Demetri Terzopoulos. Deformable models in medical image analysis: a survey. *Medical image analysis*, 1(2):91–108, 1996.

[217] Michael Kass, Andrew Witkin, and Demetri Terzopoulos. Snakes: Active contour models. *International journal of computer vision*, 1(4):321–331, 1988.

[218] Derek Molloy and Paul F Whelan. Active-meshes. *Pattern Recognition Letters*, 21(12):1071–1080, 2000.

[219] Alexandre Dufour, Roman Thibeaux, Elisabeth Labruyere, Nancy Guillén, and Jean-Christophe Olivo-Marin. 3-d active meshes: fast discrete deformable models for cell tracking in 3-d time-lapse microscopy. *Image Processing, IEEE Transactions on*, 20(7):1925–1937, 2011.

[220] Stanley Osher and Ronald Fedkiw. *Level set methods and dynamic implicit surfaces*, volume 153. Springer Science & Business Media, 2006.

[221] Vicent Caselles, Francine Catté, Tomeu Coll, and Françoise Dibos. A geometric model for active contours in image processing. *Numerische mathematik*, 66(1):1–31, 1993.

[222] Ravikanth Malladi, James Sethian, Baba C Vemuri, et al. Shape modeling with front propagation: A level set approach. *Pattern Analysis and Machine Intelligence, IEEE Transactions on*, 17(2):158–175, 1995.

[223] Hong-Kai Zhao, Tony Chan, Barry Merriman, and Stanley Osher. A variational level set approach to multiphase motion. *Journal of computational physics*, 127(1):179–195, 1996.

[224] Chunming Li, Chenyang Xu, Changfeng Gui, and Martin D Fox. Level set evolution without re-initialization: a new variational formulation. In *Computer Vision and Pattern Recognition, 2005. CVPR 2005. IEEE Computer Society Conference on*, volume 1, pages 430–436. IEEE, 2005.

[225] Chunming Li, Chenyang Xu, Changfeng Gui, and Martin D Fox. Distance regularized level set evolution and its application to image segmentation. *Image Processing, IEEE Transactions on*, 19(12):3243–3254, 2010.

[226] Martin Maška, Vladimír Ulman, David Svoboda, Pavel Matula, Petr Matula, Cristina Ederra, Ainhoa Urbiola, Tomás España, Subramanian Venkatesan, Deepak MW Balak, et al. A benchmark for comparison of cell tracking algorithms. *Bioinformatics*, 30(11):1609–1617, 2014.

[227] Stuart P Lloyd. Least squares quantization in pcm. *Information Theory, IEEE Transactions on*, 28(2):129–137, 1982.

[228] Alexandre Dufour, Vasily Shinin, Shahragim Tajbakhsh, Nancy Guillén-Aghion, Jean-Christophe Olivo-Marin, and Christophe Zimmer. Segmenting and tracking fluorescent cells in dynamic 3-d microscopy with coupled active surfaces. *Image Processing, IEEE Transactions on*, 14(9):1396–1410, 2005.

[229] Martin Maška, Arrate Muñoz-Barrutia, and Carlos Ortiz-de Solórzano. Fast tracking of fluorescent cells based on the chan-vese model. In *Biomedical Imaging (ISBI), 2012 9th IEEE International Symposium on*, pages 1316–1319. IEEE, 2012.

[230] Martin Maska, Ondrej Danek, Saray Garasa, Ana Rouzaut, Arrate Munoz-Barrutia, and Carlos Ortiz-de Solorzano. Segmentation and shape tracking of whole fluorescent cells based on the chan–vese model. *Medical Imaging, IEEE Transactions on*, 32(6):995–1006, 2013.

[231] Michael E Leventon, W Eric L Grimson, and Olivier Faugeras. Statistical shape influence in geodesic active contours. In *Computer Vision and Pattern Recognition, 2000. Proceedings. IEEE Conference on*, volume 1, pages 316–323. IEEE, 2000.

[232] Andy Tsai, Anthony Yezzi Jr, William Wells, Clare Tempany, Dewey Tucker, Ayres Fan, W Eric Grimson, and Alan Willsky. A shape-based approach to the segmentation of medical imagery using level sets. *Medical Imaging, IEEE Transactions on*, 22(2):137–154, 2003.

[233] Michael Lynch, Ovidiu Ghita, and Paul F Whelan. Segmentation of the left ventricle of the heart in 3-d+ t mri data using an optimized nonrigid temporal model. *Medical Imaging, IEEE Transactions on*, 27(2):195–203, 2008.

[234] Yuri Y Boykov and Marie-Pierre Jolly. Interactive graph cuts for optimal boundary & region segmentation of objects in nd images. In *Computer Vision, 2001. ICCV 2001. Proceedings. Eighth IEEE International Conference on*, volume 1, pages 105–112. IEEE, 2001.

[235] Herve Lombaert, Yiyong Sun, and Farida Cheriet. Fast 4d segmentation of large datasets using graph cuts. In *SPIE Medical Imaging*, pages 79622H–79622H. International Society for Optics and Photonics, 2011.

[236] D Pastor, MA Luengo-Oroz, B Lombardot, I Gonzalvez, L Duloquin, T Savy, P Bourgine, Nadine Peyriéras, and A Santos. Cell tracking in fluorescence images of embryogenesis processes with morphological reconstruction by 4d-tubular structuring elements. In *Engineering in Medicine and Biology Society, 2009. EMBC 2009. Annual International Conference of the IEEE*, pages 970–973. IEEE, 2009.

[237] David Pastor-Escuredo, Miguel A Luengo-Oroz, Louise Duloquin, Benoit Lombardot, M Ledesma-Carbayo, Paul Bourgine, Nadine Peyrieras, and Andrés Santos. Spatio-temporal filtering with morphological operators for robust cell migration estimation in in-vivo images. In *Biomedical Imaging (ISBI), 2012 9th IEEE International Symposium on*, pages 1312–1315. IEEE, 2012.

[238] Miguel A Luengo-Oroz, David Pastor-Escuredo, Carlos Castro-Gonzalez, Emmanuel Faure, Thierry Savy, Benoit Lombardot, Jose L Rubio-Guivernau, Louise Duloquin, Maria J Ledesma-Carbayo, Paul Bourgine, et al. Morphological processing: Applications to embryogenesis image analysis. *Image Processing, IEEE Transactions on*, 21(8):3518–3530, 2012.

[239] Dirk Ryan Padfield, Jens Rittscher, Thomas Sebastian, Nick Thomas, and Badrinath Roysam. Spatio-temporal cell cycle analysis using 3d level set segmentation of unstained nuclei in line scan confocal fluorescence images. In *Biomedical Imaging: Nano to Macro, 2006. 3rd IEEE International Symposium on*, pages 1036–1039. IEEE, 2006.

[240] Dirk Padfield, Jens Rittscher, and Badrinath Roysam. Spatio-temporal cell segmentation and tracking for automated screening. In *Biomedical Imaging: From Nano to Macro, 2008. ISBI 2008. 5th IEEE International Symposium on*, pages 376–379. IEEE, 2008.

[241] Dirk Padfield, Jens Rittscher, Nick Thomas, and Badrinath Roysam. Spatiotemporal cell cycle phase analysis using level sets and fast marching methods. *Medical image analysis*, 13(1):143–155, 2009.

[242] Guy Gilboa, Nir Sochen, and Yehoshua Y Zeevi. Forward-and-backward diffusion processes for adaptive image enhancement and denoising. *Image Processing, IEEE Transactions on*, 11(7):689–703, 2002.

[243] Daniel Cremers. Dynamical statistical shape priors for level set-based tracking. *Pattern Analysis and Machine Intelligence, IEEE Transactions on*, 28(8):1262–1273, 2006.

[244] Blagoy Blagoev, Irina Kratchmarova, Shao-En Ong, Mogens Nielsen, Leonard J Foster, and Matthias Mann. A proteomics strategy to elucidate functional protein-protein interactions applied to egf signaling. *Nature biotechnology*, 21(3):315–318, 2003.

[245] Debbie L Cunningham, Steve MM Sweet, Helen J Cooper, and John K Heath. Differential phosphoproteomics of fibroblast growth factor signaling: identification of src family kinase-mediated phosphorylation events. *Journal of proteome research*, 9(5):2317–2328, 2010.

[246] Sarah J Parsons and J Thomas Parsons. Src family kinases, key regulators of signal transduction. *Oncogene*, 23(48):7906–7909, 2004.

[247] Arthur Edelstein, Nenad Amodaj, Karl Hoover, Ron Vale, and Nico Stuurman. Computer control of microscopes using μmanager. *Current protocols in molecular biology*, pages 14–20, 2010.

[248] Fangtian Huang, Anastasia Khvorova, William Marshall, and Alexander Sorkin. Analysis of clathrin-mediated endocytosis of epidermal growth factor receptor by rna interference. *Journal of Biological Chemistry*, 279(16):16657–16661, 2004.

[249] Fabrizio Capuani, Alexia Conte, Elisabetta Argenzio, Luca Marchetti, Corrado Priami, Simona Polo, Pier Paolo Di Fiore, Sara Sigismund, and Andrea Ciliberto. Quantitative analysis reveals how egfr activation and downregulation are coupled in normal but not in cancer cells. *Nature communications*, 6, 2015.

[250] Takashi Joh, Makoto Itoh, Kohei Katsumi, Yoshifumi Yokoyama, Toshihiko Takeuchi, Taiji Kato, Yoshiro Wada, and Ryo Tanaka. Physiological concentrations of human epidermal growth factor in biological fluids: use of a sensitive enzyme immunoassay. *Clinica chimica acta*, 158(1):81–90, 1986.

[251] Daniel Sage, Dimiter Prodanov, Jean-Yves Tinevez, and Johannes Schindelin. Mij: making interoperability between imagej and matlab possible. In *ImageJ User & Developer Conference*, pages 24–26, 2012.

[252] Stanley R Sternberg. Biomedical image processing. *Computer*, 16(1):22–34, 1983.

[253] Ronald Aylmer Fisher. *Statistical methods for research workers.* Genesis Publishing Pvt Ltd, 1925.

[254] Yoav Benjamini and Yosef Hochberg. Controlling the false discovery rate: a practical and powerful approach to multiple testing. *Journal of the Royal Statistical Society. Series B (Methodological)*, pages 289–300, 1995.

[255] Pankaj Kumar, Germaine Goh, Sarawut Wongphayak, Dimitri Moreau, and Frédéric Bard. Screensifter: analysis and visualization of rnai screening data. *BMC bioinformatics*, 14(1):1, 2013.

[256] Patrycja Kozik, Nicola A Hodson, Daniela A Sahlender, Nikol Simecek, Christina Soromani, Jiahua Wu, Lucy M Collinson, and Margaret S Robinson. A human genome-wide screen for regulators of clathrin-coated vesicle formation reveals an unexpected role for the v-atpase. *Nature cell biology*, 15(1):50–60, 2013.

[257] Ferran Valderrama and Anne J Ridley. Getting invasive with gep100 and arf6. *Nature cell biology*, 10(1):16–18, 2008.

[258] Jillian L Dunphy, Radim Moravec, Kim Ly, Troy K Lasell, Paul Melancon, and James E Casanova. The arf6 gef gep100/brag2 regulates cell adhesion by controlling endocytosis of $\beta 1$ integrins. *Current Biology*, 16(3):315–320, 2006.

[259] Radim Moravec, Kathryn K Conger, Ryan D'Souza, Anne B Allison, and James E Casanova. Brag2/gep100/iqsec1 interacts with clathrin and regulates $\alpha 5 \beta 1$ integrin endocytosis through activation of adp ribosylation factor 5 (arf5). *Journal of Biological Chemistry*, 287(37):31138–31147, 2012.

[260] Nicola De Franceschi, Hellyeh Hamidi, Jonna Alanko, Pranshu Sahgal, and Johanna Ivaska. Integrin traffic–the update. *Journal of cell science*, 128(5):839–852, 2015.

[261] Christopher W Cowan, Yu Raymond Shao, Mustafa Sahin, Steven M Shamah, Michael Z Lin, Paul L Greer, Sizhen Gao, Eric C Griffith, Joan S Brugge, and Michael E Greenberg. Vav family gefs link activated ephs to endocytosis and axon guidance. *Neuron*, 46(2):205–217, 2005.

[262] Hiroyuki Nagai, Sayaka Yasuda, Yusuke Ohba, Mitsunori Fukuda, and Takeshi Nakamura. All members of the epi64 subfamily of tbc/rabgaps also have gap activities towards ras. *Journal of biochemistry*, 153(3):283–288, 2013.

[263] Evelyn Fuchs, Alexander K Haas, Robert A Spooner, Shin-ichiro Yoshimura, J Michael Lord, and Francis A Barr. Specific rab gtpase-activating proteins define the shiga toxin and epidermal growth factor uptake pathways. *The Journal of cell biology*, 177(6):1133–1143, 2007.

[264] Laurent Chesneau, Daphné Dambournet, Mickaël Machicoane, Ilektra Kouranti, Mitsunori Fukuda, Bruno Goud, and Arnaud Echard. An arf6/rab35 gtpase cascade for endocytic recycling and successful cytokinesis. *Current Biology*, 22(2):147–153, 2012.

[265] Matthew NJ Seaman, Michael E Harbour, Daniel Tattersall, Eliot Read, and Nicholas Bright. Membrane recruitment of the cargo-selective retromer subcomplex is catalysed by the small gtpase rab7 and inhibited by the rab-gap tbc1d5. *Journal of cell science*, 122(14):2371–2382, 2009.

[266] Michael E Harbour, Sophia YA Breusegem, Robin Antrobus, Caroline Freeman, Evan Reid, and Matthew NJ Seaman. The cargo-selective retromer complex is a recruiting hub for protein complexes that regulate endosomal tubule dynamics. *Journal of cell science*, 123(21):3703–3717, 2010.

[267] Matthew NJ Seaman. The retromer complex–endosomal protein recycling and beyond. *Journal of cell science*, 125(20):4693–4702, 2012.

[268] Matthew NJ Seaman, Alexis Gautreau, and Daniel D Billadeau. Retromer-mediated endosomal protein sorting: all washed up! *Trends in cell biology*, 23(11):522–528, 2013.

[269] Christopher A Lamb, Hannah C Dooley, and Sharon A Tooze. Endocytosis and autophagy: Shared machinery for degradation. *Bioessays*, 35(1):34–45, 2013.

[270] Doris Popovic and Ivan Dikic. Tbc1d5 and the ap2 complex regulate atg9 trafficking and initiation of autophagy. *EMBO reports*, page e201337995, 2014.

[271] Brian P Ceresa and Steven J Bahr. rab7 activity affects epidermal growth factor: epidermal growth factor receptor degradation by regulating endocytic trafficking from the late endosome. *Journal of Biological Chemistry*, 281(2):1099–1106, 2006.

[272] Ming Zhang, Li Chen, Shicong Wang, and Tuanlao Wang. Rab7: roles in membrane trafficking and disease. *Bioscience reports*, 29(3):193–209, 2009.

[273] Tuanlao Wang, Ming Zhang, Zexu Ma, Ke Guo, Vinay Tergaonkar, Qi Zeng, and Wanjin Hong. A role of rab7 in stabilizing egfr-her2 and in sustaining akt survival signal. *Journal of cellular physiology*, 227(6):2788–2797, 2012.

[274] Phillip A Vanlandingham and Brian P Ceresa. Rab7 regulates late endocytic trafficking downstream of multivesicular body biogenesis and cargo sequestration. *Journal of Biological Chemistry*, 284(18):12110–12124, 2009.

[275] Letizia Lanzetti, Vladimir Rybin, Maria Grazia Malabarba, Savvas Christoforidis, Giorgio Scita, Marino Zerial, and Pier Paolo Di Fiore. The eps8 protein coordinates egf receptor signalling through rac and trafficking through rab5. *Nature*, 408(6810):374–377, 2000.

[276] M Alejandro Barbieri, Richard L Roberts, Aysel Gumusboga, Hilary Highfield, Carmen Alvarez-Dominguez, Alan Wells, and Philip D Stahl. Epidermal growth factor and membrane trafficking egf receptor activation of endocytosis requires rab5a. *The Journal of cell biology*, 151(3):539–550, 2000.

[277] Lenka Martinu, Ademi Santiago-Walker, Hongwei Qi, and Margaret M Chou. Endocytosis of epidermal growth factor receptor regulated by grb2-mediated recruitment of the rab5 gtpase-activating protein rn-tre. *Journal of Biological Chemistry*, 277(52):50996–51002, 2002.

[278] Andrea Palamidessi, Emanuela Frittoli, Nadia Ducano, Nina Offenhauser, Sara Sigismund, Hiroaki Kajiho, Dario Parazzoli, Amanda Oldani, Marco Gobbi, Guido Serini, et al. The gtpase-activating protein rn-tre controls focal adhesion turnover and cell migration. *Current Biology*, 23(23):2355–2364, 2013.

[279] Alexander K Haas, Evelyn Fuchs, Robert Kopajtich, and Francis A Barr. A gtpase-activating protein controls rab5 function in endocytic trafficking. *Nature Cell Biology*, 7(9):887–893, 2005.

[280] Letizia Lanzetti, Andrea Palamidessi, Liliana Areces, Giorgio Scita, and Pier Paolo Di Fiore. Rab5 is a signalling gtpase involved in actin remodelling by receptor tyrosine kinases. *Nature*, 429(6989):309–314, 2004.

[281] Tetsuo Yamazaki, Kristien Zaal, Dale Hailey, John Presley, Jennifer Lippincott-Schwartz, and Lawrence E Samelson. Role of grb2 in egf-stimulated egfr internalization. *Journal of cell science*, 115(9):1791–1802, 2002.

[282] Jung-Mao Hsu, Chun-Te Chen, Chao-Kai Chou, Hsu-Ping Kuo, Long-Yuan Li, Chun-Yi Lin, Hong-Jen Lee, Ying-Nai Wang, Mo Liu, Hsin-Wei Liao, et al. Crosstalk between arg 1175 methylation and tyr 1173 phosphorylation negatively modulates egfr-mediated erk activation. *Nature cell biology*, 13(2):174–181, 2011.

[283] Ellen D Stück, Randolph N Christensen, J Russell Huie, C Amy Tovar, Brandon A Miller, Yvette S Nout, Jacqueline C Bresnahan, Michael S Beattie, and Adam R Ferguson. Tumor necrosis factor alpha mediates gaba a receptor trafficking to the plasma membrane of spinal cord neurons in vivo. *Neural plasticity*, 2012, 2012.

[284] Rushika M Perera, Roberto Zoncu, Terrance G Johns, Marc Pypaert, Fook-Thean Lee, Ira Mellman, Lloyd J Old, Derek K Toomre, and Andrew M Scott. Internalization, intracellular trafficking, biodistribution of monoclonal antibody 806: A novel anti-epidermal growth factor receptor antibody. *Neoplasia*, 9(12):1099–1110, 2007.

[285] John P Holleran, Jianxin Zeng, Raymond A Frizzell, and Simon C Watkins. Regulated recycling of mutant cftr is partially restored by pharmacological treatment. *Journal of cell science*, 126(12):2692–2703, 2013.

[286] EJ Adie, S Kalinka, L Smith, MJ Francis, A Marenghi, ME Cooper, M Briggs, NP Michael, G Milligan, and S Game. A ph-sensitive fluor, cypher 5, used to monitor agonist-induced g protein-coupled receptor internalization in live cells. *Biotechniques*, 33(5):1152–1157, 2002.

[287] Hui Li, Zhao-Wen Duan, Ping Xie, Yu-Ru Liu, Wei-Chi Wang, Shuo-Xing Dou, and Peng-Ye Wang. Effects of paclitaxel on egfr endocytic trafficking revealed using quantum dot tracking in single cells. *PloS one*, 7(9), 2012.

[288] Nir Osherov and Alexander Levitzki. Epidermal-growth-factor-dependent activation of the src-family kinases. *European Journal of Biochemistry*, 225(3):1047–1053, 1994.

[289] Mirko HH Schmidt, Frank B Furnari, Webster K Cavenee, and Oliver Bögler. Epidermal growth factor receptor signaling intensity determines intracellular protein interactions, ubiquitination, and internalization. *Proceedings of the National Academy of Sciences*, 100(11):6505–6510, 2003.

[290] Qian Wang, Greg Villeneuve, and Zhixiang Wang. Control of epidermal growth factor receptor endocytosis by receptor dimerization, rather than receptor kinase activation. *EMBO reports*, 6(10):942–948, 2005.

[291] Boyan K Garvalov, Franziska Foss, Anne-Theres Henze, Ioanna Bethani, Sabine Gräf-Höchst, Devendra Singh, Alina Filatova, Higinio Dopeso, Sascha Seidel, Miriam Damm, et al. Phd3 regulates egfr internalization and signalling in tumours. *Nature communications*, 5, 2014.

[292] Chaojie Gong, Jubo Zhang, Lan Zhang, Yingcong Wang, Hui Ma, Weizhong Wu, Jiefeng Cui, Yanhong Wang, and Zhenggang Ren. Dynamin2 downregulation delays egfr endocytic trafficking and promotes egfr signaling and invasion in hepatocellular carcinoma. *American journal of cancer research*, 5(2):702, 2015.

[293] Louis J Lombardo, Francis Y Lee, Ping Chen, Derek Norris, Joel C Barrish, Kamelia Behnia, Stephen Castaneda, Lyndon AM Cornelius, Jagabandhu Das, Arthur M Doweyko, et al. Discovery of n-(2-chloro-6-methyl-phenyl)-2-(6-(4-(2-hydroxyethyl)-piperazin-1-yl)-2-methylpyrimidin-4-ylamino) thiazole-5-carboxamide (bms-354825), a dual src/abl kinase inhibitor with potent antitumor activity in preclinical assays. *Journal of medicinal chemistry*, 47(27):6658–6661, 2004.

[294] Jyoti Nautiyal, Pralay Majumder, Bhaumik B Patel, Francis Y Lee, and Adhip PN Majumdar. Src inhibitor dasatinib inhibits growth of breast cancer cells by modulating egfr signaling. *Cancer letters*, 283(2):143–151, 2009.

[295] Yu-Chin Lin, Meng-Hsuan Wu, Tzu-Tang Wei, Shu-Hui Chung, Kuen-Feng Chen, Ann-Lii Cheng, and Ching-Chow Chen. Degradation of epidermal growth factor

receptor mediates dasatinib-induced apoptosis in head and neck squamous cell carcinoma cells. *Neoplasia*, 14(6):463–IN3, 2012.

[296] William H Kruskal and W Allen Wallis. Use of ranks in one-criterion variance analysis. *Journal of the American statistical Association*, 47(260):583–621, 1952.

[297] Henry B Mann and Donald R Whitney. On a test of whether one of two random variables is stochastically larger than the other. *The annals of mathematical statistics*, pages 50–60, 1947.

[298] Chun Hung Li and CK Lee. Minimum cross entropy thresholding. *Pattern Recognition*, 26(4):617–625, 1993.

[299] CH Li and Peter Kwong-Shun Tam. An iterative algorithm for minimum cross entropy thresholding. *Pattern Recognition Letters*, 19(8):771–776, 1998.

[300] Duaa H AlSaeed, Ali El-Zaart, and Ahmed Bouridane. Minimum cross entropy thresholding using entropy-li based on log-normal distribution for skin cancer images. In *Signal-Image Technology and Internet-Based Systems (SITIS), 2011 Seventh International Conference on*, pages 426–430. IEEE, 2011.

[301] Gražvydas Lukinavičius, Claudia Blaukopf, Elias Pershagen, Alberto Schena, Luc Reymond, Emmanuel Derivery, Marcos Gonzalez-Gaitan, Elisa DEste, Stefan W Hell, Daniel Wolfram Gerlich, et al. Sir-hoechst is a far-red dna stain for live-cell nanoscopy. *Nature communications*, 6, 2015.

[302] John H McDonald. *Handbook of biological statistics*, volume 2. Sparky House Publishing Baltimore, MD, 2009.

[303] Itziar Pinilla-Macua and Alexander Sorkin. Methods to study endocytic trafficking of the egf receptor. *Methods in cell biology*, 130:347–367, 2015.

[304] Morten P Oksvold, Nina Marie Pedersen, Lise Forfang, and Erlend B Smeland. Effect of cycloheximide on epidermal growth factor receptor trafficking and signaling. *FEBS letters*, 586(20):3575–3581, 2012.

[305] Eric Macia, Marcelo Ehrlich, Ramiro Massol, Emmanuel Boucrot, Christian Brunner, and Tomas Kirchhausen. Dynasore, a cell-permeable inhibitor of dynamin. *Developmental cell*, 10(6):839–850, 2006.

[306] Alexander Levitzki and Aviv Gazit. Tyrosine kinase inhibition: an approach to drug development. *Science*, 267(5205):1782–1788, 1995.

[307] Mikala Egeblad, Ole H Mortensen, Léon CLT van Kempen, and Marja Jäättelä. Bibx1382bs, but not ag1478 or pd153035, inhibits the erbb kinases at different concentrations in intact cells. *Biochemical and biophysical research communications*, 281(1):25–31, 2001.

[308] Inger Helene Madshus and Espen Stang. Internalization and intracellular sorting of the egf receptor: a model for understanding the mechanisms of receptor trafficking. *Journal of cell science*, 122(19):3433–3439, 2009.

[309] Christophe Lamaze and Sandra L Schmid. Recruitment of epidermal growth factor receptors into coated pits requires their activated tyrosine kinase. *The Journal of Cell Biology*, 129(1):47–54, 1995.

[310] Fangtian Huang and Alexander Sorkin. Growth factor receptor binding protein 2-mediated recruitment of the ring domain of cbl to the epidermal growth factor receptor is essential and sufficient to support receptor endocytosis. *Molecular biology of the cell*, 16(3):1268–1281, 2005.

[311] Yi Wang, Steven Pennock, Xinmei Chen, and Zhixiang Wang. Endosomal signaling of epidermal growth factor receptor stimulates signal transduction pathways leading to cell survival. *Molecular and cellular biology*, 22(20):7279–7290, 2002.

[312] Qian Wang, Xinmei Chen, and Zhixiang Wang. Dimerization drives egfr endocytosis through two sets of compatible endocytic codes. *Journal of cell science*, 128(5):935–950, 2015.